Application of the Radiosity Approach to the Radiation Balance in Complex Terrain

DISSERTATION

zur

Erlangung der naturwissenschaftlichen Doktorwürde
(Dr. sc. nat.)

vorgelegt der

Mathematisch-naturwissenschaftlichen Fakultät
der
Universität Zürich
von

Nora Helbig
aus Deutschland

Promotionskomitee
Prof. Dr. Wilfried Haeberli (Vorsitz)
Dr. Michael Lehning (Leitung der Dissertation)
Dr. Henning Löwe (Leitung der Dissertation)

Zürich 2009

Contents

Summary

This thesis addresses the detailed description of the radiation balance in complex terrain to improve the determination of local surface characteristics. The radiation balance in complex terrain is best described by a three-dimensional radiation balance model, which accounts for terrain influences. However, here, the radiation balance model has to remain a module of the modular model system Alpine3D for alpine surface processes. This means, the atmosphere is included by only one horizontal layer in the radiation balance model such that it can be driven by a single, exposed radiation measurement. Therefore, the development of the radiation balance model is restricted in the sense of complexity.
In particular, the research of this thesis focussed on the development of a radiation balance model which accounts for a detailed treatment of (i) shading and (ii) multiple terrain reflections and emissions but which, in the same time, remained a module of the surface process model Alpine3D.

The radiation balance model in Alpine3D computes spatial incident direct and diffuse sky radiation values under cloudy sky conditions from empirical parameterisations. Those parameterisations are critically reviewed, extended and partly replaced.
In order to enable an accurate representation of shading from mountains as well as of visibility between surfaces more robust algorithms are implemented that determine mutual visibility between individual grid surfaces. Additionally, the representation of steep terrain ridges by digital height models is improved by applying the extraction method of terrain parameters of Corripio (2002).
The radiosity approach is selected to satisfy the restrictions of the development of a detailed radiation balance model that accounts for anisotropic terrain effects but remains a module of the surface process model Alpine3D. Thereby, the radiosity approach is applied for the first time to compute the three-dimensional radiation balance in complex terrain. Its application can be seen to fill the presently large gap in complexity between three-dimensional radiation models for a cloudy atmosphere and models applying the so-called isotropic view factor approach (that approximates the visible terrain by means of an isotropic surface). In contrast to the isotropic view factor approach the radiosity approach uses anisotropic view factors and does include (anisotropic) multiple terrain reflections. The radiosity equation was first introduced in computer graphics applying techniques originally developed in thermal engineering to describe the exchange of radiant energy between surfaces.
Some numerical methods are extended and tailored to special characteristics of the radiation problem: Progressive Refinement iteration is chosen to solve the discretised radiosity equation in complex terrain. The iteration order criterion of Cohen et al. (1988) with the largest unshot radiant power in the model domain is adapted to include the terrain view factor sum. A new stopping criterion was developed for the iterative solution of the linear system of the radiosity equation. This criterion can be related to the true error via some bound.

The newly developed radiation balance model is verified with point measurements and sensitivity studies.

On the one hand, permanent radiation measurements at Weissfluhjoch study site at 2540 m a.s.l. close to Davos, Switzerland are used. For clear sky days the modelled values with the reviewed and extended clear sky parameterisations resemble the measured components well. It turned out as a main result that the lack of an adequate decomposition model for the extraction of cloudy sky radiation components out of one measured global radiation value is leading to inaccurately modelled radiation components. The measured diffuse sky radiation is mostly overestimated whereas the measured direct radiation is mostly underestimated by the modelled values.

On the other hand, a new measurement is designed to characterise the terrain radiation. Modelled and measured terrain reflected radiation values agree quite well. A measured horizon line with a tachymeter confirms that the new visibility algorithm works well.

In order to assess the radiosity approach in the context of existing model approaches a comparison is made with both, simpler models and more sophisticated models. When compared to a full three-dimensional radiative transfer Monte Carlo model for a cloudy atmosphere, namely MYSTIC, the agreement is quite good on a clear sky day, i.e. when the clear sky parameterisations are used in the radiation balance model. When compared to simulations with the simpler isotropic view factor approach it could be shown that the radiosity approach is superior the more shading occurred, i.e. the more complex the terrain is or the lower the sun elevation angles are.

It is common to determine the terrain view factor sum for the isotropic view factor approach from the sky view factor. Therefore, frequently used methods to approximate the sky view factor from horizon angles are reviewed and common sources of errors are outlined by deriving the continuum equation for the sky view factor. One common source of error is the assumption of the equality between the sky view factor and the solid angle of the sky. And one other common source of error is the assumption that the horizon angle can be derived by neglecting the actual inclination of the viewing surface.

In order to derive some general behaviour of the radiation balance in complex terrain the radiosity equation is solved on Gaussian random fields taken as digital height models. Mean terrain reflected radiation values are computed as a function of sun elevation, varying (homogeneous) albedos and typical terrain length scales. This analysis reveals that the model is applicable to the whole range of topographies. Additionally, for a best estimate of terrain reflected radiation the grid cell resolution has to be small against the typical width of mountains/valleys in the domain, which again has to be small against the domain extension. Remarkably high values of mean terrain reflected radiation are obtained depending on mean slopes and albedos.

Another comparison between the anisotropic view factor approach (i.e. with the radiosity model) and the isotropic view factor approach is conducted, this time on Gaussian random fields taken as digital height models. From this comparison a rule of thumb was derived: Mean terrain reflected radiation values from the isotropic view factor approach are roughly the same as those computed by the anisotropic view factor approach, however, the spatial distribution of terrain reflected radiation varies remarkably between both view factor approaches.

The effective albedo is studied with regard to a mean local albedo on Gaussian random fields with a mean slope of 30°. Resulting effective albedos vary with the sun elevation angle and are lower than mean local albedos. Largest differences between mean and effective albedos occur for an albedo of 0.5 and lowest for an albedo of 0.1 and 0.9.

As an application of the new radiation balance model the whole surface process model Alpine3D is used to model spatial winter road surface temperatures. For a specific part of the Gotthard motorway, spatial differences of incident radiation coming from shading and terrain reflected radiation do have only little influence on modelled road surface temperatures. One possible explanation is assumed to be the missing coupling of air temperatures and incident radiation values in the surface process model Alpine3D. In some cases, this resulted in large deviations of modelled surface temperatures and measured values.

This thesis introduces a completed, well defined physical and validated three-dimensional radiation balance model in complex terrain which, most important, allows to study systematically the influence of terrain effects (shading and anisotropic multiple terrain reflections) on the radiation balance. It is shown that the new radiation balance model performs well on a variety of topographies. Thus, the application of the radiosity approach in the radiation balance model is found to be valuable to investigate terrain influences on radiation balances. With regard to the application of the radiation balance model as a module of the whole modular model system Alpine3D the most important future investigation points are outlined. First, the lack of an accurate determination of spatial incident direct and diffuse sky radiation under cloudy sky conditions might lead to wrongly determined terrain reflected radiation and should therefore be further studied. Second, the missing coupling of spatial air temperature to spatial incident radiation is leading to wrongly model surface temperatures.

Zusammenfassung

In dieser Arbeit wurde die Strahlungsbilanz in komplexem Gelände detailliert behandelt, um die Beschreibung von lokalen Oberflächeneigenschaften zu verbessern. Dabei sollte die Strahlungsbilanz in komplexem Gelände durch ein dreidimensionales Strahlungsbilanzmodell beschrieben werden, welches die Geländeeinflüsse explizit berücksichtigt. Gleichzeitig sollte das Strahlungsmodell ein Modul des modularen Modellsystems Alpine3D zur Beschreibung von alpinen Oberflächenprozessen bleiben. Dies bedeutet, dass die Atmosphäre durch eine horizontale Schicht im Strahlungsmodell beschrieben wird, so dass das Strahlungsmodell nur einen exponierten Strahlungsmesswert an der Oberfläche benötigt. Daher war die Entwicklung des Strahlungsmodells im Hinblick auf seine Komplexität beschränkt.
Im einzelnen konzentriert sich die Arbeit auf die Entwicklung eines Strahlungsbilanzmodells welches (i) Abschattung und (ii) Mehrfachreflektion am Gelände sowie Emission vom Gelände behandelt, und welches aber dennoch ein Modul des Oberflächenprozessmodells Alpine3D bleibt.

Das bisherige Strahlungsmodell in Alpine3D berechnet räumlich einfallende direkte und diffuse Himmelsstrahlung für eine bewölkte Atmosphäre anhand von empirischen Parametrisierungen. Diese Parametrisierungen wurden überprüft, ergänzt und teilweise ersetzt.
Um Abschattung durch Berge sowie Sichtbarkeit zwischen Oberflächen genauer zu berücksichtigen, wurden robustere Algorithmen implementiert, welche nun die Sichtbarkeit zwischen einzelnen Gitteroberflächen bestimmen. Zusätzlich wurde, durch die Anwendung des Algorithmus von Corripio (2002) zur Bestimmung der Geländeparameter, die Abbildung von steilen Berggraten durch digitale Höhenmodelle verbessert.
Der Radiosity Ansatz wurde gewählt, um ein detailliertes Strahlungsbilanzmodell zu entwickeln, welches anisotrope Geländeeinflüsse behandelt und gleichzeitig ein Modul des Modells Alpine3D für die Beschreibung von Oberflächenprozessen bleibt. Dabei wurde der Radiosity Ansatz zum ersten Mal angewendet, um die dreidimensionale Strahlungsbilanz in komplexem Gelände zu berechnen. Die Anwendung des Radiosity Ansatzes schliesst teilweise die zur Zeit noch recht grosse Lücke zwischen auf der einen Seite recht komplexen dreidimensionalen Strahlungsmodellen für bewölkte Atmosphären und auf der anderen Seite vereinfachten Modellen, welche das Gelände durch eine isotrope Fläche annähern (isotroper 'view factor' Ansatz). Im Gegensatz zum isotropen 'view factor' Ansatz benutzt der Radiosity Ansatz anisotrope 'view factors' und berücksichtigt (anisotrope) Mehrfachreflektionen. Die Radiosity Gleichung wurde zuerst im Computergrafikbereich eingeführt. Dabei werden Methoden angewendet, welche ursprünglich für die Wärmetechnik entwickelt wurden, um den Austausch von Strahlungsenergie zwischen Oberflächen zu beschreiben.
In dieser Arbeit wurden einige numerische Methoden erweitert und angepasst, damit sie für die Berechnung des Strahlungsaustausches in komplexem Gelände angewendet werden können: Das Progressive Refinement Iterationsverfahren wurde ausgewählt, um die diskretisierte Radiosity Gleichung in komplexem Gelände zu lösen. Das Kriterium welches die Rei-

henfolge der Iteration anhand der grössten zur Verfügung stehenden Strahlungsleistung (Cohen et al. (1988)) bestimmt, wurde durch die Summe der Gelände 'view factors' erweitert. Des weiteren wurde ein neues Kriterium zum Abbruch der iterativen Lösung des linearen Radiosity Gleichungssystems entwickelt. Dieses Kriterium kann mit dem wahren Fehler mittels einer Schranke in Beziehung gesetzt werden.

Das neu entwickelte Modell wurde mit Punktmessungen und Sensitivitätsstudien verifiziert. Zum einen wurden dazu permanente Strahlungsmessungen vom Weissfluhjoch Versuchsfeld in 2540 m ü.M., nahe Davos, Schweiz benutzt. An Strahlungstagen stimmen die modellierten Werte, welche mit den überprüften und erweiterten Parametrisierungen für Strahlungstage berechnet wurden, gut mit den gemessenen Werten überein. Ein wichtiges Ergebnis besteht in dem Nachweis, dass das Fehlen eines geeigneten Modells zur Aufspaltung des einzigen Messwertes der Globalstrahlung zur Berechnung von Strahlungskomponenten für bewölkte Tage zu ungenau modellierten Strahlungskomponenten führt. Die gemessene diffuse Himmelsstrahlung wird dann von den modellierten Werten meistens überschätzt, während die gemessene direkte Strahlung meistens unterschätzt wird.
Zum anderen wurde ein neuer Messaufbau entworfen, um die reflektierte Geländestrahlung zu bestimmen. Modellierte und gemessene reflektierte Geländestrahlung stimmen gut überein. Eine mit einem Tachymeter eingescannte Horizontlinie bestätigte den neu implementierten Algorithmus zur Berechnung der Sichtbarkeit.
Um die Einordnung des Radiosity Ansatzes zwischen vereinfachten und komplizierteren Modellen zu überprüfen, wurde das Modell zunächst mit dem vollständigen dreidimensionalen Monte Carlo Strahlungstransfermodell MYSTIC für eine bewölkte Atmosphäre verglichen. Für einen Strahlungstag stimmen die modellierten Strahlungskomponenten gut überein, sofern im neuen Strahlungsmodell die Parametrisierungen für Strahlungstage verwendet werden. Ein Vergleich mit der Anwendung des vereinfachten isotropen 'view factor' Ansatzes hat gezeigt, dass der Radiosity Ansatz genauere Werte liefert und zwar um so genauere, je mehr Abschattung im Gebiet auftritt, d.h. je komplexer das Gelände oder je niedriger der Sonnenstand ist.
Die für den isotropen 'view factor' Ansatz benötigte Summe der Gelände 'view factors' wird üblicherweise aus dem 'sky view factor' abgeleitet. Daher wurden die üblicherweise verwendeten Methoden, den 'sky view factor' anhand von Horizontwinkeln abzuschätzen, überprüft. Häufige Fehlerquellen wurden herausgestellt, indem die Kontinuumgleichung für den 'sky view factor' hergeleitet wurde. Eine häufige Fehlerquelle ist dabei die Annahme der Gleichheit zwischen 'sky view factor' und dem Raumwinkel des sichtbaren Himmels. Eine andere ist die Annahme, dass Horizontwinkel bestimmt werden können ohne die Neigung der betrachtenden Oberfläche miteinzubeziehen.
Um das allgemeine Verhalten von kurzwelliger reflektierter Geländestrahlung zu überprüfen, wurden zufällig generierte Topographien (Gauss'sche Zufallsfelder) als digitale Höhenmodelle verwendet. Mittlere reflektierte Strahlungswerte wurden als Funktion von Sonnenstand, variierenden (homogenen) Albedowerten und typischen Geländelängenskalen berechnet. Diese Analyse zeigte, dass das Modell in einer Vielzahl von Topographien angewendet werden kann. Dabei wurde eine beste Schätzung der reflektierten Geländestrahlung ermittelt, wenn die Gitterzellenauflösung klein gegenüber typischen Breiten von Bergen/Tälern im Modellgebiet und diese ausserdem klein gegenüber der Modellgebietsgrössen waren. Bemerkenswert hohe Werte an reflektierter Geländestrahlung wurden bereits bei mittleren Hangneigungen sowie mittleren Albedowerten modelliert.
Ein weiterer Vergleich zwischen dem anisotropen 'view factor' Ansatz (d.h. dem Radios-

ity Ansatz) und dem isotropen 'view factor' Ansatz wurde, anhand von zufällig generierten Topographien als digitale Höhenmodelle, durchgeführt. Aus diesem Vergleich kann für die reflektierte Geländestrahlung die folgende Faustregel abgeleitet werden: die mittlere reflektierte Geländestrahlung wird von beiden Ansätzen annähernd gleich berechnet; die räumliche berechnete Verteilung der reflektierten Geländestrahlung unterscheidet sich jedoch erheblich zwischen beiden Ansätzen.
Die effektive Albedo wurde mit der mittleren lokalen Albedo auf Gauss'schen Zufallsfeldern als digitale Höhenmodelle mit einer mittleren Hangneigung von 30° verglichen. Dabei variierten effektive Albedowerte mit dem Sonnenstand und waren niedriger als die mittleren lokalen Albedowerte. Die grössten Unterschiede zwischen mittleren Albedo- und effektiven Albedowerten wurden für eine mittlere Albedo von 0.5 ermittelt, die geringsten Unterschiede für eine mittlere Albedo von 0.1 und 0.9.
Als eine Anwendung des neuen Strahlungsmodells wurde das gesamte Oberflächenprozessmodellsystem Alpine3D zur Modellierung von Oberflächentemperaturen auf der Strasse angewendet. Dabei hatten räumlich einfallende Strahlungsunterschiede auf einem Autobahnabschnitt am Gotthard, hervorgerufen durch Abschattung oder reflektierte Geländestrahlung, keinen massgeblichen Einfluss auf die modellierten Strassenoberflächentemperaturen. Es wird vermutet, dass dies an der fehlenden Kopplung zwischen Lufttemperaturen und einfallender Strahlung im Oberflächenprozessmodell Alpine3D liegt. In einigen Fällen führte dies zu grossen Unterschieden zwischen modellierten und gemessenen Oberflächentemperaturen auf der Strasse.

Diese Arbeit stellt ein vollständiges, physikalisch definiertes und validiertes dreidimensionales Strahlungsbilanzmodell für komplexes Gelände vor. Als ein wesentliches Ergebnis erlaubt dieses Modell den Einfluss von Gelände (Abschattung sowie anisotrope Mehrfachreflektion) systematisch zu untersuchen. Es wurde gezeigt, dass das neue Strahlungsbilanzmodell auf verschiedenen Topographien sehr gut anwendbar ist. Daher ist die Anwendung des Radiosity Ansatzes im Strahlungsbilanzmodell sehr geeignet, um Geländeeinflüsse auf Strahlungsbilanzen zu untersuchen.
Im Hinblick auf die Anwendung des Strahlungsbilanzmodells als ein Modul des gesamten modularen Modellsystems Alpine3D werden die wichtigsten zukünftigen Arbeitspunkte herausgestellt. Zum einen ist es nicht möglich, genaue Werte für räumliche direkte und diffuse Himmelsstrahlung für eine bewölkte Atmosphäre zu bestimmen. Das führt dazu, dass auch die reflektierte Geländestrahlung falsch bestimmt wird. Zum anderen führt die fehlende Kopplung zwischen räumlichen Lufttemperaturen und räumlich einfallender Strahlung zu falschen modellierten Temperaturen an der Geländeoberfläche.

Part I

Introduction

1 Research introduction

1.1 Motivation

A highly detailed surface energy balance forms a sound basis for the computation of surface characteristics such as surface, soil or snow pack temperatures. The radiation balance is an essential component of the energy balance. Therefore, a detailed radiation balance is required in order to determine local surface characteristics. The most important effects which have to be included in the surface radiation balance in the presence of topography are (i) shading, (ii) multiple terrain reflections and (iii) terrain emissions. Shading is especially important in deep valley geometries and is more pronounced during the winter when sun elevation angles are low. Shading can reduce the incident direct radiation flux to zero, which has a strong impact on the radiation balance at certain points. In contrast, terrain reflections and emissions can lead to large additional radiation inputs. This is most pronounced for terrain surfaces that are shaded themselves but have adjacent non-shaded parts of the surface. In mountainous terrain multiple terrain reflections for shortwave radiation become even more important for snow-covered surfaces, which have large albedo values. Therefore, it is essential to include these three effects when modelling radiation distribution in mountainous terrain.

While snow typically has a large albedo, some radiation penetrates the snow surface and is absorbed in the snowpack. The amount of absorbed radiation strongly depends on the wavelength of the incident radiation. Therefore, radiation has a direct influence on snow cover evolution, surface and snow temperatures, which is important for avalanche forecasting, hydrology and glaciology. In general, all radiation is absorbed within a snow layer with depth less than several tens of centimetres (Kondratyev (1969)). The attenuation of global radiation with snow depth can approximately be described by an empirical Beer-Lambert law (Sulakvelidze and Okujava (1959)). According to pyranometric measurements of Kuzmin (1947), a 5 cm snow layer can absorb 34 to 88 % of global radiation. A 10 cm layer can absorb 56-98%. Therefore, practically all global radiation is absorbed by a 10 cm snow layer if the attenuation coefficient is large. However, for low attenuation coefficients, global radiation is not absorbed until a depth of 60 cm. In wet snow the attenuation of transmitted radiation strongly increases. From measurements of the radiative fluxes at different snow depths in Summit, Greenland, Meirold-Mautner and Lehning (2004) concluded that snow is acting as a spectral filter for radiation. They found that only 2.35 % of the surface value is measured 10 cm below the surface for visible light at 660 nm. In contrast, almost all incident longwave radiation is absorbed directly at the snow surface. Longwave radiation entering into the snow pack is therefore negligible. Nevertheless, since shortwave radiation penetrates the snow surface and influences snow temperatures it is important to describe the surface radiation balance highly detailed.

Local shading from mountains or from trees also has a direct influence on surface temperatures. This can often be seen in inhabited regions. Shaded road sections are covered by snow while on road sections in the sun the snow already started to melt. Consequently, shading has a strong influence on road surface ice formation. A detailed treatment of the radiation balance is therefore essential for an application of a radiation balance model for road surface temperature simulations in complex terrain.

In complex terrain, in forests or built-up areas one often distinguishes between effective and local albedo values. Effective albedo values take into account multiple reflections of the surrounding topography, trees, buildings etc. They are therefore representative for a larger area and considerably lower than mean local albedo of the same area. Amongst others, Kylling et al. (2000a), Schmucki et al. (2001), Weihs et al. (2001) and Fortuniak (2008) investigated effective albedos for different applications. For example Kylling et al. (2000a) found for Tromsø (Norway) that average albedos are reduced by about 0.2 (wavelength range of 0.32-0.5 μm) if the large fraction of open water was included in their three-dimensional MC modelling. Even though the above studies mostly focus on UV radiation, it is clear that the results will be similar for visible shortwave radiation. These results show the importance of multiple terrain reflections on the radiation budget even in mesoscale models: Multiple reflections within a mesoscale grid cell of 2-7 km are multiple energy losses characterised by the effective albedo. This leads to a reduced radiation leaving the grid cell, which results in an enhanced local albedo of that cell. With overestimated local mean albedo values, according to the land use class/snow or ice cover, the reflected radiation is overestimated. Note that this is enhanced for complex terrain. Thus, a detailed computation of the surface radiation balance in model domains with small grid cells in complex terrain allows estimating effective albedo values for e.g. mesoscale models with large grid cell resolutions.

1.2 Objectives

The main objective of this thesis is an accurate modelling of the surface radiation balance in micro- to mesoscale complex (alpine) terrain for various applications. The modelling in this thesis was conducted by a coupled surface process model, called Alpine3D (Lehning et al. (2004)) which can be driven from a single, exposed radiation measurement. A level of complexity was aimed for the model that can be classified between complex three-dimensional radiative transfer models for a cloudy atmosphere and models that apply the isotropic view factor approach which does not include (anisotropic) multiple terrain reflections but only single isotropic terrain reflections/emissions. The new radiation balance model should include all topographic effects such as shading, anisotropic multiple terrain reflections and anisotropic single terrain emissions but should not require more radiation input than the single radiation measurement value.

Highly complex models resolve for a three-dimensional cloudy atmosphere including multiple terrain reflections as well as emissions. Examples are the MYSTIC Monte Carlo model (Mayer (2000a)) or the spherical harmonics discrete method for UV irradiance (Degünther et al. (1998)). In contrast, terrain reflections and emissions are often included by means of the isotropic view factor approach by a variety of models (e.g. Nunez (1980), Moore et al. (1993), Corripio (2002), Oliphant et al. (2003), Bellasio et al. (2005), Hock and Holmgren (2005), Müller and Scherer (2005), Wang et al. (2006)). Anisotropic terrain reflection and emission models exist that solve the equation for diffuse irradiance (Kondratyev and Manolova (1960)). This is done by dividing the obstructed sky hemisphere into spherical portions having different surface properties such as albedo or emissivity values (e.g. Olyphant (1986b) for longwave,

Martius (2002) and Letsinger and Olyphant (2007) for short- and longwave radiation). Even though this approach is more accurate than the isotropic view factor approach, it is highly inaccurate for distant terrain surfaces since the spherical portions are getting broader for terrain that is located further away. In that case different surface properties (e.g. slope, slope azimuth, albedo and emissivity) have to be combined per solid angle opening. That simplification leads to under- or overestimated terrain reflections and emissions especially in case of partly snow covered terrain.
The specific research objectives of the thesis are:

- An accurate consideration of (local) shading from mountains.
- Implementation of anisotropic multiple terrain reflected and terrain emitted radiation.
- Implementation of a method that accounts for accurate terrain influences up to mesoscale model domains. This method should also allow for small grid cell extensions of 25 m or smaller.
- Verification of the new model with point measurements and sensitivity studies. Additionally, a general characterisation of terrain reflected radiation in terms of the geometry of complex terrain by using random digital height models was conducted.
- Investigation of terrain influences, such as shading, on local winter road surface temperature simulations.

1.3 Thesis structure

This thesis is composed of five parts. In the first thesis part the motivation, objective and structure of the research are given, the second part provides the theory and model definitions, the third part comprises the validation by measurements and sensitivity analysis, the fourth part presents an application of the model system Alpine3D and in the fifth part the conclusion and an outlook are given. The three parts are split in overall twelve chapters that have the following content:

- **Chapter 1** gives the motivation for the research topic and states the research objectives including an overview of the thesis organisation.
- **Chapter 2** presents the terrain discretisation and terrain parameters. The new mutual terrain surfaces visibility algorithm and sun-or-shadow detection algorithm are presented.
- **Chapter 3** provides in detail the theory of the present three-dimensional radiation balance model which is part of the coupled surface process model Alpine3D.
- **Chapter 4** provides the theory and implementation details of the radiosity approach. The radiosity approach was first introduced in computer graphics from techniques originally developed in thermal engineering to describe the exchanges of radiant energy between surfaces. This approach was chosen to account for anisotropic multiple shortwave terrain reflections as well as longwave terrain emissions. The full anisotropic view factor concept between individual surfaces, implemented by a uniform but adaptive area subdivision, is presented.

- **Chapter 5** describes the structure and some theory of the main modules of the modular model for alpine surface processes called Alpine3D.
- **Chapter 6** shows a comparison of measured and modelled horizon angles, i.e. the validation of the visibility algorithm.
- **Chapter 7** presents the validation of the empirical parameterisations that are implemented to compute spatial direct, diffuse sky and longwave sky radiation. Permanent measurements are obtained from an alpine site at Weissfluhjoch study site at 2540 m a.s.l. close to Davos, Switzerland.
- **Chapter 8** describes the measurement set-up to determine terrain reflected radiation values. Comparisons of measured terrain reflected radiation are presented with computed values with the radiosity model, by using the isotropic view factor approach and with the Monte Carlo model MYSTIC.
- **Chapter 9** provides the validation of some model parts by applying sensitivity studies e.g. the influence of terrain parameters is studied.
- **Chapter 10** presents a study of the generic behaviour of terrain reflected radiation by means of Gaussian random fields as topographies. A systematic study of the influence of terrain characteristics on terrain reflected radiation is presented. In addition, the randomly generated topographies were used to study the differences between the radiosity and commonly applied isotropic view factor approaches more thoroughly. Furthermore, the behaviour of the correlation of mean albedo and effective albedo values is investigated.
- **Chapter 11** presents the application of the model system Alpine3D on winter road surface temperature computations. A specific part of the Gotthard motorway (Kanton Uri, Switzerland) was chosen to verify the simulated surface temperatures with point measurements.
- **Chapter 12** summarises the achievements of the research and gives an outlook on possible future work.

Part II

Theory and model definitions

2 Terrain discretisation and terrain parameters

In this chapter the extraction method of terrain parameters from digital height models (DHM) is presented. This includes slope orientation as well as mutual visibility and sun-or-shadow implementation.
A different extraction method of terrain parameters is introduced to enable the representation of steep mountainous terrain ridges. More robust algorithms replace the former implementations of mutual visibility and sun-or-shadow.

2.1 Terrain parameters from digital height models (DHM)

A thorough examination of the earth's surface reveals a major difficulty if one wants to define the terrain parameters at a certain point. Even if urban objects or vegetation are neglected the terrain surface in complex mountainous terrain appears to be very rough. By using a DHM with a particular spatial resolution, the entire terrain roughness on scales below the resolution is simply suppressed. This implies, that the prediction of the radiative flux for a particular point might strongly depend on the spatial resolution of the DHM. In addition, different methods of discretising surface-height gradients (slope) from the DHM might also have a significant influence on the results (cf. Section 9.2, p.129). Therefore, a precise definition is necessary which discretisation methods are used. The extraction process of terrain parameters slope angle, azimuth angle and surface normal from DHM is described in this section. In addition, the terrain parameters highlight possible sources of inherent errors due to the chosen extraction method (Section 9.2, p.129).

A DHM is a discretisation of the real, continuous surface height $z(x, y)$ and is given as an array of terrain elevations z_{ij} with $i = 0, 1..N_x - 1,\ j = 0, 1..N_y - 1$ in a domain of size $L_x = L_y = L$ with a given horizontal resolution $\Delta x = \Delta y$. They usually represent the terrain height above sea level without vegetation and buildings. In this work mainly grids from Swisstopo (WWW)[1] are used with square horizontal grid cells of size $\Delta x = \Delta y = 25$ m, and a mean height accuracy for the Alps of 3 m. More precisely, the height z_{ij} is assigned to the **center** of the grid cell ij. In general, a normal vector at a point x, y on a surface is given by $\vec{n}(x, y) = (-\partial_x z(x, y), -\partial_y z(x, y), 1)$.

Until now, Horn (1981)'s algorithm for estimating the normal vector $(n_{x,ij}, n_{y,ij}, 1)$ of a grid cell ij was applied. A mean height was computed using the heights of the surrounding grid

---

[1] In this thesis WWW indicates a reference to a website (cf. References).

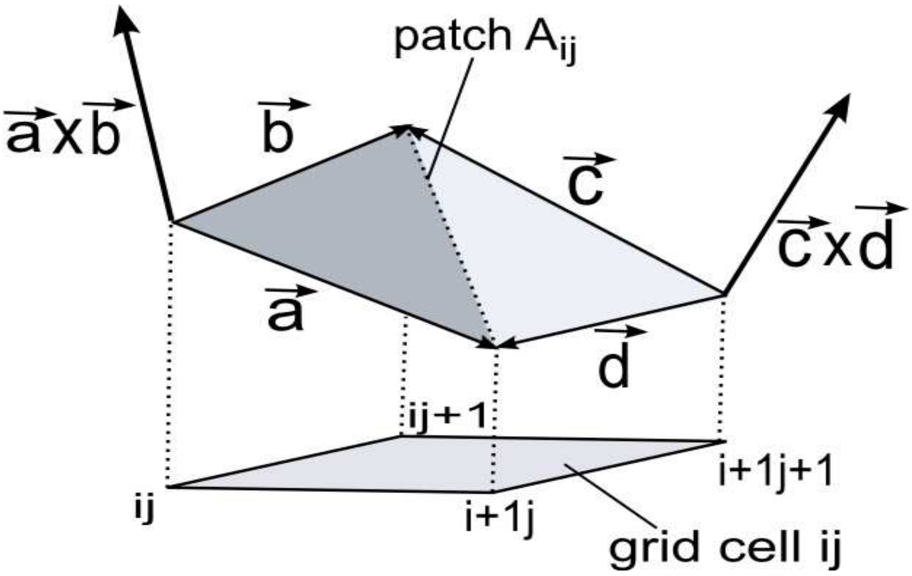

Figure 2.1: Schematic for a horizontal grid cell ij compared to a patch A_{ij} with the vectors determined for the normal vector computation.

cells (eight-neighbor algorithm)

$$\begin{aligned} n_{\mathrm{x},ij} &= \frac{(z_{i+1j+1} - z_{i-1j+1}) + 2\,(z_{i+1j} - z_{i-1j}) + (z_{i+1j-1} - z_{i-1j-1})}{8\,\Delta x} \\ n_{\mathrm{y},ij} &= \frac{(z_{i-1j+1} - z_{i-1j-1}) + 2\,(z_{ij+1} - z_{ij-1}) + (z_{i+1j+1} - z_{i+1j-1})}{8\,\Delta x}\;. \end{aligned} \tag{2.1}$$

Hodgson (1995) showed that the eight-neighbor algorithm calculates the gradient for an equivalent area of up to twice the cell size and therefore flattens slopes in rough terrain. Especially mountain ridges are not described properly. Hodgson (1998) concludes from his investigation of different surface slope angle algorithms that the most accurate algorithm is one using only the four nearest neighbors in the grid array (Fleming and Hoffer (1979), Ritter (1987)). The algorithm presented by Corripio (2002) is in accordance with this fact and is selected here to represent rough mountainous terrain.

Corripio (2002) developed an algorithm which divides a rectangle grid cell into two triangles and computes an average of the resulting two surface normal vectors: $\vec{a} \times \vec{b}$ and $\vec{c} \times \vec{d}$, with $\vec{a} = (\Delta x, 0, z_{i+1j} - z_{ij})$, $\vec{b} = (0, \Delta x, z_{ij+1} - z_{ij})$, $\vec{c} = (-\Delta x, 0, z_{ij+1} - z_{i+1j+1})$ and $\vec{d} = (0, \Delta x, z_{i+1j} - z_{i+1j+1})$ (cf. Fig 2.1). He points out that $\vec{n}$ is independent of the chosen diagonal. The average surface normal vector $\vec{n}$ of a grid cell ij is then given by

$$\vec{n}_{ij} = \begin{pmatrix} \Delta x\,(z_{ij} - z_{i+1j} + z_{ij+1} - z_{i+1j+1})/2 \\ \Delta x\,(z_{ij} + z_{i+1j} - z_{ij+1} - z_{i+1j+1})/2 \\ \Delta x\,\Delta x \end{pmatrix}\;. \tag{2.2}$$

The surface normals are also assigned to the center of the appropriate patch. At the model domain boundary the normal vector components are computed according to a constricted version of Eq. (2.1).

Although the determination of the surface normal vector $\vec{n}$ is sufficient to describe the orientation of a patch, for completeness the surface slope and azimuth angle equations are also given here since they are required elsewhere. At first the surface slope angle ζ_s of a patch is determined by

$$\zeta_{\mathrm{s},ij} \;=\; \mathrm{acos}(\frac{n_{\mathrm{z},ij}}{|\vec{n}_{ij}|}) \tag{2.3}$$

where in this model $n_{\mathrm{z},ij}$ is set to one. The surface azimuth angle φ_s is determined according to Hodgson (1998) counting clockwise from north with the surface normal vector components of Eq. (2.2)

$$\begin{array}{lcllcl} \varphi_{\mathrm{s},ij} &=& \text{undefined} & \text{if } n_{\mathrm{x},ij} &=& 0 \;\wedge\; n_{\mathrm{y},ij} \;=\; 0 \\ \varphi_{\mathrm{s},ij} &=& \text{south facing} & \text{if } n_{\mathrm{x},ij} &=& 0 \;\wedge\; n_{\mathrm{y},ij} \;<\; 0 \\ \varphi_{\mathrm{s},ij} &=& \text{north facing} & \text{if } n_{\mathrm{x},ij} &=& 0 \;\wedge\; n_{\mathrm{y},ij} \;\geq\; 0 \\ \varphi_{\mathrm{s},ij} &=& 90 \;-\; \mathrm{atan}(\frac{n_{\mathrm{y},ij}}{n_{\mathrm{x},ij}}) & \text{if } n_{\mathrm{x},ij} &>& 0 \\ \varphi_{\mathrm{s},ij} &=& 270 \;-\; \mathrm{atan}(\frac{n_{\mathrm{y},ij}}{n_{\mathrm{x},ij}}) & \text{if } n_{\mathrm{x},ij} &<& 0 \end{array} \quad . \tag{2.4}$$

It remains to specify, how the surface of the terrain is represented. At each grid cell the surface is decomposed into planar, rectangular surface **patches** A_{ij} with normal vector $\vec{n}_{ij}$ such that the projections of the corners of the rectangle onto the horizontal plane coincide with the grid cell corners (Fig. 2.1). Note that this common treatment of the surface differs from a triangulated surface since it contains “holes”. Finally, a convenient shorthand notation for double indices ij is introduced. By consecutively enumerating all points in the plane row by row, a single index $I = jN_x + i,\; I = 0, 1..N-1 := N_xN_y$ can be used, such that, e.g. the height z_{ij} can also be denoted by z_I. This will be helpful to simplify the notation in particular for the radiosity equations in the next chapter which involve matrices.

2.2 Mutual visibility / Sun-or-shadow detection

According to Nagy (1994) two points are mutually visible if the line connecting them does not intersect surface in between. For objects or surfaces this visibility could be further restricted by not allowing partial occlusion. In general, visibility and sun-or-shadow detection can be treated in the same manner. This is possible because a patch is in the sun when the patch and the sun are mutually visible. Sun-or-shadow information changes with the position of the sun whereas mutual visibility is fixed for a given topography. The so-called horizon of a patch is therefore the maximum visibility of that patch in predefined directions.

The knowledge of sun-or-shadow and mutual visibility is important for the radiation balance in complex terrain: Obviously, mutual visibility will determine if two surface patches can actually exchange radiation and sun-or-shadow determines if a patch actually receives direct radiation. For discretised surfaces, two different types of shading have to be distinguished namely horizon-shading and self-shading. In self-shading, simply the patch orientation is compared to the actual position of the sun by computing the incidence angle θ (white colored surfaces in Fig. 2.2 are self-shaded). In contrast, horizon-shading of a patch is determined by the mutually visibility with the sun (red colored surfaces in Fig. 2.2 are horizon-shaded). Horizon-shading can include self-shading except for the case of a planar inclined slope when the sun has an elevation angle equal to the slope. Depending on the implementation of the visibility algorithm, horizon-shading also captures this case of self-shading or self-shading has to be accounted for separately. Self-shading is usually included by multiplying the incident

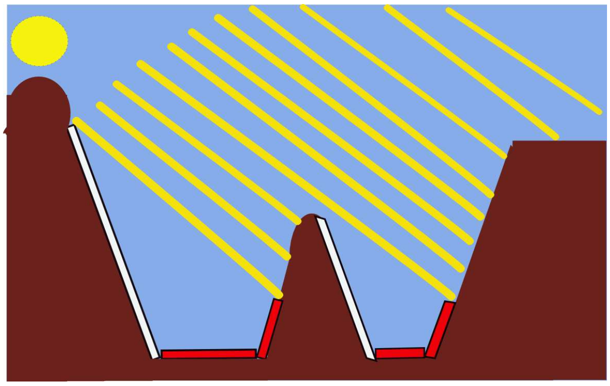

Figure 2.2: Schematic for self-shaded surfaces (white) and horizon-shaded surfaces (red) in complex terrain.

direct SW radiation with the cosine of the incident angle of the sun θ (Eq. (3.13) and Eq. (3.34)). The patch is self-shaded if the product is lower or equal zero. Note that for continuous, smooth surfaces self-shading always implies horizon-shading such that this concept is solely required for discretised surfaces.

Shading is accounted for in different meteorological applications because of its dominant influence on the SW surface radiation balance in complex terrain. For example by applying a classical ray tracing method, Borel et al. (1998) found that the inclusion of shading may decrease the incident radiation by 20 to 60 %, influencing the duration of the existence of a snow cover. Colette et al. (2003) added a new subroutine to the Advanced Regional Prediction System (ARPS, version 5.0.0 Beta3c) to include both, self-shading and horizon-shading. Their motivation originated from studies of Whiteman et al. (1989a) and Whiteman et al. (1989b), in which the influence of direct radiation on the local circulation and the overall radiation budget in elevated valleys was investigated. Whiteman (2000) discussed the influence on delaying sunrise in complex terrain which results in the subroutine SOLSUB for all basic solar radiation computations, now including the delay in local sunrise induced by self-shading. Furthermore, an extensive field study within the deep Alpine Riviera Valley in southern Switzerland confirmed the spatial and temporal variability of the net radiation and its influence on valley wind days (Matzinger et al. (2003)). They note that the dominant influence of direct SW radiation in complex topography leads to a variety of local radiation microclimates. After adding the new shading subroutine to ARPS, Colette et al. (2003) compared simulations with and without the usage of the shading subroutine. They concluded that horizon-shading needs to be included in simulations, especially at high spatial resolution in complex terrain. For a real valley topography shortly after local sunrise 22 % of the model domain was horizon-shaded and 29 % self-shaded. Furthermore, they found that horizon-shading has a strong influence on the onset of upslope winds and hence on the break-up of inversions in deeper valleys. Chow et al. (2004) applied the extended ARPS version in the Riviera Valley and compared the simulations to the observations during the MAP-Riviera field study. They confirmed the significant influence of shading on the incident radiation, especially during sunrise and sunset. The largest difference between modelled incident SW radiation with and without shading was close to 300 $\mathrm{Wm^{-2}}$ at 6 UTC on east-facing slopes.

Numerous sun-or-shadow and visibility algorithms, respectively exist at different levels of

accuracy and required computation time. The most common (and fast) sun-or-shadow methods determine a maximum visibility angle (horizon angle) by tracing rays in certain fixed azimuthal sectors. The resulting horizon angles are assumed to be valid for the whole sector. Visibility angles are determined e.g. in fixed horizontal step lengths along the ray (Nunez (1980), Dozier and Bruno (1981), Corripio (2002)). But even among those, the horizon angle itself is computed by different methods. Stewart (1998) developed a more accurate and faster approach to derive approximate horizon angles compared to the computational expensive grid cell wise requesting. He computes the horizon angle for a number of sample cells in a sector. Upon completion, the horizon angle is known for all cells in contrast to first compute the complete horizon of one cell before moving to the next cell. The main shortcoming of the azimuthal sector method is that by computing the horizon angle for a sector along one ray and assuming that angle to be valid for the whole sector, leads to greater errors the larger the model domain is. The reason for this is the increase in beam width for increasing distances from the observing point.
Minnich et al. (2002) determined visibility for their view factor based radiative heat transfer model for Telluride. In order to exclude surfaces that are oriented in opposite directions they first applied dot product tests between surface normal and distance vectors. Thereafter an occlusion test for partial or complete occlusion was performed for the remaining surfaces. The latter was conducted by projecting the considered surfaces in pairs on a two-dimensional plane to test if they overlap.

For the present radiation balance model a more accurate but slightly slower algorithm than the azimuthal sector method is used to compute the mutual visibility and the sun-or-shadow indicator function which are denoted by χ_{IJ} and $\chi_{\mathrm{sun},I}$, respectively. The new algorithm is described below.

Two patches A_I and A_J are defined to be mutually visible, i.e. $\chi_{IJ} = 1$, if all heights z of *intermediate* patches $\mathrm{A}_{J_{\mathrm{inter}}}$ lie below the connecting line between the two patch centers. Therefore, the algorithm searches for any $(z_{J_{\mathrm{inter}}} - z_I)/r_{IJ_{\mathrm{inter}}}$ larger than $(z_J - z_I)/r_{IJ}$. The time consuming visibility test is then immediately stopped if a larger $(z_{J_{\mathrm{inter}}} - z_I)/r_{IJ_{\mathrm{inter}}}$ is found and χ_{IJ} is set to zero. With this method partial visibility is not accounted for. The *intermediate* grid cells J_{inter} are taken to be those which are traversed by the search path i.e. the projection of the connecting line onto the horizontal plane (shaded grid cells in Fig. 2.3). The *intermediate* stepwise sequence of grid cells are found similar to the fast traversal algorithm for ray tracing of Amanatides and Woo (1987) (Fig. 2.3). For this, the horizontal azimuth angle φ_{IJ} as seen from grid cell I to a grid cell J is computed by

$$\begin{aligned} \varphi_{IJ} &= \arccos\left(\frac{-(b-j)}{\sqrt{(i-a)^2+(j-b)^2}}\right) & \\ \varphi_{IJ} &= 2\pi - \varphi_{IJ} & \textbf{if } ((a-i) \leq 0) \end{aligned} \tag{2.5}$$

where $I = jN_x + i$ and $J = bN_x + a$ (see Section 2.1, p.17). Thereby the azimuth angle φ is counted counterclockwise from south. The intersection points of the search path with the borders of *intermediate* grid cells are computed to detect the next traversed grid cell: The intersections of the search path with the grid can be subdivided into two types, i.e. intersections with **horizontal** grid lines and intersections with **vertical** grid lines (cf. Fig 2.3). The main observation is now that crossing a horizontal intersection point moves the search to the neighboring grid cell in y direction whereas crossing a vertical intersection point moves the search to the neighboring grid cell in x direction. Thus, traversing the

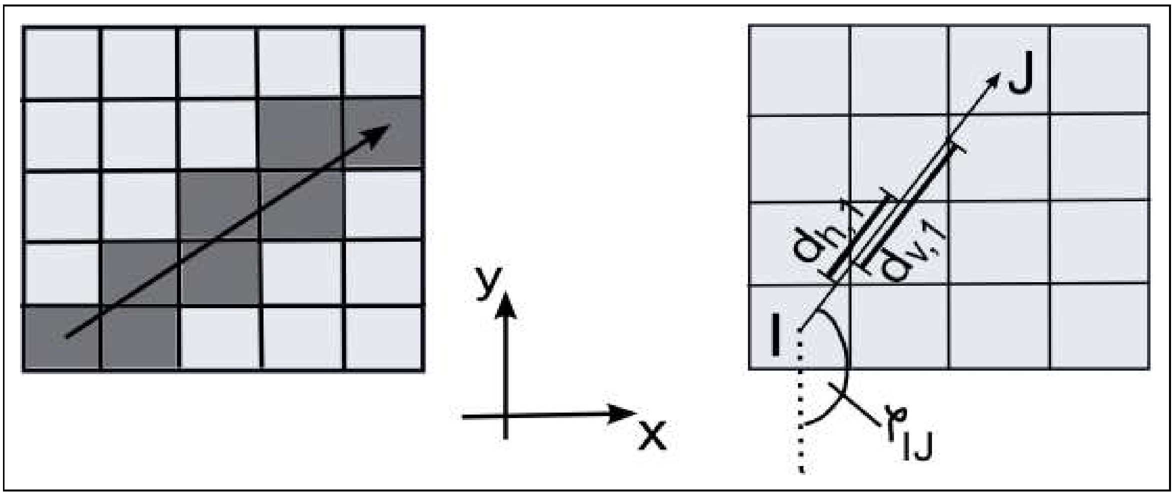

Figure 2.3: Figure similar to in Encarnação et al. (1997): A schematic to illustrate the stepwise traversal algorithm for ray tracing of Amanatides and Woo (1987). The *intermediate* grid cells J_{inter} are taken to be those which are traversed by the search path (shaded grid cells) (on the left hand). Two distance between two consecutive intersections of either type is constant ($d_{\text{v},1}$, $d_{\text{h},1}$).

search path and hopping from one intersection point to the next results in the complete sequence of 'intermediate' grid cells. Note, that the old implementation did not guarantee, that all intermediate grid cells have been found. More precisely, the algorithm can be stated as follows:
The distance between two consecutive intersections of either type is constant and given by

$$\begin{array}{rcl} d_{\text{v},1} & = & \Delta x/\ \sin(\varphi_{IJ}) \\ d_{\text{h},1} & = & -\Delta x/\ \cos(\varphi_{IJ})\ , \end{array} \tag{2.6}$$

respectively. Now hopping from one intersection point to the next means traversing the search path. At each point one considers the current distance d_{v}, d_{h} to the next intersection point of a respective type. The minimum of these distances determines which intersection will be crossed next. Since here, the search path starts from the center of grid cell I one can easily verify that the initial distances are given by

$$\begin{array}{rcl} d_{\text{v},0} & = & d_{\text{v},1}/2 \\ d_{\text{h},0} & = & d_{\text{h},1}/2 \end{array} \tag{2.7}$$

Note that the initial distances would be different if the search path's origin would not be set in the grid cell center. At first the initial distances $d_{\text{v},0}$, $d_{\text{h},0}$ are assigned the current distances $d_{\text{v}} = d_{\text{v},0}$, $d_{\text{h}} = d_{\text{h},0}$.
The steps, $step_{\text{x}}$ and $step_{\text{y}}$, along the search path from I to J, are derived from the grid cell differences between the two investigated cells $I = jN_x + i$ and $J = bN_x + a$ and can be $+1, -1$ or 0. Therefore, the required steps in x direction are computed by $step_{\text{x}} = a - i$ and the steps in y direction by $step_{\text{y}} = b - j$. The algorithm is summarised in the following:

The maximum distance d_{v} is increased by $d_{\text{v},1}$

$$\begin{array}{c} \textbf{for}\ \ [(|d_{\text{v}}|\ <\ |d_{\text{h}}|)\ \&\&\ (|step_{\text{x}}|\ >\ 0)]\ ||\ (d_{\text{h}}\ ==\ 0) : \\ \\ d_{\text{v}}\ =\ d_{\text{v}}\ +\ d_{\text{v},1} \end{array} \quad . \tag{2.8}$$

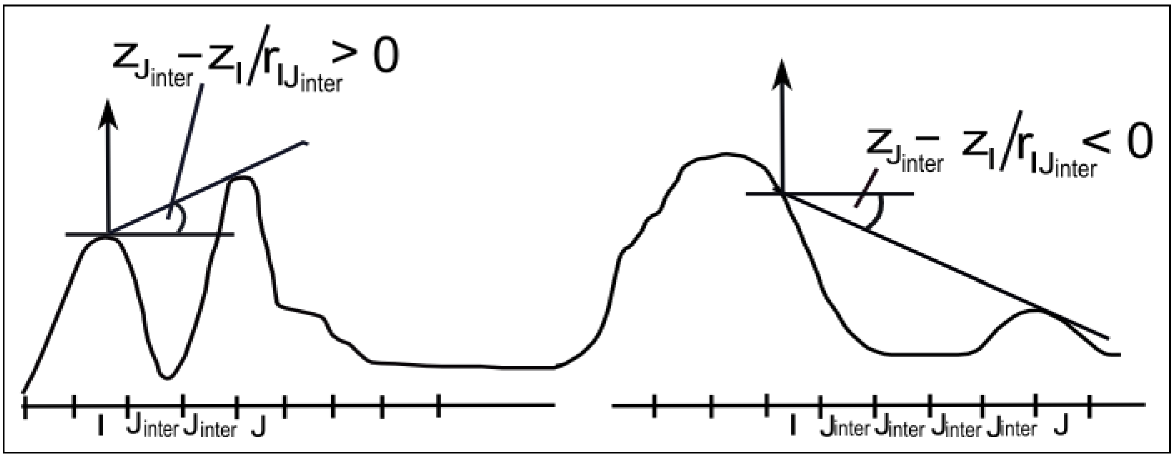

Figure 2.4: Visibility detecting. As indicated the algorithm searches for any $(z_{J_{\mathrm{inter}}} - z_I)/r_{IJ_{\mathrm{inter}}}$ larger than $(z_J - z_I)/r_{IJ}$ but considers also for lower patches with negative ratios.

The maximum distance d_{h} is increased by $d_{\mathrm{h},1}$

$$\begin{aligned} &\textbf{for}\ [(|d_{\mathrm{v}}| > |d_{\mathrm{h}}|)\ \&\&\ (|step_{\mathrm{y}}| > 0)]\ ||\ (d_{\mathrm{v}} == 0):\\ &d_{\mathrm{h}} = d_{\mathrm{h}} + d_{\mathrm{h},1} \qquad . \end{aligned} \tag{2.9}$$

Both maximum distances are increased by $d_{\mathrm{v},1}$ and $d_{\mathrm{h},1}$, respectively

$$\begin{aligned} &\textbf{for}\ [(|d_{\mathrm{v}}| == |d_{\mathrm{h}}|)\ \&\&\ (|step_{\mathrm{x}}| > 0)\ \&\&\ (|step_{\mathrm{y}}| > 0)]:\\ &d_{\mathrm{v}} = d_{\mathrm{v}} + d_{\mathrm{v},1} \qquad .\\ &d_{\mathrm{h}} = d_{\mathrm{h}} + d_{\mathrm{h},1} \end{aligned} \tag{2.10}$$

Sun-or-shadow is detected in the same way, i.e. $\chi_{\mathrm{sun},I} = 1$ if all heights of *intermediate* grid cells between I and the very boundary cell J, which is located in the direction of the sun azimuth, are below the line connecting the patch and the sun. This implies that the sun-or-shadow indicator $\chi_{\mathrm{sun},I}$ indicates if a patch A_I is **horizon shaded**. This is implemented by searching for any $(z_{J_{\mathrm{inter}}} - z_I)/r_{IJ_{\mathrm{inter}}}$ larger than $\sin(\pi/2 - \theta_{\mathrm{z}})$. If such an *intermediate* grid cell is found the search is stopped and $\chi_{\mathrm{sun},I}$ is set to zero. Since partial visibility is not accounted for, partial shading is also not accounted for here. The stepwise sequence of grid cells traversed by the search path is also computed similarly to the fast traversal algorithm for ray tracing of Amanatides and Woo (1987) as described above. The choice of the projection of the line connecting a patch and the sun on the appropriate boundary patch implies that the number of boundary grid cells determines the azimuthal resolution of the horizon line for each patch. Therefore, the accuracy of the implemented algorithm is mostly limited by the horizontal grid cell resolution of the DHM, the DHM mean height accuracy and the simplification of presuming regular rectangular grid cells in the model domain. Triangular irregular networks can represent topological information more realistically since they do describe the surface continuously instead of containing "holes".

Note that none of the χ_{IJ} are stored but that they are recomputed when required for the view factor computation (Section 4.1.2, p.47). Accordingly, $\chi_{\mathrm{sun},I}$ are recomputed for the appropriate sun position. A storage of all χ_{IJ} would lead to an additional memory requirement

Figure 2.5: Local horizon-shading on a house roof due to trees is leading to delayed hoarfrost melt for the shaded parts (N. Helbig).

of a double array of the order of $N \times N$ entries. Thus, the removal of the storage of horizon angles enables the computation of model domains with large grid cell numbers.

In contrast to horizon-shading self-shading is easily detected by checking if the cosine of the incident angle θ (Eq. (3.13)) of the sun is negative.

By comparing $(z_{J_{\text{inter}}} - z_I)/r_{IJ_{\text{inter}}}$ with $(z_J - z_I)/r_{IJ}$ and $\sin(\pi/2 - \theta_{\text{z}})$, respectively a horizontal viewing patch is assumed instead of the inclined patch. But thanks to the chosen algorithm search also negative horizon angles are captured (cf. Fig. 2.4). Nevertheless, the actual horizon of a patch is given by: max(0°, horizon angle). Even though horizon angles $\leq$ zero do not alter the sun-or-shadow indicator for sun elevation angles larger zero (sunrise), negative horizon angles are essential to determine mutual visibility of lower terrain surfaces. In complex terrain, the neglect of lower terrain surfaces, leads to underestimated incident terrain radiation. Therefore, as will be pointed out in Section 9.4, p.134, a (sky) view factor derived from a horizontal viewing patch with only positive horizon angles does not account for all visible terrain below the horizontal patch. Thus, it is stressed that the sky view factor is not simply the solid angle covering the visible sky. This assumption is leading to erroneous (sky) view factors and thus, to erroneous incident terrain radiation.

The size of the model domain should be chosen carefully. If the model domain does not include the highest visible surrounding mountain peaks shading errors result due to an underestimation of horizon angles. The horizon angles for border patches looking out of the model domain are chosen to be zero.

Note that additional heights of obstacles like trees or houses are not included in the used DHM's. They can only be accounted for by adding mean representative heights to the DHM heights z. This leads to new horizon angles since then trees are not implemented as raised parallel planes compared to the original DHM height plane instead completely new patch orientations result. Nevertheless, this is a first rough solution to account for the additional tree height.

Finally, an example of local horizon-shading due to trees is given in Fig. 2.5. As can be seen the local shading has a clear impact on hoarfrost melting at the house roof.

3 3D-model for incident broadband solar SW and LW radiation

The present radiation balance model (a module of Alpine3D) computes spatial shortwave (SW) and longwave (LW) radiation components. For SW radiation, this is done by estimating a mean atmospheric transmittance as well as by applying a statistical model based on the clearness index and from an exposed point measurement of global radiation. The model treats the atmosphere vertically integrated, i.e. the model does not solve the radiative transfer equations at different vertical levels. Instead, the spatial distribution of the radiative fluxes is calculated at the surface. For the clearness index the top of atmosphere radiative flux is additionally determined. All parameterisations in the model only consider simple one-band (broadband) SW and LW radiation instead of the fully resolved solar radiation spectrum. Spatial broadband LW radiation is computed from an exposed point measurement or from cloud covers observation at one site. Multiple SW terrain radiation reflections have been implemented (Chapter 4, p.45) replacing the former single terrain reflection estimation. LW single terrain emission is now implemented similar to the multiple SW terrain reflections (Chapter 4, p.45).
The radiation balance model applied in this study is the result of the work of many people. While many changes have been implemented in the model, the main contributions are briefly specified here:

The primary work leading to an "areal energy balance model" (AEB model) over a complex snow-covered topography with a diurnal resolution was conducted by Plüss (1997). He characterised all fluxes of the energy balance at the snow-atmosphere interface at a high alpine location by direct measurements and modelling. His modelling was based on parameterisations obtained from the literature. However, new parameterisations for snow surface albedo, snow surface temperature and LW terrain emission were derived from the measurements during the ablation period only. In the LW terrain emission parameterisation he included atmospheric effects between the emitting and receiving terrain surfaces. Consequently, the AEB model accounts for terrain emission as well as single scattering from terrain for SW radiation. SW terrain reflections and LW terrain emissions were included by Plüss (1997). He implemented the basic equations of Kondratyev (1969) for the calculation of the radiation from the unobstructed sky fraction of the hemisphere and from the fraction of the hemisphere obstructed by terrain.
Riber (2001) refined the AEB model from diurnal to hourly resolution and for mid-winter conditions. Iterating the energy balance equation with the snow surface temperature determined by Stefan-Boltzmann's law did this on the one hand. And on the other hand the introduction of an outgoing or ingoing vertical heat flux at the one layer snow pack below, thereby replacing the constant ground heat flux of Plüss (1997). AEB was then called an "extended AEB model" (ExtAEB) and was further evaluated by Fierz et al. (2003).
At the same time Martius (2002) merged all ExtAEB model parts written in different programming languages, changed the implemented calculation algorithm for the horizon of Funk

(1984) and introduced the view factor concept (Oke (1987)). The model was renamed "distributed energy balance model for alpine terrain" (DEBAT).
Afterwards a one-dimensional model of vegetation, snow and soil (SNOWPACK) (Bartelt and Lehning (2002), Lehning et al. (2002a) and Lehning et al. (2002b)) was coupled to DEBAT. The parameterisation of surface albedo values, the computation of surface temperature as well as the turbulent fluxes became redundant since those were then computed by SNOWPACK (Section 5.4, p.82). The newly coupled model system was assigned the name Alpine3D and consisted of the radiation balance module and the SNOWPACK module. In the meantime more modules are added to the coupled model system Alpine3D (Section 5, p.79). Alpine3D is briefly described for a hydrological application in Lehning et al. (2006).
Landl (2007) extended the LW terrain parameterisation in the radiation balance module of Alpine3D, which was still based on a melting snow surface (Plüss (1997)), allowing for a wider range of surface and air temperatures and varying distances between emitting and receiving surfaces.

In the following sections, a detailed description of the present radiation balance model is given. The radiation balance model is now completely revised. Several additional or more recent parameterisations are implemented to complete the radiation balance computation accurately. Minor changes are conducted concerning the adaptation of constants to recent research values or to regional conditions of the Eastern Alps. The main changes are the introduction of a diffuse sky radiation for clear sky conditions in a hourly resolution (Eq. (3.39)), the substitution of the formula for the relative optical mass for clean dry air by the corrected formula of Kasten and Young (1989) (Eq. (3.16)), the introduction of a correction for the altitude dependence of the total transmittance from Bintanja (1996) (Eq. (3.33)), the substitution of the solar declination formula by the one of Bourges (1985) (Eq. (3.3)), the introduction of an adjusting coefficient for diffuse sky radiation under cloudy sky conditions (Eq. (3.45)) and the substitution of the decomposition model for the direct and diffuse sky SW radiation under cloudy sky conditions of Erbs et al. (1982) by a combination of the models of Reindl et al. (1990) (Section 3.1.3, p.37).
Additionally, the loose concept of the view factor approach has been extended and reformulated in terms of a radiosity approach to compute the radiation exchange in complex terrain (Chapter 4, p.45).

3.1 SW surface radiation balance model

In this section the equations to determine spatial broadband global radiation S_g under cloudy sky conditions by means of one exposed measured global radiation value $S_\mathrm{g}^\mathrm{meas}$ are given. Broadband SW radiation stands for integrated values over the complete visible solar spectrum. Global radiation S_g generally consists of SW direct, diffuse sky and reflected terrain (Section 4.2, p.58) radiation. However the reflected terrain radiation is assumed to be zero at the exposed measurement site (no visible terrain). All spatial clear sky radiative fluxes are derived theoretically for one layer at the surface by treating the atmosphere as a vertically integrated column. By comparing the computed radiative flux at the top of the atmosphere with the exposed measured global radiation flux at the surface, information about cloudiness is obtained and can be incorporated.
On the one hand, the lower computational complexity of such a simplified surface radiation balance model allows for the modelling of very local radiation patterns since much higher

resolved digital height models (DHM) can be used. Consequently, the local terrain influences shading (Section 2.2, p.19), SW terrain reflections and LW terrain emissions (Chapter 4, p.45) can be accounted for in detail. On the other hand, the simplification of a vertical integrated atmosphere and the derivation of spatial cloudy SW radiation from one measurement are leading to larger errors than those computed with a three-dimensional atmospheric model.

3.1.1 Astronomical relationships

In order to motivate the astronomical relationships for radiation balance modelling a simple but illustrative example is given, namely an analemma. Fig. 3.1 shows a picture of an analemma in Davos, Switzerland produced by Meier (2007). A photograph of the sun is taken each day over a period of one year at exactly the same position and at exactly the same time. By overlaying all images the apparent position of the sun at the sky follows the figure “eight”. This effect is due to the earth’s ecliptic orbit as well as due to its tilted rotational axis. Consequently, applications which rely on the sun position with a greater accuracy than the deviations indicated by Fig. 3.1 should take into account these astronomical relationships.

Total solar irradiance

The total solar energy at all wavelengths per unit time incident on a unit area perpendicular to rays of the sun at one astronomical unit AU is often called the solar constant. Thereby, one AU is defined as the mean distance $r_0 = 1.496 \text{ x } 10^{11}$ m between earth and sun. But in fact, the solar constant is not constant and is therefore called total solar irradiance TSI. Its slow variation is monitored in long term series measurements from space. Presently, the average TSI value is 1366.1 Wm^{-2} (Fröhlich and Lean (1998), Fröhlich (2006)) which is used in this study.

Eccentricity correction factor E_0

Due to the elliptical orbit of the earth around the sun the actual TSI received on the earth is proportional to the ratio between the mean earth-sun distance r_0 and the current earth-sun distance r. Many formulas exist to express the varying distance of the earth around the sun on the ecliptic plane in a simple mathematical form. This is traditionally done by a Fourier series expansion. Here, the more accurate formula of Spencer (1971) is used with a maximum error of 0.0001 (accuracy based on the year 1950). Thus, the diurnal changing dimensionless eccentricity correction factor E_0 of the orbit of the earth is given by

$$\begin{aligned} E_0 = (\tfrac{r_0}{r})^2 = 1.00011 \; &+ 0.034221 \; \cos\Gamma + 0.00128 \; \sin\Gamma \\ &+ 0.000719 \; \cos 2\Gamma + 0.000077 \; \sin 2\Gamma \,, \end{aligned} \tag{3.1}$$

where the day angle Γ is the angle between the radius vector and the radius vector on 1 January in the ecliptic plane (also called mean anomaly in astronomy) (cf. Fig. 3.2). Assuming a circular orbit, each day d_n in a year is assigned a day angle Γ (Spencer (1971))

$$\Gamma = \frac{2\pi \; (d_\mathrm{n} - 1)}{365.2425} \,. \tag{3.2}$$

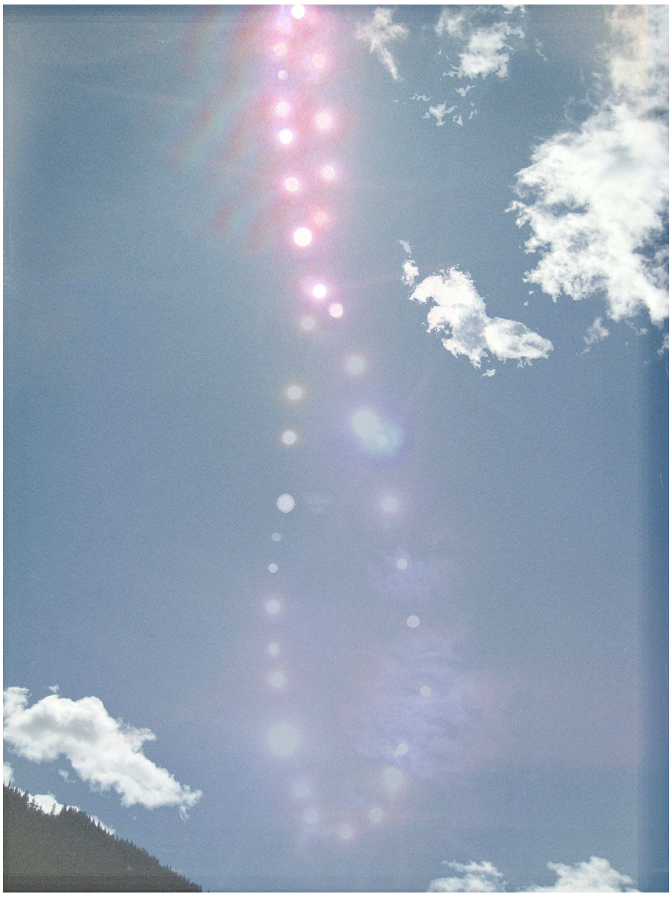

Figure 3.1: An analemma produced by Meier (2007) during a school project at Schweizerische Alpine Mittelschule in cooperation with the Physikalisch-Meteorologisches Observatorium Davos, World Radiation Center in Davos, Switzerland (PMOD/WRC (WWW)) is shown.

The day number d_n is one on 1 January and always 365 on 31 December. The accuracy of Eq. (3.1) varies slightly if a constant year length of 365 days would also be applied for leap years. Therefore, the mean year length of 365.2425 days of the Gregorian calendar was introduced in Spencer (1971)'s formula.

Solar declination angle δ

The description of the solar declination angle δ is based on the fixed equatorial coordinate system in which the z-axis coincides with the earth's rotational axis (cf. Fig. 3.2). The rotation of the earth around its axis causes the diurnal variation of incident radiation and the rotation of the earth around the sun causes the seasonal variation of incident radiation. In the equatorial coordinate system the position of the sun is defined by the declination angle δ, i.e. the angle of the line connecting the centers of the sun and the earth to the equatorial plane, (angular separation from the equatorial plane) and by a hour angle (angular separation from the spring equinox). The declination angle δ changes continuously and has in the northern hemisphere the maximum 23.45° at the summer solstice and the minimum

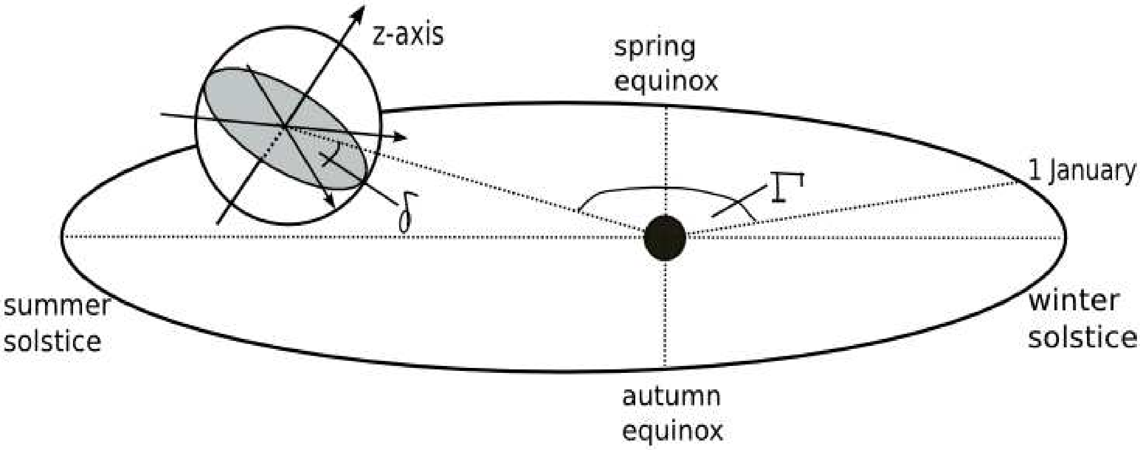

Figure 3.2: The elliptical orbit of the earth around the sun with spring and autumn equinox points of time, declination angle δ, day angle Γ and the fixed equatorial coordinate system in which the z-axis coincides with the earth's rotational axis.

-23.45° at the winter solstice (the seasons pertain to the northern hemisphere, reverse is true for the southern hemisphere). The angle is zero at the spring and autumn equinoxes (Fig. 3.2). As noted by Duffie and Beckman (2006), the largest possible change of the declination angle within 24 hours (which occurs at the equinoxes) is about 0.4°. If the daytime change in declination angle is neglected a maximum error of only 0.4° can arise in calculating solar azimuth and zenith angles. Different solutions exist to calculate the daily declination angle with different degrees of accuracy. The formula of Spencer (1971) is replaced by that of Bourges (1985) to reduce the maximum error of 0.034° to 0.02°. Accordingly, the declination angle δ in radians is given by

$$\begin{aligned}\delta = (0.3723 &+ 23.2567\ \sin\Gamma_{\mathrm{ne}} - 0.758\ \cos\Gamma_{\mathrm{ne}}\\ &+ 0.1149\ \sin 2\Gamma_{\mathrm{ne}} + 0.3656\ \cos 2\Gamma_{\mathrm{ne}}\\ &- 0.1712\ \sin 3\Gamma_{\mathrm{ne}} + 0.0201\ \cos 3\Gamma_{\mathrm{ne}})\ \pi\ /\ 180\end{aligned} \tag{3.3}$$

where Γ_{ne} is the day angle in radians relative to spring equinox time. The day angle Γ_{ne} is calculated similar to the day angle Γ (Eq. (3.2)) with a day number d_{ne}, relative to the spring equinox time

$$d_{\mathrm{ne}} = d_{\mathrm{n}} - 0.5 - n_0\ . \tag{3.4}$$

If d_{ne} is negative the mean year length 365.2425 needs to be added. The spring equinox time n_0 counted in days from the beginning of the year can be calculated according to Bourges (1985)

$$n_0 = 78.801 + 0.2422\ (\mathrm{Year} - 1969) - \mathrm{INT}(0.25\ (\mathrm{Year} - 1969))\ . \tag{3.5}$$

Which is valid for years after 1969. The INT() denotes the *integer part* function. For determining the spring equinox time for the first half of the 21st century the first summand in Eq. (3.5) is recalculated. This summand stands for the spring equinox day of the first year of the second half of the 20th century. It is 79.3542 for the actual period starting on 1 January 2000 with spring equinox day on 20 March 2000 at 8:30 UTC+1.

Local apparent solar time

The local apparent solar time is used in all of the sun-angle equations and is taken as a unified reference time. Local apparent solar time or true solar time is the time indicated by sundials and is based on the apparent solar day. In contrast, local mean solar time is an artificial average of local apparent time and is indicated by clocks. An apparent solar day is defined as the interval of time that the sun requires to complete one cycle to return to the local meridian. Due to the elliptical orbit of the earth around the sun and due to the tilted axis of the earth relative to the ecliptic plane, the length of an apparent solar day varies throughout a year. This means that although the sun always traverses the local meridian at solar noon this does not need to correspond to noon measured in local mean time. One solar day measured in local mean solar time lasts 24 hours. The deviation of local mean time relative to the local apparent time is accounted for by the equation of time E_t. The equation of time E_t is therefore the required correction for the conversion of local mean time to local apparent solar time and can reach up to 16 minutes. It is computed from a truncated Fourier series (Spencer (1971), Iqbal (1983))

$$\begin{aligned} E_\mathrm{t} \;=\; 229.18\,(0.000075 \; &+ 0.001868\;\cos\Gamma \;-\; 0.032077\;\sin\Gamma \\ &- 0.014615\;\cos 2\Gamma - \;0.04089\;\;\sin 2\Gamma)\;. \end{aligned} \tag{3.6}$$

The constant 229.18 minutes $= 24 \cdot 60/2\pi$ converts the radians into minutes (Iqbal (1983)). This formula is accurate to within 35 seconds, again based on the year 1950.
Local standard time is local mean solar time with reference to a certain meridian. The conversion of local standard time to local mean solar time is conducted by a geographical longitude correction (time zone correction). Thereby, the difference between the longitude L_st on which the local standard time is based and the local longitude L_loc of a local position is corrected. Both are related by

$$L_\mathrm{st} \;=\; 15\;\mathrm{INT}(\frac{L_\mathrm{loc}}{15} \pm\; 0.5)\;, \tag{3.7}$$

where the "+" applies to positive (east direction) and the "-" to negative L_loc (west direction). Since the sun requires four minutes to cross 1° of longitude the time zone correction is obtained, in minutes, from

$$\text{time zone correction } = 4\;(L_\mathrm{loc} - L_\mathrm{st})\;.$$

Finally, the local apparent solar time can be related to local standard time by its two corrections according to

$$\text{local apparent solar time } = \text{ local standard time } + \text{ time zone correction } + E_\mathrm{t}\;. \tag{3.8}$$

Note that summer time is not accounted for.

Position of the sun

A horizontal coordinate system is used to describe the position of the sun for a specific observer on the earth (here the center of the model domain) in terms of the azimuth angle ψ and zenith angle θ_z (cf. Fig. 3.3). In the horizontal coordinate system the local horizon of an observer represents the zero plane. Because this coordinate system is fixed to the earth all

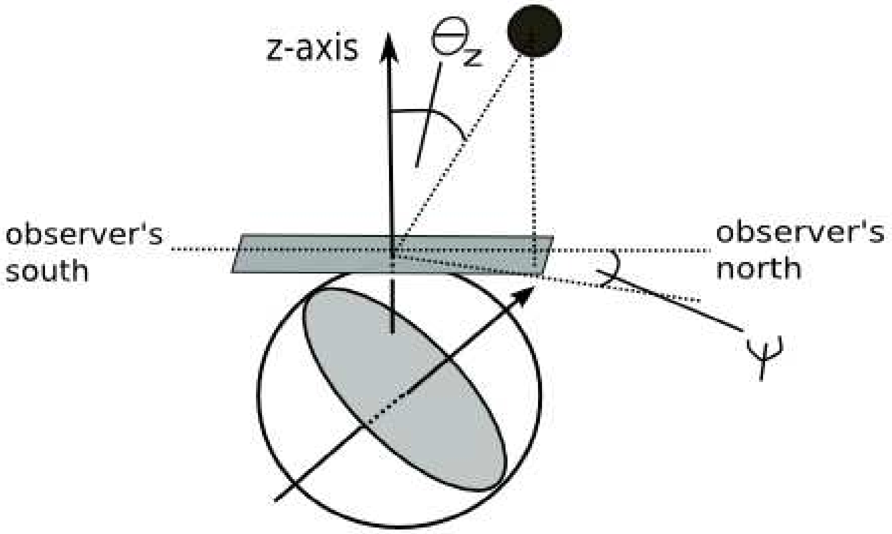

Figure 3.3: The horizontal coordinate system is shown to describe the position of the sun for a specific observer on the earth in terms of the azimuth angle ψ and zenith angle θ_z.

angles are time dependent. Additionally, the coordinates of the sun depend on the observer position on earth. Since here, typical model domains are of at maximum mesoscale sizes the azimuth ψ and zenith angle θ_z of the sun at the center of the model domain can be used for the entire domain. In addition, the sun can be treated as a point radiation source at infinite distance.

The first sun coordinate, the azimuth angle ψ, is defined as the angle between the projection of the sun-earth vector and the true north projection on the horizontal plane of the observer's horizon. It is calculated around the horizon in radians and measured clockwise from north (Oke (1987))

$$\cos\psi \;=\; (\sin\delta\;\cos\phi \;-\; \cos\delta\;\sin\phi\;\cos w)\;/\;\sin\theta_\mathrm{z}\;. \tag{3.9}$$

Note that if the mean solar time is larger than twelve the azimuth angle needs to be subtracted from 2π. ϕ is the geographical latitude of the center of the model domain in ° which is inserted in radians in Eq. (3.9). θ_z is the zenith angle of the sun. w is the hour angle of the sun based on the apparent solar day which is inserted in radians. As noted before, at apparent solar noon the sun crosses the local meridian. However, for the rest of the day the sun has an angular displacement east or west of the local meridian. This angular displacement is called hour angle w. It is zero at solar noon, positive in the morning, negative in the afternoon and changes 15° per hour throughout the year since the earth's rotation speed is 15° per hour. The hour angle w is computed for a horizontal coordinate system in ° as follows (Oke (1987))

$$w \;=\; 15\;(12\;-\;\text{local apparent time})\;. \tag{3.10}$$

The second sun coordinate, the zenith angle θ_z, is defined as the angle between the sun point and the zenith direction, the z-axis in the horizontal coordinate system. It is calculated according to Oke (1987)

$$\cos\theta_\mathrm{z} \;=\; \sin\phi\;\sin\delta + \cos\phi\;\cos\delta\;\cos w\;. \tag{3.11}$$

with ϕ, w and δ in radians.

Incidence angle θ

The local incidence angle θ on a tilted surface is the angle between the sun vector and the surface normal to that surface. On a horizontal surface the incidence angle equals the zenith angle θ_z given by Eq. (3.11). On an arbitrary tilted surface the incidence angle θ can be determined from the scalar product between the sun vector $\vec{s}$, i.e. the vector from the observer to the sun point, and the surface normal $\vec{n}$ to the observer surface (Funk (1984)). The surface normal vectors $\vec{n}_I$ have to calculated for every individual grid cell I. Thereby I indicates the position of the grid cell in the model domain with I, going from zero to N-1 and $N=\text{dim}i\times\text{dim}j$ (dim$i$, dim$j$ number of grid cells in i and j direction, respectively). In contrast to the surface normal vectors $\vec{n}_I$ one sun vector $\vec{s}$ is valid for all grid cells but is recalculated for each time step. This is consistent with the constant position of the sun for all grid cells per time step (previous section).
The sun vector $\vec{s}$ is given for a left handed coordinate system, where the x-axis increases eastwards and the y-axis increases northwards, and the azimuth angle ψ, converted to be counted counterclockwise from south, by

$$\begin{aligned} s_x &= \sin\psi\ \cos(\pi/2 - \theta_z) \\ s_y &= -\cos\psi\ \cos(\pi/2 - \theta_z) \\ s_z &= \sin(\pi/2 - \theta_z)\ . \end{aligned} \tag{3.12}$$

Thus, the incidence angle θ_I of an arbitrary inclined grid cell I is given by (Funk (1984))

$$\cos\theta_I = (\vec{n}_I \cdot \vec{s}) \ / \ (||\,\vec{n}_I\,||\ ||\,\vec{s}\,||) \tag{3.13}$$

where the surface normal vector $\vec{n}_I$ is calculated from the DHM as in Eq. (2.2).

3.1.2 Direct and diffuse sky radiation under clear skies

The incident global radiation S_g consists of incident direct (**b**eam) radiation S_b, incident **d**iffuse sky radiation S_d, due to scattering processes in the atmosphere, and incident radiation S_t received from the surrounding **t**errain, due to reflections. The latter will be discussed in detail in Section 4, p.45. Measurement stations within automatic meteorological measurement networks, like the ANETZ[1] network of the Federal Office of Meteorology and Climatology in Switzerland, usually record the incident global radiation S_g. In contrast, stations that permanently record the *individual* components of radiation, i.e. either diffuse sky S_d or direct S_b, are rare. It is however necessary to obtain these individual components if one wants to infer the spatial incident SW radiation for a model domain in complex terrain from a single exposed measured global radiation S_g^{meas}: roughly speaking, the direct component S_b additionally depends on the orientation of the surface whereas the isotropic diffuse sky component additionally depends on the sky view factor $F_{\text{sky}I}$ (cf. Section 4.2, p.58 Eq. (4.42)). If just a single measured value of global radiation S_g is available both components must be estimated by an empirical decomposition method. This section describes how a single set of measured values of air temperature T_a, air pressure p, relative humidity rh, and global radiation S_g as well as the astronomical relationships presented in Section 3.1.1, p.27, is used to

---

[1] German: Automatisches Netz

calculate the spatial distribution of broadband, direct S_{b} and diffuse sky S_{d} radiation under clear sky conditions. This is done by determining a mean vertically integrated atmospheric transmittance for each grid cell in the model domain.

The spatial interpolated values of air temperature T_{a}, air pressure p, and relative humidity rh (computed in the main Alpine3D module; cf. Section 5.2, p.79) are used to mimic the varying atmospheric conditions within the domain which in turn are used to compute the spatially varying transmitted radiation from the top of atmosphere S_{toa} value. With Eq. (3.1), the diurnal value of top of atmosphere radiation S_{toa} can be expressed as follows

$$S_{\mathrm{toa}} \;=\; \mathrm{TSI}\; E_0 \;. \tag{3.14}$$

The top of atmosphere S_{toa} radiation describes the mean energy incident on a surface normal to the sun vector $\vec{s}$ at the top of the atmosphere (extraterrestrial irradiance).

Due to scattering processes by molecules (Rayleigh-scattering) and by aerosols (Mie-scattering) as well as absorption processes by different components of the atmosphere, only a fraction of the top of atmosphere radiation S_{toa} is received as global radiation at the surface even under clear sky conditions. In order to obtain the spectrally integrated direct and diffuse sky radiation components, simple broadband transmittance functions are applied to S_{toa} in order to represent the scattering and absorption processes. Following Beer's law, the attenuation of beam intensity is given by

$$S \;=\; S_0\; \mathrm{e}^{(-k\; m)} \tag{3.15}$$

with the exponent describing the optical depth (dimensionless). Here, k is the total broadband extinction coefficient of a homogeneous medium (area per mass) and $m = \int_0^{\mathrm{s}_1} \rho\; \mathrm{d}s$ represents the mass of a substance in a column of unit cross section, the optical path length also called the optical mass. According to Iqbal (1983), the relative optical air mass m_{r} (dimensionless) m_{r} is defined as the ratio of the optical path along the oblique path to the vertical path in the local zenith direction (normal to the horizontal plane of the observer's horizon), i.e. *relative* to the zenith direction. In fact m_{r} should be computed separately for every atmospheric constituent, namely clean dry air, water vapor, ozone and aerosol, to take into account the different attenuations. However, as pointed out by Iqbal (1983), determining these individual attenuations is difficult. Therefore, the relative optical mass for clean dry air m_{r} is used for all constituents. Kasten and Young (1989)'s revised m_{r} formula is used

$$m_{\mathrm{r}} \;=\; \frac{1}{\cos\theta_{\mathrm{z}} \;+\; 0.50572\;(96.07995 \;-\; \theta_{\mathrm{z}})^{-1.6364}} \tag{3.16}$$

with θ_{z} in degree. The maximum error of m_{r} compared to the true values of relative optical air mass is 0.432 % at θ_{z}=90° and is less than 0.125 % for θ_{z} <88.5° (Kasten (1993)). In some transmittance parameterisations a pressure correction needs to be applied to the relative optical mass m_{r} in Eq. (3.16) since m_{r} is only valid for standard conditions. Therefore, a relative optical air mass m_{a} (or absolute optical air mass) (dimensionless) which is valid under actual conditions, is defined separately and usually approximated for local conditions by

$$m_{\mathrm{a},I} \;=\; m_{\mathrm{r}}\; \frac{p_I}{p_0} \;. \tag{3.17}$$

The exponential $\mathrm{e}^{(-k\; m)}$ in Eq. (3.15) is also referred to as the total broadband transmittance function, which subsumes the influence of various atmospheric constituents. The attenuation effect of these is often assumed to be additive, resulting in a simple multiplication of their transmittance functions. In the following the implemented transmittance functions for direct radiation are briefly described. These are all taken from Bird and Hulstrom (1981) unless specified otherwise.

Rayleigh-scattering is scattering by air molecules that have particle small diameters compared to the wavelength of the radiation. The broadband transmittance function by Rayleigh-scattering τ_r is parameterised by

$$\tau_{\mathrm{r},I} \;=\; \mathrm{e}^{(-0.903\ m_{\mathrm{a},I}^{0.84}(1\ +\ m_{\mathrm{a},I}\ -\ m_{\mathrm{a},I}^{1.01})}\ , \tag{3.18}$$

with the optical air mass $m_{\mathrm{a},I}$ for local conditions. The broadband transmittance function τ_g due to absorption by uniformly mixed gases such as CO_2 and O_2 also involves $m_{\mathrm{a},I}$ and is estimated by

$$\tau_{\mathrm{g},I} \;=\; \mathrm{e}^{(-0.0127\ m_{\mathrm{a},I}^{0.26})}\ . \tag{3.19}$$

The broadband transmittance function τ_o due to absorption by ozone is given by

$$\begin{aligned}\tau_\mathrm{o} \;=\; 1 \;&-\; 0.1611\ U_3\ (1\ +\ 139.48\ U_3)^{-0.3035} \\ &-\; 0.002715\ U_3\ (1\ +\ 0.044\ U_3\ +\ 0.0003\ U_3^2)^{-1}\ ,\end{aligned} \tag{3.20}$$

where U_3 is the total amount of ozone in an oblique column of air in the atmosphere

$$U_3 \;=\; U_0\ m_\mathrm{r}\ . \tag{3.21}$$

and U_0 is the total amount of ozone in a vertical column (vertical ozone layer thickness) in cm valid for standard conditions. Therefore, Eq. (3.21) involves the relative optical mass m_r **without** air pressure correction. The vertical ozone layer thickness U_0 varies with latitude and season. For this model a mean U_0 was applied from daily mean total ozone data measured at the Light Climatic Observatory in Arosa, Switzerland (LKO (WWW)) (see also Staehelin et al. (1998)). A mean vertical ozone layer thickness value of U_0=0.32 cm was obtained from daily data from 1 January 1998 to 31 December 2004.
The broadband transmittance function τ_w due to absorption by water vapor is given by

$$\tau_{\mathrm{w},I} \;=\; 1\ -\ 2.4959\ U_{1,I}\ \frac{1}{(1\ +\ 79.034\ U_{1,I})^{0.6828}\ +\ 6.385\ U_{1,I}} \tag{3.22}$$

with the total amount of precipitable water $U_{1,I}$ in an oblique column in cm at each grid cell I

$$U_{1,I} \;=\; wp_{0I}\ m_\mathrm{r}\ . \tag{3.23}$$

Here wp_{0I} represents the amount of precipitable water in a vertical column from surface in cm at each grid cell I and is determined according to Leckner (1978). The air pressure and air temperature correction is included in the numerical prefactor of

$$wp_{0I} \;=\; 0.493\ \frac{rh_I\ e_{\mathrm{s},I}}{T_{\mathrm{a},I}}\ . \tag{3.24}$$

with the air temperature T_a in K. Therein e_s is the saturation vapour pressure in Pa over a flat water or ice surface. The saturation vapour pressure is determined here from the empirical equations of Magnus transformed by Murray (1967)

$$e_{\mathrm{s},I} \;=\; 610.78\ \mathrm{e}^{\frac{17.27\ (T_{\mathrm{a},I}\ -\ 273.16)}{T_{\mathrm{a},I}\ -\ 35.86}} \quad \text{for } T_{\mathrm{a},I}\ \geq\ 273.16 \tag{3.25}$$

$$e_{\mathrm{s},I} \;=\; 610.78\ \mathrm{e}^{\frac{21.88\ (T_{\mathrm{a},I}\ -\ 273.16)}{T_{\mathrm{a},I}\ -\ 7.66}} \quad \text{for } T_{\mathrm{a},I}\ <\ 273.16 \tag{3.26}$$

where the melting point of water is taken to be 273.16 K (triple point).
The total broadband transmittance function τ_{a} due to Mie-scattering and due to absorption by aerosols is valid for local conditions because the parameterisation contains the optical air mass m_{a}, I at each grid cell I. In contrast to the other broadband transmittance functions τ_{a} is based on spectral attenuation at only two wavelengths λ: 0.38 μm and 0.5 μm. According to Iqbal (1983), the lowest molecular (ozone) absorption is achieved at these two wavelengths. The transmittance function τ_{a} is given by

$$\tau_{\mathrm{a},I} \;=\; \mathrm{e}^{-k_{\mathrm{a}}^{0.873}\;(1\;+\;k_{\mathrm{a}}\;-\;k_{\mathrm{a}}^{0.7088})\;m_{\mathrm{a},I}^{0.9108}}\;\;. \tag{3.27}$$

Therein k_{a} represents the broadband aerosol optical depth (AOD) or turbidity (dimensionless) from surface in a vertical path. The spectral dependence of the AOD is often parameterised by

$$k_{\mathrm{a}} \;=\; 0.2758\;k_{\mathrm{a},0.38}\;+\;0.35\;k_{\mathrm{a},0.5} \tag{3.28}$$

where $k_{\mathrm{a},0.38}$ and $k_{\mathrm{a},0.5}$ are the AOD of a vertical column from the surface at wavelengths λ= 0.38 and 0.5 μm, respectively. For both wavelengths the AOD is derived from a single formula known as Ångström's turbidity formula (Ångstrom (1929), Ångstrom (1930), Iqbal (1983))

$$k_{\mathrm{a},\lambda} \;=\; \beta\;\lambda^{-a} \tag{3.29}$$

where a is the wavelength exponent related to the size distribution of the aerosols, with typical values between 0.5 and 2.5, and β is the Ångström's turbidity coefficient, varying from 0 to 0.5 or even higher, and representing the amount of aerosols in the vertical direction. If no measurements are available Iqbal (1983) recommends to set a=1.3±0.5, which should be valid for most natural atmospheres. Therefore, a is taken to be the mean value 1.3. But note that an uncertainty is inherent in this value having a large influence on the transmittance function τ_{a} and hence the derived S_{b} and S_{d} radiation components. Note also, that the applied wavelength exponent a is valid for the whole year, i.e. with no distinction between summer and winter values. AOD measurements at different wavelengths are conducted at the Physikalisch-Meteorologisches Observatorium Davos, World Radiation Center in Davos, Switzerland (PMOD/WRC). From these a mean AOD values at 0.5 μm wavelength of 0.076 and at 0.38 μm wavelength of 0.106 were derived for measurements of the years 2006 to 2007. Both are representing a relatively clear dry mountain air (Wehrli (2002)). With these a mean β value of 0.03 was computed for a clear atmosphere resulting in a mean constant broadband AOD (k_{a}) value of 0.055 for the present model.
For the determination of diffuse sky radiation the transmittance function due to aerosol absorption τ_{aa} and the transmittance function due to Mie-scattering τ_{as} are required. Therefore, the total broadband transmittance function τ_{a} is splitted into its two individual transmittance functions: one due to aerosol absorption τ_{aa} and one due to Mie-scattering τ_{as}. According to Bird and Hulstrom (1981) they are related as follows

$$\tau_{\mathrm{a},I} \;=\; \tau_{\mathrm{aa},I}\;\tau_{\mathrm{as},I}\;\;. \tag{3.30}$$

A term called single scattering albedo w_0, commonly applied by meteorologists, separates both processes (Bird and Hulstrom (1981) as cited by Iqbal (1983)). The single scattering albedo w_0 describes the ratio of energy scattered by Mie-scattering to total attenuation during the first entry of direct radiation into the atmosphere. The derivation of w_0 is difficult since it depends on aerosol material, shape, size and optical properties e.g. small aerosols of rural regions usually scatter more than those of urban-industrial regions. Unless detailed information is available it is common to employ fixed, wavelength independent w_0 values of e.g. ≈ 0.6 for urban-industrial regions and ≈ 0.9 for rural-agricultural regions. Here a single scattering albedo w_0 of 0.9 is applied. According to Bird and Hulstrom (1981) the transmittance by aerosols due to absorption τ_{aa} can be determined for local conditions as

$$\tau_{\mathrm{aa},I} \;=\; 1 \;-\; (1 \;-\; w_0)\,(1 \;-\; m_{\mathrm{a},I} \;+\; m_{\mathrm{a},I}^{1.06})\,(1 \;-\; \tau_{\mathrm{a},I})\;. \tag{3.31}$$

The transmittance function due to Mie-scattering $\tau_{\mathrm{as}I}$ can then be derived accordingly from $\tau_{\mathrm{a},I}/\tau_{\mathrm{aa},I}$.

Bird and Hulstrom (1980) and Bird and Hulstrom (1981) carried out an extended study on different models which compute theoretical direct normal radiation by comparing their results to the output of the SOLTRAN model (Bird and Hulstrom (1980)). On the basis of this study they constructed a new model, which is adapted for the present model. Their resulting basic equation for the incident direct radiation on a plane normal to the sun beam is

$$S_{\mathrm{b},I}^{\perp\,\mathrm{Bird}} \;=\; 0.9662\; S_{\mathrm{toa}}\;(\tau_{\mathrm{r},I}\;\tau_{\mathrm{o}}\;\tau_{\mathrm{g},I}\;\tau_{\mathrm{w},I}\;\tau_{\mathrm{a},I}), \tag{3.32}$$

with the factor 0.9662 representing the spectral interval of extraterrestrial irradiance, which is based on the spectral interval of SOLTRAN (0.3-3.0 μm) as well as on a TSI of 1353 Wm^{-2}. Here, a different factor of 0.9751 is used from Iqbal (1983) which is based on a TSI value of 1367 Wm^{-2}.

In addition Eq. (3.32) was further extended by introducing a correction b in m for the altitude dependence of the total transmittance (Bintanja (1996), Corripio (2002))

$$\begin{array}{lllll} b_I & = & 2.2 \quad 10^{-5} & z_I & \text{for } z_I \;\leq\; 3000\;m \\ b_I & = & 2.2 \quad 10^{-5} & 3000 & \text{for } z_I \;>\; 3000\;m\;. \end{array} \tag{3.33}$$

With the given modifications for direct radiation under **clear** sky incident on arbitrary tilted surfaces (by inclusion of $\cos\theta_{\mathrm{I}}$) Eq. (3.32) becomes

$$S_{\mathrm{b},I}^{\mathrm{clear}} \;=\; 0.9751\; S_{\mathrm{toa}}\;\cos\theta_{\mathrm{I}}\;\chi_{\mathrm{sun},I}\;(\tau_{\mathrm{r},I}\;\tau_{\mathrm{o}}\;\tau_{\mathrm{g},I}\;\tau_{\mathrm{w},I}\;\tau_{\mathrm{a},I}\;+\;b_I) \tag{3.34}$$

with “cs” indicating the clear sky parameterisation. Note, that Eq. (3.32) explicitely includes the sun-or-shadow function $\chi_{\mathrm{sun},I}$ which is one if a grid cell I is in the sun, and zero if the cell is in shadow. The Eq. (3.32) with all quantities specified in the last section constitutes the model for direct beam SW radiation for clear sky conditions.

In the following, the diffuse sky radiation S_{d} is derived. By additionally including a theoretically derived expression for the diffuse sky radiation the global radiation can always be computed for clear sky days even if no exposed measurement station is available. The diffuse sky radiation for clear sky conditions is computed from the above atmospheric transmittance functions (Bird and Hulstrom (1981)). The first contribution to the diffuse sky radiation for clear sky conditions comes from Rayleigh-scattering after the first pass through the atmosphere and is given by (Iqbal (1983))

$$S_{\mathrm{d},I}^{\mathrm{Rayleigh}} \;=\; 0.79\; S_{\mathrm{toa}}\;\cos\theta_{\mathrm{z}}\;\tau_{\mathrm{o}}\;\tau_{\mathrm{g},I}\;\tau_{\mathrm{w},I}\;\tau_{\mathrm{aa},I}\;\frac{0.5\;(1\;-\;\tau_{\mathrm{r},I})}{(1\;-\;m_{\mathrm{a},I}\;+\;m_{\mathrm{a},I}^{1.02})}\;. \tag{3.35}$$

Bird and Hulstrom (1981) gave an extra term in the numerator which extends $0.5(1-\tau_{\mathrm{r},I})$ to $0.5(1-\tau_{\mathrm{r},I}) + f_{\mathrm{c}}(1-\tau_{\mathrm{as},I})$. Since this extra term does not appear in Iqbal (1983) it

is also neglected here. Therein, f_c is the ratio of scattered radiation in forward direction to the total scattered radiation due to aerosols. The determination of this ratio is difficult since it depends on particle size, shape, wavelength and even on the zenith angle θ_z, because "forward" depends on the direction of the incident direct radiation. The ratio of scattered radiation f_c may vary between 0 for total backward scattering, 0.5 for isotropic scattering and one for total forward scattering. Therefore, unless detailed information is available, a fixed value of $f_\mathrm{c}= 0.84$ is used (Iqbal (1983)). Here, the ratio of scattered radiation f_c is used in the second and third contribution to the diffuse sky radiation. Similar to the assumed fixed values of w_0, a and β, the value for f_c leads to an unknown error contribution of the parameterised model for spatial direct and diffuse sky radiation.
The second contribution to the diffuse sky radiation comes from Mie-scattering

$$S_{\mathrm{d},I}^{\mathrm{Mie}} \;=\; 0.79\; S_{\mathrm{toa}}\; \cos\theta_\mathrm{z}\; \tau_\mathrm{o}\; \tau_{\mathrm{g},I}\; \tau_{\mathrm{w},I}\; \tau_{\mathrm{aa},I}\; \frac{f_\mathrm{c}\;(1\;-\;\tau_{\mathrm{as},I})}{(1\;-\;m_{\mathrm{a},I}\;+\;m_{\mathrm{a},I}^{1.02})}\;, \tag{3.36}$$

The third contribution to the total diffuse sky radiation stems from multiple reflections between the ground and the atmosphere (Iqbal (1983))

$$S_{\mathrm{d},I}^{\mathrm{mult.refl.}} \;=\; (S_{\mathrm{b},I}^{\perp}\;\cos\theta_\mathrm{z}\;+\;S_{\mathrm{d},I}^{\mathrm{Rayl.}}\;+\;S_{\mathrm{d},I}^{\mathrm{Mie}})\frac{\alpha\;\alpha_{\mathrm{a},I}}{(1\;-\;\alpha\;\alpha_{\mathrm{a},I})}\;. \tag{3.37}$$

Therein α represents a mean reflectivity (albedo) value of all surface albedo values and α_a the albedo of the clear sky (Bird and Hulstrom (1981))

$$\alpha_{\mathrm{a},I} \;=\; 0.0685\;+\;(1\;-\;f_\mathrm{c})\;(1.0\;-\;\tau_{\mathrm{as},I})\;. \tag{3.38}$$

The individual components for diffuse sky parameterisations under **clear** sky are specified for arbitrary tilted surfaces in complex topography with reduced visible sky fraction which is computed by the sky view factor $F_{\mathrm{sky},I}$ (Section 4.2, p.58 Eq. (4.42)) for each grid cell

$$S_{\mathrm{d},I}^{\mathrm{clear}} \;=\; (S_{\mathrm{d},I}^{\mathrm{Rayl.}}\;+\;S_{\mathrm{d},I}^{\mathrm{Mie}}\;+\;S_{\mathrm{d},I}^{\mathrm{mult.refl.}})\;F_{\mathrm{sky},I}\;. \tag{3.39}$$

Note that, for all diffuse sky contributions above isotropy is assumed. But in reality the diffuse sky radiation is not isotropic and shows a strong angular distribution that also depends on the sky conditions. In fact, for clear conditions, the diffuse sky radiation is not isotropic. The anisotropy is enhanced by the circumsolar radiation component, originating from the region around the solar disk, caused by strong forward scattering of the Mie-scattering process. The diffuse sky radiation is usually small under clear sky, especially for a clear dry, high altitude atmosphere and is only large under an overcast sky. But then, according to Oke (1987), the diffuse sky radiation is nearly isotropic. Therefore, the description of diffuse sky radiation as isotropic is assumed accurate enough although Iqbal (1983) points out that this will lead to an underestimation of diffuse sky radiation on south-facing slopes. With the turbidity coefficient of $\beta= 0.03$ a very clear atmosphere is assumed. This is realistic for the mountainous terrain under consideration and results in an even less anisotropic sky under clear sky conditions.

3.1.3 Direct and diffuse sky radiation under cloudy skies

In general, under cloudy sky conditions, a derivation of a mean vertically integrated atmospheric transmittance is hardly feasible. It would require detailed information of clouds on cover fraction, type, properties, thickness, position and layer numbers, which is usually not available. Therefore, an approximation is needed to derive incident direct and diffuse sky radiation for a cloudy sky from a single measured global radiation value $S_{\mathrm{g}}^{\mathrm{meas}}$. Note that even in case of clear sky different levels of humidity, atmospheric composition or aerosols appear, which alter the parameterised mean atmospheric transmittance for clear sky conditions. Therefore, the spatial direct and diffuse sky radiation for cloudy sky conditions is computed even if no "visible" clouds exist.

Many so-called decomposition models exist in the literature which determine incident direct and diffuse sky radiation. These involve the clearness index M_{t}

$$M_{\mathrm{t}} = \frac{S_{\mathrm{g}}^{\mathrm{meas}}}{S_{\mathrm{toa}} \cos\theta_{\mathrm{z}}} \tag{3.40}$$

from which the diffuse sky radiation $S_{\mathrm{d}}^{\mathrm{cloudy}}$ under cloudy sky is estimated as diffuse sky fraction M_{d}

$$M_{\mathrm{d}} = \frac{S_{\mathrm{d}}^{\mathrm{cloudy}}}{S_{\mathrm{g}}^{\mathrm{meas}}} \; . \tag{3.41}$$

However, these decomposition models are statistical models, which strongly depend on local conditions and require long-term measurement series for calibration. A comprehensive statistical decomposition model which includes dependence on latitude, longitude and altitude for various ranges of them is, however, not available. The lack of portability of decomposition models was already pointed out by Gueymard (1989b). He noted that due to the diversity of local climates in complex terrain large deviations in established correlations between M_{t} and M_{d} might occur. These deviations mostly are caused e.g. by changing turbidity or changing atmospheric transmittances with altitude, local water vapour content or turbidity. Additionally, the decomposition models differ quite strongly amongst each other since some include additional variables like solar elevation, air mass, mean solar time, meteorological parameters etc. while others are simply based on correlation numbers between M_{t} and M_{d}. This complexity complicates the search for a well-suited model. Furthermore, the models were developed for different time resolutions of the global radiation (hourly, daily and monthly-average values). Primary work was done by Liu and Jordan (1960) who first developed a decomposition model between daily clearness index M_{t} and daily diffuse sky fraction M_{d} on a horizontal surface. This model was later also used for computing the appropriate hourly indexes. Other models based on hourly data have been derived by different authors e.g. by Orgill and Hollands (1977), Erbs et al. (1982), Iqbal (1983), Reindl et al. (1990) and Boland et al. (2001).

When using a decomposition model $S_{\mathrm{g}}^{\mathrm{meas}}$ has to be measured at an exposed measurement station that is not, or only negligibly, influenced by terrain reflected radiation. In the former radiation balance model the implemented decomposition model was the one of Erbs et al. (1982). For specific applications parts of the model of Iqbal (1983) were applied. Even though the model of Erbs et al. (1982) is based on data of measurement stations with a wide range of altitudes, the included latitudes ranged from 31°N to 42°N and longitudes ranged from -72°E to -122°E are far too different from the ones in the Eastern Swiss Alps (~46.4 to 47°N and ~9 to 10.5°E). In addition, the only variable influencing the diffuse sky radiation is the clearness index M_{t}. Iqbal (1983) introduced a dependence on the solar elevation because under a partly cloud covered sky, as well as under a clear sky, the solar altitude becomes important for the diffuse sky fraction M_{d}. His statistical model is then derived from data from two French and three Canadian measurement stations with latitudes ranging from 43°N to 53°N. However, since no complete formulas of his model were found, the appropriate values for the splitting intervals had to be read by eye from the plot on, p. 272 in Iqbal (1983). Therefore, a different decomposition model, taking into account solar elevation, was tested to replace the models of Erbs et al. (1982) and Iqbal (1983).

Several decomposition models have been developed by Reindl et al. (1990) from data of five sites with at least one year data at each site. The latitudes of the measurement sites ranged from 28°N to 60°N, the longitudes ranged from -81°E to 10°E, therefore representing the Eastern Swiss Alps. Unfortunately, the high altitudes were not covered in their choice of station. Similarly to the other construction methods of the decomposition models they conducted a piecewise fitting of the diffuse sky fraction M_d to the clearness index M_t. Furthermore, they examined different variables that may affect the diffuse sky fraction. For example, they found that M_t is the most important variable in the low interval (cloudy sky) and middle interval (partly cloudy sky) of M_t. On the other hand, the solar zenith angle θ_z seems to be the dominant influencing variable for large M_t's (clear sky). This behaviour was already pointed out by Iqbal (1983). Reindl et al. (1990) developed three decomposition models with the same intervals but with additional varying variables (M_t, T_a, rh and θ_z). For the present radiation model a combination was chosen from two of their models. The first model has a dependency on M_t and θ_z whereas the second only depends on clearness index M_t. The approach of building a composition of two models was taken because very often less data or only extremely scattered data can be found in literature for clearness indexes M_t larger than 0.8. The uncertainties are probably due to the lack of data at high altitudes where the atmosphere is clean and dry resulting in higher clearness indices M_t under clear sky conditions. On the other hand, for a partly cloud covered sky the dependence of the solar elevation should be taken into account. Under cloudy sky conditions which is represented by the low interval of M_t the dependency of the solar elevation angle is assumed to be low. In that interval the dependency of M_t is chosen to be the only one. The combination of two of Reindl et al. (1990)'s models is implemented as follows

$$\begin{aligned}
M_\mathrm{t} \ \geq \ 0.78: \quad & M_\mathrm{d} = 0.147 \\[1em]
0 \ \leq \ M_\mathrm{t} \ \leq \ 0.3: \quad & M_\mathrm{d} = 1.020 - 0.248\, M_\mathrm{t} \\
& \qquad \textit{with}\ M_\mathrm{d} \leq 1.0 \\[1em]
0.3 \ < \ M_\mathrm{t} \ < \ 0.78: \quad & M_\mathrm{d} = 1.400 - 1.749\, M_\mathrm{t} + 0.177\, \sin(\pi / 2 - \theta_\mathrm{z}) \\
& \qquad \textit{with}\ M_\mathrm{d} \leq 0.97\ \textit{and}\ M_\mathrm{d} \geq 0.1 \quad .
\end{aligned} \tag{3.42}$$

According to Reindl et al. (1990) the constraints on the right hand side are due to the piecewise correlation including multiple predictor variables. The constraints for the middle interval of M_t are based on observations from their data sets. Note that the piecewise correlation of the diffuse sky fraction M_d to the clearness index M_t leads to a discontinuous diffuse sky fraction curve.

With M_d and $S_\mathrm{g}^\mathrm{meas}$ derived for the exposed measurement point, all direct and diffuse sky radiation components for clear sky conditions, $S_\mathrm{b}^\mathrm{clear}$ and $S_\mathrm{d}^\mathrm{clear}$, in the model domain are adjusted to obtain spatial direct and diffuse sky radiation components for cloudy sky conditions, $S_\mathrm{b}^\mathrm{cloudy}$ and $S_\mathrm{d}^\mathrm{cloudy}$. This is done by computing two ratios at the measurement station, namely $\mathrm{c_b}$ and $\mathrm{c_d}$. These two adjusting coefficients are assumed to correct for the mean vertically integrated transmittance functions for clear sky conditions and for the neglect of clouds. The adjusting coefficient $\mathrm{c_b}$ for direct radiation values under cloudy sky is computed as follows: The direct radiation $S_\mathrm{b}^\mathrm{cloudy}$ under cloudy sky conditions, obtained from the decomposition of $S_\mathrm{g}^\mathrm{meas}$ at the measurement station, is divided by the clear sky value $S_\mathrm{b}^\mathrm{clear}$ calculated from atmospheric transmittance functions on a horizontal plane at the measurement site (Eq. (3.34))

$$\mathrm{c_b} = \frac{S_\mathrm{g}^\mathrm{meas}\ (1 - M_\mathrm{d})}{S_\mathrm{b}^\mathrm{clear}}\ . \tag{3.43}$$

The spatial direct radiation component under cloudy sky conditions is computed according to the decomposition ratio at the measurement station

$$S_{\mathrm{b},I}^\mathrm{cloudy} = \mathrm{c_b}\ S_{\mathrm{b},I}^\mathrm{clear}\ . \tag{3.44}$$

The adjusting coefficient $\mathrm{c_d}$ for diffuse sky radiation under cloudy sky is computed as follows: The diffuse sky radiation $S_\mathrm{d}^\mathrm{cloudy}$ under cloudy sky conditions, obtained from the decomposition of $S_\mathrm{g}^\mathrm{meas}$ at the measurement station, is divided by the clear sky value $S_\mathrm{d}^\mathrm{clear}$ calculated from atmospheric transmittance functions on horizontal plane at the measurement site (Eq. (3.39))

$$\mathrm{c_d} = \frac{S_\mathrm{g}^\mathrm{meas}\ M_\mathrm{d}}{S_\mathrm{d}^\mathrm{clear}}\ . \tag{3.45}$$

The spatial diffuse sky radiation component under cloudy sky is computed according to the decomposition ratio at the measurement station

$$S_{\mathrm{d}I}^\mathrm{cloudy} = \mathrm{c_d}\ S_{\mathrm{d}I}^\mathrm{clear}\ . \tag{3.46}$$

There are two exceptions in which case Eq. (3.44) and Eq. (3.46) need further modifications. First, if no exposed measurement of $S_\mathrm{g}^\mathrm{meas}$ is available (global radiation values should be zero in the input data), and the solar elevation angle is larger than zero, then direct radiation $S_\mathrm{b}^\mathrm{cloudy}$ and diffuse sky radiation values $S_\mathrm{d}^\mathrm{cloudy}$ are obtained from the clear sky parameterisations according to Eq. (3.34) and Eq. (3.39). In that case cloudy and clear skies cannot be differentiated. Hence, the parameterised diffuse sky radiation $S_\mathrm{d}^\mathrm{clear}$ under clear sky conditions will then underestimate diffuse sky radiation $S_\mathrm{d}^\mathrm{cloudy}$ under cloudy sky conditions. In contrast, the parameterised direct radiation $S_\mathrm{b}^\mathrm{clear}$ under clear sky conditions will overestimate the direct radiation $S_\mathrm{b}^\mathrm{cloudy}$ under cloudy sky conditions. Second, if the solar elevation angle is smaller than zero but a measured global radiation value $S_\mathrm{g}^\mathrm{meas}$ is larger than zero, all measured global radiation $S_\mathrm{g}^\mathrm{meas}$ is assumed to be $S_\mathrm{d}^\mathrm{clear}$ due to the exposed measurement site. In this case diffuse sky radiation under clear sky conditions is set to the measured global radiation $S_\mathrm{g}^\mathrm{meas}$, $\mathrm{c_d}$ is set to one, and $\mathrm{c_b}$ set to zero.

The incident global radiation S_g under cloudy sky conditions can now be determined for each grid cell I by

$$S_{\mathrm{g},I} = S_{\mathrm{b},I} + S_{\mathrm{d},I} + S_{\mathrm{t},I} \tag{3.47}$$

with $S_\mathrm{b} = S_\mathrm{b}^\mathrm{cloudy}$ and $S_\mathrm{d} = S_\mathrm{d}^\mathrm{cloudy}$. Beside the contributions S_b and S_d from the sun and sky, respectively there is an additional term S_t which stems from reflections from the **terrain**. This contribution is discussed in detail in Section 4.2, p.58.

Finally, it is noted that for the computation of the clearness index M_t the total S_toa is used and that, in contrast to Eq. (3.34), no wavelength restriction is made. Since a pyranometer does not measure the whole wavelength range, i.e. 0.3 to 3 μm, the remaining energy of the spectrum is accounted for by calibration (Marty (2001)).

3.2 LW surface radiation balance model

In this section the total incident broadband LW radiation L_{inc} on arbitrarily tilted surfaces is derived. Incident radiation L_{inc} consists of **a**tmospheric counter radiation L_{a} (from now on called LW sky radiation) and a contribution L_{t} which stems from the surrounding **t**errain. Under the assumption that an exposed measurement of incident radiation $L_{\mathrm{inc}}^{\mathrm{meas}}$ has an almost vanishing terrain contribution the spatial incident radiation L_{inc} can also be computed for the rest of the model domain.

In the following subsections, the equations to determine spatial broadband incident LW radiation at the surface are given. As for SW radiation, the atmosphere transmittance is treated vertically integrated. The broadband wavelength range is constricted to the transmittance of the silicon or glass dome of the applied pyrgeometer which is here 3.5-50 μm from the Eppley Precision Infrared Radiometer (PIR) (Marty (2001)).

3.2.1 LW sky radiation

Any object of a temperature above absolute zero (0 K) emits radiation. If the object is in thermal equilibrium, the radiation is called black body radiation. Planck's law gives the spectral flux density of a black body, and the total emitted flux is obtained by integrating over all wavelengths yielding Stefan-Boltzmann's law

$$L_{\mathrm{emission}} \; = \; \varepsilon \; \sigma_{\mathrm{SB}} \; T^4 \; . \tag{3.48}$$

Here, $\sigma_{\mathrm{SB}} = 5.76 \; 10^{-8} \; \mathrm{Wm^{-2}K^{-4}}$ is the Stefan-Boltzmann constant and ε=1 is the emissivity of a black body. However, black bodies, i.e. radiative sources in thermal equilibrium with its surrounding can hardly be found in nature. A phenomenological, but widely used generalisation of Stefan-Boltzmann's law is that of a grey body which simply employs $\varepsilon < 1$ in Eq. (3.48). This is also the common approach to model atmospheric emissions. LW radiation from the sky mainly originates from water vapor, carbon dioxide and ozone. However, airborne solid materials and other gases also contribute to LW sky radiation. Therefore, less radiation is measured at higher altitudes and for clear skies.

In the present surface radiation model two options to obtain spatial LW sky radiation are implemented:

First, if a direct exposed horizontally surface measured LW sky radiation value $L_{\mathrm{a}}^{\mathrm{meas}}$ is available the emissivity of the atmosphere ε_{a} at the measurement station is obtained from

$$\varepsilon_{\mathrm{a}} \; = \; \frac{L_{\mathrm{a}}^{\mathrm{meas}}}{\sigma_{\mathrm{SB}} \; (T_{\mathrm{a}}^{\mathrm{meas}})^4} \; . \tag{3.49}$$

By recalling that the measured air temperature is spatially interpolated (cf. Eq. (5.1)) a spatial isotropic radiation incident on tilted surfaces in the entire domain can then be determined with the sky view factor $F_{\mathrm{sky},I}$ (cf. cf. Section 4.2, p.58 Eq. (4.42)) by

$$L_{\mathrm{a},I} \; = \; \varepsilon_{\mathrm{a}} \; \sigma_{\mathrm{SB}} \; T_{\mathrm{a},I}^4 \; F_{\mathrm{sky},I} \; . \tag{3.50}$$

Second, not only spatial but also permanent point measurements of sky radiation are relatively sparse. However, observations of the cloud fraction n_{c} are obtained more frequently. Therefore, an additional parameterisation of $L_{\mathrm{a},I}$ in terms of the cloud cover fraction is implemented for higher flexibility. Different parameterisations exist to derive isotropic L_{a} from cloud cover fraction observations n_c in eights from an exposed observation site as well as from T_a and rh measurements (Section 3.1.2, p.32). Konzelmann et al. (1994) developed a parameterisation for L_a in Wm^{-2} based on measurement data on the Greenland Ice Sheet. Their parameterisation is implemented in the model under the assumption that arctic conditions are similar to the alpine climate. The parameterisation is given by

$$L_{\mathrm{a},I} \;=\; ((0.23 \;+\; 0.483\; (\tfrac{e_{\mathrm{a},I}}{T_{\mathrm{a},I}})^{\frac{1}{8}})\;(1 \;-\; n_\mathrm{c}^3) \;+\; 0.963\; n_\mathrm{c}^3)\; \sigma_\mathrm{SB}\; T_{\mathrm{a},I}^4\; F_{\mathrm{sky},I} \tag{3.51}$$

where the prefactor of $(1 - n_\mathrm{c}^3)$ describes the clear sky emissivity (dimensionless) with the numerical summand 0.23 representing a clear sky emissivity of a completely dry atmosphere as calculated by LOWTRAN7 (Konzelmann et al. (1994)). In contrast, the numerical prefactor of n_c^3 describes the emissivity of a completely overcast sky (dimensionless). For Eq. (3.51) the air temperature $T_{\mathrm{a},I}$ is used in K. The required vapour pressure $e_{\mathrm{a},I}$ in Pa is obtained from

$$e_{\mathrm{a},I} \;=\; rh_I\; e_{\mathrm{s},I}\;. \tag{3.52}$$

The saturation vapour pressure $e_{\mathrm{s},I}$ is determined from Eq. (3.25) and depends on air temperature $T_{\mathrm{a},I}$. Note that the estimation of L_a from cloud observation is very unreliable due to different types of clouds representing similar cloud cover fractions but having different effects on radiative fluxes (Konzelmann et al. (1994)). In addition, cloud observations depend on the individual observers and are rarely conducted at the same points in time as the radiation measurements.

3.2.2 Parameterisation of LW terrain emissions

Plüss (1997) developed a parameterisation for LW terrain emission that includes the effects of the atmosphere between the emitting and receiving terrain surfaces. He used the radiative transfer model LOWTRAN7 (Kneizys et al. (1988)) which is a low-resolution propagation model and computer code for predicting atmospheric transmittance and background radiance for a given atmospheric path at low spectral resolution. Within sensitivity studies he emitted from a surface with a surface temperature T_s at a given distance through a predefined atmosphere at varying zenith angles. The variation of zenith angles showed little differences in the computed radiance values. In addition for his parameterisation he assumed that the distance of the emitting surface A_J plays a minor role. Therefore, he developed a parameterisation that is only a function of air temperature $T_{\mathrm{a},I}$ of the receiving surface A_I and surface temperature $T_{\mathrm{s},J}$ of the emitting surface.

Landl (2007) extended this LW terrain emission parameterisation to a wider range of surface and air temperatures and included varying distances. Existing LOWTRAN7 simulations of Plüss (1997) were recalculated with emitting surfaces with surface temperatures from 253 up to 273 K in steps of 10 K (melting snow surface) and a fixed zenith angle of 70° and extended them by MODTRAN4 (Berk et al. (1999)) simulations. MODTRAN4 is a radiative transfer model for atmospheric correction to a moderate resolution LOWTRAN code. These simulations were conducted for $T_{\mathrm{s},J}$ between 253 K and 293 K in steps of 10 K for five different $T_{\mathrm{a},I}$ and varying distances between the emitting and receiving surface. Thereby, it was assumed that $T_{\mathrm{a},I}$ fluctuations do not occur within the overall model time step. The statistical parameterisation resulting from MODTRAN4 simulations is given by

$$\begin{aligned} L_{\mathrm{t},I} \;=\; \big[\; & 0.000009886\; (\ln(r_{IJ}))^{1.07}\; (T_{\mathrm{a},I} \;-\; T_{\mathrm{s},J}) \;+\; 0.000003456\; T_{\mathrm{a},I} \\ & +\; 0.0001452\; T_{\mathrm{s},J} \;-\; 0.0304 \;\big]\; F_{IJ}\; 10000\; \pi\;. \end{aligned} \tag{3.53}$$

The statistical formula parameterises the diffusely emitted terrain radiation of a grid cell surface A_J by accounting for attenuation within the air column to a grid cell surface A_I. It does account for the background radiation within that column but does not include scattering into the air column nor for emission processes of the air in the column. This formula does not account for varying compositions of the atmosphere or altitudes. In Eq. (3.53) r_{IJ} is the distance between two grid cell surfaces A_I and A_J (here the natural logarithm (the base-e logarithm) of the distance is involved) and $T_{\mathrm{a},I} - T_{\mathrm{s},J}$ is the temperature difference between the surface temperature $T_{\mathrm{s},J}$ of an emitting surface A_J and the air temperature $T_{\mathrm{a},I}$ of a receiving surface A_I. In that way, a constant air temperature $T_{\mathrm{a},I}$ is assumed for the air column between both grid cells. The diffusely emitted LW radiation fraction of a surface A_J that arrives on a surface A_I is determined by the view factor F_{IJ} between both surfaces which is described in detail in Section 4.1.2, p.47.

It should also be noted that, within the parameterisation, surface emissivity values ε_{s} have constant values of one. The assumption of a LW surface emissivity of one is reasonable for snow surfaces which are quite insensitive to snow pack parameters (Warren (1982)). A snow emissivity of 0.99 was measured by Griggs (1968). Therefore, the emissivity value for surfaces without snow is slightly overestimated in the model. Typical mean values are given in Oke (1987). Bare soil emissivity values vary between 0.9 for dry soil and 0.98 for wet soil, for roads covered by asphalt a value of 0.95 is given. The emission of natural surfaces may be approximately considered to be isotropic (Kondratyev (1969)).

Landl (2007) found that the terrain emission should be taken into account for distances varying up to one to two kilometres, depending on the surface temperatures. This is in contrast to an earlier statement of Martius (2002) who assumed that the influence becomes negligible for distances larger than 500 m. Here, LW terrain radiation influence is assumed to be negligible for distances larger than 1500 m.

The total incident LW radiation is determined for each grid cell by

$$L_{\mathrm{inc},I} \;=\; L_{\mathrm{a},I} \;+\; L_{\mathrm{t},I} \;. \tag{3.54}$$

4 3D-model for broadband SW terrain reflections and LW emissions

Since an enclosure for a surface can be considered as a kind of envelope consisting of surrounding surfaces or open areas (Siegel and Howell (2002)) mountainous terrain can be considered as part of such an enclosure similarly as it is assumed in e.g. computer graphics. The sky fraction is then interpreted as an opening, which is an area of zero reflectivity but can act as a radiation source. In order to compute the radiation exchange in a real complex environment the global illumination needs to be determined. For a surface radiation balance model, the global illumination can be computed with the radiosity approach.
In this chapter the radiosity approach, the view factor concept and the iterative solution of the linear system of the radiosity equation are first introduced in a general way. Afterwards the application of the radiosity approach to the SW and LW radiation balance is described.

4.1 Radiosity approach

4.1.1 Introduction

The radiosity approach and the ray tracing have been the first methods to describe the global illumination of a surface in an environment in computer animations or indoor design. Local illumination for a surface considers local surface properties and direct incident light sources. Global illumination on the other hand, also includes interreflections between surfaces and therefore leads to a more realistic illumination (Encarnação et al. (1997)). In computer graphics applications, for more realistic images with increasingly complex geometries, the classical (finite element) radiosity method was more and more replaced by Monte Carlo (MC) ray tracing (Jensen (2003)). Nevertheless, here, the radiosity approach is considered to be valuable for the computation of the surface radiation balance in complex terrain.

The ray tracing method, introduced by Whitted (1980), is shortly summarised here:
Ray tracing is a method that simulates the process of light distribution according to the laws of specular reflection and refraction. It is therefore suitable for environments with highly reflecting as well as transparent surfaces. A ray from the eye is traced through each grid cell into the environment. If a ray hits a surface the local illumination model is computed and two new rays, a reflected and a refracted ray are created (Encarnação et al. (1997)). If a ray hits a surface before reaching the light source, the ray is called a shadow ray. Otherwise the ray is called an illumination ray (Schaefer (1999)). However, ray tracing has also serious drawbacks (Encarnação et al. (1997)), which renders it inadequate for the computation of distributed radiation in complex terrain:

- Global diffuse light is not accounted for in conventional ray tracing algorithms.

- Interactions between surfaces and light sources are accounted for but interactions between surfaces are neglected.
- The light distribution is computed for a fixed position of the observer and requires to be recomputed if this position needs to be changed (view-dependent solution).

The second original method for the computation of global illumination, the radiosity approach was first introduced in computer graphics by Goral et al. (1984). It originated from techniques developed in thermal engineering to comprehend the exchange of radiant energy between surfaces. A detailed historical overview of the development of radiant energy exchange computation methods is given in Siegel et al. (1991). The radiosity method is based on the conservation of energy. It assumes the stationary exchange of radiative energy between diffuse reflecting (Lambertian) and partly absorbing surfaces in the presence of an external energy source. Due to the diffuse reflecting and emitting of all surfaces a view-independent solution can be calculated for a fixed light source. Furthermore, the radiosity approach accounts for distances between surfaces in the radiosity exchange computation. The radiosity method is called a physical illumination method although from all physical effects playing a role for light propagation only diffuse reflections are included (Encarnação et al. (1997)).
A characteristic feature of an illumination model is that light can be linearly superimposed since different light sources are not influencing each other. The radiosity equation results by integrating over all other discrete patches in an environment instead of over all incidence angles. Furthermore, it assumes the radiance to remain unchanged between two patches and all patches to be ideal diffuse reflectors or emitters. By including the emissivity $E(x)$ of patch $A(x)$, the radiosity $B(x)$ is given by (Encarnação et al. (1996))

$$B(x) \;=\; E(x) \;+\; \rho(x) \int_A B(x') \,\frac{\cos\vartheta(x)\;\cos\vartheta(x')\;\mathrm{d}A(x')\;\chi(x,x')}{\pi\;|x\;-\;x'|^2}\;. \tag{4.1}$$

Here, ϑ is the angle between the surface normal of the patch and the viewing direction, and $\chi(x, x')$ the mutual visibility of the two patches (Section 2.2, p.19). The radiosity $B(x)$ is the hemispherically integrated radiant flux per unit area *leaving* the patch (radiant exitance) in Wm^{-2} (Goral et al. (1984)). In order to solve Eq. (4.1), which is a Fredholm integral equation of the second kind, traditionally a finite element (FE) method is applied. A comprehensive overview on more sophisticated numerical methods for integral equations of the second kind can be found in Atkinson (1997). In Cohen and Wallace (1993) all steps to solve Eq. (4.1) by a FE method are given. On each individual patch the radiosity function is approximated by a linear sum of constant *basis functions*. The discretisation of the radiosity equation Eq. (4.1) leads to

$$B_I \;=\; E_I \;+\; \rho_I \sum_{J=0}^{N-1} B_J\, F_{IJ}\;. \tag{4.2}$$

The discretised radiosity equation assumes a closed environment consisting of a set of patches on which the surface properties, e.g. reflectivity, are specified and uniform for each patch (Goral et al. (1984)). The radiative transfer (RT) within a mesh of surfaces is calculated patchwise due to the FE approach. According to Goral et al. (1984) for each patch A_I the radiosity B_I can therefore be written as a sum of its own direct emission E_I in Wm^{-2} and the radiosities B_J from all patches N within the enclosure of patch A_I multiplied by the ideally diffuse reflectivity of the receiver ρ_I (dimensionless). The fraction of B_J received by patch A_I is further specified by the view factor F_{IJ} which will be described in detail in the next section. The emission E_I represents the light/radiation source for the environment. If all E_I's are zero all B_I's are zero as well.

Note again that in computer graphics applications the classical radiosity method is mostly replaced by MC ray tracing (Jensen (2003)). Similar to ray tracing in MC ray tracing a ray from the eye is traced through each grid cell. In contrast to ray tracing, in MC ray tracing if a ray hits a surface **random** rays are traced from this point. Some important shortcomings of the radiosity approach compared to MC ray tracing are given by Jensen (2001): Only diffuse reflections are accounted for whereas in MC ray tracing any type of bidirectional reflectance distribution function (BRDF) and specular reflections are feasible. The memory consumption is low in MC ray tracing, additionally to a lower computing complexity (Jensen (2001)). On the other hand, the main problem with MC ray tracing is variance seen as noise in the solution. Even though this variance can be reduced by using more rays, since the convergence rate is quite slow of MC ray tracing, a large number of rays might be required to obtain a low variance (Jensen (2001)). Therefore, in this thesis the radiosity approach was implemented to describe the radiation balance in complex terrain. Additionally, the also named shortcoming of the radiosity method of the requirement of a precomputed true solution B (Jensen (2001)) is circumventable by a stopping criterion as will be introduced in Section 4.2.2, p.67.

4.1.2 View factor computation

The discrete radiosity equation (Eq. (4.2)) involves the quantities F_{IJ} which are referred to as view factors (also form factors, configuration factors, shape factors etc.) In this section a derivation of these purely geometric quantities is given. View factors are essential for the radiosity method and were originally introduced to understand the exchanges of radiant energy between surfaces in thermal engineering (Siegel and Howell (1978)). According to Siegel et al. (1991) between 1920 and 1930 view factors were treated explicitly in various studies, e.g. Nusselt (1928). Earlier studies to radiation exchange between surfaces did not define the view factors explicitly, e.g. Christiansen (1883) or Sumpner (1894).

The view factor F_{IJ} describes the radiation exchange between *gray* surfaces, i.e. surfaces that emit and reflect diffusely. A view factor F_{IJ} can be interpreted as the fraction of the entire radiant flux emitted by patch A_I which is received by patch A_J

$$F_{IJ} \;=\; \frac{\text{radiant power (or radiant flux) leaving } A_I \text{ and received by } A_J}{\text{total radiant power leaving } A_I} \;. \tag{4.3}$$

Therefore, view factors only depend on patch geometry (cf. Fig. 4.1). In order to compute the radiant flux which is received by A_J its apparent solid angle has to be computed. The differential solid angle $\mathrm{d}\Omega(x)$ at point x subtended by a differential area $\mathrm{d}A(x')$ as seen from $\mathrm{d}A(x)$ can be expressed in terms of the two polar angles, i.e. the zenithal angle $\vartheta(x')$ and azimuthal angle $\varphi(x')$

$$\mathrm{d}\Omega(x) \;=\; \sin\vartheta(x')\;\mathrm{d}\vartheta(x')\;\mathrm{d}\varphi(x')\;. \tag{4.4}$$

A differential area $\mathrm{d}A(x')$ at point x' viewed from a point x can also by expressed by means of the polar angles

$$\mathrm{d}A(x') \;=\; \frac{|x\;-\;x'|^2}{\cos\vartheta(x')}\;\sin\vartheta(x')\;\mathrm{d}\vartheta(x')\;\mathrm{d}\varphi(x')\;, \tag{4.5}$$

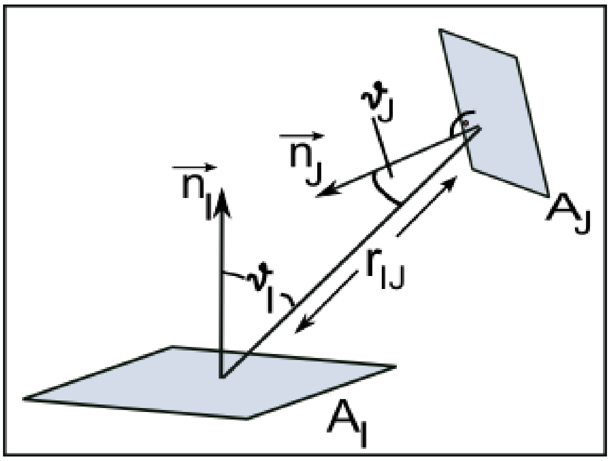

Figure 4.1: Schematic to illustrate the involved parameters for the view factor computation between two patches A_I and A_J.

where the Euclidean distance between x and x' is denoted by $|x - x'|$. Inserting Eq. (4.4) in Eq. (4.5) gives $\mathrm{d}\Omega(x)$ filled by $\mathrm{d}A(x')$ as seen from $\mathrm{d}A(x)$ at point x

$$\mathrm{d}\Omega(x) \;=\; \frac{\cos\vartheta(x')\;\mathrm{d}A(x')}{|x \;-\; x'|^2}\;. \tag{4.6}$$

A detailed view factor derivation can be found in e.g. Goral et al. (1984), Cohen and Wallace (1993) or Encarnação et al. (1996). The derivation below roughly follows Goral et al. (1984) and Encarnação et al. (1996). Both are based on thermal engineering studies. The radiance (or specific intensity) $R(x, \Omega(x))$ in $\mathrm{Wm^{-2}sr^{-1}}$ received at point x within the solid angle $\Omega(x)$ pointing to a point x' per unit time is

$$R(x, \Omega(x)) \;=\; \frac{\mathrm{d}P(x)}{\cos\vartheta(x)\;\mathrm{d}\Omega(x)} \tag{4.7}$$

with $\mathrm{d}P(x)$ in $\mathrm{Wm^{-2}}$ as incident radiant flux on $\mathrm{d}A(x)$ from the direction $\vartheta(x)$ within $\mathrm{d}\Omega(x)$ per unit time and per unit unprojected area.
By definition for a Lambertian surface the radiance does not depend on the solid angle, i.e. $R(x, \Omega(x)) = R(x)$ (perfectly diffuse surface). Hence, by integrating over the solid angle of the hemisphere, the total incident radiant flux $P(x)$ of a unit surface can be computed

$$\begin{aligned} P(x) &= \int_{\text{hemisphere}} \mathrm{d}\Omega(x)\; R(x)\; \cos\vartheta(x) \\ &= R(x) \int_{\varphi=0}^{2\pi} \int_{\vartheta=0}^{\pi/2} \mathrm{d}\vartheta(x)\; \mathrm{d}\varphi(x)\; \cos\vartheta(x)\; \sin\vartheta(x) \\ &= R(x)\; \pi \;. \end{aligned} \tag{4.8}$$

From Eq. (4.7) an equation for the radiant intensity $I(x)$ (with $\mathrm{d}I{=}\mathrm{d}P\mathrm{d}A/\mathrm{d}\Omega$) in $\mathrm{Wsr^{-1}}$ can be derived. Solving Eq. (4.7) for $\mathrm{d}P(x)$, multiplying by $\mathrm{d}A(x)$ and dividing by $\mathrm{d}\Omega(x)$ results for a Lambertian surface in

$$\mathrm{d}I(x) \;=\; R(x)\,\mathrm{d}A(x)\;\cos\vartheta(x)\;. \tag{4.9}$$

Hence, the radiant intensity $I(x)$ of a Lambertian radiator is proportional to the cosine of the angle between surface normal and radiating direction, which is called the Lambertian Cosine

Law.

The derivation of the view factors is started for two infinitesimal surfaces with differential areas $\mathrm{d}A(x)$ and $\mathrm{d}A(x')$. Solving Eq. (4.7) for $\mathrm{d}P(x)$, multiplying by $\mathrm{d}A(x)$ and inserting Eq. (4.6) and Eq. (4.8) gives the fraction of the radiant flux arriving at $\mathrm{d}A(x')$

$$\mathrm{d}P(x)\ \mathrm{d}A(x) \ = \ \frac{P(x)\ \cos\vartheta(x)\ \cos\vartheta(x')\ \mathrm{d}A(x)\ \mathrm{d}A(x')}{\pi\ |x\ -\ x'|^2}\ . \tag{4.10}$$

This is the basic RT law (Encarnação et al. (1996)). The discretised form of Eq. (4.10), i.e. the fraction of the radiant flux arriving at A_J, then reads

$$\mathrm{d}P_I\ \mathrm{d}A_I \ = \ \frac{P_I\ \cos\vartheta_I\ \cos\vartheta_J\ \mathrm{d}A_I\ \mathrm{d}A_J}{\pi\ r_{IJ}^2} \tag{4.11}$$

where r_{IJ} describes the Euclidean distance between the two patches A_I and A_J. Since the total flux is given by P_I the view factor for two differential surfaces can be inferred from the definition in Eq. (4.3)

$$F_{\mathrm{d}A_I\mathrm{d}A_J} \ = \ \frac{\cos\vartheta_I\ \cos\vartheta_J\ \mathrm{d}A_J}{\pi\ {r_{IJ}}^2}\ . \tag{4.12}$$

For the computation of the view factor from a differential surface $\mathrm{d}A_I$ to a finite area A_J an integration about A_J is performed

$$F_{\mathrm{d}A_I A_J} \ = \ \int_{A_J} \frac{\cos\vartheta_I\ \cos\vartheta_J\ \mathrm{d}A_J}{\pi\ {r_{IJ}}^2}\ . \tag{4.13}$$

For the computation of the view factor between two finite surfaces A_I and A_J a double area integral is solved since this view factor is defined as the area average of Eq. (4.13)

$$F_{A_I A_J} \ = \ F_{IJ} \ = \ \frac{1}{A_I} \int_{A_I} \int_{A_J} \frac{\cos\vartheta_I\ \cos\vartheta_J\ \mathrm{d}A_I\ \mathrm{d}A_J\ \chi_{IJ}}{\pi\ {r_{IJ}}^2}\ . \tag{4.14}$$

In the last equation the mutual visibility χ_{IJ} (see Section 2.2, p.19) is made explicit. In fact, in all above view factor equations the additional term for mutual visibility between the appropriate two patches has to be included.

In the following, three important properties of view factors are given:

1. A reciprocity relationship regardless of the patch sizes is valid and can be derived by multiplying Eq. (4.14) by A_I

   $$F_{A_I A_J}\ A_I \ = \ \int_{A_I} \int_{A_J} \frac{\cos\vartheta_I\ \cos\vartheta_J\ \mathrm{d}A_I\ \mathrm{d}A_J\ \chi_{IJ}}{\pi\ {r_{IJ}}^2}\ .$$

   Multiplying the corresponding Eq. (4.14) for $F_{A_J A_I}$ by A_J gives

   $$F_{A_J A_I}\ A_J \ = \ \int_{A_J} \int_{A_I} \frac{\cos\vartheta_I\ \cos\vartheta_J\ \mathrm{d}A_J\ \mathrm{d}A_I\ \chi_{JI}}{\pi\ {r_{IJ}}^2}$$

   leading to the so-called reciprocity relation

   $$F_{A_I A_J}\ A_I \ = \ F_{A_J A_I}\ A_J\ . \tag{4.15}$$

2. If a patch is planar or convex the patch does not see itself and its own view factor is zero
$$F_{II} \;=\; 0 \; . \tag{4.16}$$
3. In an enclosure of N patches the entire emitted energy of each of some patch A_I has to be distributed to all patches of the enclosure. This leads to the normalisation property (energy conservation)
$$\sum_{J=0}^{N-1} F_{IJ} \;=\; 1 \; . \tag{4.17}$$

Properties Eq. (4.15) and Eq. (4.16) reduce the amount of view factor calculations to $N(N-1)/2$). Note that property Eq. (4.17) forms a valuable tool to verify if view factors are computed correctly.

Before carrying on with view factor computation methods, Eq. 4.2 is rewritten in terms of power by means of Eq. (4.15) leading to
$$B_I A_I = E_I A_I + \rho_I \sum_{J=0}^{N-1} B_J F_{JI} A_J \; . \tag{4.18}$$
This was done to point out that F_{IJ} in Eq. (4.2) actually should be F_{JI}, the fraction of B_J that arrives on the patch A_I, but which is transformed to F_{IJ} by applying the reciprocity relationship (Eq. (4.15)) on Eq. (4.18) leading to Eq. (4.2).

Next, a short overview of numerical and analytical methods for the computation of the double area integral in Eq. (4.14) is given.
Analytical solutions for surfaces of very specific shapes and orientations, such as parallel rectangular plates, or circular disks, are tabulated by Siegel and Howell (1978). Goral et al. (1984) converted surface integrals into contour integrals using the Stokes' theorem. Schroeder and Hanrahan (1993) developed a formula to compute view factors for general polygonal configurations. However, for general applications with arbitrary complex geometries the integrals have to be evaluated numerically.
The first numerical method was presented by Nusselt (1928). The view factor for two finite surfaces is approximated with the view factor from a differential area to a finite area (Eq. (4.13)). This is done by using the equivalence between the view factor and the projection of the area A_J on the unit-hemisphere surrounding dA_I. Delta-like view factors are thus obtained by splitting the hemisphere into small delta-like solid angles. Cohen and Greenberg (1985) improved that approach by projecting onto a hemicube which is easier split up into equally sized elements. Apart from that the creation of a set of linear coordinates on a sphere for defined locations is difficult. They also introduced a so-called z-buffer algorithm that looks for the closest surface within projections onto the same element of the hemicube. In this way they produced the first applicable view factor computation method. Baum et al. (1989) extended this approach with a hybrid method with analytical and numerical (hemicube method) techniques. If the hemicube assumptions are violated, due to proximity, visibility and aliasing (surfaces do not project onto whole numbers of hemicube pixels) inaccuracies, the view factors $F_{A_I A_J}$ are determined analytically by applying the Stokes' theorem onto the inner integral. The outer integral was still solved numerically. Wallace et al. (1989) improved a ray tracing algorithm to avoid sampling problems in the hemicube algorithm.

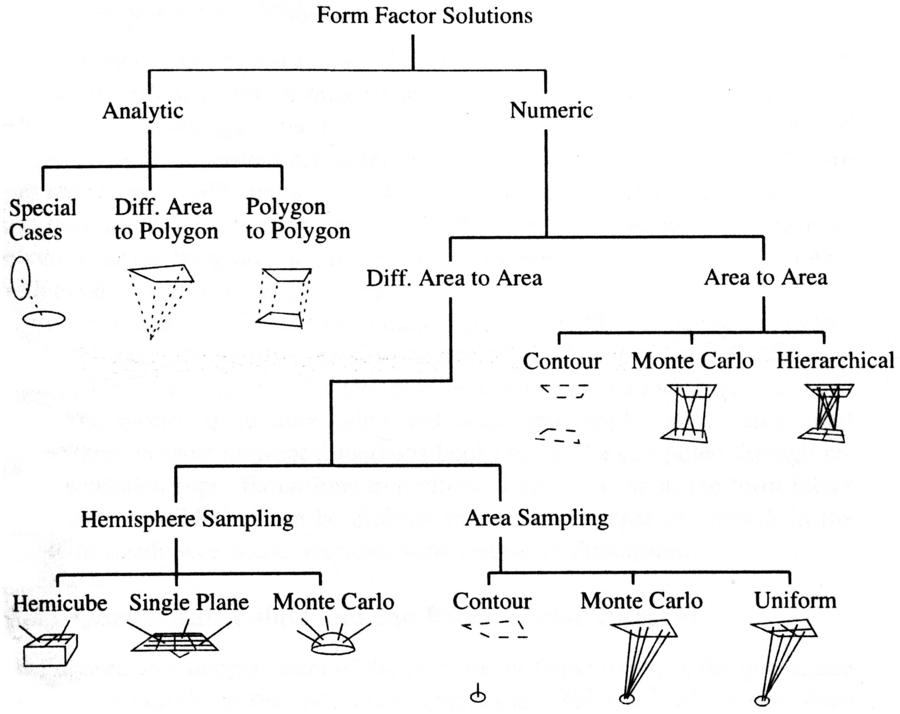

Figure 4.2: Overview of view factor computation methods (Figure from Cohen and Wallace (1993)) showing various analytic and numeric methods.

They determined view factors from differential to a finite surface $F_{\mathrm{d}A_I A_J}$ by tracing rays from $\mathrm{d}A_I$ to uniformly distributed ΔA_J on the source A_J. If the ray detects visibility for a ΔA_J the view factor is determined by approximating ΔA_J by a surface of specific shape and orientation for which the integral could be easily solved analytically. Zhou and Peng (1992) replaced the hemicube by two so-called plane buffers, the view factor and shading buffer, to determine $F_{\mathrm{d}A_J A_I}$. Since the view factor buffer appears on a plane tangent to the source patch the aliasing problem was eliminated. The Monte Carlo method combined with a FE technique was applied by Vujicic et al. (2006). In this method $F_{A_I A_J}$ is determined from F_{IJ}=total number of rays hitting A_J/(total number of rays) emitted from patch A_I. An overall overview about various view factor computation methods is shown in Fig. 4.2.

Here, $F_{A_I A_J}$ is computed with a straight-forward numerical integration scheme with a uniform but adaptive area subdivision (substructuring) of the considered finite rectangular patches A_I, A_J (cf. Section 2.2, p.19). This can be regarded as a sort of "area sampling" (cf. Fig. 4.2). The view factors between two finite surfaces A_I and A_J are subdivided in N_p and N_q, respectively small rectangular subpatches of size $\mathrm{d}A_P$, $\mathrm{d}A_Q$. On these subplanes view factor variations are assumed to be negligible. Summing the individual subplane view factors yields a numerical solution of the double area integral (cf. Fig. 4.3)

$$F_{IJ} \;=\; \frac{1}{A_I}\,\chi_{IJ} \sum_{P=0}^{N_p-1} \sum_{Q=0}^{N_q-1} \frac{\cos\vartheta_P \;\cos\vartheta_Q \;\mathrm{d}A_P \;\mathrm{d}A_Q}{\pi \; {r_{PQ}}^2} \; . \tag{4.19}$$

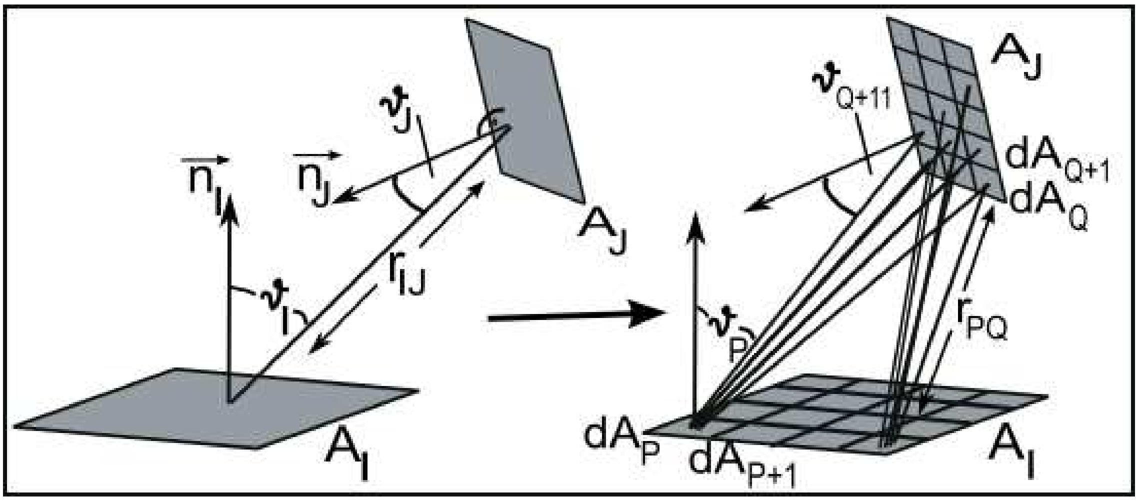

Figure 4.3: Schematic for the uniform but adaptive area subdivision computation method of view factors: Two finite patches A_I and A_J (left hand) are substructured into subpatches $\mathrm{d}A_P$, $\mathrm{d}A_Q$ to solve the double area integral of Eq. (4.14) for the view factor computation (right hand).

Note that in this study the view factors are calculated only if A_I and A_J are mutually visible. Two patches are taken to be entirely mutually visible if the centers of the patches are mutually visible. Therefore, partial occlusion is not accounted for. As can be seen in Fig. 4.3, the angles ϑ_I and ϑ_J can differ substantially from the angles ϑ_P, ϑ_Q of the subpatches. Similarly, the center distance r_{IJ} between A_I and A_J can deviate strongly from the center distances r_{PQ} between two subpatches. The latter is especially true in complex terrain when large slope angles lead to enlarged inclined patch sizes. The threshold of substructuring x_{sub} (dimensionless) is obtained following McCluney (1994) for a patch A_I

$$x_{\text{sub}I} = \frac{\text{max lateral dimension of } A_I}{r_{IJ}} . \tag{4.20}$$

McCluney (1994) suggested that a finite source can be approximated by a point source if its maximum lateral dimension is less than 10% of the distance to it. This threshold is applied for both patches A_I and A_J here even though only one patch actually represents a source as defined by McCluney (1994). Each of the side lengths of A_I and A_J are splitted so that the substructuring threshold is valid for the maximum side length of each of the large patches separately.

4.1.3 Jacobi/Gauss-Seidel iteration

In this and the next section, three iteration methods are described that are commonly applied to solve the linear system of equations. In general, iteration methods solve equations by starting with an initial guess to the true solution. Per iteration step the approximated solution is improved until a prescribed accuracy is achieved. The solution is said to be *converged.*

Before, starting with the description of the iteration methods the discretised radiosity equation (Eq. (4.2)) is rewritten in matrix form to make clear that the FE formulation of the radiosity equation leads to a system of N linear equations

$$\begin{bmatrix} B_0 \\ B_1 \\ \vdots \\ B_{N-1} \end{bmatrix} = \begin{bmatrix} E_0 \\ E_1 \\ \vdots \\ E_{N-1} \end{bmatrix} + \begin{bmatrix} \rho_0 F_{00} & \dots & \rho_0 F_{0N-1} \\ \rho_1 F_{10} & \dots & \rho_1 F_{1N-1} \\ \vdots & \vdots & \vdots \\ \rho_{N-1} F_{N-10} & \dots & \rho_{N-1} F_{N-1N-1} \end{bmatrix} \begin{bmatrix} B_0 \\ B_1 \\ \vdots \\ B_{N-1} \end{bmatrix} \tag{4.21}$$

for the unknowns B_I. Or, in a more compact form $\boldsymbol{M}B = E$

$$\begin{bmatrix} 1-\rho_0 F_{00} & \dots & -\rho_0 F_{0N-1} \\ -\rho_1 F_{10} & \dots & -\rho_1 F_{1N-1} \\ \vdots & \vdots & \vdots \\ -\rho_{N-1} F_{N-10} & \dots & 1-\rho_{N-1} F_{N-1N-1} \end{bmatrix} \begin{bmatrix} B_0 \\ B_1 \\ \vdots \\ B_{N-1} \end{bmatrix} = \begin{bmatrix} E_0 \\ E_1 \\ \vdots \\ E_{N-1} \end{bmatrix} \tag{4.22}$$

where $\boldsymbol{M}$ is the matrix called radiosity matrix. The radiosity matrix $\boldsymbol{M}$ has certain properties that help to decide which numerical algorithm is best for the solution of the linear system of radiosity equations. Three are named here:

- A matrix is said to be row diagonally dominant (RDD) if

  $$|M_{II}| > \sum_{J \neq I}^{N-1} |M_{IJ}| \ , \quad \forall I \ . \tag{4.23}$$

  The radiosity matrix is RDD which was observed by Cohen and Greenberg (1985). This is readily seen: Since the sum of all view factors $\sum_{J=0}^{N-1} F_{IJ}$ of one patch cannot by definition exceed one (Eq. (4.17)), the sum of the view factors in one row will always be equal (closed environment) or less than one (open environment). In addition, the considered patches are planar thus the view factor F_{II} is zero (Eq. (4.16)). Since the surface reflectivity ρ is always less than one the row sum, consisting of products of view factors and reflectivity, will always be less than the diagonal element that equals one (due to $F_{II} = 0$).

- A matrix is said to be column diagonally dominant (CDD) if

  $$|M_{JJ}| > \sum_{I \neq J}^{N-1} |M_{IJ}| \ , \quad \forall J \ . \tag{4.24}$$

  The CDD is not necessarily given for radiosity matrices $\boldsymbol{M}$, but according to Gortler et al. (1994) CDD is true for the matrix of the transformed linear system given in Eq. (4.18). Since $F_{JI}A_J$ is symmetric, the corresponding matrix $\boldsymbol{M}$ is also RDD.

- Furthermore according to Cohen and Wallace (1993) the radiosity matrix $\boldsymbol{M}$ can be fairly sparse for a complex environment since a lot of patches do not "see" each other. However, since radiation is a non-local interaction, individual rows might still contain a considerable number of entries.

Goral et al. (1984) solved the linear system of N equations directly by means of a Gaussian elimination scheme. $\mathcal{O}(N^3)$ operations were necessary to compute all N^2 view factors and the mutual visibility χ_{IJ} (Section 2.2, p.19). The view factor and mutual visibility computation are the most time consuming parts of the radiosity algorithm. In computer graphics a lot of effort was spent on improving the iterative solution of Eq. (4.2) and the view factor computation.

The RDD of the radiosity matrix $\boldsymbol{M}$ guarantees that the iterative solution of the linear system of radiosity equations will converge for any initial estimate of the solution by using a standard iterative method like Jacobi (JA) and Gauss-Seidel (GS) iteration. The description of iteration methods is therefore started with a brief summary of JA and GS.
In JA iteration the radiosities for all patches are calculated from the radiosity values of the previous sweep through the **whole** matrix ($B^{(k-1)}$)

$$B_I^{(k)} = E_I + \rho_I \sum_{J=0}^{N-1} B_J^{(k-1)} F_{IJ} \tag{4.25}$$

where k is the iteration step. After a complete update of all N radiosities, i.e. after N iteration steps, the new values are used for the next sweep through the matrix. Note that in Eq. (4.25) $\boldsymbol{N}$ iteration steps are indicated by $k-1$ but that the iteration step counting is implemented in that way by increasing it (by one) when a patch receives radiation from other patches.
The following general Pseudo-Code describes the JA iteration:

```
for all $I$
    $B_I = E_I$
    $\Delta B_I = E_I$    // remembering ”old” radiosity distribution
while not converged
    for each $I$ in turn
        $B_I = E_I + \rho_I \sum_{J \neq I}^{N-1} \Delta B_J F_{IJ}$
    $\Delta B_I = B_I$    // updating the ”old” radiosities after $N$ iteration steps
```

In contrast, GS iteration uses updated radiosities as soon as they are available for the calculation of the radiosity distribution of the current sweep through all variables

$$B_I^{(k)} = E_I + \rho_I \sum_{J=0}^{I-1} B_J^{(k)} F_{IJ} + \rho_I \sum_{J=I+1}^{N-1} B_J^{(k-1)} F_{IJ} \ . \tag{4.26}$$

Note that here, $k-1$ indicates **one** iteration step. The following general Pseudo-Code describes the GS iteration (from Gortler et al. (1994)):

```
for all $I$
    $B_I = E_I$
while not converged
    for each $I$ in turn
        $B_I = E_I + \rho_I \sum_{J \neq I}^{N-1} B_J F_{IJ}$
    applying the current $B_I$
```

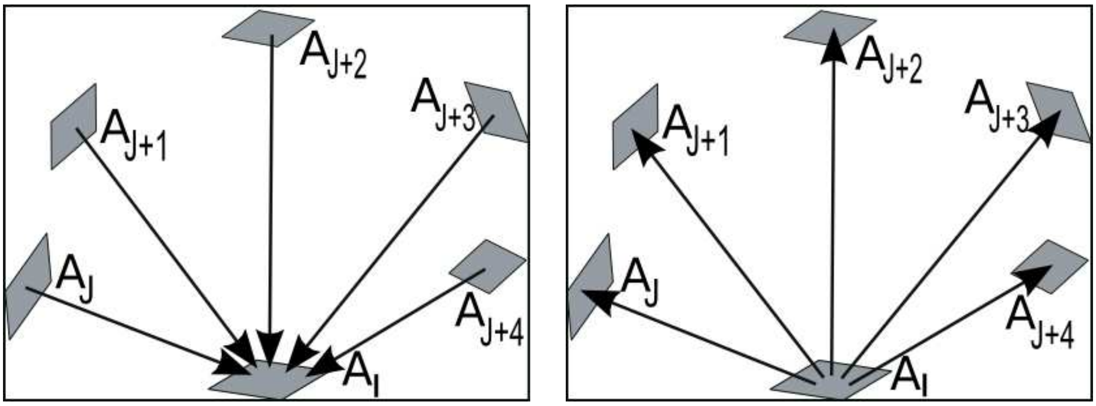

(a) (b)

Figure 4.4: Schematic of the two principles, gathering and shooting radiosity, of the commonly applied iteration methods to solve the linear system of the radiosity equation: (a) Gathering radiosity to a patch A_I from all patches A_J, (b) Shooting radiosity from a patch A_I to all patches A_J.

Thus, the only difference between JA and GS iteration is the time when updated variables are used. JA and GS can be seen as algorithms that **gather** the radiation of all other patches in the environment to one patch A_I (cf. Fig. 4.4(a)). Therefore, one gathering step, i.e. per iteration step k, updates the radiosity of only one patch and needs $\mathcal{O}(N)$ operations. It is clear that one patch A_I is updated through the dot product of B with the corresponding row I of the radiosity matrix. If radiosity is computed for each patch of the model domain, every row needs to be multiplied by B, resulting in $\mathcal{O}(N^2)$ operations. The initial estimate for the radiosities is taken as the emissions E_I of each patch.

In JA iteration only single terrain reflections are accounted for in N iteration steps. In GS iteration multiple reflections are accounted for within N iteration steps. GS is therefore converging faster to the true solution. For both iteration methods all $N \times N$ view factors have to be known for the N iteration steps since every patch is gathering radiation from all other patches. Therefore JA and GS iteration are also called full-matrix methods.

Full-matrix methods are not applicable in large complex environments. For example, to store the view factor matrix ($N \times N$ entries) with e.g. 64999 float numbers for an environment consisting of 209×311 patches requires approximately 32 Gbyte. Even though precomputed view factors accelerate the radiosity computation, the large memory requirement to store the view factor matrix is remarkable. Additionally, most of the view factor matrix entries will be zero because most patches are not mutually visible ($\chi_{IJ} = 0$). Furthermore, in most environments only a few patches are strong reflectors or emitters while at the same time being ”seen” by a lot of other patches. This means that only a few patches can induce large radiosity changes on other patches. Therefore, JA and GS iteration need a lot of complete passes through the radiosity matrix to achieve a converged solution, despite the fact that only a small number of patches actual exchange radiation during these sweeps. The redundant iteration steps result in an additional time cost. As will be shown in the next subsection, these iteration steps are not necessary and can be circumvented by an improved iteration method.

4.1.4 Progressive Refinement iteration

Progressive Refinement or Progressive Radiosity (PR) was introduced by Cohen et al. (1988) to solve the radiosity algorithm. Later, Gortler et al. (1994) showed that PR is actually an implementation of Southwell Relaxation completed by N JA iteration steps. PR differs from JA and GS iteration in two ways. First, as with GS, all radiosities B are updated simultaneously for each iteration step k. Second, instead of looping over all patches A in order, for one step k the patch A_I with the most unshot radiant power $\Delta B_I A_I$ is **shooting** its unshot radiosity ΔB_I to mutual visible A_J's (Fig. 4.4(b)). In each iteration step the radiosity values are updated according to

$$B_J^{(k+1)} \;=\; B_J^{(k)} \;+\; \rho_J \, \Delta B_I^{(k)} \, F_{JI} \tag{4.27}$$

where I is the patch A_I with the largest unshot radiosity ΔB_I. Thereafter, the shooting patch's unshot radiosity ΔB_I is set to zero and all unshot radiosities ΔB_J are increased by the computed amount of radiosity (second summand of Eq. (4.27)). The overall aim of PR is to decrease convergence time by rearranging the order of considered patches according to its "relevance" for the iteration. The main advantage of PR's looping order is that for each iteration step only one column of the radiosity matrix is required, since one iteration step consists of multiplying the integer value B_I of the shooting patch with a column of the radiosity matrix. Therefore, during one shooting step, i.e. one iteration step, all other patches are updated simultaneously. One shooting step requires $\mathcal{O}(N)$ operations, in contrast to N gathering steps for one patch with JA/GS iteration resulting in $\mathcal{O}(N^2)$ operations to update all patches only once.
The following general Pseudo-Code describes the PR iteration (Gortler et al. (1994)):

```
for all $I$
  $B_I = E_I$
  $\Delta B_I = E_I$            // unshot radiosity
while not converged
  pick $I$, such that $\Delta B_I A_I$ is largest
    for every patch $A_J$
        compute $F_{JI}$
        $\Delta rad = \rho_J \, \Delta B_I \, F_{JI}$
        $\Delta B_J = \Delta B_J + \Delta rad$
        $B_J = B_J + \Delta rad$
    applying the current $B_J$
    $\Delta B_I = 0$
```

A patch that has already shot its unshot radiosity ΔB_I can still receive radiation of other patches A_J and can therefore be a shooting patch several times. In order to reduce the number of shootings from the same patch and to account for interreflections of patches that do not receive radiosity within the first iteration steps, an ambient correction term $\widehat{\Delta B}_I$ can be added to ΔB_I. This iteration method is called overshooting. The overshooting amount $\widehat{\Delta B}_I$ then comprises an estimate of possible future shot radiation (Gortler et al. (1994)). A general Pseudo-Code describing the PR iteration by means of an ambient term can be found e.g. in Gortler et al. (1994)). In order to determine the best ambient term for overshooting, a good estimate of possible future shot radiation is required since after a shooting step in PR iteration with an ambient term, the unshot radiosity ΔB_I of patch A_I is set to $-\widehat{\Delta B}_I$.

4.1.5 Stopping criteria

Stopping criteria are required to terminate the iterative solution if a presumed accuracy limit (stopping tolerance) is reached. In general, a solution is accurate if the norm of the error $\varepsilon^{(k)}$ is sufficiently small

$$\varepsilon^{(k)} = B - B^{(k)} . \tag{4.28}$$

Therein, B is the true radiosity solution and $B^{(k)}$ is the iterated solution after the kth iteration step.

Suitable vector norms are given by the ℓ_p norms $\| x \|_p$ for $p = 1, 2...$ of a vector, defined as

$$\| \varepsilon^{(k)} \|_p = \left(\sum_I |B_I - B_I^{(k)}|^p \right)^{(1/p)} \tag{4.29}$$

or by the maximum norm ℓ_∞, defined as

$$\| \varepsilon^{(k)} \|_\infty = \max_I |B_I - B_I^{(k)}| . \tag{4.30}$$

Naturally, the suitability of a particular error norm depends on the application. It is stressed that an accuracy condition on the error (Eq. (4.28)) does not help to terminate the iteration since the true solution B is not known in advance. Furthermore, the true solution changes for every new light source distribution. Nevertheless, stopping criteria involving the true solution were often applied e.g. by Cohen et al. (1988), Baum et al. (1989) and Gortler et al. (1994). A common way out is the use of heuristic stopping criteria: the iteration is stopped if some parameter, e.g. the difference between two consecutive solutions $\| B^{(k)} - B^{(k-1)} \|_p$ becomes sufficiently small e.g. Bu and Deprettere (1989).

The drawback of such heuristic criteria is that the norm of the error (Eq. (4.28)) can usually not be inferred from the smallness of such a quantity. The rigorous way out is to use a stopping criterion, which can be related to the error. An example is provided by the so-called residual $r^{(k)}$

$$r^{(k)} = \boldsymbol{M} B^{(k)} - E \tag{4.31}$$

which can be computed at each iteration step. Since the error can be related to the residual via $\varepsilon^{(k)} = \boldsymbol{M}^{-1} r^{(k)}$ the following inequality

$$\| \varepsilon^{(k)} \|_p < \| \boldsymbol{M}^{-1} \|_p \| r^{(k)} \|_p \tag{4.32}$$

between the error norm and the residual norm holds true. Hence, a physically motivated accuracy condition $\| \varepsilon^{(k)} \|_p < \varepsilon$ on the error with a stopping threshold ε can always be met by simply stopping the iteration if $\| r^{(k)} \|_p < \varepsilon / \| \boldsymbol{M}^{-1} \|_p$.

In previous work, Baranoski et al. (1995) used the largest unshot radiant power: $\max(r_I^{(k)} A_I)$ and also tested the ℓ_2 vector norm of the residual: $\| r^{(k)} \|_2$. A posteriori bounds and error estimates without involving the true solution were also derived by Lischinski et al. (1994). Their tightest bounds on radiosity include the estimation of maxima and minima (upper and lower bounds) of the matrix $\boldsymbol{M}$ as well as of the emission.

However, computing the residual and the bounds presented by Lischinski et al. (1994) requires $\mathcal{O}(N^2)$ additional operations per iteration step, which may remarkably slow down the iteration. Therefore, heuristic criteria are often used in favor of rigorous bounds since they are faster to compute. Here, a bound will be presented (Section 4.2.2, p.67) which is related to the error and does not require $\mathcal{O}(N^2)$ additional operations per iteration step.

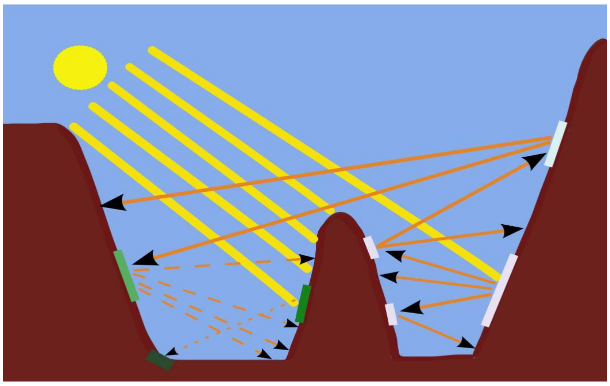

Figure 4.5: Schematic for multiple terrain reflections in mountainous terrain depending on surface reflectivity.

4.2 Radiosity approach for SW radiation balance in complex terrain

Multiple reflections have to be included on inclined surfaces in complex terrain. This is especially important during winter seasons with high mean snow reflectivities in the shorter wavelength range of the solar radiation spectrum (cf. Fig. 4.5). For finer resolved DHM's, steeper inclined surfaces are more frequent and consequently more terrain interactions appear.
In this section, first the current state of research of modelling of reflected radiation is given. Second, the radiosity approach is derived for the application in a radiation model with a homogeneous atmosphere over complex terrain.

The importance of SW terrain radiation reflections and LW terrain emissions for mountainous terrain is well documented.
Whiteman et al. (1989a) conducted radiation budget measurements within Colorado's deep Brush Creek Valley to investigate radiation and surface energy budget microclimates. By using radiometers oriented horizontally and parallel to the ground, they detected large anisotropies in measured diffuse radiation, indicating a large influence of single or multiple terrain reflections. Matzinger et al. (2003) confirmed the spatial and temporal variability of SW and LW radiation and its influence on valley wind days by an extensive field study within the deep Alpine Riviera Valley in southern Switzerland. They measured the incident and reflected global radiation on several sites on a cross-section through the valley. This revealed the occurrence of anisotropic diffuse reflected radiation.

The radiosity method was implemented to account for multiple surface reflections mostly in the field of urban meteorology. Verseghy and Munro (1989) gave an overview of the first studies that investigated and quantified the SW radiation balance in an urban setting. In order to quantify the urban surface feedbacks more precisely, the results of several simplifying assumptions in a rigorous model of the SW radiation balance, based on radiation enclosure theory (radiosity method) were compared, to field measurements. A building courtyard was chosen for modelling. When the impact of multiple reflections by adjacent walls was neglected, they identified an average error of up to 15 Wm^{-2}, depending on view factor and albedo values and the overall amount of incident SW radiation. A similar average error was found for the assumption of isotropic diffuse sky radiation. There is still a need to extend these quantified error definitions for arbitrary wall orientations, view factors and varying amounts of incident SW radiation. Furthermore, this study reveals the need for SW radiation balance models in urban settings that are not too simplified. Even though a variety of methods exist to account for the net radiation distribution in urban settings, according to Harman et al. (2004), little is known about what should be included. Therefore, they extended Verseghy and Munro (1989)'s study to a variety of two-dimensional urban geometries and materials to account for different albedo and emissivity values. They conclude that urban street canyon models need to compute at least single reflection whereas multiple reflections are preferable. In Borel et al. (1998) the radiosity approach was proposed in a preliminary study as a possible methodology for computing the radiation balance in mountainous terrain. By considering the radiation exchange between two opposite mountain slopes, the amount of the energy balance can increase by about 40% for surfaces without snow and up to 150 % for snow-covered surfaces. However, a systematic study of the radiosity approach applied to mountainous terrain is still missing.

Besides the radiosity approach different methods with various levels of complexity exist to account for additional effects such as shading and multiple anisotropic terrain reflection in the radiation balance.

A variety of simple models commonly apply the so-called isotropic view factor approach to estimate terrain reflected or emitted radiation. Thereby, the isotropic view factor approach utilises that all visible terrain can be described by one minus the sky view factor F_{sky} at each grid cell (for the sky view factor cf. Eq. (4.42)). Thus, a differentiation between varying surface properties or spatially varying incident radiation values is not possible since by applying this approach an isotropy of surface properties and single terrain reflected radiation is assumed. This approach can be found in energy or radiation balance models (e.g. Nunez (1980), Moore et al. (1993), Corripio (2002), Oliphant et al. (2003), Hock and Holmgren (2005), Wang et al. (2006)), diagnostic meteorological models (Bellasio et al. (2005)) or the Nonhydrostatic Mesoscale Model (NMM) with a grid- and subgrid-scale radiation parameterisation scheme (Müller and Scherer (2005)). Within these models, the isotropic view factor is estimated from horizon angles in individual azimuth intervals, and multiplied by the incident global radiation at patch A_I. This results in a rough estimate for an additional isotropic contribution from single terrain reflected radiation. Müller and Scherer (2005) were the first to apply such a method to a grid- and subgrid-scale radiation parameterisation scheme for arbitrarily fine resolved topography within the NMM.

Anisotropic terrain reflection and emission models divide the obstructed part of the hemisphere, i.e. the terrain into spherical portions (e.g. Olyphant (1986b) for LW, Letsinger and Olyphant (2007) for SW and LW radiation). Even though this anisotropic approach is more accurate than the isotropic approach, it does not account for all information available by grid data, i.e. the DHM and surface properties (e.g. slope and slope azimuth, albedo or emissivity values).

Regarding realistic models, there are basically two common approaches which allow to compute the three-dimensional RT in complex terrain. The first approach is the (deterministic) spherical harmonics discrete ordinate method (SHDOM) by Evans (1998). Spherical harmonics (for the source function) and discrete ordinates to represent the radiance field are used. SHDOM is most widely used since it is an efficient, flexible and publicly available method (Cahalan et al. (2005)). For example, in Degünther et al. (1998), SHDOM is used to conduct a case study on the interaction between a cloud free atmosphere and a model domain with inhomogeneous surface albedo for ultraviolet (UV) irradiance. The second approach is the (stochastic) Monte Carlo (MC) method (Marchuk et al. (1980)). MC is also widely used for three-dimensional RT calculations. The radiation balance is computed by tracing the stochastic trajectories of photons through the atmosphere. All interactions of individual photons, with the atmosphere and the ground as boundary surfaces, are accounted for. Two MC examples are named here. The first, MYSTIC is a photon tracing method that calculates three-dimensional radiation fluxes accounting for inhomogeneous surface albedo values and topography in cloudy atmospheres (Mayer (1999), Mayer (2000a), Kylling et al. (2000a)). The second from Chen et al. (2006) computes the SW radiant flux for a real three-dimensional topography underneath a clear sky. It should be noted that the quality of RT computation with MC strongly depends on the quantity of photons. Therefore, the RT can be well controlled but the computational speed is increasing in parallel with the quantity of photons. SHDOM models are faster than MC methods but errors are more difficult to understand (Cahalan et al. (2005)). An intercomparison of complex three-dimensional RT models is given in Cahalan et al. (2005).

Presently, the gap in complexity between realistic RT models for a cloudy atmosphere and isotropic view factor approaches is large. To partly fill this gap, the radiosity approach is used in this study to compute the three-dimensional radiation balance in complex terrain. The radiosity method can be regarded as a three-dimensional RT model where the topography is composed of individual diffuse emitter/reflector (Lambertian) surfaces and the sky is represented by the sky view factor F_{sky} (cf. Eq. (4.42)). This method is well suited to study the effect in topography but is not a realistic three-dimensional RT model for a cloudy atmosphere as the above-described MC or SHDOM methods. For this study the radiosity method was applied in order to simulate the RT in mountainous terrain but neglecting the detailed feedback with clouds. However, some feedback is included with the parameterisations of the diffuse sky radiation under clear sky conditions (Eq. (3.37)).

In the following, the radiosity equation Eq. (4.1) is rederived in the context of the SW radiation balance over complex topography to keep track of the required assumptions. The derivation starts from Eq. (4.8) applied to the broadband global radiation flux incident at point x with $P(x) = S_{\mathrm{g}}(x)$ leaving a surface x. The integral over the hemisphere in Eq. (4.8) is decomposed into directions pointing to the sky and to the terrain $S_{\mathrm{g}}(x) = S_{\mathrm{sky}}(x) + S_{\mathrm{t}}(x)$. The SW radiation from the sky $S_{\mathrm{sky}}(x)$ is composed of the direct solar beam radiation S_{b} and the isotropic diffuse sky radiation S_{d} (Section 3.1.2, p.3.1.2 and Section 3.1.3, p.3.1.3)

$$S_{\mathrm{sky}}(x) \;=\; S_{\mathrm{b}}(x) \;+\; S_{\mathrm{d}}(x)\ . \tag{4.33}$$

Thereby, $S_{\mathrm{sky}}(x)$ is not influenced by any terrain reflected radiation $S_{\mathrm{t}}(x)$. This assumption excludes feedbacks of the surface on downward radiances $R(x, \Omega(x))$ from the sky which are considered as independent radiation sources into the surface. Note that the sky view factor F_{sky} is considered as an opening of zero reflectivity. This assumption might be questionable for UV radiation. Since, for UV radiation under clear sky conditions, Degünther et al. (1998) found that surface albedo variations on flat terrain in more than 10-12 km away from a specific site still had noticeable impacts. This impact was even larger for cloudy conditions. Kylling and Mayer (2001) conducted three-dimensional RT modelling with MYSTIC for a model domain including the island of Tromsø, Norway. They determined ratios of incident radiation of snow-covered (albedo of 0.8) to snow free (albedo of 0.07) conditions by varying

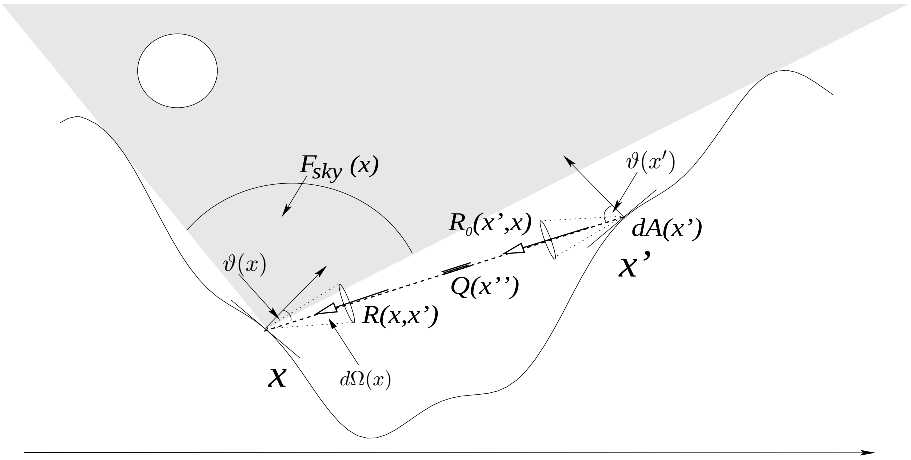

Figure 4.6: Cross-section of a valley to demonstrate the radiation transfer equation (Eq. (4.35)).

the height of the snowline. For a clear sky a relative enhancement in erythemal weighted irradiance of 1.4 compared to the snow free condition was found.

The integral over directions pointing to the terrain in the general Eq. (4.8) is rewritten as an integration over non-occluded parts of the whole terrain surface A by using the differential solid angle in Eq. (4.6)

$$S_{\mathrm{g}}(x) \;=\; S_{\mathrm{sky}}(x) \;+\; \int_A \mathrm{d}A(x')\;\frac{\cos\vartheta(x)\;\cos\vartheta(x')}{|x\;-\;x'|^2}\chi(x,x')\;R(x,x')\;. \tag{4.34}$$

Here, $R(x,x')$ is the radiance received within the differential solid angle $\mathrm{d}\Omega(x)$ around the direction pointing to x' (cf. Fig. 4.6) and $\chi(x,x')$ denotes mutual visibility, i.e. $\chi(x,x')=1$ if x "sees" x' and zero otherwise (Section 2.2, p.19). The received radiance $R(x',x)$ is determined by the usual one-dimensional RT equation within the atmospheric column between x' and x. In the absence of scattering **into** the atmospheric column, the transmittance function τ (cf. Section 3.1.2, p.32 for broadband transmittance functions) and a possible isotropic volume source $Q(x'')$ at x'' of a homogeneous medium between x' and x are described by (cf. e.g. Liou (2002))

$$R(x,x') = R_0(x',x)\;\tau(x',x)\;+\;\int_x^{x'}\mathrm{d}(x'')\;Q(x'')\;\tau(x'',x)\;. \tag{4.35}$$

The boundary condition, i.e. the radiance emitted within the differential solid angle $\mathrm{d}\Omega(x)$ around the direction pointing to x is denoted by $R_0(x',x)$. Furthermore, all surface sources are assumed to be isotropically emitting

$$R_0(x',x) = R_0(x')\;. \tag{4.36}$$

The above set of equations is further specified to arrive at Eq. (4.1), which is applicable for the computation of broadband SW radiation transfer between surfaces in mountainous terrain:

1. For the computation of reflected broadband SW radiation the atmosphere in Eq. (4.35) is neglected, i.e. Q=0 and τ=1. This implies that $R(x,x') = R_0(x',x)$, i.e. the

conservation of emitted radiance between x' to x. Thus, the dominant contribution comes from the surface. With increasing distance between two points this assumption will break down and the influence of the atmosphere between both points will dominate.

2. The ideally diffuse emitting surface sources are described in terms of mean surface albedo (or reflectivity) values $\alpha(x)$. Lambertian surfaces with $\alpha(x')S_{\mathrm{g}}(x') = R_0(x')\pi$ (cf. Eq. (4.8)) are a common, reasonable assumption also in RT models for a cloudy atmosphere. A good example of an ideal diffuse reflector from a macroscopic perspective would be a microscopically very rough surface, e.g. chalk. Hemispherical directional reflectance factors (HDRF) were measured with a Goniometer by Odermatt et al. (2005) over snow in Davos (Switzerland) and with a Gonio-spectrometer by Bourgeois et al. (2006) over snow in Greenland. HDRF is a non-dimensional equivalent to the BRDF. HDRF is determined by ground observations where hemispherical incident irradiance and directional outgoing radiance are measured (Bourgeois et al. (2006)). According to them, the HDRF of snow-covered surfaces is nearly isotropic at noon and anisotropy increases with increasing solar zenith angles (larger forward scattering) and wavelength. However, in complex terrain larger solar zenith angles are expected to be of less importance due to shading. Additionally, according to Ångstrom (1925), snow free surfaces are close to ideally diffuse reflecting surfaces. Here, the error arising from the assumption that all patches are Lambertian reflectors is assumed to be minor compared to the error arising from neglecting cloud backscattering or radiation attenuation of the air column between two patches.

The above simplifications lead to the linear integral equation for the incident SW radiation

$$S_{\mathrm{g}}(x) \;=\; S_{\mathrm{sky}}(x) \;+ \frac{1}{\pi}\int_A \mathrm{d}A(x')\;\frac{\cos\vartheta(x)\;\cos\vartheta(x')}{|x\;-\;x'|^2}\chi(x,x')\;(\alpha(x')\;S_{\mathrm{g}}(x'))\;. \tag{4.37}$$

By introducing the radiosity $B(x) = \alpha(x)S_{\mathrm{g}}(x)$ and referring to the emission $E(x)$ the reflected radiation from the sky: $E(x) = \alpha(x)S_{\mathrm{sky}}(x)$ Eq. (4.37) demonstrates the relationship with the radiosity equation (Eq. (4.1)). Note that the integral represents the incident terrain reflected radiation S_{t} and each patch can be seen as an individual light/radiation source. Hence, mountainous terrain is considered as part of an enclosure bounded by the surrounding topography and the sky. The latter is represented by the sky view factor $F_{\mathrm{sky}}(x)$

$$F_{\mathrm{sky}}(x) \;=\; \frac{1}{\pi}\int_{\mathrm{sky}} \mathrm{d}\Omega(x)\;\cos\vartheta(x)\;. \tag{4.38}$$

Before carrying on, the sky view factor is briefly described. As mentioned earlier, F_{sky} is used to represent the visible sky fraction and can be seen as one large patch. Thus, they can be derived from anisotropic terrain view factor sums using the normalisation property of view factors (cf. Eq. (4.17)). The terrain view factor sum $1 - F_{\mathrm{sky}(x)}$ as seen from a patch $A(x)$ can be determined by integrating over all terrain horizon angles $\vartheta_{\mathrm{h}}(x)$ in the sloped coordinate system for each azimuth angle $\varphi(x)$

$$1\;-\;F_{\mathrm{sky}}(x)\;=\;\int_0^{2\pi}\mathrm{d}\varphi(x)\;\int_{\frac{\pi}{2}-\vartheta_{\mathrm{h}}(\varphi(x))}^{\frac{\pi}{2}}\frac{\mathrm{d}\vartheta(x)\;\sin\vartheta(x)\;\cos\vartheta(x)}{\pi} \tag{4.39}$$

which leads to

$$\begin{aligned} 1 - F_{\mathrm{sky}}(x) &= \frac{1}{\pi} \int_0^{2\pi} \mathrm{d}\varphi(x) \left[\frac{\sin^2\vartheta(\varphi(x))}{2} \right]_{\frac{\pi}{2}-\vartheta_{\mathrm{h}}(\varphi(x))}^{\frac{\pi}{2}} \\ &= \frac{1}{2\pi} \int_0^{2\pi} \mathrm{d}\varphi(x) \left[1 - \sin^2(\tfrac{\pi}{2} - \vartheta_{\mathrm{h}}(\varphi(x)))\right] \\ &= 1 - \frac{1}{2\pi} \int_0^{2\pi} \mathrm{d}\varphi(x) \cos^2(\vartheta_{\mathrm{h}}(\varphi(x))) \end{aligned} \tag{4.40}$$

with the continuous equation for the sky view factor $F_{\mathrm{sky}}(x)$ at each patch $A(x)$ derived from horizon angles

$$F_{\mathrm{sky}}(x) = \frac{1}{2\pi} \int_0^{2\pi} \mathrm{d}\varphi(x) \cos^2(\vartheta_{\mathrm{h}}(\varphi(x))) \; . \tag{4.41}$$

Note that Eq. (4.41) reveals the right formula for the sky view factor which is not simply the solid angle covering the visible sky, as erroneously assumed by some authors, but that the inclination at x has to be considered. Note furthermore, that the insertion of a horizon angle $\vartheta_{\mathrm{h}}(\varphi(x))$, which is derived as seen from an inclined patch $A(x)$, is important. Using the normalisation property of view factors the discretised sky view factor $F_{\mathrm{sky},I}$ at grid cell I is also given from the sum of terrain view factors at patch A_I by

$$F_{\mathrm{sky},I} = 1 - \sum_{J=0}^{N-1} F_{IJ} \; . \tag{4.42}$$

Note further, that an albedo of zero is assumed for the sky patch. In that way, it depicts an opening of zero reflectivity.

Finally, the discretised formulation of Eq. (4.37) is given by

$$S_{\mathrm{g},I} = S_{\mathrm{sky},I} + \sum_{J=0}^{N-1} (\alpha_J \, S_{\mathrm{g},J}) \, F_{IJ} \; . \tag{4.43}$$

The ideally diffuse mean surface albedo α can be seen as an integrated value of the hemispherical spectral reflectivity over the SW radiation spectrum. The mean surface albedo is defined as the ratio of total (hemispherical) reflected radiation to total incident radiation. Mean constant surface albedo values are assigned to each snow free land use class throughout a simulation. In case of canopy or snow-covered patches, new albedo values for the specific patches are computed within the coupled SNOWPACK module (Section 5.4, p.82) from the snow properties.

4.2.1 Progressive Refinement iteration

Despite the analogy between the SW radiation balance and the radiosity problem in computer graphics it remains the question if common iteration methods also apply directly to the SW radiation balance problem. This is not obvious a priori since both systems mainly differ in the geometry: closed environments such as rooms versus complex topographies with the sky at the top as an area of zero reflectivity. Additionally, mountainous model domains generally cover a large area in order to capture the horizon accurately but at the same time often maintain small horizontal patch resolutions Δx to accurately represent local surface properties. Thus, the model domains usually have large numbers of grid cells. Since the geometry determines the entries of the matrix of the linear system and thereby the convergence properties of the iteration methods and since the view factor and mutual visibility computation are the

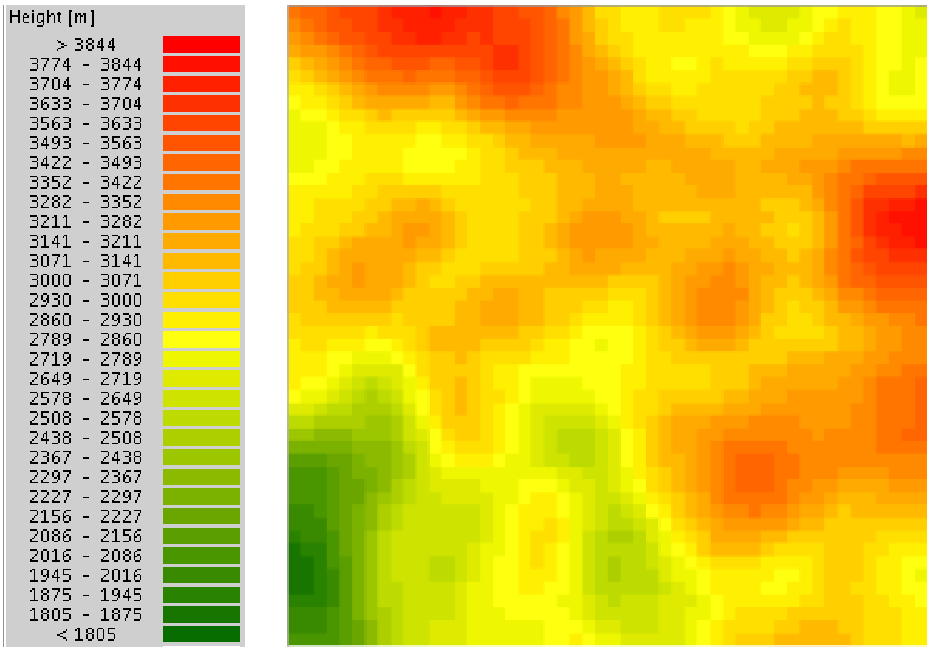

Figure 4.7: DHM used for comparison of JA, GS and PR iteration characteristics. The Gaussian random field taken as DHM consists of 50×50 patches, a homogeneous horizontal resolution of 25 m and a constant land use of bare soil with a homogeneous surface albedo value of 0.9. The mean model domain slope angle is 62°.

most time consuming parts of the radiosity algorithm it seems worthwhile to have a closer look at this issue.

In order to solve Eq. (4.43), JA, GS and PR iteration were tested to verify if these can be applied for mountainous model domains.
This subsection outlines why PR iteration was chosen to solve the linear system of radiosity equations. The extension of the PR iteration by an ambient term, called overshooting (Section 4.1.4, p.56), is neglected here. First, a good estimate for possible future shot radiation is required, which is difficult to obtain. Second, according to Gortler et al. (1994), no simple proofs exist that the overshooting algorithm always converges to the right solution, although it was the fastest converging method in their test cases. Furthermore, more operations per iteration step are required which lead to a higher computation time compared to PR without an ambient term.

The performance of the iteration methods is compared by the model domain shown in Fig. 4.7. A homogeneous land use of bare soil with constant homogeneous surface albedos was chosen. A Gaussian random field was used as DHM with a mean height vector $\overline{z_I}$ =2000 m and an exponential covariance matrix $\overline{(z_I - \overline{z_I})(z_J - \overline{z_J})} = \sigma^2 e^{-(\frac{|x_I - \vec{y}_I|}{\xi})}$ with ξ=250 and σ=750. The constant horizontal grid resolution was Δx=25 m. The model was smoothed by averaging the height z value together with the surrounding 24 height values. The model domain comprises 50 × 50 grid cells.
The linear system of equations (Eq. (4.37)) is either solved by PR (Section 4.1.4, p.56) or by JA/GS (Section 4.1.3, p.52) iteration. These three iteration methods were compared in terms

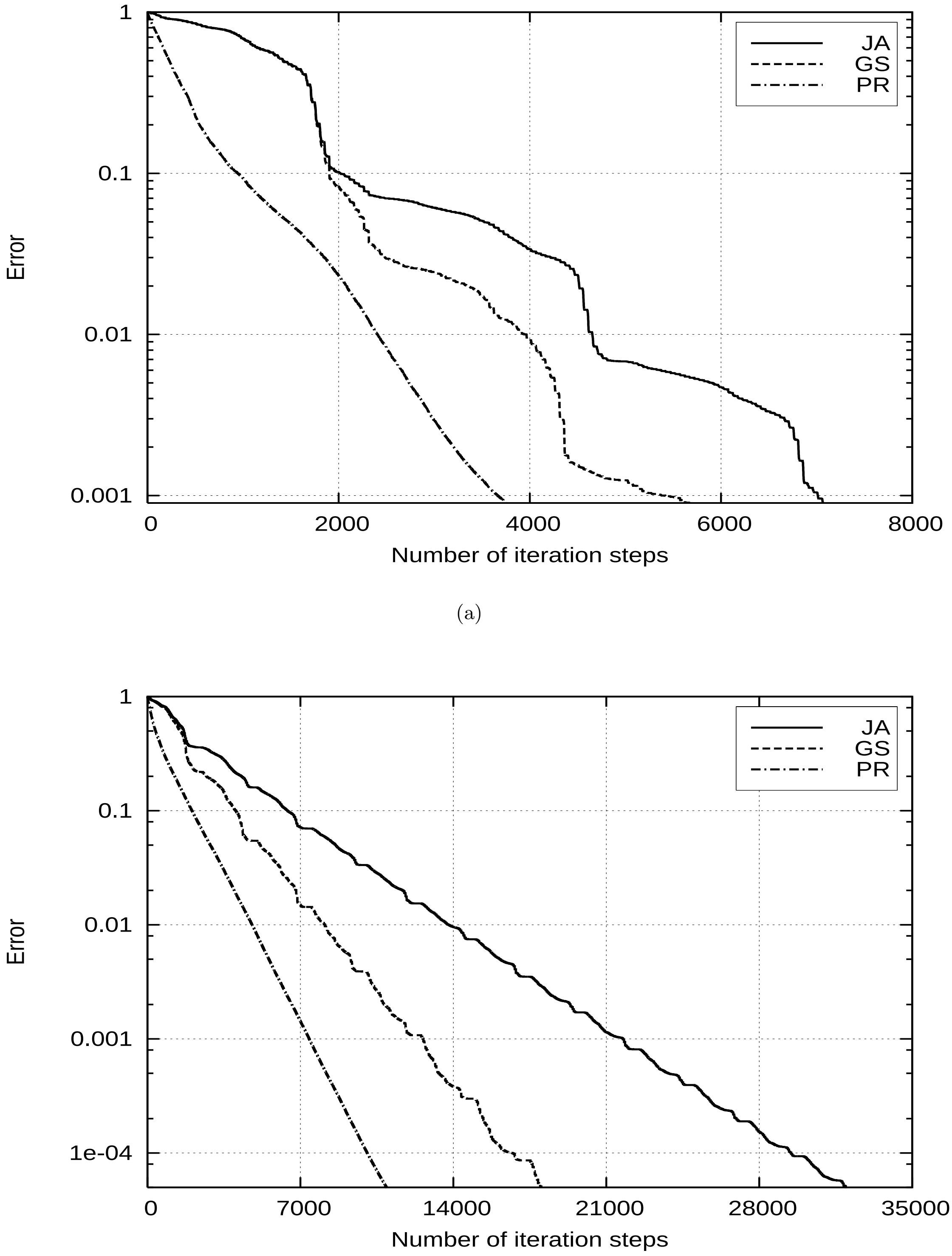

(a)

(b)

Figure 4.8: Comparison of the normalised error $\varepsilon^{(k)}$ with ℓ_2 vector norm: $\| B - B^{(k)} \|_2 / \| B - E \|_2$ (indicated by "Error") at each iteration step for JA, GS and PR iteration by the model domain shown in Fig. 4.7: (a) albedo of 0.2, (b) albedo of 0.9.

of required iteration steps to achieve a converged solution and to achieve a presumed accuracy in Fig. 4.8. In Fig. 4.8(a) a small homogeneous albedo value of 0.2 was chosen whereas in Fig. 4.8(b) a large one of 0.9 was used. For comparison the true solution B was approximated by a "long" GS iteration which was terminated if the ℓ_2 norm of the normalised residual (Eq. (4.31)) was lower than 10^{-12} (18274 iteration steps for α=0.2 and 47678 iteration steps for α=0.9). For comparison only one solar elevation of 22.4° with a sun azimuth angle ψ=344.3° was tested. The single exposed measured global radiation value $S_\mathrm{g}^\mathrm{meas}$ was 448.9 Wm^{-2}. The displayed behaviour on a semi-logarithmic plot implies an exponential decay of the error as a function of the number of iteration steps for either method. Note that one iteration step with PR iteration equals one **shooting** step, i.e. all N patches receive radiosity from the shooting patch. In contrast, one iteration step with GS/JA iteration equals one **gathering** step, i.e. only one patch receives radiosity from all other patches. Apparently, the iteration methods differ with respect to the *rate* i.e. the slope in the semi-logarithmic plot. This rate is larger for PR when compared to the other methods. For larger albedo values, more reflections occur leading to a delayed convergence compared to lower albedo values. In both cases JA is converging slowest and PR iteration fastest. As expected, GS is faster than JA iteration since updated radiosity values are used as soon as they are available.

Originally, the PR method suggests a shooting criterion which determines the shooting patch with the largest amount of unshot radiosity according to the largest unshot power $\Delta B_I \; A_I$ (see Cohen et al. (1988) and Gortler et al. (1994)). However, this criterion has a drawback when applied to open topographies: Mountain peaks with a large unshot radiosity would often been chosen but hardly "see" any terrain and thus have only little influence on the final solution. Therefore, the shooting criterion applied here, additionally includes the sum of terrain view factors at each patch to avoid redundant shootings from mountain peaks that can often reflect a lot of direct and diffuse sky radiation (large S_sky)

$$\textit{shooting criterion} \; : \; \max_I \left(\Delta S_{\mathrm{g},I} \; A_I \; \sum_{J=0}^{N-1} F_{IJ} \right) \tag{4.44}$$

with $\Delta S_{\mathrm{g},I} = \alpha_I S_{\mathrm{sky},I}$. Therefore, only patches which receive much direct and diffuse sky radiation **and** have a large albedo **and** "see" much of the terrain are selected as shooting patches. At the start of an iteration process the selected patches are mainly inclined snow-covered surfaces at the upper valley sides.

The above described PR iteration adapted to the SW surface radiation balance can be formulated as Pseudo-Code as follows

```
for all $I$
  $S_{\mathrm{g},I} = \alpha_I \, (S_{\mathrm{b},I} + S_{\mathrm{d},I})$
  $\Delta S_{\mathrm{g},I} = \alpha_I \, (S_{\mathrm{b},I} + S_{\mathrm{d},I})$   // unshot radiosity
while not converged
  pick $I$, such that $\Delta S_{\mathrm{g},I} \; A_I \; \sum_{J=0}^{N-1} F_{IJ}$ is largest
   for every patch $A_J$
      compute $F_{JI}$
      $\Delta rad = \alpha_J \; \Delta S_{\mathrm{g},I} \; F_{JI}$
      $\Delta S_{\mathrm{g},J} = \Delta S_{\mathrm{g},J} + \Delta rad$
      $S_{\mathrm{g},J} = S_{\mathrm{g},J} + \Delta rad$
```

```
applying the current $S_{\mathrm{g},J}$
$\Delta S_{\mathrm{g},I} = 0$
```

Implementation details

PR iteration was found to solve Eq. (4.43) best for model domains in complex terrain that have a large number of patches thanks to an overall low memory requirement. Additionally, PR iteration requires less iteration steps to converge thanks to its efficient iteration order with the shooting criterion (cf. Eq. (4.44)). But since with GS iteration more iteration steps are possible within the same amount of time with precomputed view factors F_{IJ} GS iteration remains preferable for specific applications. The extensive computation time needed to determine mutual visibility (Section 2.2, p.19) between every pair of patches, as well as the substructuring to obtain accurate view factors F_{IJ} (Section 4.1.2, p.47), slows down each iteration/shooting step. Note that one shooting step includes the computation of mutual visibility and view factors to N patches. In addition, a shooting patch can be chosen several times, in which case view factors and mutual visibility, have to be recomputed. Depending on the stopping tolerance in PR iteration in most cases not all view factors are required why they are more efficiently determined on the fly. As a consequence, two PR iteration versions are presented for the radiosity approach applied on the SW radiation balance in complex terrain:

1. In the case of sufficient memory capacity all view factors are stored either during the model run or in an external look-up table. Nevertheless, PR iteration is applied due to the efficient iteration/shooting order resulting in overall less computation time compared to GS.
2. In the case of not sufficient memory capacity PR iteration is applied by computing view factors and visibility on the fly with a rather slow but at least feasible simulation. If GS is applied the computation of the N view factors for each of the N patches per iteration/gathering step would lead to an enormous prolongation of the computation time.

The product $A_I \sum_{J=0}^{N-1} F_{IJ}$, required for the computation of the shooting criterion (Eq. (4.44)), and the sky view factor $F_{\mathrm{sky},I}$ (Eq. (4.42)), required for the computation of the incident diffuse sky radiation, are computed once $\forall I$ at the beginning of the model run and are stored for the whole model run. Two matrices of only N entries are necessary. In the case of the second PR iteration version, presented above, the information is favourably stored in an external look-up table since this leads to a considerable speed-up at the beginning of a model run.

4.2.2 Stopping criteria

As outlined in Section 4.1.5, p.57, a stopping criterion should ideally have the property of being related to the error $\varepsilon^{(k)}$ (Eq. (4.28)) via some bound. In the literature, heuristic criteria are often used which lack this property or the residual $r^{(k)}$ (Eq. (4.31)) is used with its computational overhead of $\mathcal{O}(N^2)$ per iteration step. In this section, a new stopping criterion is introduced which can be (i) computed with $\mathcal{O}(N)$ operations and (ii) rigorously related

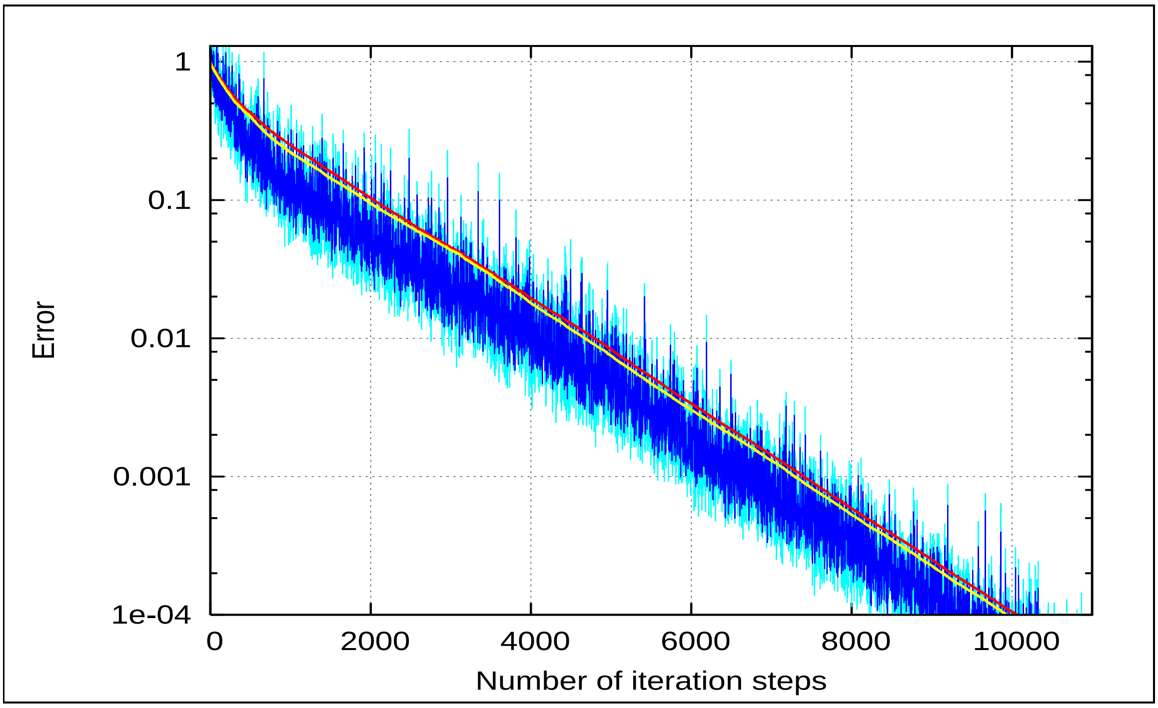

Figure 4.9: Comparison of different normalised stopping criteria with lℓ_2 vector norm at each iteration step with PR iteration and an albedo of 0.9 by the model domain shown in Fig. 4.7: The error $\varepsilon^{(k)}$ (Eq. (4.28)) (red line), the residual $r^{(k)}$ (Eq. (4.31)) (yellow line), the backward difference $\| B^{(k)} - B^{(k-1)} \|_p$ (light blue line) and the backward and forward difference $\| B^{(k)} - B^{(k-1)} \|_p + \| B^{(k+1)} - B^{(k)} \|_p$ (blue line).

to the error via some bound. This criterion is introduced in the following and the bound is derived subsequently in detail. To simplify matters, all equations are from now on expressed in terms of radiosity instead of SW radiation. This is done to keep track of the error $\varepsilon^{(k)}$ (Section 4.1.5, p.57) and to derive a general new criterion. The reader which is not interested in the mathematical details is directly referred to Eq. (4.64).

Before carrying on by deriving the stopping criterion two heuristic criteria as well as the residual error $r^{(k)}$ are briefly compared to the error $\varepsilon^{(k)}$ (Eq. (4.28)) to further outline the necessity of a stopping criterion that is related to $\varepsilon^{(k)}$.
In Fig. 4.9 the performance of PR iteration with different stopping criteria is compared by the model domain shown in Fig. 4.7. The model set-up was chosen similar as described in Section 4.2.1, p.63 for Fig. 4.8.
The error $\| \varepsilon^{(k)} \|_p$ (Eq. (4.28)) is shown versus the residual $\| r^{(k)} \|_p$ (Eq. (4.31)), a heuristic criterion with the backward difference $\| B^{(k)} - B^{(k-1)} \|_p$ (Bu and Deprettere (1989)) and a heuristic criterion with the backward and forward difference $\| B^{(k)} - B^{(k-1)} \|_p + \| B^{(k+1)} - B^{(k)} \|_p$. For all criteria the ℓ_2 vector norm was chosen and all are normalised with their corresponding initial value. The error $\| \varepsilon^{(k)} \|_2$ (Eq. (4.28)) is computationally very fast and decreases smoothly. However, since the true solution B is required in advance this criterion is not applicable for a changing light distribution. The residual $\| r^{(k)} \|_2$ resembles $\| \varepsilon^{(k)} \|_2$ very well. However, the large computation times as well as the need for all view factors for the matrix multiplication make this stopping criterion not applicable. Both these

errors form an upper envelope for the oscillations of the criteria with the backward difference and the backward and forward difference. These oscillations rather origin in the computed relative deviations between radiosity distributions of successive iteration steps instead of differences to a fixed distribution. The criterion with the backward difference oscillates even more than the one with the forward and backward difference. Even though these two heuristic criteria based on radiosity changes require only a small amount of computation time in contrast to the residual $\parallel r^{(k)} \parallel_p$ they are not applicable. This is due to the complicating error oscillations and most important since they cannot be related to the error $\varepsilon^{(k)}$.

An error estimator $\varepsilon^{\star(k)}$, which, similar to the shooting criterion (cf. Eq. (4.44)), considers the distribution of the current amount of unshot radiant power throughout the model domain is defined

$$\varepsilon_J^{\star(k)} \;=\; \Delta B_J^{(k)}\; A_J \sum_{I=0}^{N-1} F_{JI}\ . \tag{4.45}$$

Note that the ℓ_1 norm of it can be computed in $\mathcal{O}(N)$. In the following, it is shown that (i) $\parallel \varepsilon^{\star(k)} \parallel_1$ is a monotonically decreasing sequence which is then subsequently used to prove the error bound (ii) $\parallel \varepsilon^{(k)} \parallel_1 < \mu \parallel \varepsilon^{\star(k)} \parallel_1$ with some geometry dependent constant μ.

(i) According to the PR algorithm (cf. Section 4.1.4, p.56) the unshot radiosity at patch A_J after completion of iteration step $k+1$ can be written as

$$\Delta B_J^{(k+1)} \;=\; \Delta B_J^{(k)} \;+\; (1 \;-\; \delta_{JI_k})\; \Delta B_{I_k}^{(k)}\; \rho_J\; F_{JI_k} \;-\delta_{JI_k}\; \Delta B_J^{(k)} \tag{4.46}$$

where I_k denotes the unique sequence of grid cell indices which are picked by the shooting criterion (Eq. (4.44)), in other words: the largest amount of unshot radiosity at iteration step k can be found at patch A_{I_k}. The ℓ_1 norm of the estimator $\varepsilon^{\star(k)}$ (Eq. (4.45)) is given by

$$\parallel \varepsilon^{\star(k+1)} \parallel_1 = \sum_{J=0}^{N-1} |\varepsilon_J^{\star(k+1)}| \;=\; \sum_{J=0}^{N-1} |\Delta B_J^{(k+1)}\; A_J \sum_{I=0}^{N-1} F_{JI}|\ . \tag{4.47}$$

Since $\Delta B_J^{(k)}$, A_J and all F_{IJ} are non-negative, the l_1 vector norm can be written without taking absolute values. Inserting Eq. (4.46) into Eq. (4.47) and using the reciprocity relationship of view factors (Eq. (4.15)) leads to

$$\parallel \varepsilon^{\star(k+1)} \parallel_1 = \sum_{J=0}^{N-1} \Big[(\Delta B_J^{(k)} A_J \;+\; (1-\delta_{JI_k})\Delta B_{I_k}^{(k)}\; \rho_J\; F_{I_kJ} A_{I_k} \;-\; \delta_{JI_k} \Delta B_J^{(k)} A_J)\Big] \sum_{I=0}^{N-1} F_{JI}\ . \tag{4.48}$$

Simplifying and factoring out $\varepsilon^{\star(k)}$ gives

$$\parallel \varepsilon^{\star(k+1)} \parallel_1 = \parallel \varepsilon^{\star(k)} \parallel_1 \;+ \Delta B_{I_k}^{(k)}\; A_{I_k} \sum_{J=0}^{N-1} \left[\rho_J\; F_{I_kJ} \sum_{I=0}^{N-1} F_{JI}\right] \;-\; \Delta B_{I_k}^{(k)}\; A_{I_k} \sum_{I=0}^{N-1} F_{I_kI}\ . \tag{4.49}$$

By defining

$$\mu^{(k)} \;=\; \sum_{I=0}^{N-1} F_{I_kI} \;-\; \sum_{J=0}^{N-1} \left[\rho_J\; F_{I_kJ} \sum_{I=0}^{N-1} F_{JI}\right]\ . \tag{4.50}$$

the last equation can be written as

$$\parallel \varepsilon^{\star(k+1)} \parallel_1 = \parallel \varepsilon^{\star(k)} \parallel_1 \;-\; \Delta B_{I_k}^{(k)}\; A_{I_k}\; \mu^{(k)}\ . \tag{4.51}$$

Hence it remains to be shown that $\mu^{(k)} > 0$ to complete the proof. The row sum over view factors is at most one for a closed environment (Eq. (4.17)). This maximum will never be attained for the applied real model domains here, hence $\sum_{I=0}^{N-1} F_{JI}$ is always lower one. Accordingly, one ends up with

$$\mu^{(k)} \; > \; \sum_{I=0}^{N-1} F_{I_k I} \; - \; \sum_{J=0}^{N-1} \rho_J F_{I_k J} \; > \; 0 \tag{4.52}$$

where the last inequality simply follows from the fact that all reflectivity values are strictly less one. As a consequence, the norm of the estimator $\varepsilon^{\star(k)}$ (Eq. (4.47)) decreases monotonically.

(ii) According to the PR algorithm the estimate $B^{(k)}$ of the solution after the kth iteration step can be written as follows

$$B_J^{(k)} \; = \; B_J^{(0)} \; + \; \rho_J \sum_{l=1}^{k} \Delta B_{I_l}^{(l)} \; F_{JI_l} \tag{4.53}$$

in terms of the shooting sequence I_l, $l = 1...k$. Given the convergence of the PR method, the exact solution can be obtained in the limit $k \rightarrow \infty$

$$B_J \; \equiv \; B_J^{(\infty)} \; = \; B_J^{(0)} \; + \; \rho_J \sum_{l=1}^{\infty} \Delta B_{I_l}^{(l)} \; F_{JI_l} \; . \tag{4.54}$$

Since $\Delta B_{I_l}^{(l)}$ is non-negative, all $B_J^{(k)}$ are monotonically increasing with k. Therefore, the ℓ_1 vector norm of the error $\varepsilon^{(k)}$ can be written without taking absolute values

$$\| \, \varepsilon^{(k)} \, \|_1 = \| \, B \; - \; B^{(k)} \, \|_1 = \sum_{J=0}^{N-1} \; B_J \; - \; B_J^{(k)} \; . \tag{4.55}$$

Inserting Eq. (4.53) and Eq. (4.54) leads to

$$\| \, \varepsilon^{(k)} \, \|_1 = \sum_{J=0}^{N-1} \left[\rho_J \sum_{l=k+1}^{\infty} \; \Delta B_{I_l}^{(l)} \; F_{JI_l} \right] \; . \tag{4.56}$$

Resorting, presuming employing the maximum of ρ and replacing F_{JI_l} by $F_{I_l J} A_{I_l} / A_J$ with the reciprocity relationship (Eq. (4.15)) results in

$$\| \, \varepsilon^{(k)} \, \|_1 \leq \; \max_J \rho_J \sum_{l=k+1}^{\infty} \left[\Delta B_{I_l}^{(l)} \; A_{I_l} \; \sum_{J=0}^{N-1} \frac{F_{I_l J}}{A_J} \right] \; . \tag{4.57}$$

By considering only the smallest A_J within the model domain, A_J is drawn out of the sum over all J in Eq. (4.57). The remaining $\sum_{J=0}^{N-1} F_{I_l J}$ cannot exceed one for an open environment (Eq. (4.17)) and is set to the maximum, therefore

$$\| \, \varepsilon^{(k)} \, \|_1 \leq \; \frac{\max_J \rho_J \; \max_I (\sum_{J=0}^{N-1} F_{IJ})}{\min_J A_J} \; \sum_{l=k+1}^{\infty} \; \Delta B_{I_l}^{(l)} \; A_{I_l} \; \; . \tag{4.58}$$

Solving Eq. (4.51) for $\Delta B_{I_k}^{(k)}\ A_{I_k}$ and inserting it in Eq. (4.58) results in

$$\| \varepsilon^{(k)} \|_1 \leq \frac{\max\limits_J \rho_J \ \max\limits_I (\sum_{J=0}^{N-1} F_{IJ})}{\min\limits_J A_J} \sum_{l=k+1}^{\infty} \frac{(\varepsilon^{\star(l)} \ - \ \varepsilon^{\star(l+1)})}{\mu^{(l)}} \ . \tag{4.59}$$

Replacing $\mu^{(k)}$ by its minimum and employing the monotonic decrease of $\varepsilon^{\star(k)}$, the error $\varepsilon^{(k)}$ is bounded by $\varepsilon^{\star(k)}$ via

$$\| \varepsilon^{(k)} \|_1 \leq \frac{\varepsilon^{\star(k)}}{\min\limits_k \mu^{(k)}} \ \frac{\max\limits_J \rho_J \ \max\limits_I (\sum_{J=0}^{N-1} F_{IJ})}{\min\limits_J A_J} \ . \tag{4.60}$$

The bound can be further simplified. The minimum of $\mu^{(k)}$ is estimated, by assuming that the minimum of $\mu^{(k)}$ over all iteration steps is given by the minimum over all patches A_I of the model domain. Therefore, the minimum of $\mu^{(k)}$ can be written as

$$\min_k \mu^{(k)} \ = \ \min_I \ \{ \sum_{J=0}^{N-1} F_{IJ} \ - \ \sum_{J=0}^{N-1} \rho_J \ F_{IJ} \ \sum_{K=0}^{N-1} F_{JK} \} \ . \tag{4.61}$$

Again, by applying the fact that the view factor sum cannot exceed one (Eq. (4.17)), Eq. (4.61) results in

$$\min_k \mu^{(k)} \ \geq \ \min_I \ \{ \sum_{J=0}^{N-1} F_{IJ} \ - \ \max_J (\sum_{K=0}^{N-1} F_{JK}) \ \sum_{J=0}^{N-1} \rho_J \ F_{IJ} \} \ . \tag{4.62}$$

By further replacing the reflectivity value ρ by its maximum of all reflectivities in the model domain the inequality reduces to

$$\min_k \mu^{(k)} \ \geq \ (1 \ - \ \max_J \ \rho_J \ \max_J (\sum_{K=0}^{N-1} F_{JK})) \ \min_I \ (\sum_{J=0}^{N-1} F_{IJ}) \ . \tag{4.63}$$

Since the view factor sum cannot exceed one Eq. (4.60) can then be written as

$$\| \varepsilon^{(k)} \|_1 \leq \frac{\max\limits_I \ \rho_I}{\min\limits_I \ (\sum_{J=0}^{N-1} F_{IJ}) \ \min\limits_I \ A_I \ (1 \ - \ \max\limits_I \ \rho_I)} \ \| \varepsilon^{\star(k)} \|_1 \tag{4.64}$$

The tightness of this bound is partly controlled by the factor

$$Y \ = \ \frac{\max\limits_I \ \rho_I}{\min\limits_I \ (\sum_{J=0}^{N-1} F_{IJ}) \ \min\limits_I \ A_I \ (1 \ - \ \max\limits_I \ \rho_I)} \ . \tag{4.65}$$

In order to asses the tightness of the bound Eq. (4.64), $\| Y \varepsilon^{\star(k)} \|_1$ and $\| \varepsilon^{(k)} \|_1$ are compared in a test run for the model domain shown in Fig. 4.7. An albedo of 0.2 was chosen in Fig. 4.10(a) and an albedo of 0.9 in Fig. 4.10(b). Similar to the test run for Fig. 4.8 and Fig. 4.9 the true solution B is obtained in advance by GS iteration. The model set-up was chosen similar as described in Section 4.2.1, p.63 for Fig. 4.8. Both errors are normalised by the unshot radiosity distribution $\| \Delta B^{(0)} \|_1$ at iteration start.

As can be seen in the semi-logarithmic plots of Fig. 4.10 both errors show an exponential

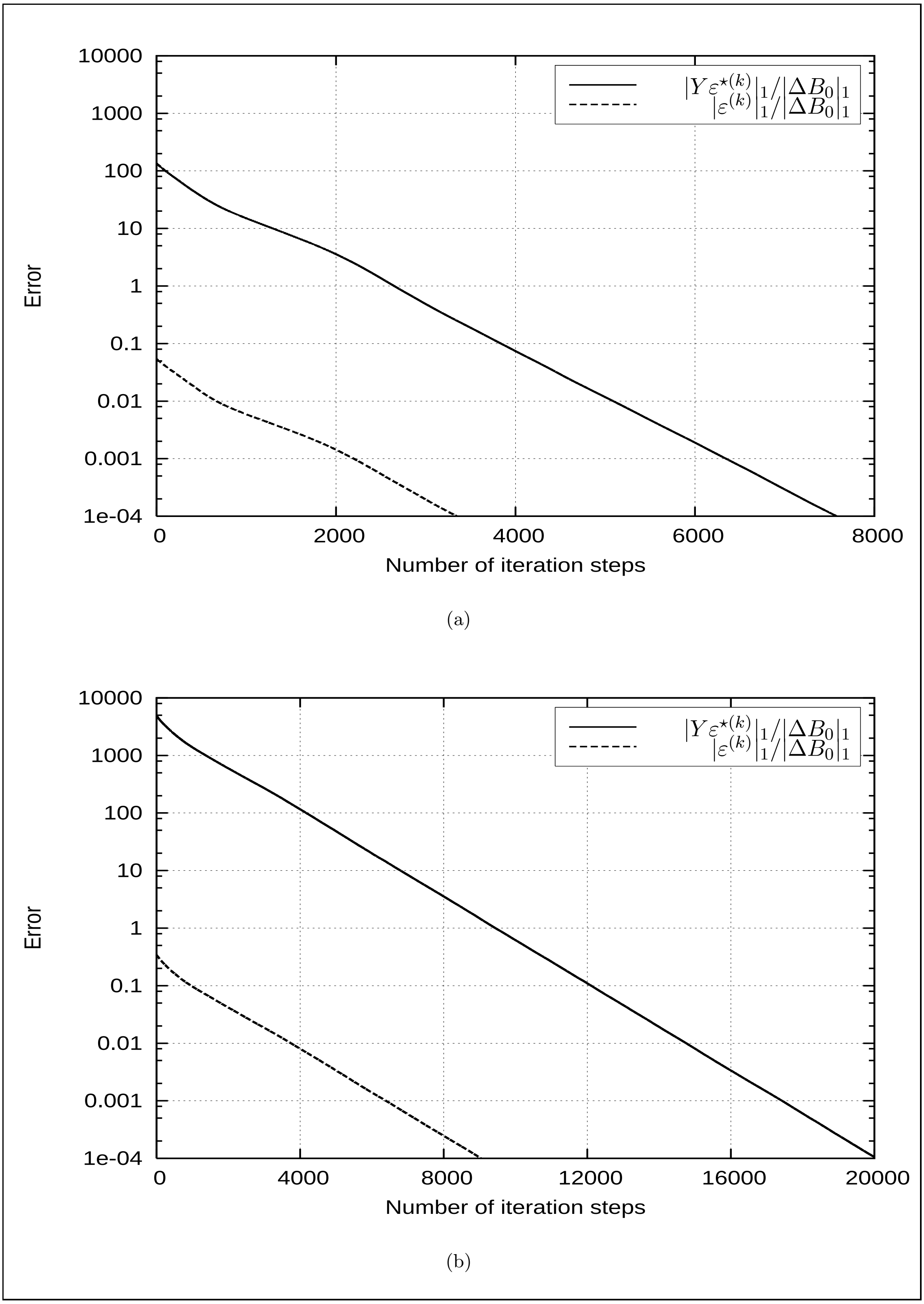

(a)

(b)

Figure 4.10: The new error criterion is compared to the true error (cf. Eq. (4.64)) for each iteration step by the model domain shown in Fig. 4.7: (a) albedo of 0.2, (b) albedo of 0.9.

decay with approximately the same slope rates as a function of the iteration steps. Overall, more iteration steps are required to converge for the larger albedo value of 0.9 (Fig. 4.10(b)). Since $\parallel Y\varepsilon^{\star(k)} \parallel_1$ was bounded in such a way that it remains larger than $\parallel \varepsilon^{(k)} \parallel_1$ overall more iteration steps are required for $\parallel Y\varepsilon^{\star(k)} \parallel_1$. This ovestimation of $\parallel Y\varepsilon^{\star(k)} \parallel_1 / \parallel \Delta B^{(0)} \parallel_1$ varies with the maximum albedo. Clearly, this arises due to the loose validation of the bound between both errors, i.e. the rather pessimistic estimation by using maxima and minima. Especially the assumption of a maximum view factor sum of one (cf. for Eq. (4.64)) is a very pessimistic estimation. The overestimation of the error is lower the lower the maximum albedo value is in the model domain. Thus, by the examples in Fig. 4.10 it could be shown that the new stopping criterion $\varepsilon^{\star(k)}$ (Eq. (4.45)) is well bounded by the factor Y (Eq. (4.65)) to $\varepsilon^{(k)}$. However, the performance of the bound could be further improved by tightening some estimations when computing the bound between both errors. Nevertheless, with this more pessimistic bound it is guaranteed that not too less iteration steps are used.

Finally, an appropriate stopping tolerance, i.e. the accuracy limit of the iteration, is defined for the new stopping criterion.

For the stopping tolerance, the iteration error, the limit is the measurement accuracy of a standard net pyranometer, i.e. +/-10%. If $\varepsilon^{\star(k)}$ reaches a stopping threshold value ε the iteration is stopped. Here, the limit is chosen to be represented by 10% of the total reflectable radiation at iteration start $\Delta B^{(0)}$

$$\parallel \varepsilon^{(k)} \parallel_1 \leq \; Y \;\; \parallel \varepsilon^{\star(k)} \parallel_1 \leq \; Y \; \varepsilon \; < \; 0.1 \; \parallel \Delta B^{(0)} \parallel_1 \; . \tag{4.66}$$

Employing the bound (Eq. (4.65)) the accuracy (Eq. (4.66)) can be guaranteed if

$$\varepsilon \; = \; \frac{0.1 \; \parallel \Delta B^{(0)} \parallel_1}{Y} \; . \tag{4.67}$$

In this way the stopping threshold ε depends on the topography and the maximum surface reflectivity via Y as well as the mean unshot radiosity. The stopping threshold ε has to be computed for each time step. The stopping criterion $\varepsilon^{\star(k)}$ is used in the following way

$$\parallel \varepsilon^{\star(k)} \parallel_1 \leq \; \varepsilon \; := \; \frac{0.1 \; \parallel \Delta B^{(0)} \parallel_1}{Y} \; . \tag{4.68}$$

Note that stopping tolerances can be chosen according to the desired level of accuracy. The threshold value given here was selected within the accuracy limits of the radiation measurement instruments. Additionally, besides of the described iteration error, more errors are contributing to the solution of the radiosity equation e.g. the discretisation error (for more information see e.g. Atkinson (1997)).

Implementation details

In addition to the lower iteration step bound an arbitrarily chosen bound for iteration start is introduced. This was necessary for very low $\parallel \Delta B^{(0)} \parallel_\infty$, e.g. for low solar radiation input in the early morning or evening hours. Iterating model domains with radiosity values, which are very low, lead to extended computation time instead of an overall gain in spatial radiosity values due to negligible exchanged radiosity values. But since individual patches A_I in the sun have a $\Delta B_I^{(0)} > 0$, although shaded patches of course do not, the l_∞ was chosen instead of comparing a mean unshot radiosity distribution at iteration start. An arbitrarily lower bound of 40 Wm^{-2} was chosen for $\parallel \Delta B^{(0)} \parallel_\infty$ for patches with a view factor sum $\sum_{J=0}^{N-1} F_{IJ} > 0.1$. The latter condition was necessary to prevent that iteration is started when only mountain peak patches are receiving $\Delta B_I^{(0)} >$ zero since these patches cannot induce many radiosity changes at all.

Furthermore, a second lower iteration step bound is presented for simulations that do not require a highly detailed radiosity exchange computation. Note that this criterion was not used for the simulations in Part III but can be advantageous for other studies and was therefore introduced here.

By determining the difference of $\parallel B \; - \; E \parallel_p$ an estimate of the fraction of the total exchanged radiosity in the model domain is possible. Applying the triangle inequality on the difference of $\parallel B \; - \; E \parallel_1$ leads to

$$\parallel B \; - \; E \parallel_1 \leq \parallel B \; - \; B^{(k)} \parallel_1 \; + \; \parallel B^{(k)} \; - \; E \parallel_1 \; . \tag{4.69}$$

The first term on the right hand is approximated by Eq. (4.64) and the second term can be computed directly. Therefore, the fraction of the total exchanged radiosity in the model domain can be computed for every iteration step. The first term of Eq. (4.69) converges to zero with increasing iteration steps whereas the second term approaches the fixed value of $\parallel B - E \parallel_1$. Accordingly, both terms can be requested for the decision of stopping an iteration since a sufficiently accurate solution can be reached earlier if a very large amount of radiosity is already exchanged.

The accuracy limit for the fraction of the already exchanged radiosity in the model domain, i.e. second term on the right hand side of Eq. (4.69), is chosen in the same way as for Eq. (4.68). As soon as the fraction $\parallel B^{(k)} - E \parallel_1$ reaches 10 % of the total reflectable radiation at iteration start $\Delta B^{(0)}$, the iteration is stopped since a relatively large amount of radiosity is already exchanged then

$$\parallel B^{(k)} \; - \; E \parallel_1 \geq \; 0.1 \; \parallel \Delta B^{(0)} \parallel_1 \; . \tag{4.70}$$

4.3 Radiosity approach for LW radiation balance in complex terrain

As for the SW diffuse sky radiation component, the LW sky component varies strongly in complex terrain. Additionally, the limited visible sky (sky view factor) increases emitted terrain radiation even during nights. Thus, terrain emissions have to be included on inclined surfaces in complex terrain. The importance of LW terrain emissions was pointed out for mountainous terrain in various studies, which are listed in Section 4.2, p.58. In this section some of these are described in more detail:

Olyphant (1986b) pointed out that in rugged terrain LW emissions enhance incident LW radiation and lead to spatial inhomogeneities in snowmelt. The commonly used isotropic view factor approach is especially inaccurate if the considered terrain surface is very heterogeneous. Comparisons of LW terrain emission computations with the isotropic view factor approach and by numerical integration of the equation for diffuse irradiance presented e.g. by

Kondratyev and Manolova (1960) revealed that in almost all cases the isotropic view factor approach underestimates incident LW terrain radiation L_{t}. Matzinger et al. (2003) measured incident éW radiation L_{inc} to be generally highest at valley-floor sites, decreasing with height within the valley. They concluded that these patterns arise due to an increase of "cold" radiation from the less obstructed sky at higher elevations. And on the other hand they arise due to the decreased sky view factor at the valley bottom which is replaced by warm emitting "side walls". From sensitivity studies Sicart et al. (2006) found that in general total incident LW radiation $L_{\mathrm{inc},I}$ at a point I is more sensitive to the sky view factor $F_{\mathrm{sky},I}$ than to the surface temperature $T_{\mathrm{s},J}$ at other sites J. However, when LW sky radition L_{a} is low, LW terrain emission from warm snow free slopes can increase L_{inc} by up to 60 % for valley slopes of 35°.

In Section 4.2, p.58 it was outlined that the radiosity approach is best suited to describe the SW radiation exchange in mountainous terrain. The same is valid for diffuse LW terrain radiation emissions in mountainous terrain.
Here, the derivation of the radiosity equation for the SW radiation balance over complex topography (Section 4.2, p.58) is partly repeated for the LW radiation balance over complex topography. Some of the simplifications can also be applied to LW radiation.
The derivation starts from Eq. (4.8) this time applied to the LW radiation flux incident at point x. The integral over the hemisphere in Eq. (4.8) is also decomposed into directions pointing to the sky and to the terrain $L(x) = L_{\mathrm{sky}}(x) + L_{\mathrm{t}}(x)$. The LW radiation from the sky $L_{\mathrm{sky}}(x)$ consists solely of incident isotropic LW sky radiation L_{a} (Section 3.2.1, p.3.2.1)

$$L_{\mathrm{sky}}(x) \;=\; L_{\mathrm{a}}(x)\;. \tag{4.71}$$

Thereby, as assumed for $S_{\mathrm{sky}}(x)$, $L_{\mathrm{sky}}(x)$ is not influenced by any terrain contributions $L_{\mathrm{t}}(x)$. Therefore, the radiance $R(x, \Omega(x))$ from the sky is an independent radiation source into the surface. Eq. (4.34), Eq. (4.35) and Eq. (4.36) are assumed to be valid accordingly as for the SW radiation balance. The set of equations is further specified to compute the broadband LW radiation transfer in mountainous terrain:

1. In contrast to SW radiation, for broadband LW radiation the atmosphere in Eq. (4.35) is not completely neglected since absorption of LW radiation is more pronounced than absorption of SW radiation. Q=0 but $\tau \neq 1$ are chosen to account for the radiance absorption between x' and x. With increasing distance between two points, scattering out of the air column will dominate and terrain emissions become negligible. The implemented statistical formula (Eq. (3.53)) parameterises the diffusely emitted terrain radiation of a patch A_J to a patch A_I ($\tau \neq 1$) by accounting for attenuation within the air column. It accounts for background radiation within the column but does not include scattering into the air column or internal emission processes within the air column (Q=0). Landl (2007) found that LW terrain emissions should be taken into account for distances up to 1 to 2 km, depending on surface temperatures. Here, LW terrain radiation influence is assumed negligible for distances larger than 1500 m. Eq. (4.35) is empirically parameterised by means of an assumed air column that is filled with the constant surface air temperature of the receiving patch, as given in Eq. (3.53) (in its discretised form) (Landl (2007)).

2. The ideally diffuse emitting surface sources are described in terms of mean surface emissivity values $\varepsilon_{\mathrm{s}}(x')$. Lambertian emitting surfaces with $R_0(x)\pi = \varepsilon_{\mathrm{s}}(x')\sigma T_{\mathrm{s}}(x')^4$

(cf. Eq. (4.8)) are a common, reasonable assumption also in RT models for a cloudy atmosphere. According to Kondratyev (1969) the emission of natural surfaces can be considered isotropic. Within the LW terrain parameterisation used here (Eq. (3.53)), surface emissivity values have constant values of one, as discussed in Section 3.2.2, p.42. Again, the error arising from the assumption that all patches are Lambertian emitters is assumed to be minor compared to the error arising from the neglect of cloud backscattering or from the error due to the parameterised radiation attenuation of the homogeneous air temperature column between two patches.

In contrast to the radiosity equation Eq. (4.1) applied to the SW radiation balance, the above simplification of surface emissivity values of one leads to one integral over the surface instead of to the integral equation Eq. (4.37). It can be written as

$$L_{\mathrm{inc}}(x) \;=\; L_{\mathrm{a}}(x) \;+\; L_{\mathrm{t}}(x) \tag{4.72}$$

with $L_{\mathrm{t}}(x)$ determined by a parameterisation accounting for the surface temperature at x' (cf. Section 3.2.2, p.42, Eq. (4.34)). Thereby, each patch A_I emits LW radiation according to the Stefan-Boltzmann's law. With Eq. (4.72) mountainous terrain is considered as part of an enclosure bounded by the surrounding topography and the sky.
The discrete formulation of Eq. (4.72) is given by

$$L_{\mathrm{inc},I} \;=\; L_{\mathrm{a},I} \;+\; \sum_{J=0}^{N-1} L_{\mathrm{t},J} \tag{4.73}$$

with L_{t} determined according to Eq. (3.53). Hence, to compute Eq. (4.73) no iteration method is required.

Implementation details

On principle expression Eq. (4.73) for the incident LW radiation flux can simply be evaluated if all view factors are stored. This is however not the case if the model is used in limited-memory-mode where the view factors are computed only on request during PR. The sum in Eq. (4.73) can then be evaluated approximately by only taking into account its dominant terms. These are detected similarly to the shooting criterion Eq. (4.44) which control the PR iteration in the SW radiation. The solution process can be seen as N JA iteration steps reduced by the number of pairs of patches that are more than 1500 m apart. The choice of the iteration method for the SW radiation balance of Eq. (4.43) considered the available memory capacity. Therefore, whether PR iteration is chosen with or without a stored view factor matrix for the SW radiation balance, a version of it has to be applied for the LW radiation balance. Thus, for the computation of the LW radiation balance, in the following some parts of PR iteration applied on the SW radiation balance are accordingly presented. But note that in case of enough memory capacity the solution of Eq. (4.73) can be obtained without any shooting order, stopping criterion and stopping threshold.

First, the order of which the largest amount of unshot LW radiosity is selected similar to that developed for the SW radiation balance (Eq. (4.44))

$$\textit{shooting criterion} \;:\; \max_{I} \left(\Delta L_{\mathrm{inc},I}\; A_I \sum_{J=0}^{N-1} F_{IJ} \right) \tag{4.74}$$

with ΔL_{inc} the unshot LW radiosity at iteration start $\Delta L_{\mathrm{inc},I} = \sigma_{\mathrm{SB}}\ T_{\mathrm{s},I}^4$ at iteration start. Thus, the initial terrain radiation distribution is computed by Stefan-Boltzmann's law, assuming an emissivity of one (cf. Section 3.2.2, p. 42), but is not applied for the actual radiation exchange computation. This is since the determination of the shooting order cannot be derived in advance from the parameterised L_{t} (Eq. (3.53)).

If PR without stored view factor matrix is chosen the additional restriction for patches that are not further apart than 1500 m reduces the number of redundant view factor computations. For distances larger than 1500 m the LW terrain emission is assumed to be negligible (Section 3.2.2, p.42). The LW surface radiation balance can be formulated as Pseudo-Code as follows

```
for all $I$
  $L_{\mathrm{inc},I} = L_{\mathrm{a},I}$
  $\Delta L_{\mathrm{inc},I} = \sigma_{\mathrm{SB}}\ T_{\mathrm{s},I}^4$    // unshot radiosity
while accuracy not attained or $k \leq N$
  pick $I$, such that $\Delta L_{\mathrm{inc},I}\ A_I\ \sum_{J=0}^{N-1} F_{IJ}$ is largest
    for every patch $A_J$
        if ($r_{IJ} \leq 1500$ m)    // only than the LW influence is necessary
        { compute $F_{JI}$
        $\Delta rad = L_{\mathrm{t},I}$
        $L_{\mathrm{inc},J} = L_{\mathrm{inc},J} + \Delta rad$ }
  $\Delta L_{\mathrm{inc},I} = 0$
```

Second, the new stopping criterion for SW radiation is applied for LW radiation computation for $k \leq N$ by neglecting $\max_I \rho_I$ in Eq. (4.64)

$$\parallel \varepsilon^{(k)} \parallel_1 \leq \frac{\varepsilon^{\star(k)}}{\min\limits_I \left(\sum_{J=0}^{N-1} F_{IJ}\right)\ \min\limits_I\ A_I}\ . \tag{4.75}$$

Note that the adaptation of the stopping criterion (Eq. (4.64)) is only a rough method to enable the introduction of a stopping threshold for the LW radiation computation. This criterion is presented here since it worked well for the investigated cases in this study. But this might be questionable in other cases since for an emissivity of one, which implies an albedo of one, Eq. (4.64) is actually not valid.

The additional different coefficient on the right hand in Eq. (4.64) for the correlation between $\varepsilon^{(k)}$ and $\varepsilon^{\star(k)}$ is now called Z. Setting the stopping threshold $\varepsilon^{\mathrm{lw}}$ similarly to Eq. (4.67) results in

$$\parallel \varepsilon^{\star(k)} \parallel_1 \leq\ \varepsilon^{\mathrm{lw}}\ :=\ \frac{0.1\ \parallel \Delta B^{(0)} \parallel_1}{Z}\ . \tag{4.76}$$

A second criteria similar to Eq. (4.70) is neglected for the LW terrain emission due to the low iteration steps. At maximum N terms are accounted for in Eq. (4.73) for all I. The number of patches actually receiving LW terrain emission is further reduced thanks to the distance restriction of 1500 m.

5 Coupled model for alpine surface processes: Alpine3D

The presented radiation balance model is a module of the modular model system Alpine3D for alpine surface processes. The whole model system is actively developed at WSL, Federal Institute for Snow and Avalanche Research SLF, Davos, Switzerland. It has been successfully applied for different applications, with varying module focuses. A first overview about Alpine3D is given in Lehning et al. (2004) and once again in Lehning et al. (2006) together with a hydrological application. Further model applications comprise the prediction of surface temperatures on ski pistes for the ideal choice of the wax for ski competitions (Schirmer (2005), Landl (2007)), runoff catchment simulations at Goldbergkees, Austria (Michlmayr et al. (2008)) and in the Dischma valley (EU (WWW)) and also snowdrift applications for a steep mountain ridge Gaudergrat, Switzerland (Lehning et al. (2007)) and on the Sonnblick glacier, Austria (Mott et al. (2007)).

In the present study the focus is on the radiation balance module which is described in detail in Section 3, p.25 and Section 4, p.45. Additionally, the SNOWPACK module was used which is, in its original version, described in Bartelt and Lehning (2002), Lehning et al. (2002a) and Lehning et al. (2002b). It is not the aim of this study to give a detailed description of the present version of the SNOWPACK module. Instead, in this chapter the Alpine3D model structure and the required input data are presented.

5.1 Model structure

The overall Alpine3D module structure is given in Fig. 5.1. As can be seen all modules interact with the SNOWPACK module. Individual modules can be switched off, but SNOWPACK always has to be used. The modular model system Alpine3D for alpine surface processes consists of a three-dimensional radiation balance model, a one-dimensional model of soil, vegetation and snow (SNOWPACK), a three-dimensional snowdrift model and a conceptual zero-dimensional runoff model (Fig. 5.1). The inout module controls the input data. Surface data assimilation can be enabled via the data assimilation module. Alpine3D can be deployed on a dedicated GRID environment as it is parallelised by PopC++, an object oriented extension of C++ for code parallelisation (Nguyen and Kuonen (2007)).

5.2 Input data

Required input data for all modules consist of a DHM, landuse class information and soil and snow layer characteristics at each grid cell (e.g. bare soil, meadow, deciduous forest, water, road etc.). One-dimensional radiation input is necessary for the radiation balance

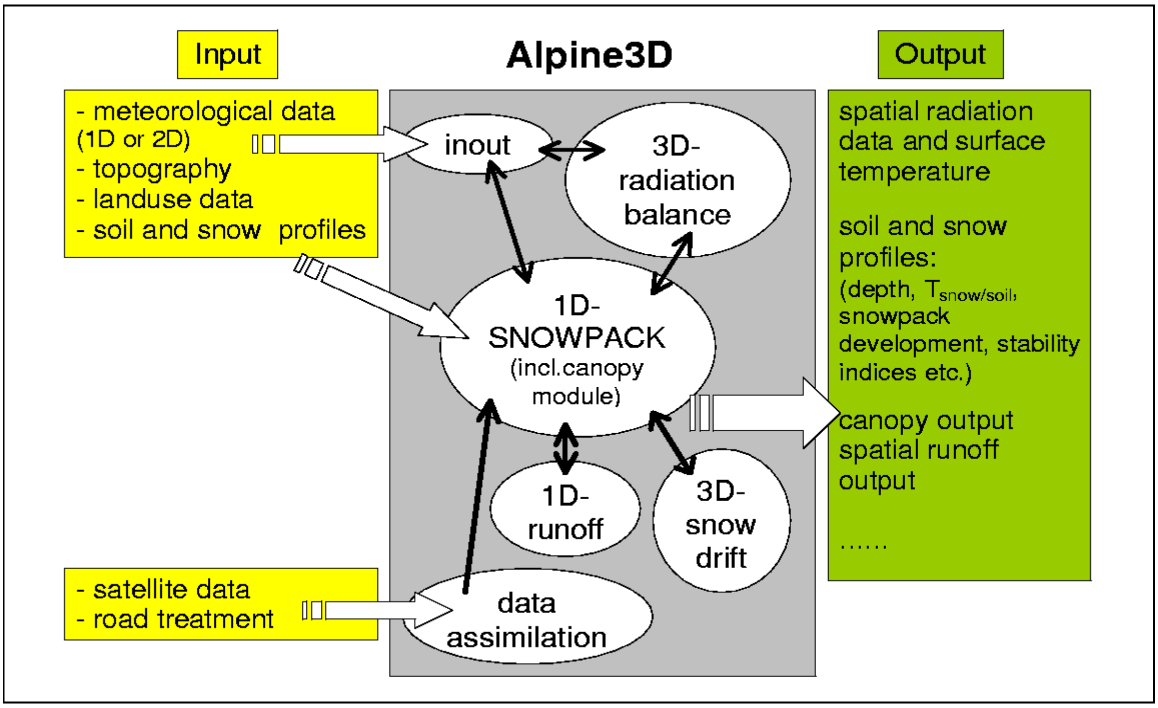

Figure 5.1: Schematic for the model structure of the modular alpine surface process model Alpine3D.

computation. Further meteorological input data can be one- or two-dimensional (left hand side of Fig. 5.1). Three-dimensional wind components are read in if snowdrift is computed by the snowdrift module.

DHM's (cf. Section 2.1, p.17) with different horizontal resolutions can be used. Lowest horizontal resolutions are only limited by the overall computer memory. Since the largest memory is presently required within the radiation balance computation the lowest possible horizontal resolutions are limited by the radiation balance module as discussed in Section 4.2, p.58.

Landuse information is obtained for Switzerland from areal statistics extracted from digital aerial photographs (Swisstopo (WWW)) by the Federal Office of Statistics in Switzerland in 100 m horizontal resolution (BFS (WWW)) and is converted to 25 m horizontal resolution. If specific landuse classes (e.g. roads or bridges) are not included or if newer information is available on orthoimages this is usually introduced by means of underlaying orthoimages of Swisstopo (WWW). A likewise geographic information system (Schirmer (2005)) was used to lay landuse grids on top of orthoimages and to convert individual grid cells.

Detailed soil layer characteristics are required for each landuse class as well as a detailed snow profile. An arbitrary number and depth of the soil and snow pack can be chosen. Required individual layer or node characteristics are: *layer age*, layer thickness Δz, node temperature (for snow surface: T_{ss}), layer volume fraction of ice θ_{i}, water θ_{w}, vapor θ_{v} and soil θ_{s} (with a soil fraction being zero for snow), soil density ρ_{s}, soil heat conductivity λ_{s}, soil heat capacity c_{ps}, mean/effective soil grain radius r_{gs} or snow grain radius r_{gss}, snow grain bond radius r_{bss}, snow dendricity dd_{ss}, snow sphericity sp_{ss}, snow type marker (tracks the history of grain development) and mass of surface hoar formed or sublimated. If a landuse class contains canopy the vegetation height, leaf area index and fraction of throughfall for the vegetation are required as well. Mean constant roughness length and snow free surface albedo values are assigned to each landuse class. Mean snow surface and canopy albedo values are computed in SNOWPACK at each time step. Lower boundary conditions can be chosen to be either Dirichlet (fixed soil or snow pack bottom temperature) or Neumann (geothermal heat flux at soil bottom).

One-dimensional meteorological input data can be obtained from an exposed meteorological measurement station. It consists of global radiation S_{g}, incident LW radiation L_{inc} or cloud cover fraction n_c, air temperature T_{a}, wind velocity $|v|$, relative humidity rh and *precipitation rate*. The point measurements are spatially interpolated as follows:

The measured air temperature $T_{\mathrm{a}}^{\mathrm{meas}}$ in K is spatially interpolated according to the "1976 U.S. Standard Atmosphere" (Stull (2000)) with a constant lapse rate of 0.0065 Km^{-1} for geopotential heights H below 11 km. Thus, at a grid cell I at height z_I the temperature is calculated from

$$T_{\mathrm{a},I} \;=\; T_{\mathrm{a}}^{\mathrm{meas}} \;-\; (z_I \;-\; z^{\mathrm{station}})\; 0.0065 \;, \tag{5.1}$$

where z^{station} is the height z at the measurement station. Note, that when applying this interpolation method, the interpolated air temperature T_{a} does not depend on local characteristics such as surface orientation (shading) or local winds. Air pressure p in hPa is also interpolated by the standard atmosphere equations for air temperature T_{a} and pressure for geopotential heights H below 11 km according to the "1976 U.S. Standard Atmosphere" (Stull (2000))

$$p_I \;=\; p_0\,(1 \;-\; \frac{0.0065\; H_I}{288.15})\;. \tag{5.2}$$

The constant 288.15 K represents the standard sea-level air temperature and p_0=1013.25 hPa the standard air pressure at sea level. Due to the variation of gravity with height z and latitude ϕ, usually the geopotential height H is applied instead of height z above sea level. The geopential height H The geopotential height H_I at each grid cell I is computed by

$$H_I \;=\; \frac{R_0\; z_I}{(R_0 \;+\; z_I)} \tag{5.3}$$

with R_0=6356766 m being the average radius of the earth. The measured relative humidity rh in dimensionless is currently assumed to be constant throughout the model domain, i.e. independent of the heights z_I. Mean wind velocity $|v|$ (in ms^{-1}), relative humidity rh (dimensionless) and *precipitation rate* (in mmh^{-1}) are assumed to be homogeneous throughout the model domain.

Two-dimensional meteorological input data consists of spatially interpolated two-dimensional fields of air temperature T_{a}, wind velocity $|v|$, relative humidity rh and *precipitation rate* from an arbitrary amount of meteorological stations within or nearby the model domain. The applied interpolation schemes are similar to those presented in Garen and Marks (2001) and Klok et al. (2001).

In most cases hourly mean values from meteorological input data are used here.

5.3 Three-dimensional radiation balance module

The three-dimensional radiation balance module of Alpine3D is the broadband radiation balance model described in detail in Chapter 3, p.25 and in Chapter 4, p.45. Spatial distributed radiation values are obtained in case of one-dimensional as well as in case of two-dimensional meteorological input data from an one-dimensional global radiation value S_g, an incident LW radiation value L_inc or a cloud cover fraction n_c.

The radiation balance module is called first, i.e. before SNOWPACK, in each model time step and computes spatial global radiation S_g and incident LW radiation L_inc as part of the surface energy balance. The energy balance is computed within SNOWPACK delivering surface temperature T_s and, in case of snow, the snow surface albedo α_ss for the radiation balance. Therefore, within the radiation balance module the surface temperature T_s distribution and snow surface albedo α_ss distribution are used from the previous time step. Note that this might have an influence on computed radiation balance values e.g. at sunset or sunrise or during snow ablation phases.

5.4 One-dimensional snow pack module: SNOWPACK

The SNOWPACK module solves the one-dimensional energy- and mass balance. SNOWPACK is a FE snow cover model that computes stratigraphical microstructure and metamorphism for the three-component snow cover of air, water and ice. A detailed derivation of all originally implemented SNOWPACK equations is presented in Bartelt and Lehning (2002), Lehning et al. (2002a) and Lehning et al. (2002b) and is not repeated here. Note that the turbulent fluxes are computed in SNOWPACK. The proposed formulas for stable conditions of Stearns and Weidner (1993) are used in a slightly changed manner. In case of unstable conditions the proposed formulas of Paulson (1970) are applied. But according to Landl and Lehning (2008) current implementations of stability corrections can be inadequate for inclined as well as flat surfaces in alpine terrain. Assuming neutral conditions and a minimum mean wind velocity of 1.5 ms^{-1} resulted in better modelled snow surface temperatures for a particular alpine site.

Vegetation respectively canopy is also considered within SNOWPACK. The equations are based on a single big leaf concept and therefore additional energy- and mass balance equations are solved describing the single canopy layer as a leaf.

The soil layer equations are implemented in the same manner as the snow layer equations to describe the vertical exchanges between a snow cover and soil. Therein the soil is treated as a four-component material consisting of air, water, ice and soil. Specific soil/permafrost characteristics were introduced by Lütschg (2005). These characteristics are water retention, which is depending on grain size, and thermal soil conductivity, which is depending on water and ice content. Within the soil the water transport is treated by a simple bucket model (Lehning et al. (2002a)). Lehning et al. (2002b) parameterised the air movement in the pore space of coarse grained substrate. With the soil extended SNOWPACK Lütschg and Haeberli (2005) studied the long-term effect of climate change scenarios on ground temperatures and permafrost occurrence in the Swiss alpine region, by changing mean annual air temperature T_a and summer and winter precipitation. SNOWPACK can also, according to Lehning et al. (2006), readily be extended to simulate other materials such as pavement. But note that the lateral exchange between each of the soil-snow packs is assumed to be negligible and is therefore not considered in the one-dimensional SNOWPACK model.

In case of a snow cover the surface albedo value at each grid cell is recalculated for every time step. Since the surface albedo values are most important for the computation of the radiation balance the implemented equation is given in the following:

Snow surface albedo values α_{ss} (here snow properties are indicated by lower case letters 'ss') are derived by a statistical model based on continuous measurements over three years at the Weissfluhjoch study site. First versions were published in Lehning et al. (2002b) and was replaced later on by the following not yet published version

$$\begin{array}{rclllllll} b_I & = & 1.442 & -\ 5.6\ 10^{-5}\ \rho_{\mathrm{ss},I} & & -\ 0.2735 & \theta_{\mathrm{wss},I} & +\ 6.4\ 10^{-2}\ dd_{\mathrm{ss},I} & \\ & & & -\ 7.36\ 10^{-2}\ sp_{\mathrm{ss},I} & & +\ 0.175 & r_{\mathrm{gss},I} & -\ 0.301 & r_{\mathrm{bss},I} \\ & & & -\ 6\quad 10^{-3}\ T_{\mathrm{a},I} & & +\ 4.59\ 10^{-3} & T_{\mathrm{ss},I} & +\ 7.62\ 10^{-3} & |v|_I \\ & & & -\ 1.01\ 10^{-4}\ \alpha_{\mathrm{ss},I}^{t-1}\ S_{\mathrm{g},I} & & +\ 3.33\ 10^{-2} & rh_I & -\ 5.75\ 10^{-4} & \mathit{layer\ age}_{\mathrm{ss},I} \end{array}$$

and

$$\alpha_{\mathrm{ss},I} \ = \ MAX(\ 0.3,\ MIN(0.99,\ 0.8042\ +\ ln(b_I)))\ . \tag{5.4}$$

Additionally, the mean measured wind speed $|v|$ in ms^{-1} and the global radiation S_{g} in Wm^{-2}, computed with the albedo value $\alpha_{\mathrm{ss}}^{t-1}$ of the previous time step $(t-1)$, are considered in the statistical model.
In case of canopy with a canopy height larger than 3.5 m an additional below canopy albedo value is computed for snow. In case of a canopy covered grid cell with canopy lower than 3.5 m the snow free landuse specific albedo value is applied.

The SNOWPACK model is also applicable without being coupled to the three-dimensional radiation balance module in a stand-alone version e.g. for estimating snow stability in the avalanche warning (Lehning et al. (1999)).

5.5 Additional modules

A one-dimensional runoff module was integrated into Alpine3D with adaptations as well as further developments of the hydrologic response unit model PREVAH (Gurtz et al. (2003), Zappa et al. (2003)). Thereby spatially differing runoff is obtained from the water run out at the lower boundaries of the one-dimensional SNOWPACK module at each grid cell.
Within the three-dimensional snowdrift module snow saltation (Doorschot et al. (2004)), suspension and deposition processes as well as redistribution of deposited snow are computed. Note that the snowdrift module in Alpine3D does not model avalanches. For computing the snow transport three-dimensional wind fields are modelled with the Advanced Regional Prediction system (ARPS) (Xue et al. (2000), Xue et al. (2001)) Version 5.2.4 in its Large Eddy simulations (LES) configuration. Faure et al. (2007) coupled ARPS to the alpine local model (aLMo) of the Federal Office of Meteorology and Climatology MeteoSwiss in order to obtain downscaled wind fields with horizontal resolutions of 25 m.

Part III

Measurements and simulations

Since the main objective of this thesis is an accurate modelling of the radiation balance for various applications a thorough validation of modelled values with measurements was conducted. In this thesis part validations of individual components of the model with point measurements and with sensitivity studies are presented. At the permanent measurement site at Weissfluhjoch study site above Davos (Switzerland) at 2540 m a.s.l. various radiation measurements are conducted. Incident broadband SW direct S_{b} and diffuse sky radiation S_{d} are measured permanently by the PMOD/WRC (WWW) on the long hut at the border of the study site (measurement between 0.3 and 4 μm). Additionally, incident terrain reflected radiation S_{t} was determined (Section 8.1, p.105) on two days on the long hut. Within the flat study site, incident LW radiation L_{inc} is measured permanently.

The modelling was conducted for a domain that covers the study site and the surrounding mountain peaks, including the Weissfluhjoch. The DHM is composed of 100×100 grid cells with a homogeneous horizontal grid resolution of 25 m and a mean slope angle of 25° (cf. Fig. 6.1). Varying horizontal grid cell resolutions of that model domain were only used for sensitivity studies (Section 9.1, p.127). The blue circle in Fig. 6.1 roughly indicates the Weissfluhjoch study site. For a correct model validation of an elevated horizontally mounted instrument site it was necessary to introduce a virtual plane in the model domain atop of the corresponding grid cell. This virtual plane is a horizontal plane that accounts for the height of the measuring instruments that differ from the DHM surface elevation of the corresponding grid cell. It can be introduced on arbitrary grid cells in the model domain, e.g. in the case of the long hut the virtual plane was 3.06 m above the grid cell height, resulting in a measurement height of 2543.16 m at the measurement point (Swiss National Coordinates: East: 780892, North: 189235). Unless stated otherwise, in the following sections the modelling was conducted for that specific measurement point. Note that all radiation components (including terrain reflected or emitted radiation), modelled and measured, are presented as **incident** values. In Chapter 7, p.95 and Chapter 9, 127 each time, N SW terrrain reflections as well as N LW terrain emissions were taken into account in Progressive Refinement iteration (Section 4.1.4, p.56). A distance restriction for the LW terrain emission of 1500 m was applied in the modellings (Section 3.2.2, p.42).

6 Mutual visibility / Sun-or-shadow detection

Especially in complex terrain and in model domains with high resolutions shading has a dominant influence on incident SW radiation, therefore an accurate implementation of shading was one important objective for the new radiation balance model. The validation of the sun-or-shadow and mutual visibility detection algorithm, respectively (Section 2.2, p.19) is described in this chapter. For this validation, a section of the horizon line (horizon angle within a certain azimuth angle interval) was measured, as seen from the Weissfluhjoch study site, and compared to the corresponding modelled section.

6.1 Comparison of measured and modelled horizon angles

The horizon angle of the steep east-facing slope (Fig. 6.2(a)) as seen from the measurement point was modelled with the presented algorithm (Section 2.2, p.19), extracted by digital image analysis from a panorama picture of "Atlas der Schweiz" (AdS2 (WWW)) as well as scanned by a Leica TCRP1202 tachymeter (Leica (WWW)). The accuracy of the tachymeter is 0.00054°.

In Fig. 6.2(b) the horizon angles are shown for the corresponding azimuth angle of the eastern slope as seen from P1 (cf. Fig. 6.4). The modelled horizon angles follow the angles extracted from "Atlas der Schweiz" well. A maximum error of approximately one degree occurs at an azimuth angle of about 235°. Since the same DHM of 25 m is used for visualisation in "Atlas der Schweiz" as for the modelling, a high agreement was achieved between both. The remaining differences might come from the digital image analysis process, the difference between the terrain parameters retrieval method from the DHM in the model (Section 2.1, p.17) as opposed to the visual interpolation method in "Atlas der Schweiz", or from inaccuracies in the visibility detection algorithm.

The measured horizon angles match the angles of the other two methods well. However, for azimuth angles from 206° to 285° the measured values are larger, up to 2.5°. These differences are most likely due to the fact that the ridge is flattened in the DHM, although they can also be due to minor errors from the tachymeter measurements. For a mean horizontal distance of 413 m an angle difference of 2.5° corresponds to a height difference of 18 m.

Several conclusions arise from the presented comparison:

First, horizon angle inaccuracies have larger impacts on the SW direct radiation S_b the closer the considered slope is which is an obvious consequence of geometry. Second, a 2.5° horizon angle error is minor considering a hourly time step resulting in a mean sun hour angle of 15° (Eq. (3.10)). However, this error also shows that there is a lower limit to the model time step, which is meaningful to decrease only if horizontal grid cell resolutions of the DHM are adjusted accordingly. Third, the sun azimuth angle (Eq. (3.9)) is fixed during a model time

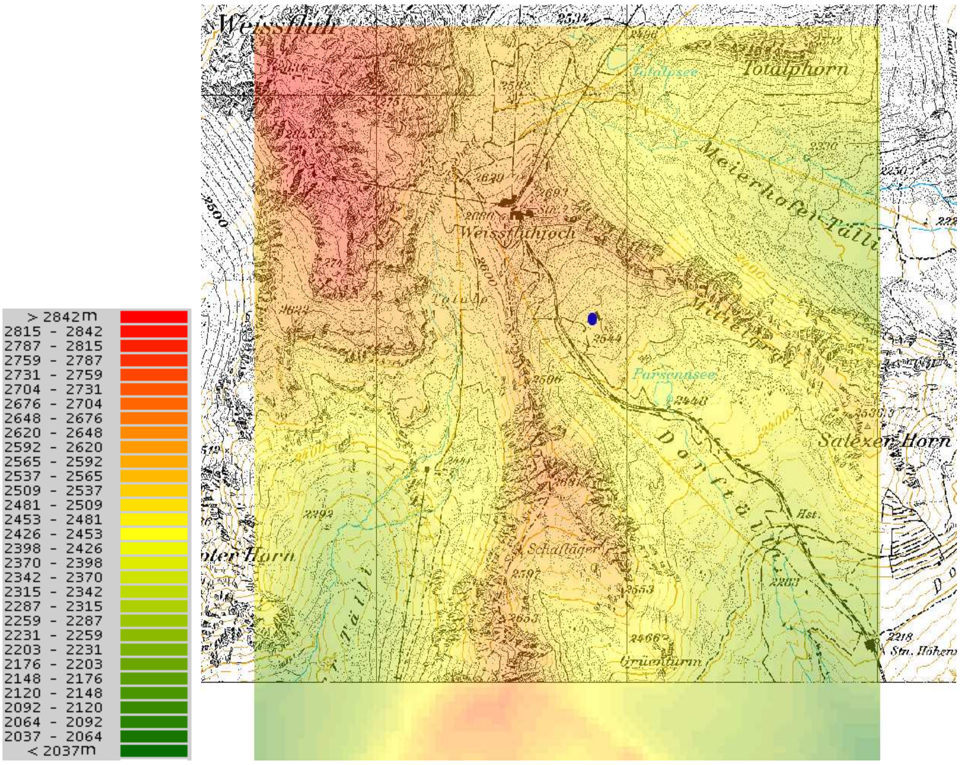

Figure 6.1: DHM for the Weissfluhjoch study site (blue circle) model domain consisting of 100×100 grid cells with a horizontal grid resolution of 25 m and a mean slope angle of 25°.

step although in reality the position of the sun, and consequently the sun-or-shadow value, varies within that time. This leads to errors in the computed sun-or-shadow values.
Nevertheless, the visibility algorithm resolves the horizon line accurately, at least within the limit of the underlying DHM (Fig. 6.2(b)) with square horizontal grid cells. But of course an inhomogeneous triangulated DHM with an accurate representation of ridges would be desirable.

The strong sensitivity of the modelled horizon line on the location of the point of view and its elevation is shown in the following.
In Fig. 6.3 all modelled horizon angles are shown without accounting for the sensor height Δz. As expected, the horizon angles are generally larger than those obtained from an elevated sensor height (cf. Fig. 6.2(b)) as well as those extracted of "Atlas der Schweiz". Nevertheless, the modelled horizon angles are still lower (differences up to 2°) than the measured ones. Additionally, the modelled horizon angles are shown for a point 50 m away (twice the grid resolution) from the actual sensor location with a Δz=0 m. This sensitivity test points out the importance of the exact selection of the location of a measurement site in the model domain. Depending on the location and elevation within the Weissfluhjoch study site, the horizon angles, and therefore radiation values, vary strongly. This can be seen from the modelled horizon angles for a point 50 m away in Fig. 6.3 and is leading to inaccurate shading times. The horizon line peak at the left outermost side of the slope (azimuth angle $\approx$ 180°-200°) is displaced by up to 5° for the modelling at point P2 which leads to considerable differences in sun-or-shadow values. For azimuth angles between 206 and 260° the largest horizon angles for all test cases are obtained due to the proximity of the surrounding slopes.

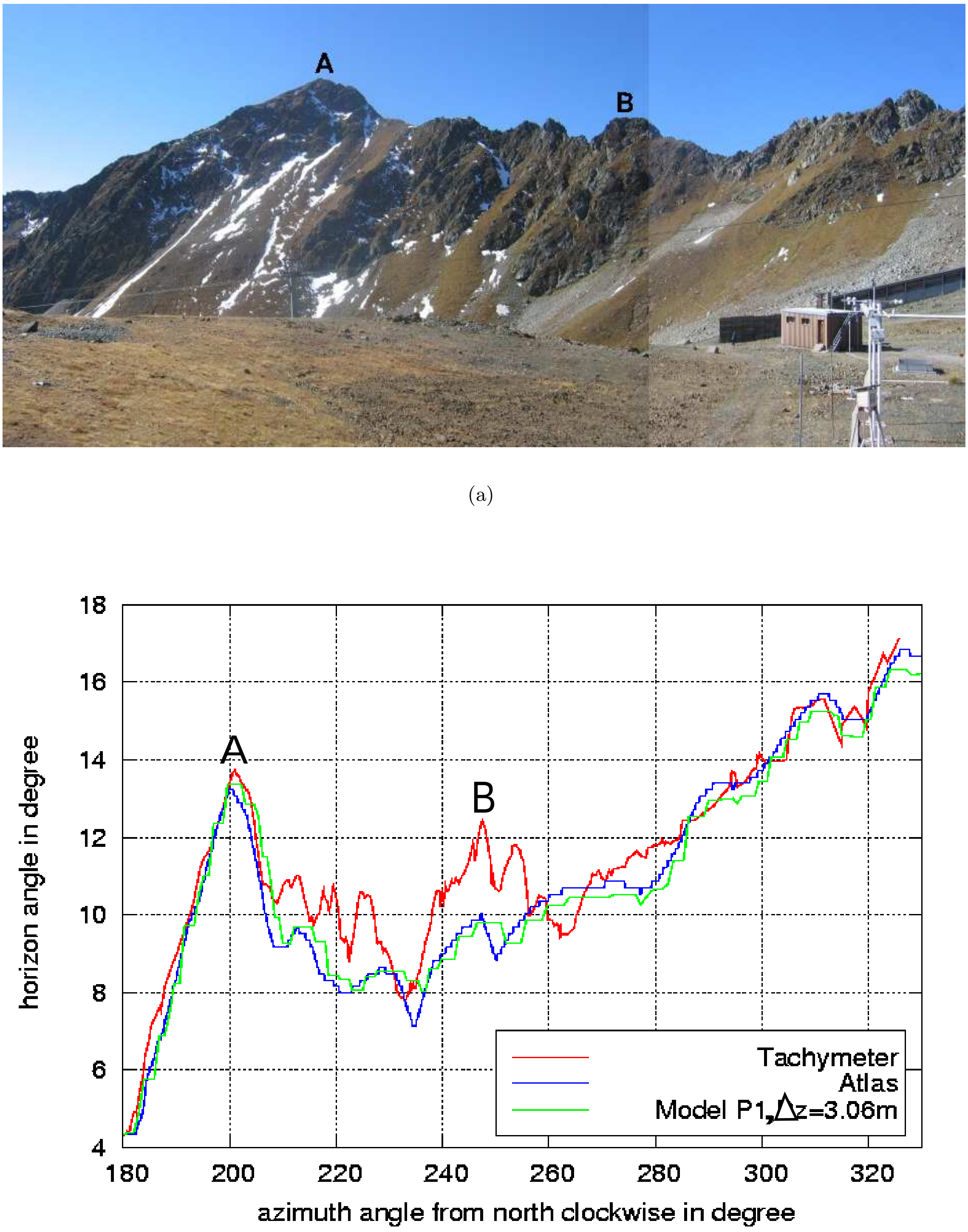

(a)

(b)

Figure 6.2: (a) Picture of the east-facing slope as seen from the measurement point at the Weissfluhjoch study site (N. Helbig). (b) Horizon angles as a function of azimuth angles.

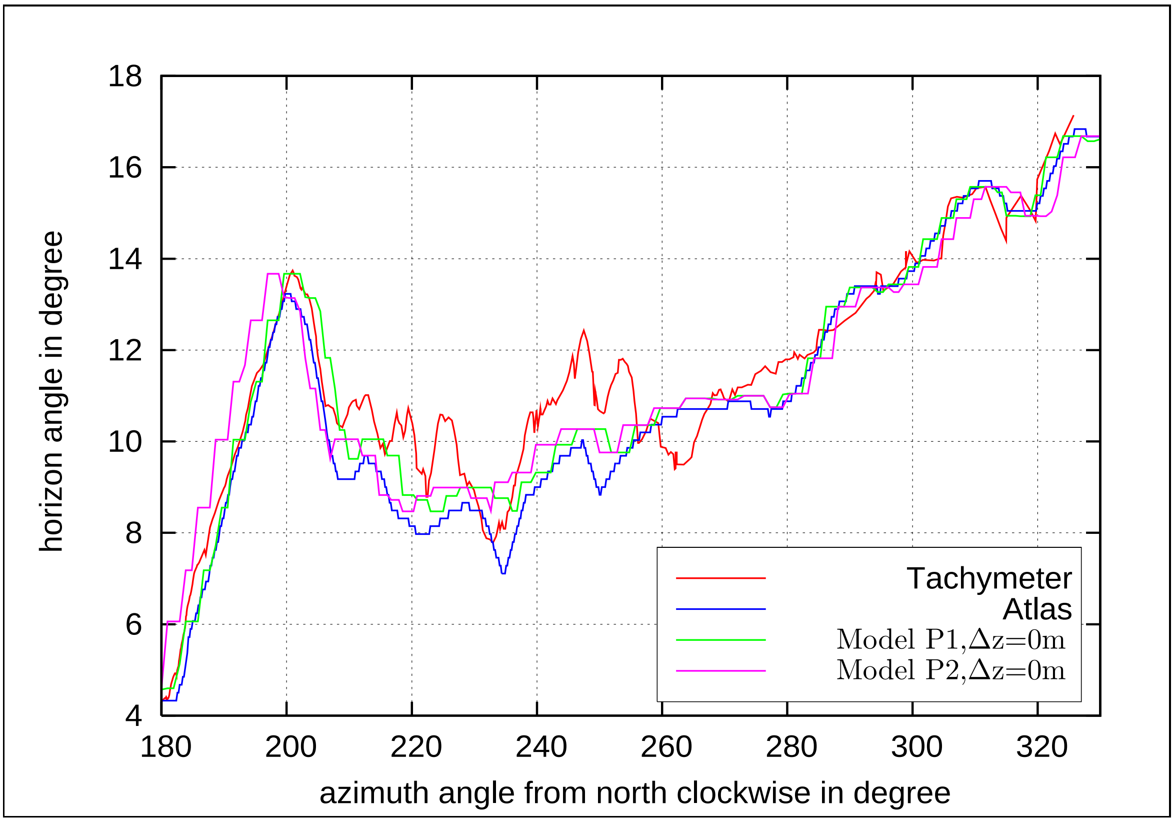

Figure 6.3: Horizon angles as a function of azimuth angles. The location of P1 is marked by the red circle and that of P2 by the blue circle in Fig. 6.4.

Figure 6.4: Picture of local shading within the Weissfluhjoch study site, taken in the morning in march (N. Helbig). Red circle (P1): Location of the SW radiation and horizon angle measurement point. Blue circle (P2): Location of the LW radiation measurement point.

A typical shading pattern for an early morning in march is shown in Fig. 6.4. Local differences within the Weissfluhjoch study site are clearly visible. The location of the SW radiation components and tachymeter measurement point on the long hut is indicated by the red circle and P1. The location of the LW radiation measurement point within the Weissfluhjoch study site is indicated by the blue circle and P2. This measurement point is about 50 m away from the long hut.

7 3D-model for incident broadband solar SW and LW radiation

Anisotropic terrain reflections / emissions are highly detailed implemented in the new radiation balance model. Therefore, it remains, before validating the terrain influence, to validate the spatial incident radiation components since those are used to compute the terrain (reflected) radiation.

7.1 SW surface radiation balance model

In this section modelled SW radiation components are compared to measurements at Weissfluhjoch study site. It was emphasised in Section 3, p.25 that the underlying theoretical expressions, the decomposition model and applied constant factors of the radiation balance model can lead to errors in the calculated spatial radiation values. This is more pronounced when atmospheric conditions deviate from dry and clean mountain air conditions on which the theoretical expressions given in Section 3.1.2, p.32 are based. An additional error appears when latitudes, longitudes and altitudes of the model domain deviate from those for which the decomposition model has been developed for (Section 3.1.3, p.37). Therefore, at first, SW radiation components obtained from different decomposition models are compared to measurements solely for two clear sky days, the 19 January 1999 and 20 April 2007. Those two days were chosen since they represent typical situations: a winter day and a spring day with a melting snow cover (ablation period). Both typical situations influence the albedo distribution (Eq. (5.4)) in the model domain and thus the incident radiation. The radiation components that are compared to measured values in this section are: incident global radiation S_g, direct radiation S_b, diffuse sky S_d and **total** diffuse radiation $S_\mathrm{d} + S_\mathrm{t}$ consisting of S_d and terrain reflected radiation S_t.

For both days meteorological input data, including measured global radiation, were obtained from a meteorological measurement station located at Weissfluhjoch at 2693 m a.s.l. The meteorological input data are hourly mean values, except for the measured global radiation values on 19 January 1999. On this day hourly global radiation for input is obtained from 10 minutes mean values at every clock hour. The high resolution of 10 minutes for the radiation input was used since it is assumed that taking averages over a small time interval at every clock hour matches best the sun position, which is calculated in the present model algorithm for each clock hour. The motion of the sun within one time step is not accounted for. Since the sun-or-shadow detection algorithm computes sun-or-shadow χ_sun at every clock hour, with the sun position calculated at exactly that clock hour, a small time interval around clock hour was assumed to best represent reality here. In contrast, on 20 April 2007 hourly mean values were chosen for the radiation input. This was done due to a more humid atmosphere on 20 April 2007. Note therefore, that on a cloudy day a larger time interval for radiation values averaging has to be chosen due to larger fluctuations of incident radiation.

All verification data was obtained from measurements at Weissfluhjoch study site at 2540 m a.s.l. The time resolution of measured radiation data was chosen according to the time resolution of the radiation input data for the modelling.
At first a homogeneous snow cover throughout the model domain was assumed for the modelling on 19 January 1999. The snow characteristics (Chapter 5, p. 79) were obtained from a snow profile on 14 January within the Weissfluhjoch study site and were used for all grid cells equally. By starting the simulation on 14 January an adapted more realistic spatial snow distribution and accordingly albedo distribution (Eq. (5.4)) was achieved accounting for terrain influences. For the modelling on 20 April 2007 the simulation was started on 1 October 2006 to obtain a realistic, inhomogeneous spatial snow and albedo distribution. All components were modelled for the virtual horizontal sensor plane in measurement height.

In Fig. 7.1 to Fig. 7.2 radiation components computed at the measurement point by the combined Reindl et al. (1990) model described in Section 3.1.3, p.37 (Eq. (3.42)) are compared to that computed with different decomposition models (Section 3.1.3, p.37) for 19 January 1999. Three models were evaluated: Erbs et al. (1982), Reindl et al. (1990) taking into account the clearness index M_t (Eq. (3.40)) and the solar zenith angle θ_z (Eq. (3.11)) (Reindl I) and Reindl et al. (1990) only taking into account M_t (Reindl II). The combined model of Reindl I and Reindl II is from now on called Reindl* (Eq. (3.42)).
In Fig. 7.1(a) the modelled diffuse sky radiation is shown. Additionally, measured total diffuse radiation and modelled terrain reflected radiation is depicted. The measured radiation was obtained using a Kipp&Zonen CM21 Pyranometer mounted on a sun tracker with a shading device for the sun. The terrain reflected radiation was modelled with Reindl*. As can be seen, all decomposition models generally overestimate the measured total diffuse radiation. A maximum amount of modelled terrain reflected radiation amount of about 16 Wm^{-2} at solar noon in Fig. 7.1(a) shows that terrain reflected radiation is not negligible. The overestimation of the modelled diffuse sky radiation emphasises the difficulties in decomposing a measured global radiation value with a decomposition model, especially if the model was not developed for the same range of altitudes and geographical coordinates. Additionally, the error will rise when the atmosphere is more humid or more polluted since no vertically layered atmosphere is considered in the computation of the spatial clear sky theoretical radiation components (Section 3.1.2, p.32). From Fig. 7.1(a) it can be seen that on 19 January 1999 the humidity has changed during the day since the measured values are not symmetric with respect to 12 UTC. The Reindl*-model shows an improvement compared to the Erbs et al. (1982)-model in the morning hours since it also depends on solar elevation.
In Fig. 7.1(b) the modelled and measured direct radiation is shown. Measured direct radiation was obtained using a Kipp&Zonen CH1 Pyrheliometer mounted on a sun tracker. Since all decomposition model examples generally overestimated the measured total diffuse radiation, measured direct radiation is underestimated. Direct radiation modelled with Reindl* approaches the measured values best at nearly all time steps. Diffuse sky radiation modelled with Reindl* is lower than with the Erbs et al. (1982)-model and direct radiation modelled with Reindl* is larger than with the Erbs et al. (1982)-model. Therefore, for that clear sky day at that specific location, the Reindl*-model approximates the measured curves best.
In Fig. 7.2 the modelled global radiation is shown. Additionally, the sum of individual measurements of total diffuse and direct radiation (cf. Fig. 7.1) is depicted. The sum of all incident SW radiation components demonstrates an overall good agreement with the sum of measured direct and total diffuse radiation. Slight overestimations of maximum 13 Wm^{-2} are observed at 11 to 14 UTC. At 15 UTC the measured global radiation is not overestimated

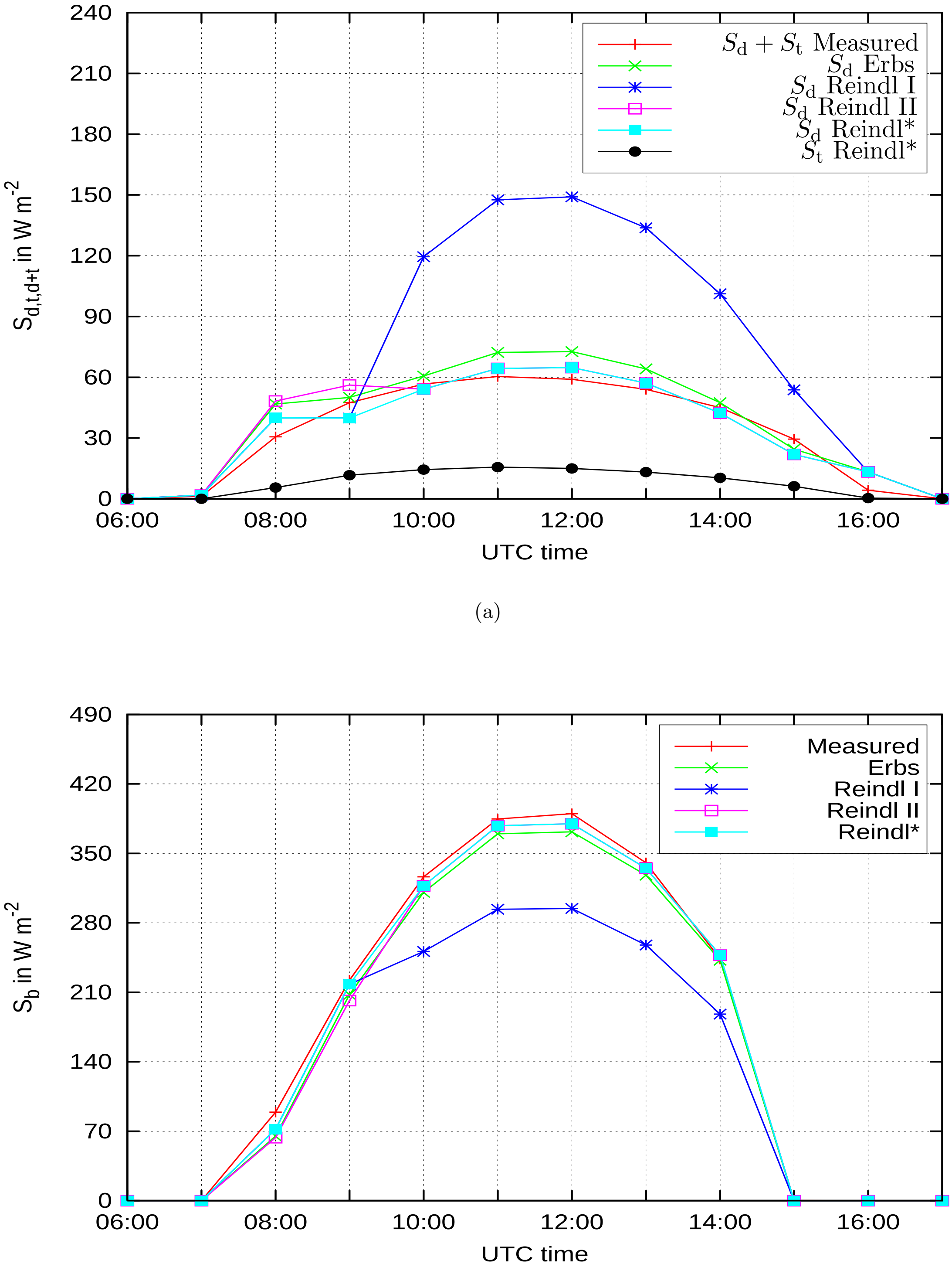

(a)

(b)

Figure 7.1: Comparison of measured and modelled radiation values on 19 January 1999 at Weissfluhjoch study site with (a) $S_\mathrm{d} + S_\mathrm{t}$, S_d, S_t and (b) S_b. The following decomposition models were used: Erbs et al. (1982), Reindl et al. (1990)'s $M_\mathrm{t}, \theta_\mathrm{z}$-model (Reindl I), Reindl et al. (1990)'s M_t-model (Reindl II) and the combined model cf. Eq. (3.42) (Reindl*).

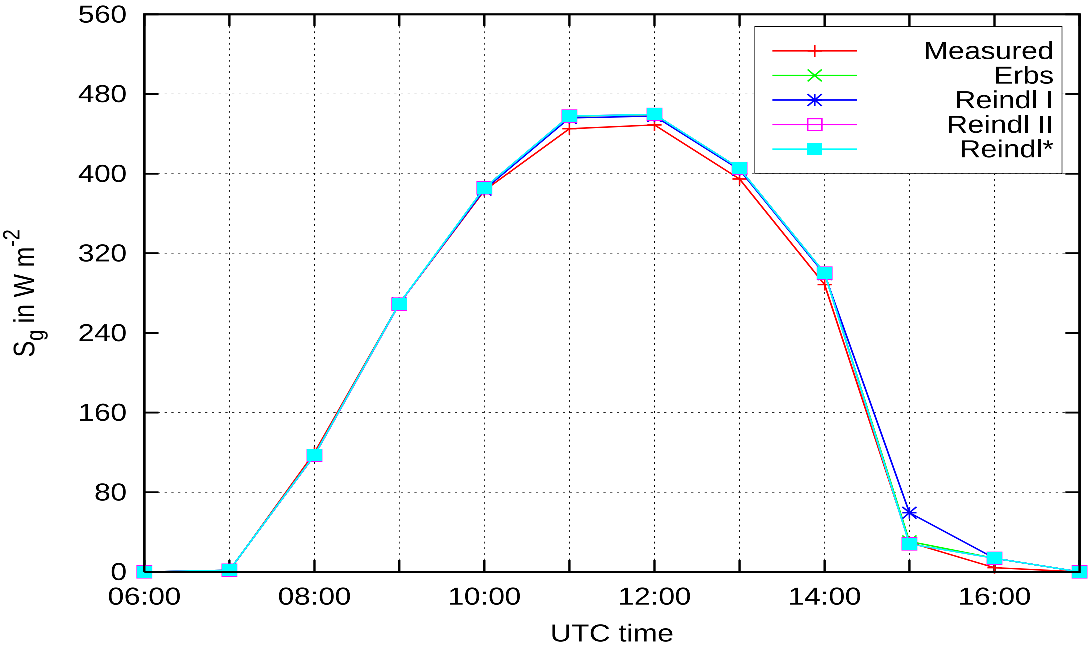

Figure 7.2: Comparison of measured and modelled global radiation values S_g on 19 January 1999 at Weissfluhjoch study site. The following decomposition models were used: Erbs et al. (1982), Reindl et al. (1990)'s M_t, θ_z-model (Reindl I), Reindl et al. (1990)'s M_t-model (Reindl II) and the combined model cf. Eq. (3.42) (Reindl*).

anymore. Therefore, it is unlikely that this error can be attributed to the terrain reflected radiation computation since then this error would arise at all time steps. This error is rather likely from measurement errors, errors due to the uncertain decomposition and/or the assumption of a vertically integrated atmosphere. All decomposition models exhibit similar global radiation trends except at 15 UTC when the global radiation values of the Reindl et al. (1990) model that takes into account clear sky index M_t and the solar elevation (dark blue line) is larger than the other models. This is due to the larger computed diffuse sky radiation (Fig. 7.1(a)).

The above analysis is now repeated with the same model set-up but for the 20 April 2007. Since the Erbs et al. (1982)-model and Reindl*-model showed the best correlation with measured radiation values for the 19 January 1999 (cf. Fig. 7.1 and Fig. 7.2) only these decomposition models are compared to measured values in the following analysis. Nevertheless, the uncertainty in determining the direct and diffuse sky radiation from one measured global radiation value by means of decomposition models is pointed out in Fig. 7.3 and Fig. 7.4.
As can be seen in Fig. 7.3(a), the diffuse sky radiation from both decomposition models again overestimates the measured total diffuse radiation. The diffuse sky radiation obtained from the Erbs et al. (1982)-model overestimates the diffuse sky radiation obtained from the Reindl*-model by a maximum of about 15 Wm^{-2}. Terrain reflected radiation is modelled with the Reindl*-model. Note that, although on 20 April 2007 terrain reflected radiation values are larger than on 19 January 1999 (cf. Fig. 7.1(a)), the fraction of incident S_t compared to incident global radiation S_g is lower for the 20 April than for the 19 January. This is likely

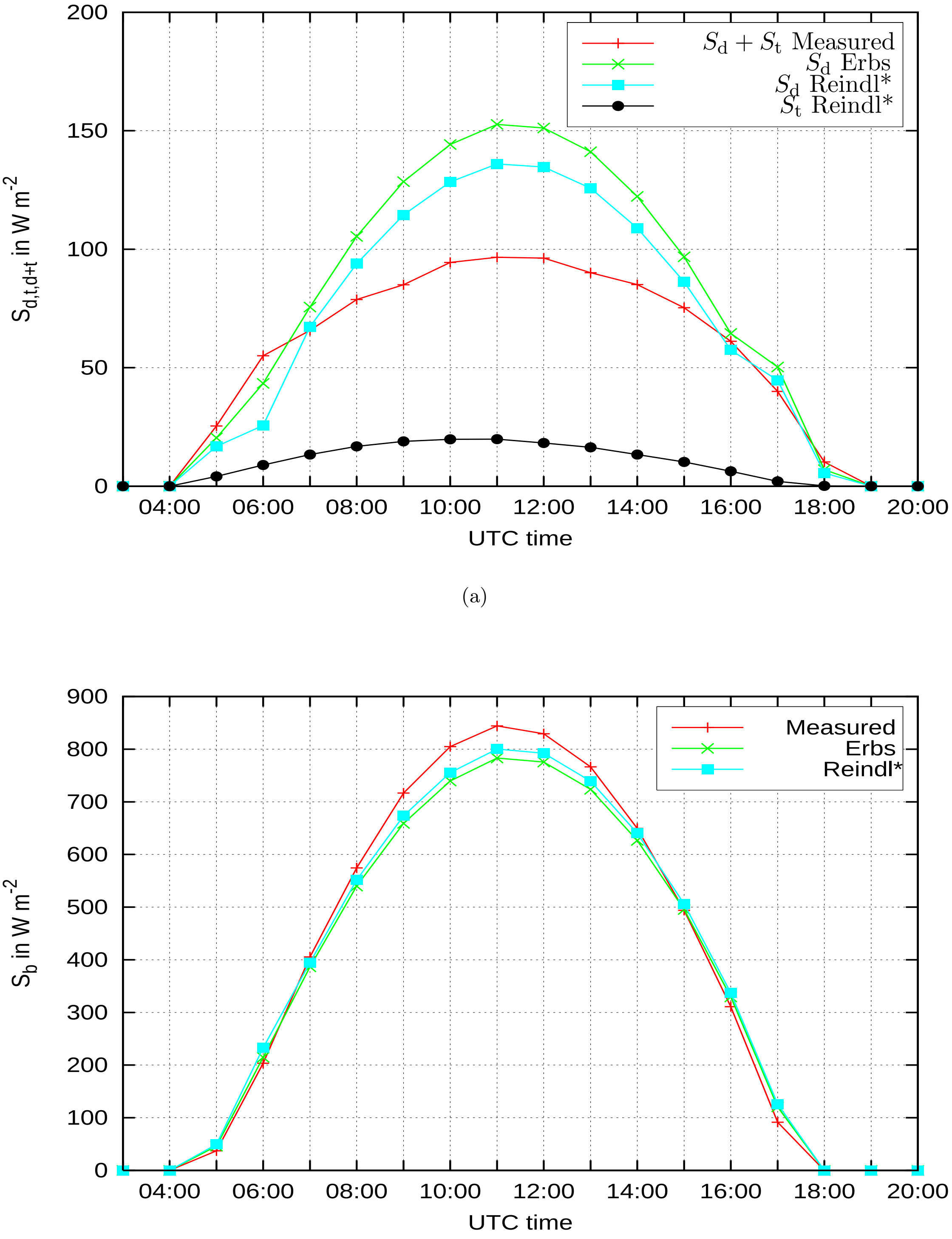

(a)

(b)

Figure 7.3: Comparison of measured and modelled SW radiation values on 20 April 2007 at Weissfluhjoch study site with (a) $S_d + S_t$, S_d, S_t and (b) S_b. The following decomposition models were used: Erbs et al. (1982), Reindl et al. (1990)'s M_t, θ_z-model (Reindl I), Reindl et al. (1990)'s M_t-model (Reindl II) and the combined model cf. Eq. (3.42) (Reindl*).

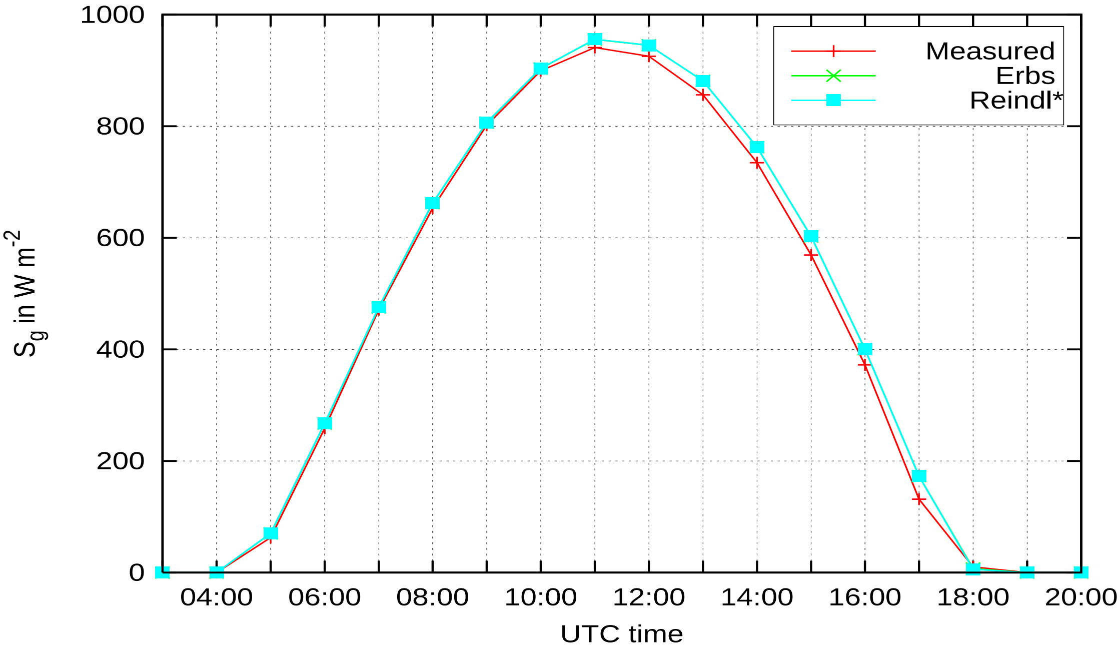

Figure 7.4: Comparison of measured and modelled global radiation values S_g on 20 April 2007 at Weissfluhjoch study site. The following decomposition models were used: Erbs et al. (1982), Reindl et al. (1990)'s $M_\mathrm{t}, \theta_\mathrm{z}$-model (Reindl I), Reindl et al. (1990)'s M_t-model (Reindl II) and the combined model cf. Eq. (3.42) (Reindl*).

due to the higher solar elevation angle on 20 April compared to 19 January that resulted in overall larger incident direct radiation values as well as in lower surface albedo values on the spring day.
As can be seen in Fig. 7.1(b), the measured direct radiation is again underestimated by both decomposition models. Additionally, the Erbs et al. (1982)-model underestimates the direct radiation obtained from the Reindl*-model by a maximum of 20 Wm^{-2}.
In Fig. 7.4 it can be seen that again all modelled global radiation values are in good agreement with measured values for most of the time steps. Larger deviations of about 20 Wm^{-2} appear from midday on that might be explained similarly as for Fig. 7.2.

Since the Reindl*-model (combined Reindl et al. (1990)-model, cf. Eq. (3.42)) showed the best agreement of the individual radiation components with measurements and because of its additional dependency on solar elevation the Reindl*-model was implemented in the radiation balance model. Recall that it is not sufficient to obtain a good agreement with measured global radiation values since individual radiation components are required at each patch to estimate the actual incident radiation in complex terrain (including visible sky fraction and shading). Of course, even with the Reindl*-model, the overall uncertainty due to the lack of portability of the decomposition models remains. Note that in the following all quantitative analysis of SW radiation data have this problem of uncertainty. However, no reliable decomposition model for the Eastern Swiss Alps was found in literature.

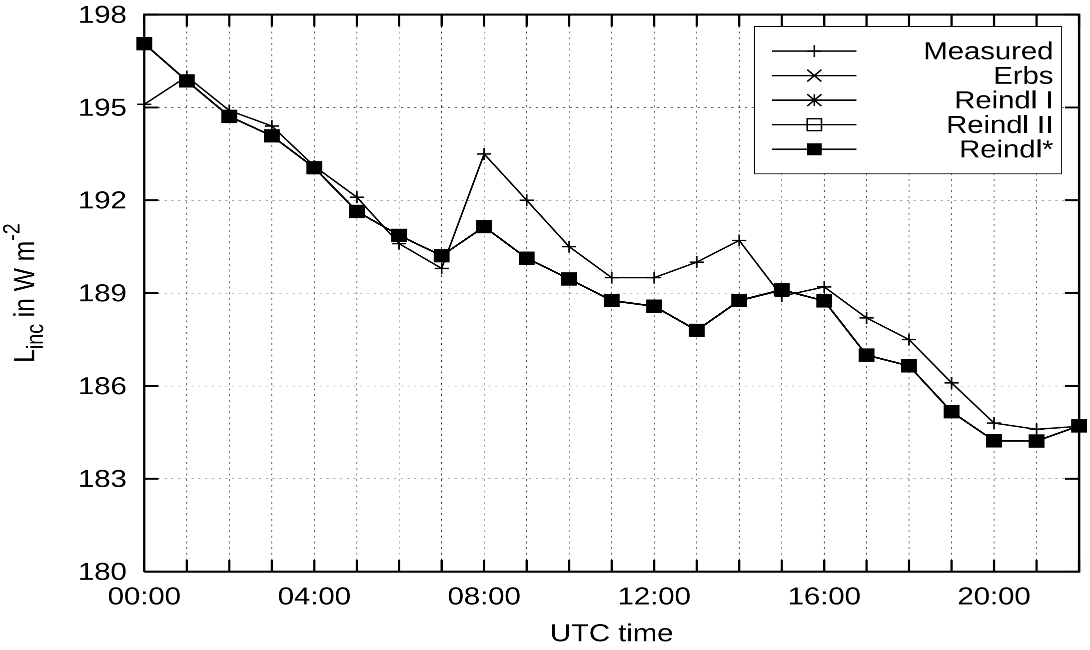

Figure 7.5: Comparison of measured and modelled incident LW radiation values L_{inc} on 19 January 1999 at Weissfluhjoch study site. The following decomposition models were used: Erbs et al. (1982), Reindl et al. (1990)'s $M_{\mathrm{t}}, \theta_{\mathrm{z}}$-model (Reindl I), Reindl et al. (1990)'s M_{t}-model (Reindl II) and the combined model cf. Eq. (3.42) (Reindl*). All modelled curves lie on top of each other.

7.2 LW surface radiation balance model

In this section, for completeness, the influence of the varying SW radiation distribution obtained from different decomposition models on modelled incident LW radiation L_{inc} is briefly investigated. This is analysed since a different albedo and surface temperature distribution and thus terrain emission is possibly obtained with different SW radiation input into the surface. For this investigation the incident LW radiation L_{inc} values with the decomposition models given for the SW radiation verification in the last section are compared to measurements at Weissfluhjoch study site. Only one of the two clear sky days chosen in the last section, the 19 January 1999, was selected for this evaluation. Note that an additional comparison is made for a "summer day" with a more humid atmosphere. This is presented in Section 9.5, p.139 together with an investigation of different terrain emission parameterisations. In this section however, the influence of different decomposition models on computed LW radiation is outlined.

The model set-up was chosen equivalent to the one presented in Section 7.1, p.95 for 19 January 1999. The location of the point for which the comparison of modelled LW radiation values and LW measurements is conducted is however differing from the one for SW radiation comparison. A different virtual plane was therefore introduced at Swiss National Coordinates: East: 780859, North: 189222 and a total DHM height of 2540 m (with a virtual plane height of 4.51 m). Even though both instrument sites are only about 50 m apart they have different sun-or-shadow values depending on the sun elevation angle (cf. Fig. 6.4). Both measurement points also have slightly different terrain view factor sums: The LW radiation measurement instruments see about 3.5 % terrain whereas the SW radiation measurement instruments see about 3.0 % terrain. This difference leads to differing incident terrain reflected and emitted radiation. Both the differing sun-or-shadow values and the differing visible terrain fractions emphasise the importance to consider for the exact position of a measurement site within a model domain if such comparisons are attempted.

In Fig. 7.5 the modelled LW radiation L_{inc} is shown. All curves of incident LW radiation L_{inc} with different SW decomposition models lie on top of each other. Measured LW radiation that includes LW terrain emission L_{t} of the same day was obtained from a Eppley Precision Infrared Radiometer (PIR) with a shading device for the sun at midday mounted in about 4.50 m above the ground. Apparently, the changing SW radiation distribution due to the different decomposition models does only lead to minimal varying values for incident LW radiation. As noted above, the minimum LW radiation differences with the different decomposition models result from varying terrain emissions due to the varying surface temperatures. Note that LW sky radiation L_{a} (Eq. (3.51)) does not depend on the SW decomposition model since it is solely obtained from the sky view factor, together with the exposed measured incident LW radiation $L_{\mathrm{a}}^{\mathrm{meas}}$ or cloud cover observation n_{c} and from a spatially interpolated air temperature T_{a}. Recall that air temperature T_{a} is only varying with DHM heights z (Eq. (5.1)) in the model system Alpine3D (Section 5.2, p.79). Thus, considering only the modelled incident LW radiation, no statement is possible which decomposition model captures the measured L_{inc} best. Nevertheless, a general good agreement between the modelled and measured incident radiation is obtained for 19 January 1999. A maximum deviation of 2.5 Wm^{-2} arises.

In Fig. 7.6(a) modelled LW sky radiation L_{a} is shown together with measured incident LW radiation L_{inc}. As pointed out above, no difference in LW sky radiation can occur by using different decomposition models for the SW radiation computation.
In Fig. 7.6(b) modelled LW terrain emission L_{t} is shown. Minimal deviations arise in modelled LW terrain emissions with different SW decomposition models which rarely be seen in Fig. 7.6(b). But note that for that specific day, if LW terrain emissions are neglected within the model, a LW radiation error between measured and modelled incident LW radiation results in a maximum of 10.7 Wm^{-2}.

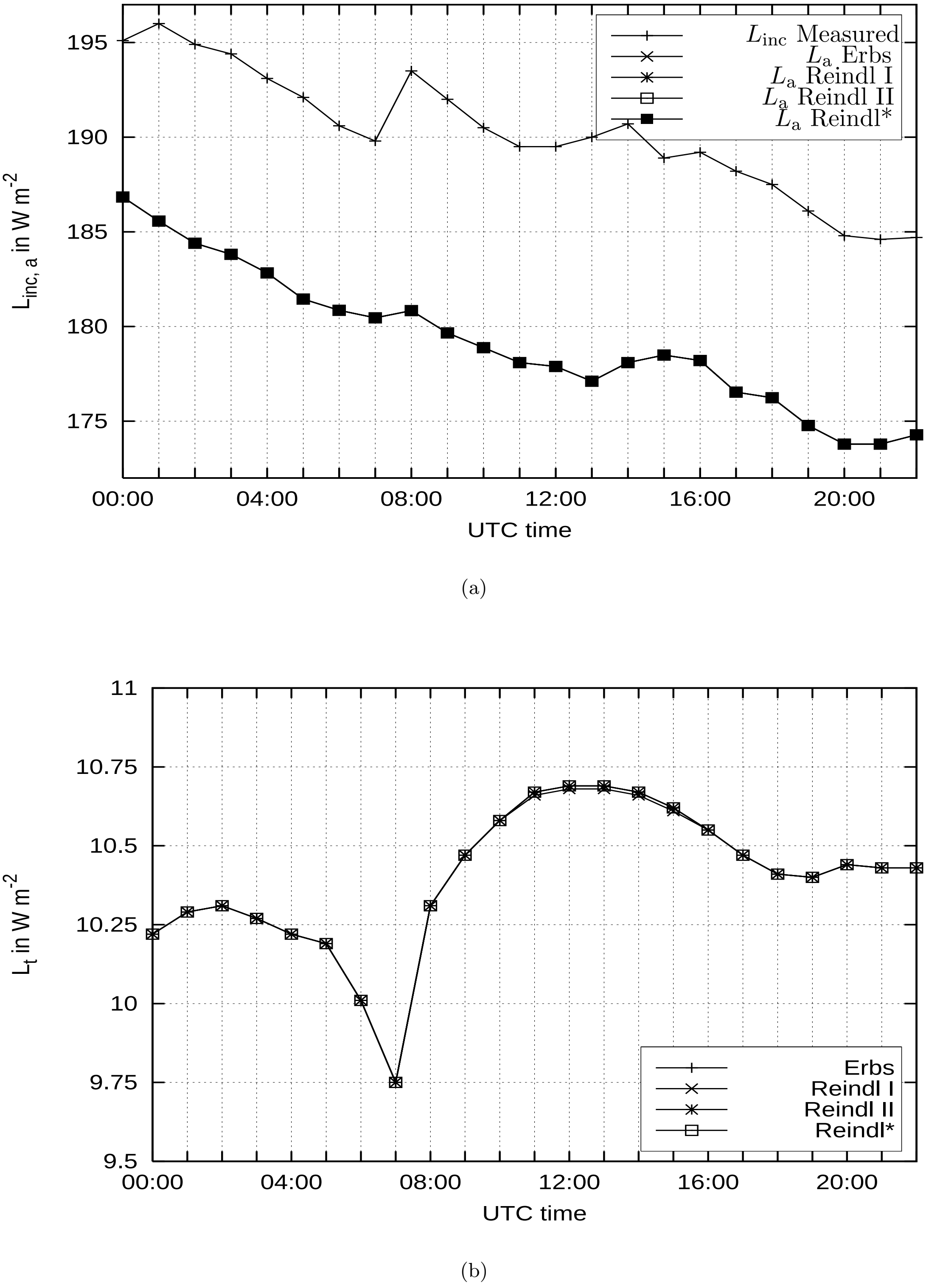

Figure 7.6: Comparison of measured and modelled LW radiation values on 19 January 1999 at Weissfluhjoch study site with (a) L_{inc}, L_{a} and (b) L_{t}. The following decomposition models were used: Erbs et al. (1982), Reindl et al. (1990)'s $M_{\mathrm{t}}, \theta_{\mathrm{z}}$-model (Reindl I), Reindl et al. (1990)'s M_{t}-model (Reindl II) and the combined model cf. Eq. (3.42) (Reindl*). All modelled curves lie on top of each other.

8 3D-model for broadband SW terrain reflections

It was pointed out in the previous chapter that the computation of spatial radiation values in complex terrain under cloudy skies by means of one exposed global radiation value is leading to errors that are difficult to classify. The assumption of a vertically integrated atmosphere in the modelled diffuse sky and direct radiation under clear sky contributes to these errors. Thus, it is difficult to verify if an additional amount of incident reflected radiation in complex terrain is modelled correctly whether solely measured global radiation or total diffuse radiation values are available. Measured relative values of terrain reflected radiation therefore lead to a first verification of modelled terrain reflected radiation.
In this chapter measured relative values of terrain reflected radiation on two days at the Weissfluhjoch study site are presented. Due to the restricted development of the radiation balance model in the sense of complexity a comparison between the modelled radiation components with the radiosity approach using anisotropic view factors and more simplified as well as more complex models is presented in this chapter. On the one hand, the radiosity model is compared to modelled values using isotropic view factors (isotropic view factor approach) and on the other hand to modelled values with the Monte Carlo (MC) model MYSTIC.

8.1 Measurement of SW terrain reflected radiation

A thorough validation of the modelled reflected radiation from the surrounding terrain would require a measurement device which is capable of i) masking the solid angle of the pyranometer hemisphere which is exposed to the sky and ii) which is separating radiation originating from the terrain from that originating from the intermediate atmosphere. However, no such measurements have been reported in literature yet. Since ii) poses, if even feasible, a major technical challenge in order to separate both components (maybe from different polarisation characteristics of both radiation components) a simpler experimental set-up is proposed in the following which tries to meet i) as close as possible.

By constructing a removable cardboard horizon around a CM21 pyranometer (PMOD/WRC (WWW)) (Fig. 8.1 and Fig. 8.2(a)) relative values of terrain reflected radiation were measured at the Weissfluhjoch study site. The horizon line of the cardboard horizon was extracted from a panorama picture produced with "Atlas der Schweiz" (AdS2 (WWW)) which is based on the 25 m DHM of Swisstopo (WWW). The instrument was mounted on a tripod beside the permanent measurement instruments on the roof of the long hut at the Weissfluhjoch study site (cf. red circle (P1) in Fig. 6.4). Permanent measurements on the roof include total diffuse radiation ($S_\mathrm{d} + S_\mathrm{t}$) (CM21 with shading disk on a tracker) and direct radiation S_b (CH1) from PMOD/WRC (WWW) (Fig. 8.2(b)). Masking and unmasking the terrain in 14 minutes intervals obtained terrain reflected radiation values. Thereby, a measurement was conducted every second and was averaged over two minutes. Only six values from 12

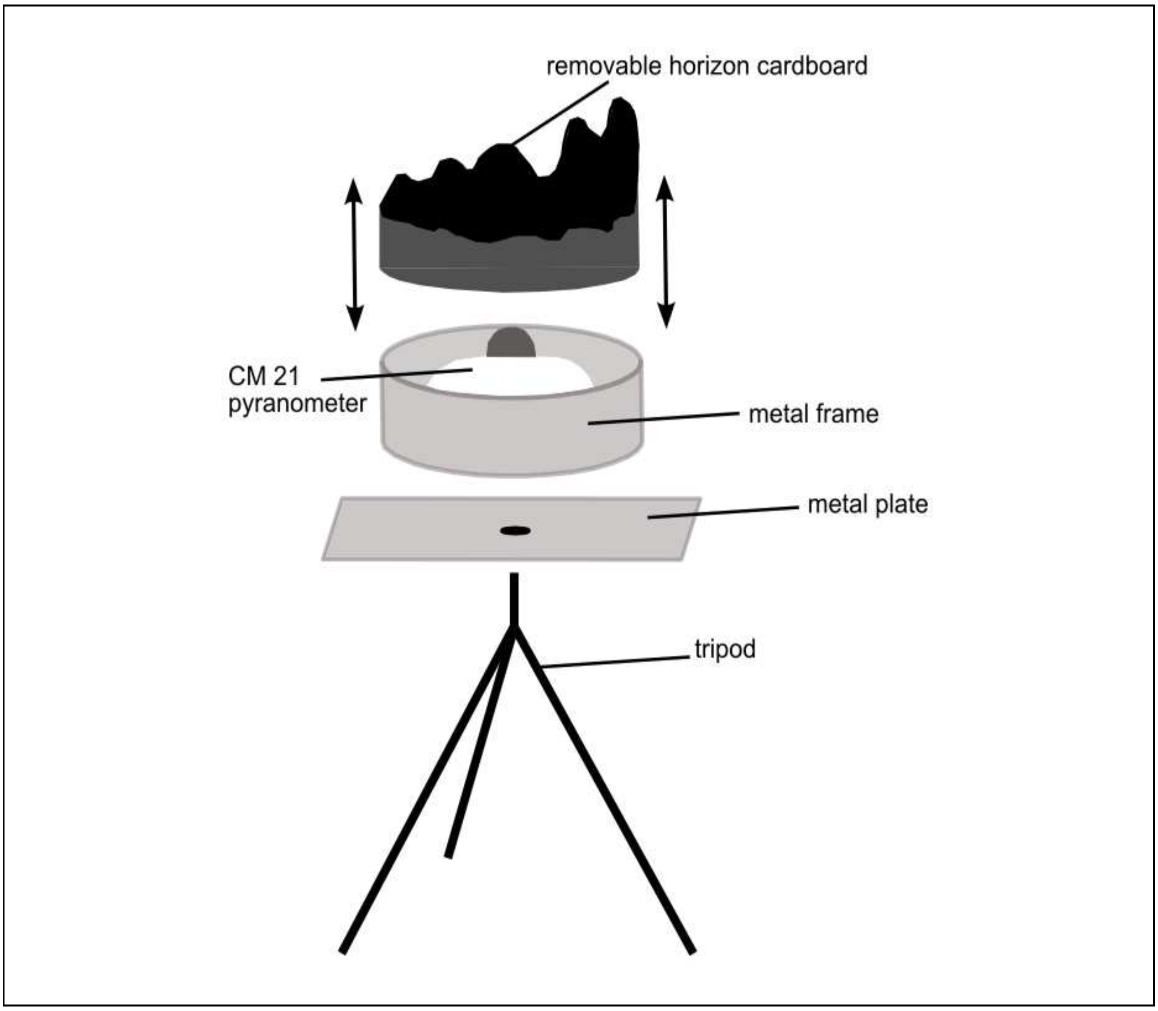

Figure 8.1: Schematic of the removable horizon device around a pyranometer for measuring relative values of terrain reflected radiation S_{t} including a black cardboard horizon, a metal frame and plate, a CM21 pyranometer and a tripod.

minutes intervals could be used for comparisons with modelled radiation values since after 12 minutes the removable cardboard horizon had to be mounted or unmounted on the device.

For comparison two days with approximately the same sun position and similar atmosphere composition (clear sky day) were selected. One was with snow cover and the other without snow cover in the surroundings. The first measurement day, on 20 April 2007, was a nearly perfect clear sky day. The snow cover was not completely homogeneous in the surroundings as can be seen from Fig. 8.3. Especially the closer west-facing slope was not completely covered by snow any more. In addition, the top of the ridges of the slopes around the Weissfluhjoch study site are steep, bare rocks which are rarely covered by snow. However, in the model they were always covered by snow leading to differences with regards to the albedos. The second measurement day should be on 22 August given a similar sun position and a hopefully similar atmosphere would allow to exclusively studying the influence of albedo. But the requirement of clear sky and snow free conditions made it impossible to measure before 24 September 2007. On 24 September 2007, in the east-facing slope some snow patches were still present

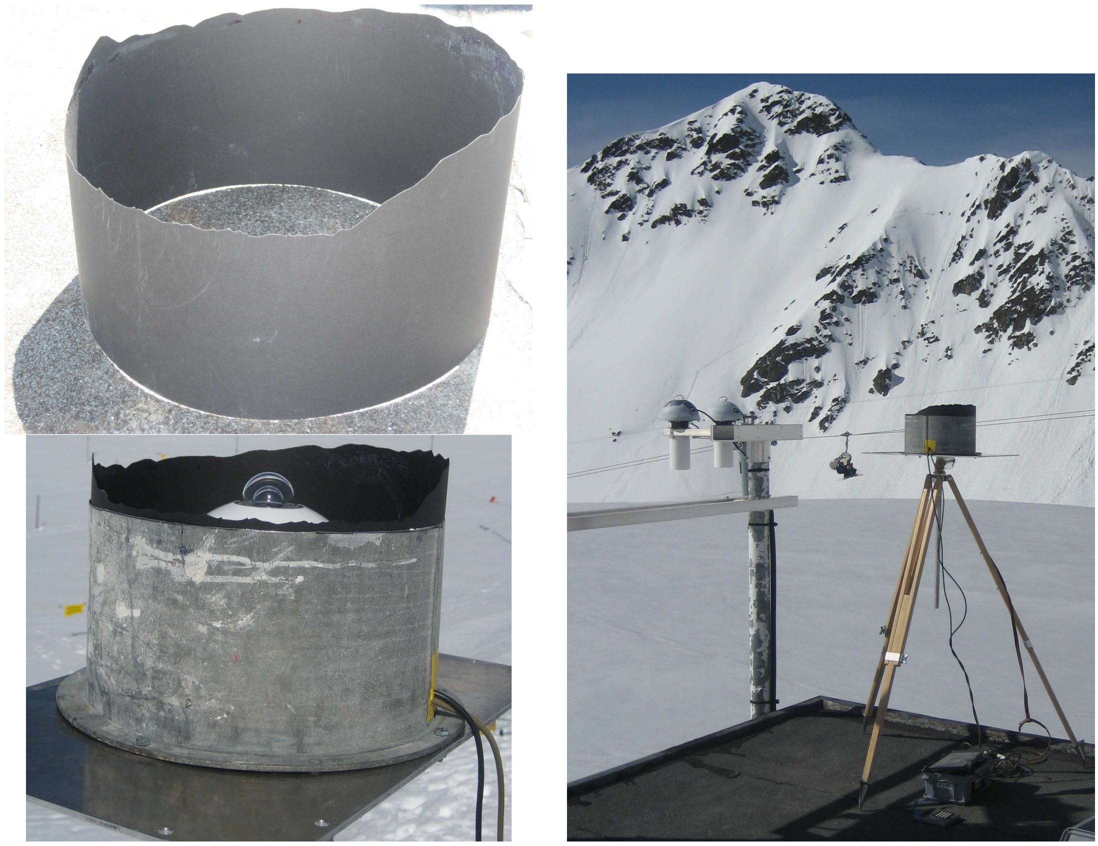
(a) (b)

Figure 8.2: A CM21 pyranometer was used to measure relative values of terrain reflected radiation: (a) Removable horizon cardboard, (b) CM21 with cardboard horizon mounted on a tripod next to the permanent measurement instruments at Weissfluhjoch study site.

from a last snow fall event several days before (Fig. 8.4(a)). But since the most influencing slope for the measurement is the west-facing slope (Fig. 8.4(b)) the snow was considered to be negligible. Therefore, the two measurement days will only provide qualitative information about the influence of large surface albedos stemming from the presence or absence of snow.

In Fig. 8.5(a) two minute raw measurements are shown for the first measurement day on 20 April whereas in Fig. 8.5(b) two minute raw measurements are shown for the second measurement day on 24 September. Global radiation measurements are compared without the influence of terrain (horizon is masked) to global radiation measurements with the influence of terrain (no horizon masking) and to the sum of the direct and total diffuse radiation measurements of the permanent PMOD/WRC (WWW) instruments (for a description cf. Section 7.1, p.95).
As a result, the influence of the terrain radiation is clearly visible, at least on 20 April. The maximum difference between measuring with and without influence of terrain is leading to


(a) (b)

Figure 8.3: Pictures of the snow cover on 20 April 2007 at Weissfluhjoch study site (N. Helbig): (a) The east-facing slope, (b) West facing, more influencing slope.

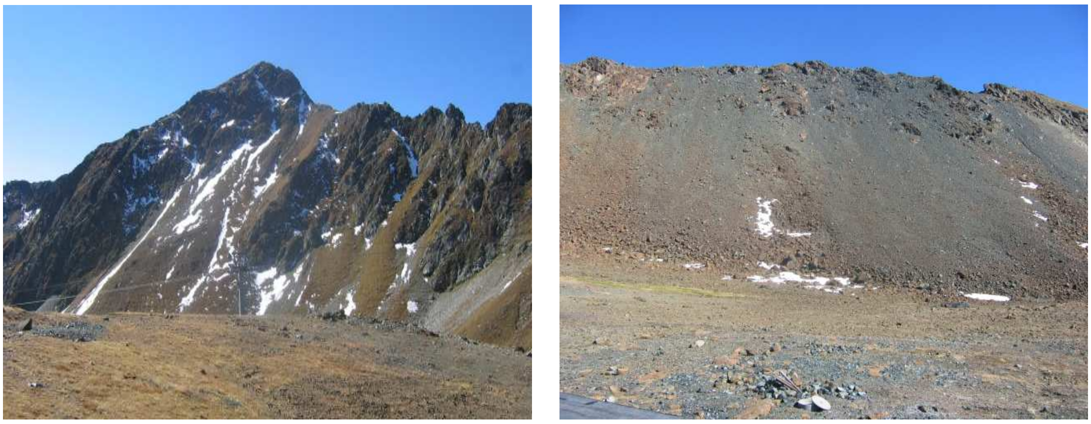
(a) (b)

Figure 8.4: Pictures of the snow patches on 24 September 2007 at Weissfluhjoch study site (N. Helbig): (a) East facing slope, (b) West facing, more influencing slope.

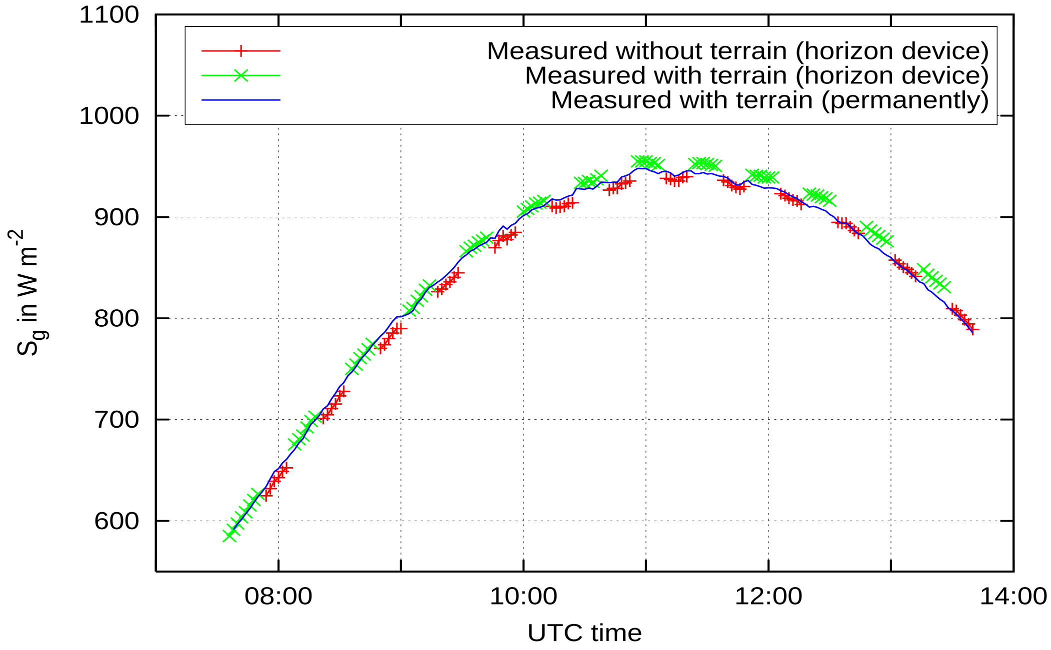

(a)

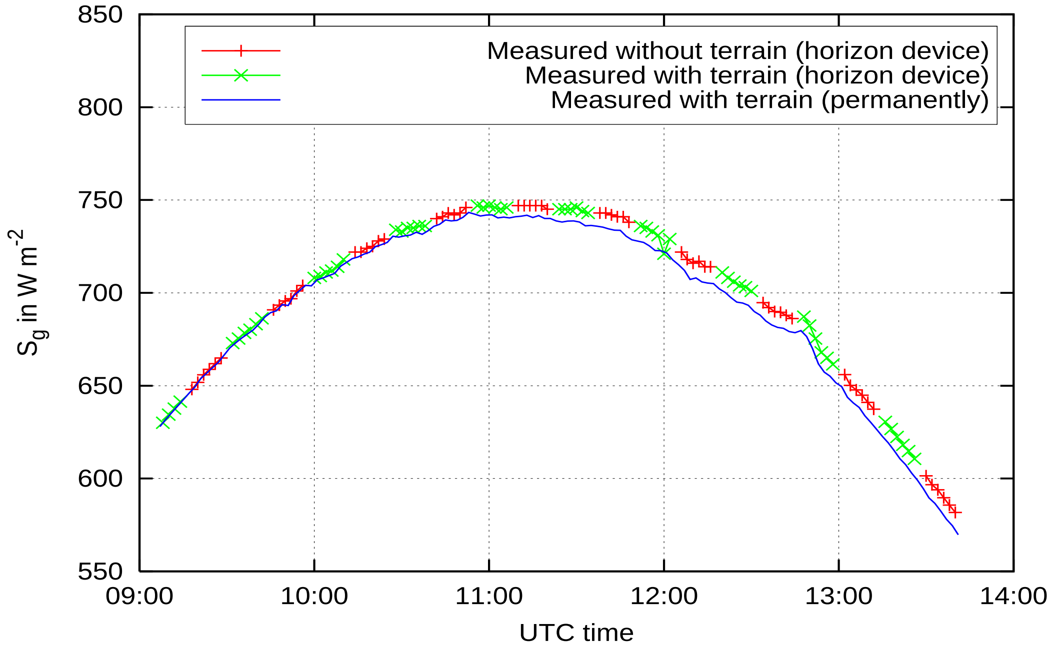

(b)

Figure 8.5: Comparison of S_g measurements at Weissfluhjoch study site: S_g measured masked (without terrain), S_g measured unmasked (with terrain) and sum of direct and total diffuse radiation measurements of the permanent PMOD/WRC (WWW) instruments: (a) 20 April, (b) 24 September.

relative values of terrain reflected radiation of about 19 Wm^{-2}. These relative values of terrain reflected radiation are in the same order of magnitude as the modelled terrain reflected radiation for 19 January (Fig. 7.1(a)). In contrast, only little radiation value differences were observed between the masked and the unmasked measurements for the second measurement day on 24 September. This was expected since lower surface albedos in the absence of snow (e.g. granite 0.12-0.18 (Stull (2000))) and bare soil (0.05 dark wet, 0.4 light dry (Oke (1987))) lead to less terrain reflected radiation. Nevertheless, after solar noon some minor differences between masked and unmasked measurements are observed. It is however unclear whether these originate from terrain reflections from the west-facing slope or whether these are caused by atmospheric disturbances (i.e. increased air humidity or small clouds) since very small altocumulus clouds appeared around 12 UTC even though they did not hide the sun once. Note therefore, that the continuous offset between the masked and unmasked measurement found on 20 April, with the larger albedo values in the surroundings of the measurement site, highlights that terrain is playing an important role. It is stressed that this is even noticeable with such a small terrain view factor of sum of 3 % at the measurement point.

As an additional quantitative cross-check, the masked and unmasked measurements are compared to the sum of the permanent measurements of direct and total diffuse radiation of the PMOD/WRC (WWW) instruments aside (cf. Fig. 8.5). On 20 April the global radiation values capture the influence of terrain before solar noon, lie in between at solar noon and do not capture the influence of terrain after solar noon. A similar trend was observed on 24 September: Before solar noon, the permanent measurements coincide well with the mobile instrument. However, after solar noon the values of the permanent instrument are consistently lower. Therefore, a systematic error is assumed to be inherent in the permanent measurements rather than that a terrain influence is falsely captured by the mobile instrument. Unfortunately, it is also difficult to verify whether the terrain view factor sum replaced by sky (no visible terrain) would lead to larger or lower global radiation. For this evaluation both measurements with its different measurement accuracies would have to be compounded, i.e. the global radiation without the influence of terrain could be increased by the diffuse sky radiation multiplied by the visible terrain fraction $S_{\mathrm{g}}^{\mathrm{masked}} + \sum_{J=0}^{N-1} F_J (S_{\mathrm{g}}^{\mathrm{masked}} - S_{\mathrm{b}}^{\mathrm{PMOD}})$. Consequently, no direct comparison was possible between the permanent measurements and the mobile global radiation measurements with or without accounting for the terrain.

At the end of this section a brief review of possible sources of errors is nevertheless given since some reasons are possible for the discrepancies between the permanent measurements of the PMOD/WRC (WWW) and the mobile measurements. First, the permanent PMOD/WRC (WWW) instruments were both calibrated 1999 whereas the mobile CM21 was calibrated in 2002. Second, the measurement accuracy for a CM21 pyranometer is ±2%, for a CH1 pyrheliometer ±10%. Third, the instruments could not be mounted exactly next to each other; they were mounted approximately three meters apart. Fourth, the build-up on the tripod, the masking and unmasking process and the horizon device itself will have introduced errors.

8.2 Comparison of measurements with radiosity approach model

In this section modelled global radiation values, with and without terrain influence, on 20 April and 24 September 2007 are validated by comparison with measured global radiation values, with and without terrain influence, at Weissfluhjoch study site. Terrain reflected radiation was modelled with the radiosity approach using anisotropic view factors.

For both days the required meteorological input data were obtained from the meteorological measurement station located at Weissfluhjoch at 2693 m a.s.l. as described for the model set-up in Chapter 7, p.95). The meteorological input data are hourly mean values. The simulation was started in October 2006 to obtain an approximately realistic spatial snow cover as well as albedo distribution taking into account terrain influences.

In Fig. 8.6, the two minutes raw measurements of global radiation, with and without terrain influence, are shown. In addition, the modelled hourly global radiation values are presented. Note that in fact only the colour crosses represent a modelled hourly value. However, the lines may be regarded as a reasonable interpolation.
For 20 April 2007 two methods of time averaging of global radiation input values were tested. First, hourly mean values at every clock hour as applied for the other meteorological inputs were used. Second, 10 minutes mean radiation values at every clock hour were tested as input values. It was found that both modelled values agree very well with the measurements for both average intervals. Only a small time shift is visible if 10 minutes mean values at every clock hour are applied as input values. Nevertheless, the sensitivity of modelled radiation data to the time averaging of radiation input data is briefly pointed out here. On the one hand, it can be assumed that hourly mean radiation input values represent the radiation input best since radiation value fluctuations, due to e.g. cloud cover or changing atmospheric humidity, are averaged out. On the other hand, it was noted before that the position of the sun is computed only once at every clock hour. The sun-or-shadow algorithm does not integrate the radiation under changing sun positions within an hourly interval. Therefore, the model computes a snapshot of the position of the sun and its emitted radiation at that specific point in time. In general, this snapshot of the position of the sun is best described by using the smallest time interval of radiation around every clock hour. In the following, hourly radiation input values were used for modelling since hourly time resolution approaches the measured radiation values closest on the two measurement days. In Fig. 8.6(a) the hourly global radiation, computed from hourly mean radiation values at every clock hour are presented for the first measurement day on 20 April 2007. The relative differences of measured terrain reflected radiation values and modelled terrain reflected radiation values are captured very well. The maximum of the measured terrain reflected radiation S_t of about 19 Wm^{-2} at 11 UTC is modelled exactly. The differences at the other time steps likely come from errors in the measurement set-up, variations due to the chosen time average interval of radiation values and due to the fact that two minutes raw measurements are compared to hourly modelled values.
For 24 September 2007 two different mean rock albedo values were tested, since a large range of mean rock albedos can be found in the literature. First, a mean bare rock albedo α of 0.28 (Gruber et al. (2004)) was used and second, a mean bare rock albedo α of 0.15 (Stocker-Mittaz et al. (2002)). Note, that in the surroundings of the Weissfluhjoch study site bare rock is the dominant land use class, other land use classes in the model domain are bare soil, subalpine meadow and urban area which have differing albedo values. Naturally, a larger amount of terrain reflected radiation was modelled with the higher bare rock albedo of 0.28. It was found that the mean bare rock value of 0.15 led to a better agreement with the measurements thus this value is used in the presented modelling. In Fig. 8.6(b) the hourly global radiation, computed from hourly mean radiation values at every clock hour is presented for the second measurement day on 24 September 2007. A mean bare rock albedo α

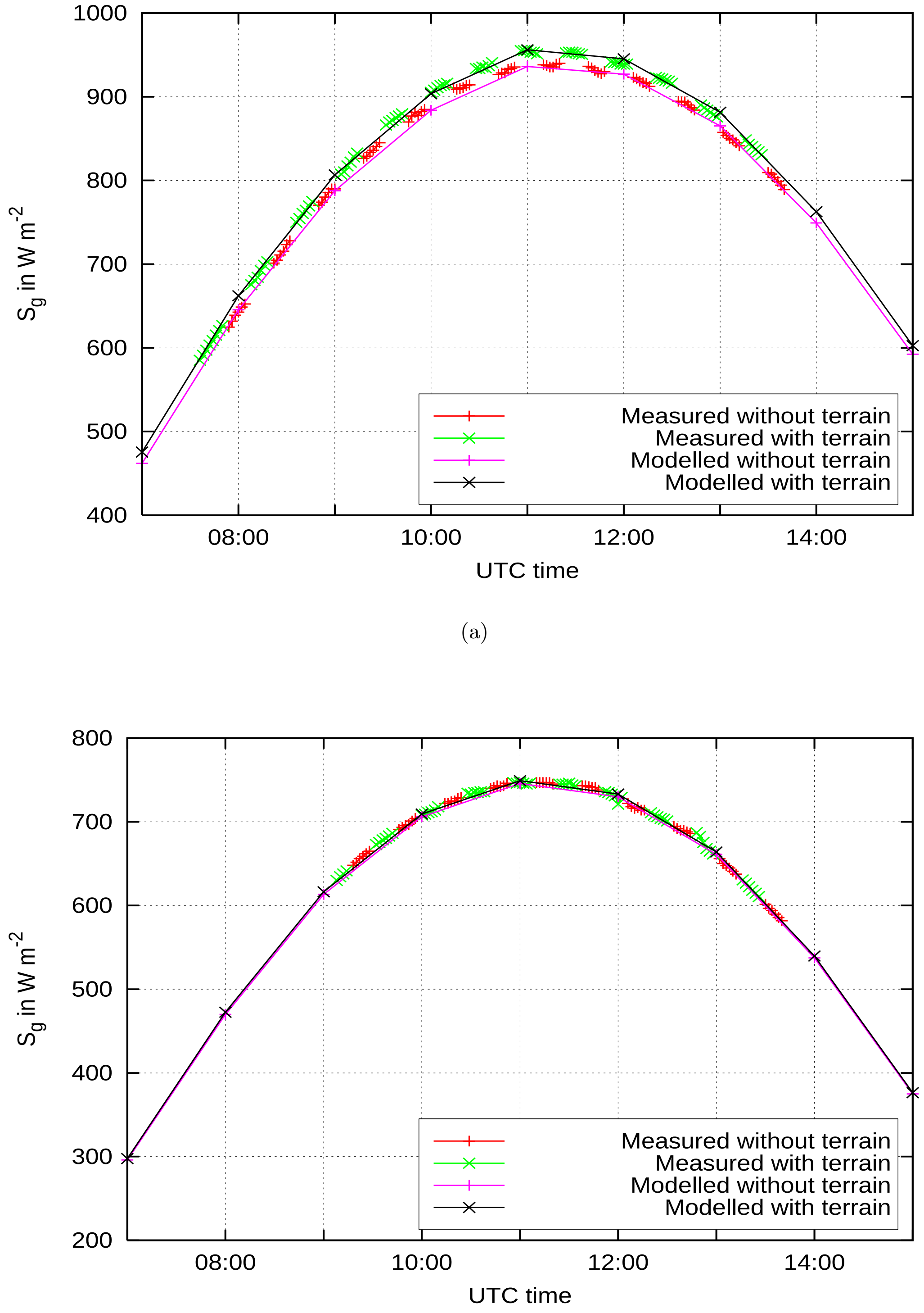

(a)

(b)

Figure 8.6: Comparison of S_g measurements to modelled values at Weissfluhjoch study site with S_g measured and modelled masked (without terrain) and unmasked (with terrain) with hourly radiation computed from hourly mean values at every clock hour: (a) 20 April 2007, (b) 24 September 2007.

of 0.15 was used. As can be seen, a mean rock albedo of 0.15 leads to a good agreement with hourly measurement values with a maximum of 3 Wm^{-2} reflected radiation. The small values show that the modelled values are almost within the accuracy of the measurement device.

It was shown that for this specific surface patch measured terrain reflected radiation is captured very well by the radiosity approach for a representative winter day with large mean surface albedos and for a summer day with low mean surface albedos.

8.3 Comparison of measurements with isotropic view factor approach model

In this section the comparison between the radiosity model using anisotropic view factors and the more simplified isotropic view factor approach is presented. This interesting investigation to determine how measured terrain reflected radiation compares with modelled radiation with the isotropic view factor approach is conducted to outline the main involved problems in estimating terrain reflected radiation from isotropic view factors. The comparison is conducted for the first measurement day on 20 April 2007.

As stated earlier, the terrain reflected radiation S_t is often estimated as an isotropic contribution determined by the terrain view factor sum at each patch $1 - F_{\mathrm{sky},I}$. The terrain view factor can be multiplied by the reflected sum of direct radiation S_b and diffuse sky radiation S_d of the same patch (e.g. Müller and Scherer (2005))

$$S_{\mathrm{t},I}^{\mathrm{l\_iso}} = (1 - F_{\mathrm{sky},I})\,\alpha_I\,(S_{\mathrm{b},I} + S_{\mathrm{d},I}) \, , \tag{8.1}$$

by the local sum of direct radiation S_b and diffuse sky radiation S_d of the horizontal surface value of the central point in the model domain (Senkova et al. (2007)) or by the mean global radiation value of the whole model domain

$$S_{\mathrm{t},I}^{\mathrm{m\_iso}} = (1 - F_{\mathrm{sky},I})\,\frac{1}{N}\sum_{J=0}^{N-1}\alpha_J\,(S_{\mathrm{b},J} + S_{\mathrm{d},J}) \, . \tag{8.2}$$

In the following, global radiation values including terrain reflected radiation obtained from both isotropic view factor approaches are compared to measured global radiation values. One reason for this comparison is that the usage of local incident radiation values (Eq. (8.1)) will lead to wrong terrain reflected radiation values on shaded patches which cannot receive terrain reflected radiation from patches with direct *and* diffuse radiation. The initial model set-up was chosen as described for 20 April 2007 in Section 8.2, p.110.

In Fig. 8.7 modelled global radiation values including terrain reflected radiation which was computed by both isotropic view factor approaches (multiplied by local or domain mean radiation) are shown for 20 April at Weissfluhjoch study site. In addition, the measured global radiation values with terrain influence from the experiment described in Section 8.1, p.8.1 are depicted. Global radiation values modelled with the two isotropic view factor approaches (Eq. (8.1) and Eq. (8.2)) differ by a maximum of about 5 Wm^{-2} and are in good agreement with the measured global radiation with terrain influence. From these results one might conclude that the isotropic view factor approach is a sufficiently accurate description of terrain radiation. However, this agreement is coincidental which is explained in the following and

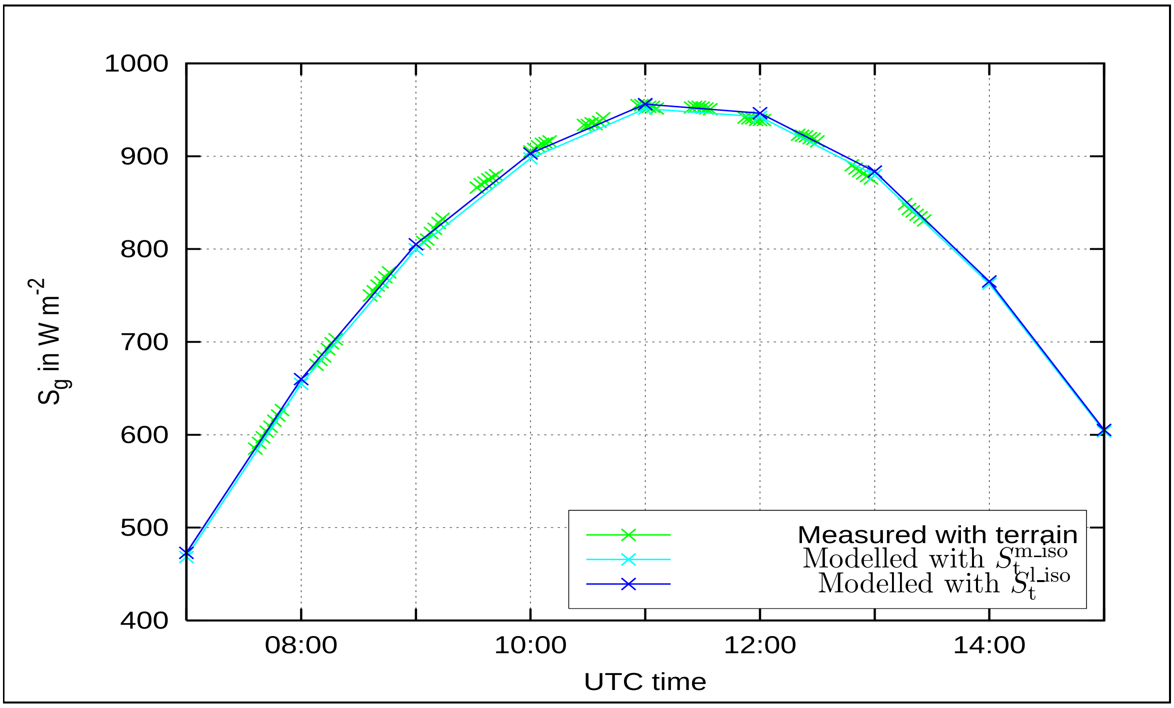

Figure 8.7: Comparison of measured $S_{\rm g}$ with terrain influence and modelled $S_{\rm g}$ with terrain influence with the isotropic view factor approaches according to Eq. (8.1) and Eq. (8.2) on 20 April at Weissfluhjoch study site.

further elaborated in the next section. Three reasons are given that only little differences exist between the two isotropic view factor approaches for the estimation of terrain reflected radiation. First, nearly homogeneous albedos exist (the model domain is covered almost homogeneously with snow) that suppress large differences in $\alpha_I(S_{{\rm b},I}+S_{{\rm d},I})$. Second, the chosen study site patch is getting both direct radiation $S_{\rm b}$ and diffuse sky radiation $S_{\rm d}$. This means here that the chosen patch is a patch that is getting approximately the mean radiation of the whole model domain. Third, from this patch only 3 % terrain is visible, thus a relatively low amount of terrain reflected radiation is obtained. Hence, for that specific patch a relatively good agreement is achieved by both isotropic view factor methods compared to the measurement. But, if more multiple terrain reflections arise, i.e. in case of steeper terrain, or with larger visible terrain fractions, larger differences between all three curves would result which is demonstrated in the next section.

The difference between all three curves was negligible on 24 September 2007. Maximum deviations of about 0.4 Wm^{-2} occurred. This good agreement is again due to only 3 % visible terrain together with the low snow free mean albedos of $\sim$ 0.2.

8.4 Comparison of radiosity and isotropic view factor approach model

In this section only modelled global radiation values are compared to outline the differences to more simplified isotropic view factor approaches. Here, modelled global radiation values with the radiosity approach using anisotropic view factors are compared to modelled global radiation values computed with the isotropic view factor approaches according to Eq. (8.1) and Eq. (8.2). The close agreement between measured global radiation and modelled global radiation with the isotropic view factor approaches, which was found in the previous section, is therefore further investigated for two different patches. This was conducted to estimate the influence in case of that the patch is **inclined**, holds a larger terrain view factor sum and receives no direct radiation. Therefore, in addition to the investigated day in the previous section, the 20 April 2007, an additional day with a lower sun elevation was chosen: 1 January 2005.

A first comparison was therefore conducted for an inclined patch on the upper east-facing slope in the model domain as used in the previous section (cf. Fig. 6.1). The initial model set-up for 20 April 2007 was chosen as described in Section 8.2, p.110.
In Fig. 8.8 the modelled global radiation with terrain influence is shown. With $1 - F_{\mathrm{sky},I} \approx 12\%$, 9% more terrain is visible at this inclined patch compared to the $1 - F_{\mathrm{sky},I} \approx 3\%$ of the horizontal Weissfluhjoch study site patch. The patch's elevation is about 89 m higher than the elevation of the Weissfluhjoch study site. Therefore, the main difference between both patches lies in the aspect and slope of the patches within the model domain. Whereas the Weissfluhjoch study site patch is flat and located in the center of the valley the new selected patch is located at the upper east-facing valley side (cf. east-facing slope in Fig. 6.2a). This different orientation is leading to differing direct and diffuse sky radiation between both patches. Consequently, as can be seen in Fig. 8.8 larger global radiation differences are obtained between all three curves compared to those visible in Fig. 8.7. From 10 to 15 UTC the patch is shaded receiving only diffuse sky radiation. At this time interval the difference between global radiation modelled with the radiosity approach and modelled with the isotropic view factor approach using locally incident radiation (Eq. (8.1)) becomes largest reaching maximum differences of 70 Wm^{-2}. This underestimation of terrain reflected radiation clearly origins in the lower direct and diffuse sky radiation due to an direct radiation of zero (shaded). However, since the surrounding patches receive direct radiation larger zero this is leading in reality to larger terrain reflected radiation at that patch than estimated by Eq. (8.1). The maximum radiation difference between incident global radiation computed with the radiosity approach and Eq. (8.1) is about 20 Wm^{-2}. In the following a second comparison is now conducted to verify if this difference will increase for larger terrain view factor sums and for larger differences in spatial surface albedo values. The latter will lead to increased multiple terrain reflections that are not captured by the isotropic view factor approaches.

For the second comparison a patch in the model domain as described in Section 11.1, p.11.1 (cf. Fig. 11.1) was selected. The model set-up was chosen similarly as described in Section 11.1, p.11.1 but for a different day: 1 January 2005. A homogeneous snow cover was assumed within the model domain. This time the chosen patch has a $1 - F_{\mathrm{sky},I} \approx 70\%$. In addition, larger mean terrain view factor sums $1 - F_{\mathrm{sky},I}$ variations within the model domain lead to a larger difference between mean direct and diffuse sky radiation and local direct and diffuse sky radiation. Additionally, the selected patch is shaded the whole day on 1 January due to low solar elevation angles in winter.
In Fig. 8.9 modelled global radiation with terrain influence is shown. Similar to the first example the underestimation of terrain reflected radiation computed by Eq. (8.1) can be clearly traced back to the lower sum of direct and diffuse sky radiation since the direct radiation is zero (shaded) at the investigated patch. These differences are in the same order of magnitude as found in the first example. Despite the larger terrain view factor $1 - F_{\mathrm{sky},I}$

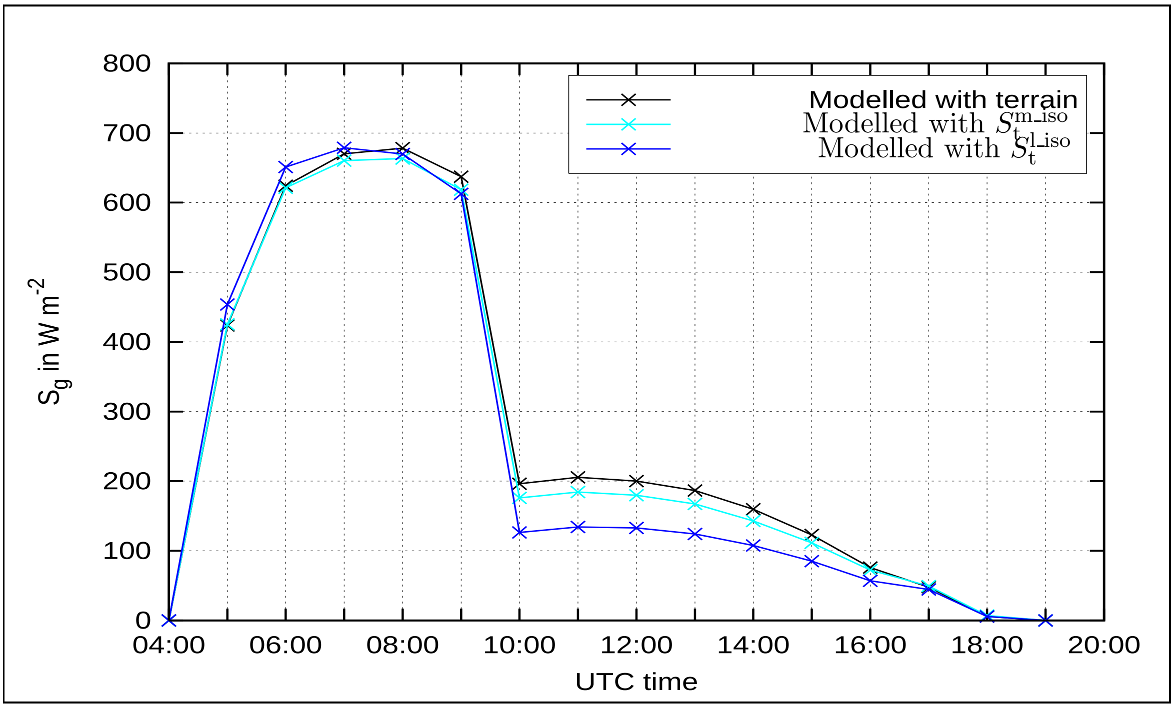

Figure 8.8: Comparison of modelled S_g with terrain influence with radiosity approach to modelled from isotropic view factor approaches: according to Eq. (8.1) and Eq. (8.2) on 20 April at an inclined upper east-facing slope patch in the model domain of Fig. 6.1.

the differences between both curves are not larger. This might be explained by the reduced terrain reflected radiation since the surrounding patches see less of the sky than the patch, and its surrounding patches, investigated in the first example. Therefore, the surrounding patches also reflect less radiation to the patch even though that patch has a larger visible terrain fraction. The largest differences between modelled global radiation with the radiosity approach and with the isotropic view factor approaches occur from ∼15 UTC to ∼16 UTC leading to another peak in the global radiation. At this time interval multiple terrain reflections are obtained that are not captured by the isotropic view factor approach. The isotropic view factor approach does not account for spatial varying global radiation, surface albedos and terrain view factors. Thus, local enhancements cannot be captured properly. This is leading, at this specific patch and time interval, to a maximum error of 110 Wm^{-2} for the difference between terrain reflected radiation modelled with the radiosity approach and from isotropic view factors with mean radiation (Eq. (8.2)). This error is even enhanced for the difference between modelled radiation with the radiosity approach and modelled radiation from isotropic view factors with local radiation (Eq. (8.1)). Maximum differences occur of 145 Wm^{-2}.

In this section, it was shown that large differences might exist between terrain reflected radiation computed with the radiosity approach using anisotropic view factors and computed from isotropic view factors. Thereby, the largest differences occurred for the isotropic view factor together with local radiation values (Eq. (8.1)). It was found, that the differences are enhanced the larger the terrain view factor sums are, the more the direct and diffuse sky radiation vary spatially and the larger the spatial surface albedo values differences are.

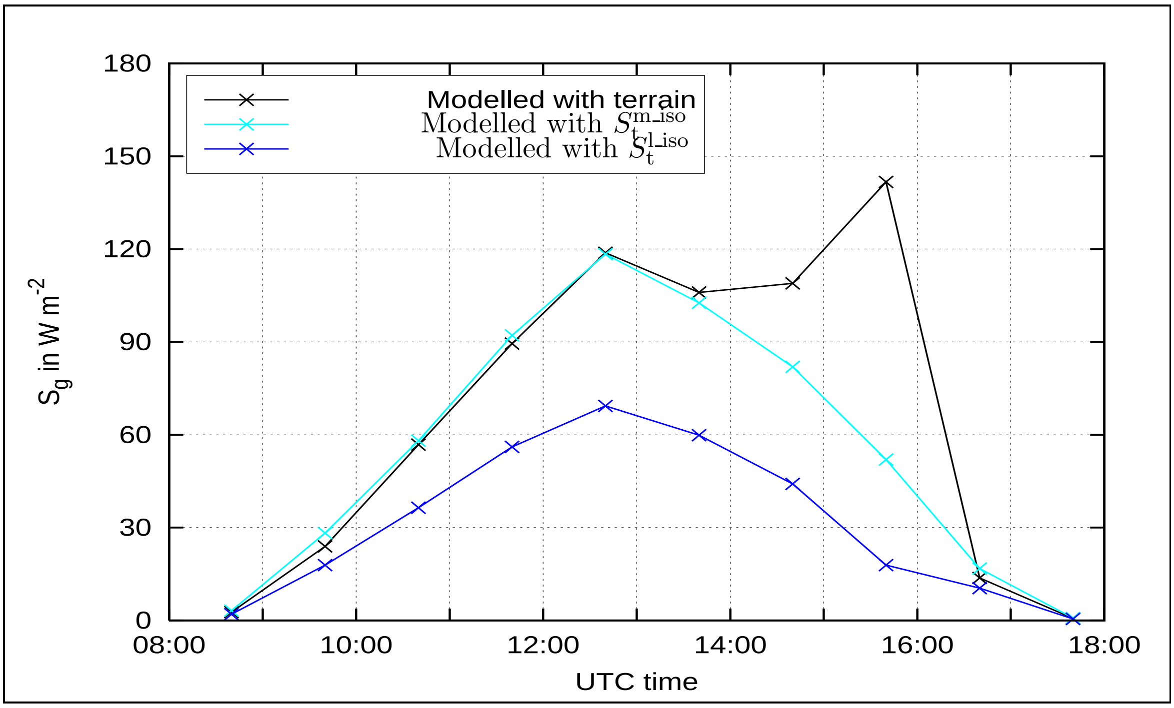

Figure 8.9: Comparison of modelled S_g with terrain influence with radiosity approach to modelled from isotropic view factor approaches: according to Eq. (8.1) and Eq. (8.2) on 1 January at an inclined patch in the model domain of Fig. 11.1.

8.5 Comparison of radiosity approach model and Monte Carlo model MYSTIC

By recalling that the radiosity approach was implemented in the present study to partly fill the gap in complexity between realistic cloud radiative transfer models and isotropic view factor approaches (cf. description in Section 4.2, p.58), it bears out to compare the radiosity model with a three-dimensional radiative transfer model accounting for inhomogeneous surface albedo values and topography in cloudy atmospheres. The comparison with isotropic view factor approaches was presented in Section 8.4, p.114. Therefore, in this section modelled global radiation values with terrain influence computed with the radiosity approach are compared to modelled global radiation values with terrain influence computed with the MC model MYSTIC. Additionally, both models are compared to the sum of measured direct and total diffuse radiation. Direct and total diffuse radiation are measured values from the permanent PMOD/WRC (WWW) instruments at Weissfluhjoch study site as described in Section 8.1, p.105. The comparison was conducted for 20 April 2007.

In Section 4.2, p.58 it was pointed out that the assumption of a sky representing an opening of zero reflectivity might lead to errors in incident radiation. E.g. Degünther et al. (1998) found that incident UV radiation is influenced from surface areas in more than 40 km away by up to 3 % under clear sky conditions. Similarly, Mayer and Degünther (2000b) found that the erythemal irradiance at a certain location is affected by surface albedo and topography far away. Thus, cloud backscattering should also be taken into account for visible SW and LW radiation and even larger model domains should be applied (e.g. 10 km in diameter or

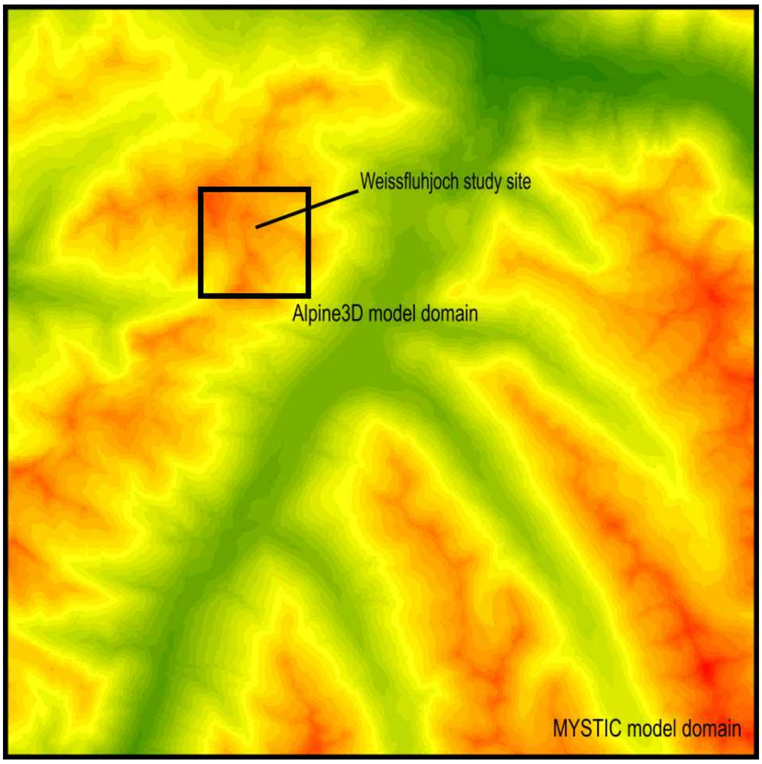

Figure 8.10: The DHM of the smaller Alpine3D model domain (cf. Fig. 6.1) is shown within the DHM of the large MYSTIC model domain around the Weissfluhjoch study site. The location of the Weissfluhjoch study site is indicated.

larger). Nevertheless, since lots of model applications in complex terrain require fine horizontal resolutions to represent local characteristics already a large number of grid cells has to be computed and stored. Thus, the applied model domain dimensions are usually limited to available computer memory. Here, a comparison is conducted between the radiosity model, which is implemented in the surface radiation balance module of Alpine3D, and a realistic three-dimensional cloudy radiative transfer model MYSTIC. MYSTIC is a MC model for tracing photons on their random paths in cloudy atmospheres. It has been developed since 1997 to investigate all kinds of three-dimensional effects, including clouds, topography, and inhomogeneous surface albedo (Mayer (1999), Mayer (2000a), Kylling et al. (2000a), Kylling et al. (2000b)). For the following comparison, the backward MC technique was applied yielding much faster results, since only those grid cells are calculated which are actually required (for an application see Emde and Mayer (2007)). Note again, that this comparison was also conducted to investigate the influence of cloud backscattering which is not included by the radiosity model but is included by the MYSTIC model.

MYSTIC simulations were conducted by B. Mayer (DLR). The model set-up for MYSTIC was chosen as follows:

- mid-latitude summer atmosphere on 20 April 2007 (Ozone Monitoring Instrument (OMI): total ozone of 335 (Dobson Unit) DU, midlatitude summer of 334.26 DU; water vapour of secondary importance above 2 km)

- A so-called default-aerosol profile, starting at 0 m a.s.l., was applied.
- SW radiation was integrated over the interval 0.25 - 4.5 μm.
- 100,000 photons were used.
- The DHM of the MYSTIC domain comprises 700x700 grid cells with 25 m horizontal resolution and was taken from Swisstopo (WWW) (cf. Fig. 8.10).
- The DHM of the Alpine3D domain comprises 100x100 grid cells with 25 m horizontal resolution and was taken from Swisstopo (WWW) (cf. Fig. 8.10).
- Backward MC computation was conducted for a 24x31 DHM around the Weissfluhjoch study site (cf. Fig. 8.10), out of the MYSTIC domain.
- Hourly albedo distribution was used for the Alpine3D domain within the MYSTIC domain. For the grid cells not included by the Alpine3D domain a mean albedo value of the Alpine3D domain was assumed: 0.6.

In Fig. 8.11 and Fig. 8.12 the modelled and measured direct, total diffuse (with terrain) and global radiation are shown for 20 April 2007 at the Weissfluhjoch study site. In both models, no additional measurement height is considered in the modelling but was included in the permanent measurements of the PMOD/WRC (WWW). The radiation components are computed for a horizontal patch. Note that the visible terrain fraction is only minimal larger than it was in measurement height. Modelled hourly radiation values modelled with the radiosity approach, implemented in the Alpine3D model, are compared to half-hourly radiation values modelled with the MC model MYSTIC. Modelled values are compared to hourly mean measured radiation values of the permanent measurement site.

In Fig. 8.11(a) the comparison for total diffuse radiation and in Fig. 8.11(b) the comparison for direct radiation is shown. It can be seen that in general the agreement is very well between all three curves for both radiation components. Both models overestimate measured total diffuse radiation of the PMOD/WRC (WWW). The radiosity model also underestimates measured direct radiation of the PMOD/WRC (WWW) whereas the modelled direct radiation with MYSTIC agrees very well with the measurements. The modelled total diffuse radiation by the MYSTIC model shows an overestimation by a maximum of about 40 Wm^{-2} and the radiosity model of about 60 Wm^{-2}. Modelled direct radiation values of the radiosity model underestimate the measured values by a maximum of about 40 Wm^{-2}. Here, the main error of both radiation components of the radiosity model is assumed to come from the incorrect decomposition of the single measured global radiation value $S_{\mathrm{g}}^{\mathrm{meas}}$ (cf. Section 7.1, p.95) to obtain direct and diffuse sky radiation values under cloudy skies. This assumption arises since a maximum overestimation of modelled diffuse sky radiation of about 40 Wm^{-2} as well as a maximum underestimation of modelled direct radiation compared to measured values was obtained for the patch in measurement height on 20 April 2007 (cf. Fig. 7.3). Therefore, the above deviations of the modelled total diffuse radiation of the radiosity model are assumed to not come from an incorrect computation of terrain reflected radiation. This is also emphasised by the fact that measured and modelled differences of terrain reflected radiation at Weissfluhjoch study site on 20 April 2007 agree very well (cf. Fig. 8.6(a)). The differences are also not coming from an incorrect horizon line computation as was demonstrated in Fig. 6.2(b) nor from incorrect computed view factors as will be shown in Section 9.3, p.132.

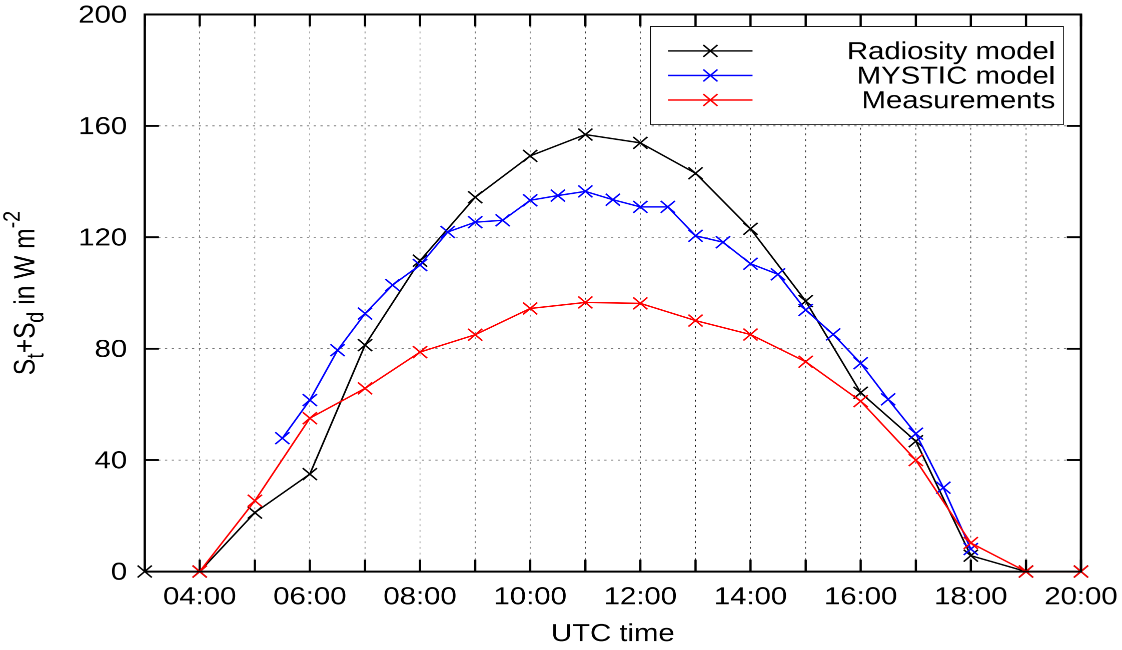

(a)

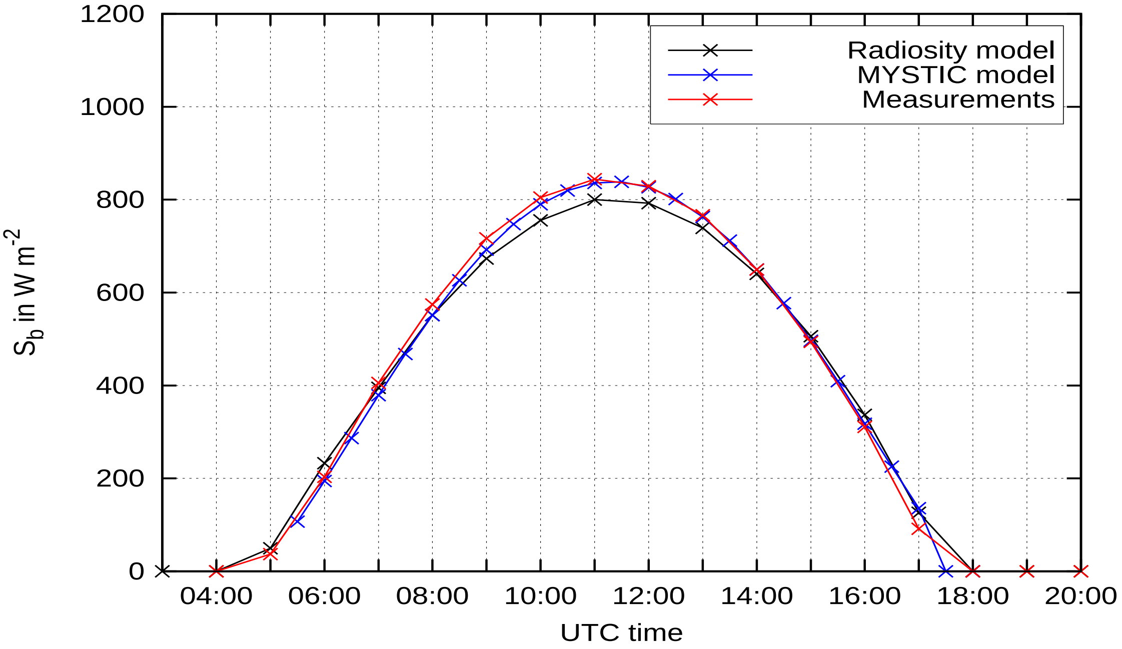

(b)

Figure 8.11: Comparison between modelled and measured radiation components on 20 April 2007 at Weissfluhjoch study site. Modelled values of the radiosity approach, implemented in Alpine3D, and the MC model MYSTIC are compared. Measured values are used from the permanent measurement site of PMOD/WRC (WWW): (a) $S_d + S_t$, (b) S_b.

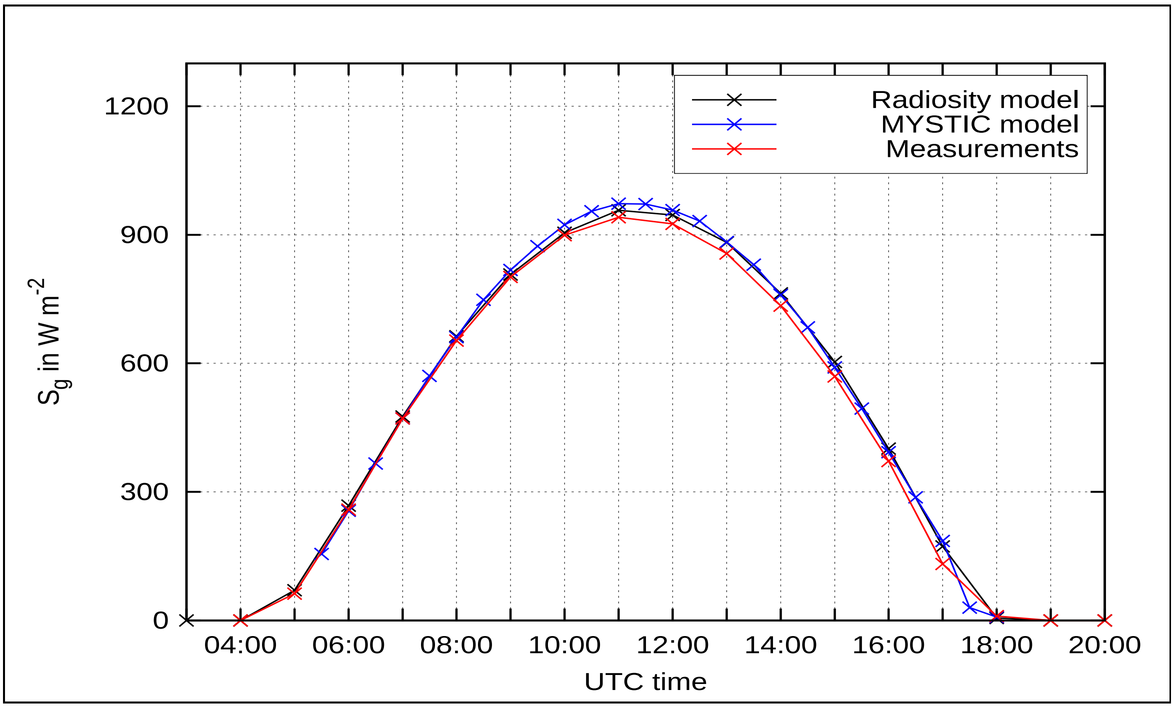

Figure 8.12: Comparison between modelled and measured S_g on 20 April 2007 at Weissfluhjoch study site. Modelled values of the radiosity approach, implemented in Alpine3D, and the MC model MYSTIC are compared. Measured values are used from the permanent measurement site of PMOD/WRC (WWW).

In Fig. 8.12 modelled and measured global radiation values are shown. As discussed in Section 7.1 , p.95, although the decomposition model does not split the measured single global radiation value correctly the modelled global radiation values in general agree well with measurements (maximum deviations of at maximum about 20 Wm^{-2} on 20 April 2007 (Fig. 7.4)). Therefore, it comes as no surprise that the global radiation values modelled with the radiosity model agree again better with measured global radiation values than with the measured individual radiation components. Since MYSTIC overestimates the total diffuse radiation, but agrees very well with measured direct radiation, in contrast to the radiosity model measured global radiation values are this time more overestimated by the MYSTIC model. Maximum differences appear of about 30 Wm^{-2}.
To summarise, it could be shown that the surface radiation balance model with the radiosity approach agrees well with the realistic three-dimensional cloudy radiative transfer model MYSTIC. Note that the comparison was conducted for an almost clear sky day, thus little cloud backscattering occurred which might have led to larger deviations between both models.

It was found that the decomposition of the single exposed measured global radiation value $S_\mathrm{g}^\mathrm{meas}$ for the computation of radiation components for cloudy skies (Section 3.1.3, p.37) introduces incident radiation errors even for a clear sky day. Therefore, an additional comparison is now presented. It was investigated if the application of the radiation components for clear sky, obtained from the theoretical parameterisations given in Section 3.1.2, p.32, leads to a better agreement with measurements as well as with modelled values with the MYSTIC model.

In Fig. 8.13 radiation components modelled without the decomposition model, modelled values with the MYSTIC model and measured values are shown on 20 April 2007 at Weissfluhjoch study site. In Fig. 8.13(a) total diffuse radiation and in Fig. 8.13(b) direct radiation is depicted. Modelled total diffuse radiation values with the radiosity model are now in good agreement with the values from the MYSTIC model. Nevertheless, both overestimate measured values by a maximum of about 40 Wm^{-2}. The modelled direct radiation now overestimates the one of MYSTIC and the measured values but is closer to the other two curves with a maximum error of 20 Wm^{-2} (Fig. 8.13(b)). This is in contrast to the earlier maximum underestimation of 40 Wm^{-2} (cf. Fig. 8.11(b)). These results demonstrate that the decomposition model does not always lead to an improvement over the theoretically determined radiation for clear sky conditions. Note that this might be different for a cloudy day.

The better agreement of both modelled radiation components when neglecting the decomposition model in the computation of the incident direct and diffuse sky radiation for the radiosity model is further investigated. For this in Fig. 8.14 diffuse sky and direct radiation values obtained from the decomposition model (radiation components for cloudy sky conditions Eq. (3.42)) are compared to radiation values obtained from the theoretical parameterisations (radiation components for clear sky conditions (Eq. (3.34), Eq. (3.39)) as well as to measured total diffuse and direct radiation values from PMOD/WRC (WWW). All modelled radiation components are computed for the location of the meteorological measurement station at Weissfluhjoch at 2693 m a.s.l. This means these values are barely influenced by any terrain due to the exposed and flat location of the measurement station. In contrast, the measured radiation values for the validation are from Weissfluhjoch study site, i.e. the surrounding terrain influences these measured total diffuse values. In order to compare the modelled diffuse sky exposed values with the measured values from the study site the modelled exposed diffuse sky radiation was multiplied by the actual sky view factor at Weissfluhjoch study site. Since the 20 April 2007 was a clear sky day only little more diffuse sky radiation was expected from the 150 m thicker atmosphere for the measured values at Weissfluhjoch study site (150 m height difference between both sites). Direct radiation values are expected to be comparable as long as no shading occurs at Weissfluhjoch study site. If no shading occurs the 150 m height difference between both sites only has a minor impact on direct radiation values.

In Fig. 8.14(a) the modelled diffuse sky and measured total diffuse radiation are shown. Both modelled diffuse sky curves overestimate the measured total diffuse radiation at Weissfluhjoch study site. Thus, even though the measured total diffuse radiation at Weissfluhjoch study site includes terrain reflected radiation the modelled diffuse sky radiation values show larger values. The theoretically parameterised diffuse sky radiation for clear sky conditions approximates the measured values better than the diffuse sky radiation modelled with the decomposition model to account for cloudy sky conditions.

In Fig. 8.14(b) the direct radiation values are compared. Again, the theoretically parameterised direct radiation for clear sky conditions approximates the measured values better than the direct radiation values modelled with the decomposition model. The theoretically parameterised direct radiation overestimates the measured values less than the direct radiation modelled with the decomposition model underestimates the measured values. As described in Section 3.1.3, p.37, the theoretically parameterised clear sky radiation values at each patch are corrected with a ratio obtained from the decomposition model at the meteorological measurement station (Weissfluhjoch) to account for the actual (cloudy) atmospheric conditions. The curves now suggest that under clear sky conditions on a winter day at high altitudes

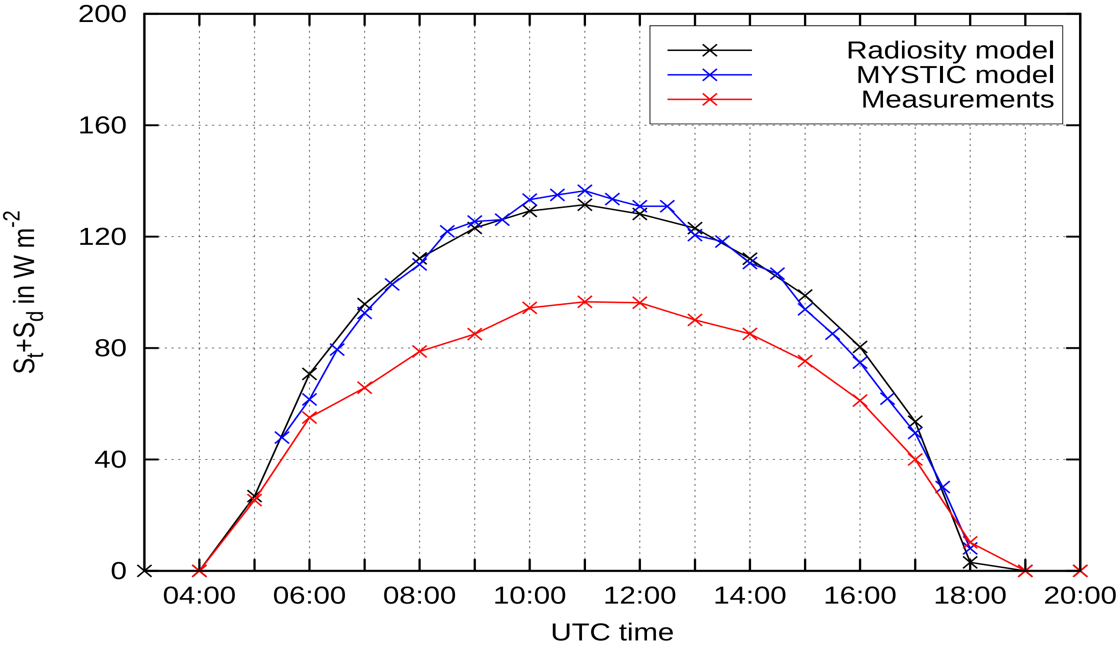

(a)

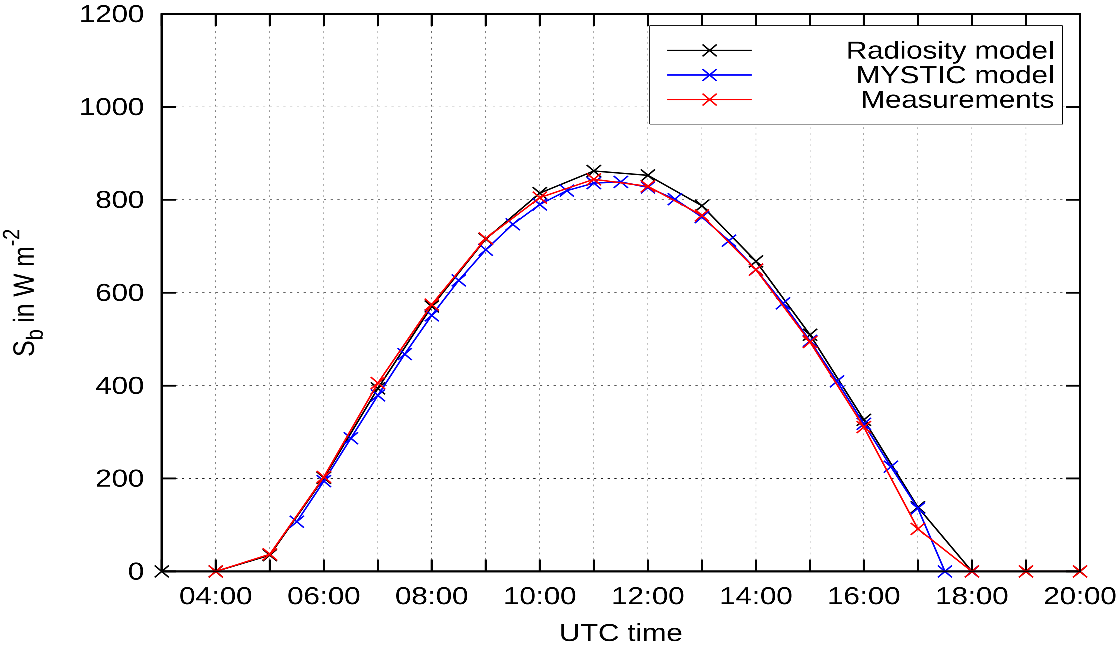

(b)

Figure 8.13: Comparison between modelled and measured radiation components on 20 April 2007 at Weissfluhjoch study site. Modelled values of the radiosity approach and the MC model MYSTIC are depicted. Note, S_d and S_b are computed **without** decomposition model. Measured values are used from the permanent measurement site of PMOD/WRC (WWW): (a) $S_\mathrm{d} + S_\mathrm{t}$, (b) S_b.

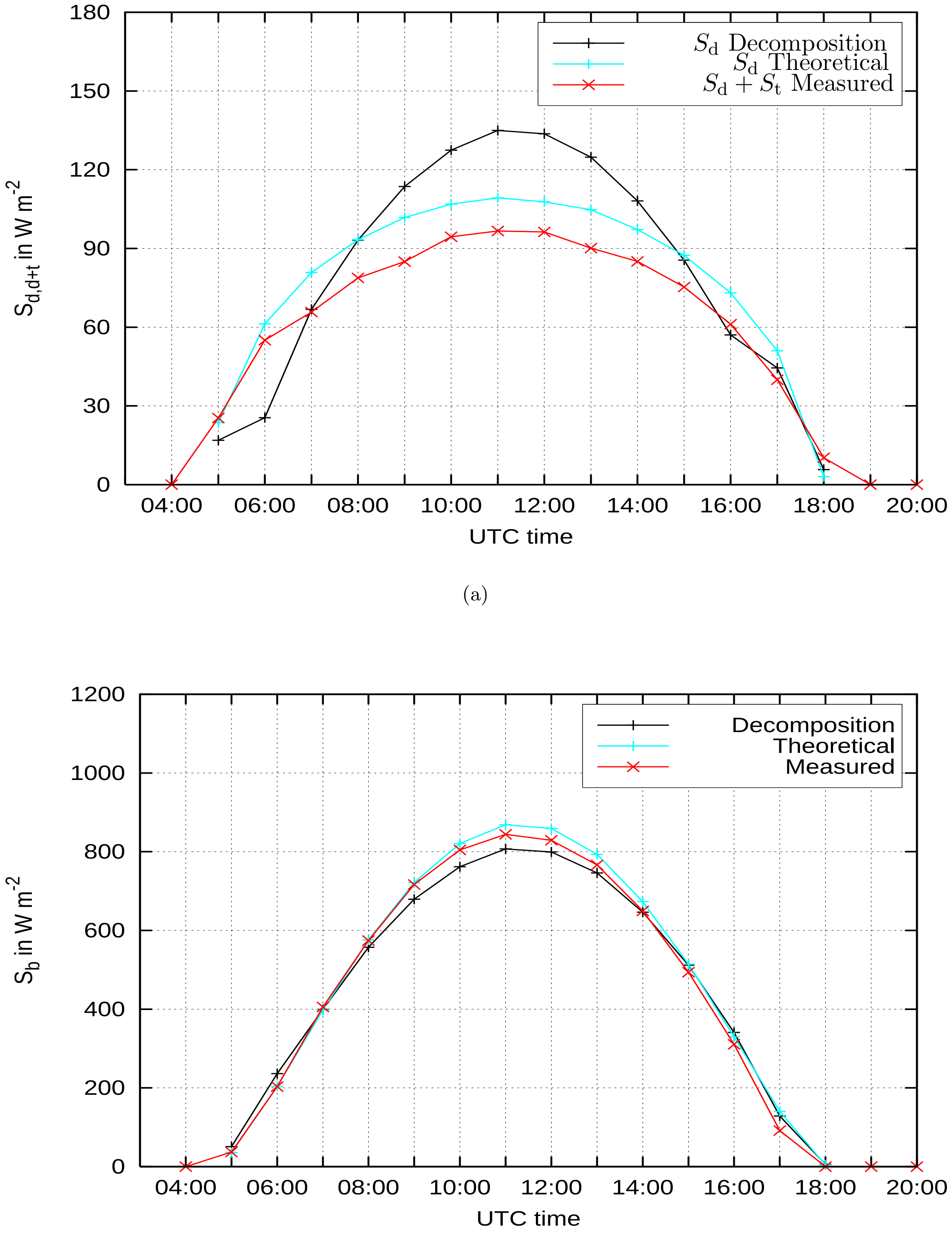

(a)

(b)

Figure 8.14: Comparison between modelled and measured radiation components on 20 April 2007 at Weissfluhjoch study site. Modelled values of the radiosity approach but once with and once **without** ('Theoretical': only clear sky parameterisation) decomposition model. Measured values are used from the permanent measurement site of PMOD/WRC (WWW): (a) S_{d}, $S_{\mathrm{d}} + S_{\mathrm{t}}$, (b) S_{b}.

it might be better not to correct the clear sky radiation values and use the theoretical parameterisations. However, it is not possible to decide in advance if the clear sky conditions apply. Note that the errors of the applied decomposition model for the Eastern Swiss Alps will probably be enhanced for a cloudy day.

Finally, possible reasons for the poor agreement of the modelled radiation values with the radiosity and the MYSTIC model compared to the permanent measurements of the PMOD/WRC (WWW) are briefly discussed.
On the one hand, the overestimated total diffuse radiation of the MYSTIC model compared to measured values might be due to a too large assumed mean surface albedo value for the grid cells in the MYSTIC model domain not included by the Alpine3D model domain (cf. Fig. 8.10). The mean albedo value is computed from albedos modelled with the coupled SNOWPACK module in Alpine3D (Section 5, p.79)) for the Alpine3D domain that was nearly homogeneous covered by snow. Thus, the resulting mean albedo of 0.6 is probably too large for the not included MYSTIC domain since the larger domain also includes dark snow free trees, buildings and other snow free patches. In a one-dimensional rough test estimation with a mean albedo of only 0.3 for the not included MYSTIC domain, approximately the measured total diffuse radiation was obtained (cf. Fig. 8.11(a)) (communication B. Mayer).
On the other hand, the poor agreement of both models with the total diffuse radiation measurements might be due to the calibration method of the shaded pyranometer (for the measurement of total diffuse radiation). Philipona (2002) noted that part of the often claimed overestimation of modelled solar radiation may be due to a considerable underestimation of solar irradiance by traditional pyranometer measurements. Therefore, he reinvestigated pyranometer calibration using three different calibration methods and a thermal control system to suppress pyranometer thermal offsets. Comparisons between the traditional "unconditioned" (without ventilation and heating) pyranometer standard World Radiation Center (WRC) calibration method at Davos and "well-conditioned" (with ventilation and heating) measurements revealed that "unconditioned" measured global and total diffuse radiation are underestimated due to pyranometer negative thermal offsets. In this standard calibration method pyranometers measuring global radiation are compared to the sum of measured direct radiation of the World Standard Group (7 absolute radiometers located at the WRC at Davos) multiplied by the cosine of the sun zenith angle and measured diffuse sky radiation of the diffuse reference pyranometer, the Eppley PSP, mounted the traditional "unconditioned" way. For two clear sky days in October with mean AOD values of 0.014 and 0.046 at 0.5 μm, respectively he found underestimations of global radiation of 8-14 Wm^{-2} for the 0.014 AOD value and of 10-15 Wm^{-2} for the 0.046 AOD value at Davos. Furthermore, Philipona (2002) note that at higher altitudes larger thermal offsets are induced due to a colder clear sky. In addition, Marty (2001) notes, that the more the actual conditions differ from those during calibration, the larger the error due to thermal offsets is. Therefore, since the permanent CM21 pyranometer at Weissfluhjoch study site was calibrated in 1999, a large fraction of the underestimated measured total diffuse radiation (cf. Fig. 8.11(a), Fig. 8.13(a) and Fig. 8.14(a)) might be explained by the WRC standard calibration method.

9 Sensitivity studies on a real topography

The model validation at specific points, presented in the previous chapters, is now extended by sensitivity studies on a real topography. Thereby, main influences on incident radiation were investigated, i.e. the influence of grid cell resolutions, terrain parameter extraction methods, view factor computation methods, sky view factor computation methods and the LW terrain parameterisation. The results are shown for selected patches or as spatial patterns to highlight the influence in terms of relative radiation value differences.

9.1 Influence of grid cell resolutions

In this section three different horizontal grid cell resolutions for the model domain around the Weissfluhjoch study site (cf. Fig. 6.1) are compared to highlight the sensitivity of grid cell resolutions with regard to incident SW radiation.

The comparison was conducted for 19 January 1999 at Weissfluhjoch study site. The model set-up was chosen as described for the modelling in Section 7.1, p.95. Three different horizontal grid cell resolutions are obtained by averaging the model domain. By simply averaging the grid heights z over four cells a 50 m resolution is obtained. By averaging over 16 grid cells this is reduced to a 100 m resolution. For each model domain the location and height of the sensor is accounted for. Note that those grid cells were compared which correspond to the same coordinates in each of the different resolved domains. It was not averaged over several grid cells in case of the 25 m and 50 m resolutions to compare with the 100 m resolution.

In Fig. 9.1 and Fig. 9.2 the modelled radiation components are shown for the three different horizontal resolutions.

In Fig. 9.1(a) direct radiation S_b is presented. Until 15 UTC all modelled radiation components for the three resolutions are similar but after 15 UTC the model domains with 100 m and 50 m grid cell resolutions overestimate direct radiation of the domain with 25 m grid resolution by about 130 Wm^{-2} due to a delayed modelled sunset. Thus, if the patch is not shaded no differences in direct radiation arise between all three model domains since the elevated receiving patch is **horizontal**, i.e. is not influenced by the resolution. Nevertheless, in case of shading the horizontal grid cell resolution of the model domain has a large influence on incident radiation values.

In Fig. 9.1(b) diffuse sky radiation S_d is shown. There are only little differences between the three differently resolved model domains. Again, this is due to the assumption of a horizontal elevated patch in all three domains (all three patch slope angles are zero). Moreover, the large sky view factors at the investigation point do not vary much between the three model domains: for 100 m: $F_{\mathrm{sky},I}$=0.982, for 50 m: $F_{\mathrm{sky},I}$=0.976 and for 25 m: $F_{\mathrm{sky},I}$=0.971.

In Fig. 9.2 terrain reflected radiation S_t is shown. As can be seen, the maximum S_t values

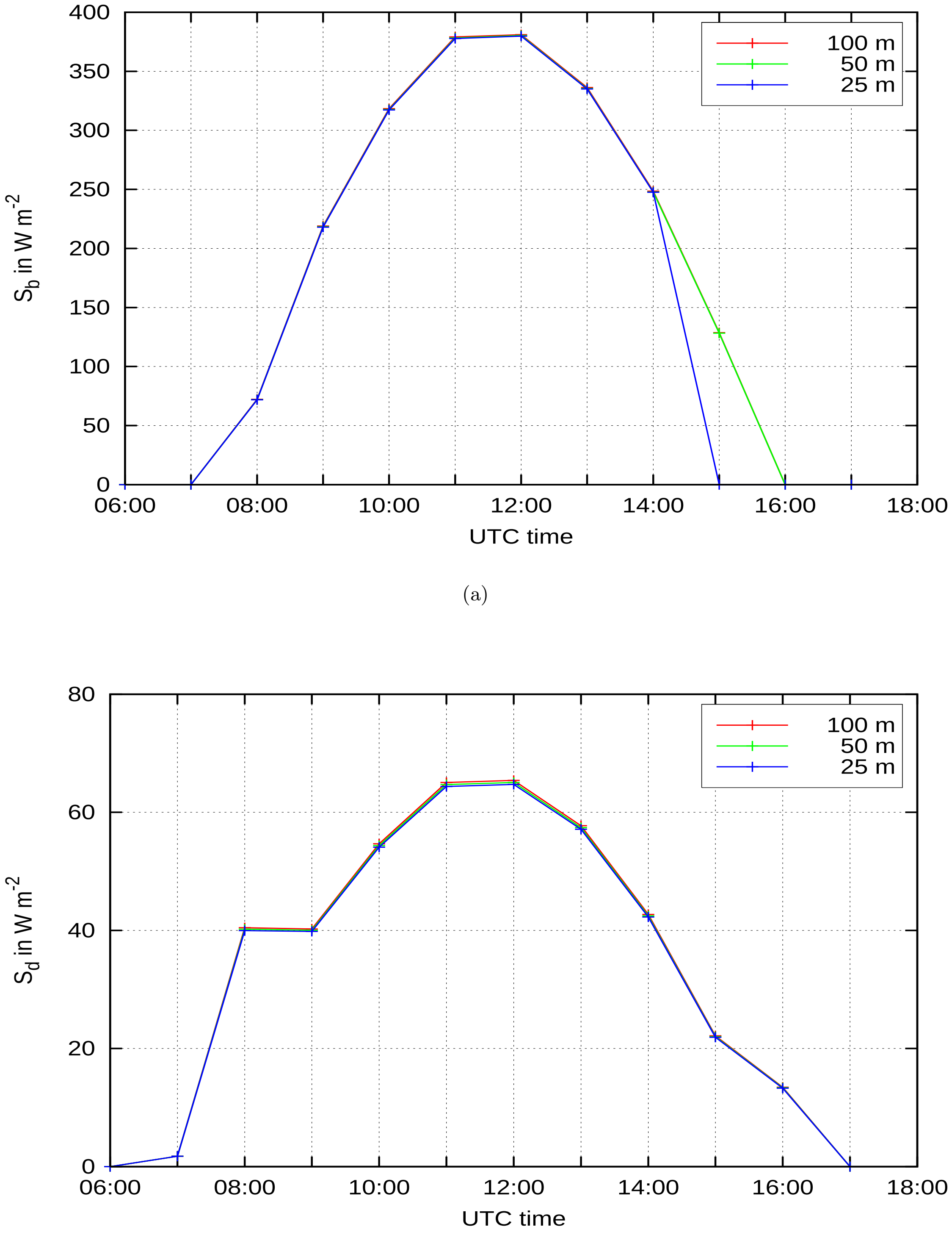

(a)

(b)

Figure 9.1: Comparison of modelled SW radiation components with regard to different horizontal resolutions of the model domain for 19 January 1999 at Weissfluhjoch study site. 100 m, 50 m and 25 m grid resolution was tested: (a) S_b, (b) S_d.

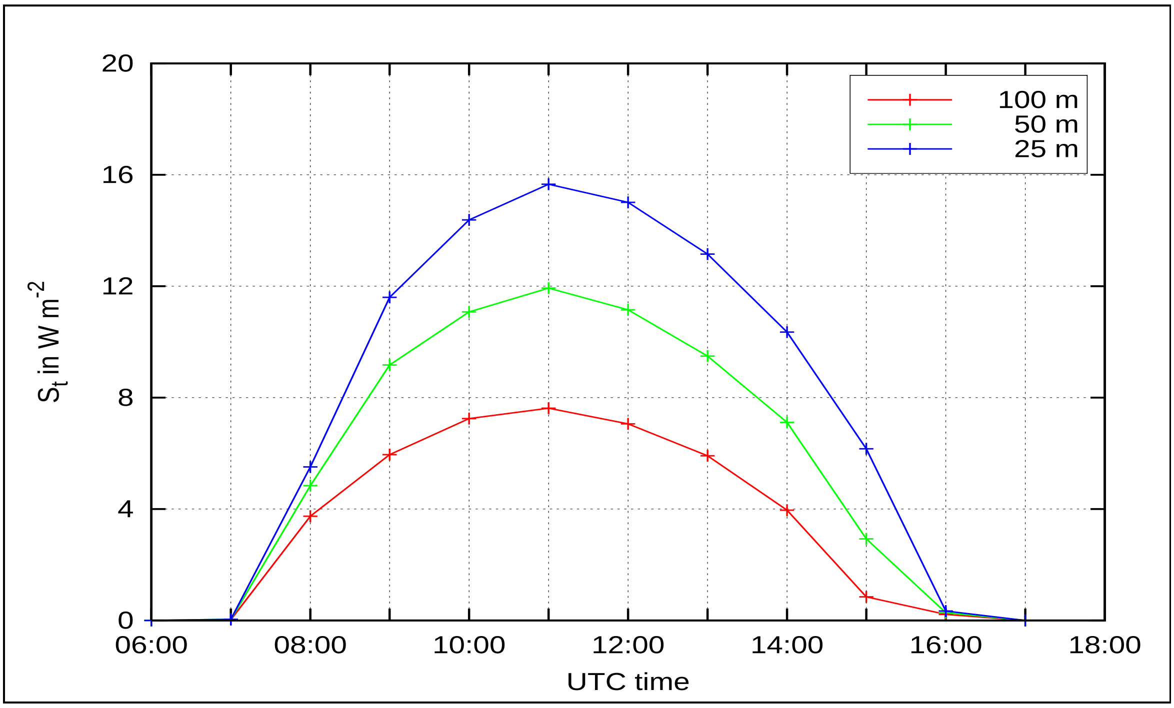

Figure 9.2: Comparison of modelled S_t with regard to different horizontal resolutions of the model domain for 19 January 1999 at Weissfluhjoch study site. 100 m, 50 m and 25 m grid resolution was tested.

are obtained for the model domain with a 25 m resolution. There is a maximum difference of 8 Wm^{-2} between modelled S_t values. Despite the relatively small differences of the sky view factor among the different model domains large differences in S_t values are observed. This is due to multiple reflections, which were accounted for in the present model. If only single reflections are accounted for less differences might result. Smaller grid cell resolutions lead to increased terrain view factors (1-$F_{\text{sky},I}$) in mountainous model domains. Therefore, more multiple terrain reflections appear in mountainous terrain for smaller grid cell resolutions.

9.2 Influence of terrain parameter extraction methods

In this section three different terrain parameter extraction methods (Section 2.1, p.17) for the model domain shown in Fig. 6.1 with a constant grid resolution of 25 m are compared to highlight the sensitivity of varying terrain slope and azimuth angle values with regard to incident SW radiation.

The comparison was conducted for 20 April 2007 for an inclined ridge patch at the top of the east-facing slope within the Weissfluhjoch model domain without an additional sensor height offset. The general model set-up was chosen as described for the modelling in Section 8.2, p.110. The three compared terrain parameter extraction methods are the eight-neighbor algorithm of Horn (1981), the four nearest neighbors algorithm of Fleming and Hoffer (1979) and the algorithm of Corripio (2002) which is implemented in the model. For the latter, rectangle grid cells are divided into two triangles and an average of the two resulting normal vectors is computed. The computed **local** surface slope ζ_s, azimuth angle φ_s (azimuth angle

counted clockwise from north) and the terrain view factor $\sum_{J=0}^{N-1} F_{IJ}$ at the patch are given in the following:
With the algorithm of Corripio (2002):

- ζ_s=19°, φ_s= 81°, $\sum_{J=0}^{N-1} F_{IJ}$=0.012

With the algorithm of Horn (1981):

- ζ_s=11°, φ_s=225°, $\sum_{J=0}^{N-1} F_{IJ}$=0.011

With the algorithm of Fleming and Hoffer (1979):

- ζ_s=15°, φ_s=244°, $\sum_{J=0}^{N-1} F_{IJ}$=0.016

In Fig. 9.3 and Fig. 9.4, the modelled radiation components are shown computed with the different terrain parameter extraction methods.
In Fig. 9.3(a) direct radiation S_b is shown. Clearly visible are the time shifts of the direct radiation due to different local surface azimuth angles. The sun rises and sets earlier when the algorithm of Corripio (2002) is compared to the other two algorithms. This is due to the local east-facing surface inclination (local azimuth angle φ_s=81°) when his algorithm is used. In contrast, local west-facing surface inclinations (local azimuth angle φ_s of 225° and 244°) are obtained when the algorithm of Horn (1981) or Fleming and Hoffer (1979) are used. Thus, the surface azimuth angles highlight how different the patch orientation is computed if different terrain parameter extraction methods are applied. In the case presented here, the in reality, east-facing ridge patch is only captured as east-facing by the algorithm of Corripio (2002). This is possible, since the DHM's used in Switzerland are defined with the grid height allocated to the lower left corner of a grid cell. Thus, the algorithm of Corripio (2002) using the height values of the four edges of a grid cell leads to the best representation of the real topography in Switzerland. Note that this can be differ if the DHM heights are allocated differently.
In Fig. 9.3(b) diffuse sky radiation S_d is shown. The patch on the ridge has a large, similar sky view factor in all three DHM extraction methods. Therefore, nearly no differences are observed in the computed diffuse sky radiation.
In Fig. 9.4 terrain reflected radiation S_t is shown. Since the largest terrain view factor sum for the chosen patch was obtained when using the algorithm of Fleming and Hoffer (1979), the largest S_t is also computed when using his algorithm. The time shifts between all three curves are most likely due to the differences in surface azimuth angles in relation to the surrounding terrain. The maximum S_t is obtained earlier when the algorithm of Horn (1981) and Fleming and Hoffer (1979) are applied. This is due to the west-facing of the patch. More terrain radiation is reflected from east-facing slopes to the west-facing patch in the morning. More terrain radiation is reflected around solar noon from south and west-facing slopes to the east-facing patch which was obtained when using the algorithm of Corripio (2002).

The sensitivity of varying patch orientations with regard to incident radiation was shown. The sensitivity is enhanced for patches with large DHM height variations around them. It was found that for Switzerland, the algorithm of Corripio (2002) using the height values of the four edges of a grid cell leads to the best representation of the real topography. Since this is depending on the grid height allocation in the DHM on ridges in steep mountainous terrain the terrain parameter extraction method has to be selected carefully to avoid radiation errors.

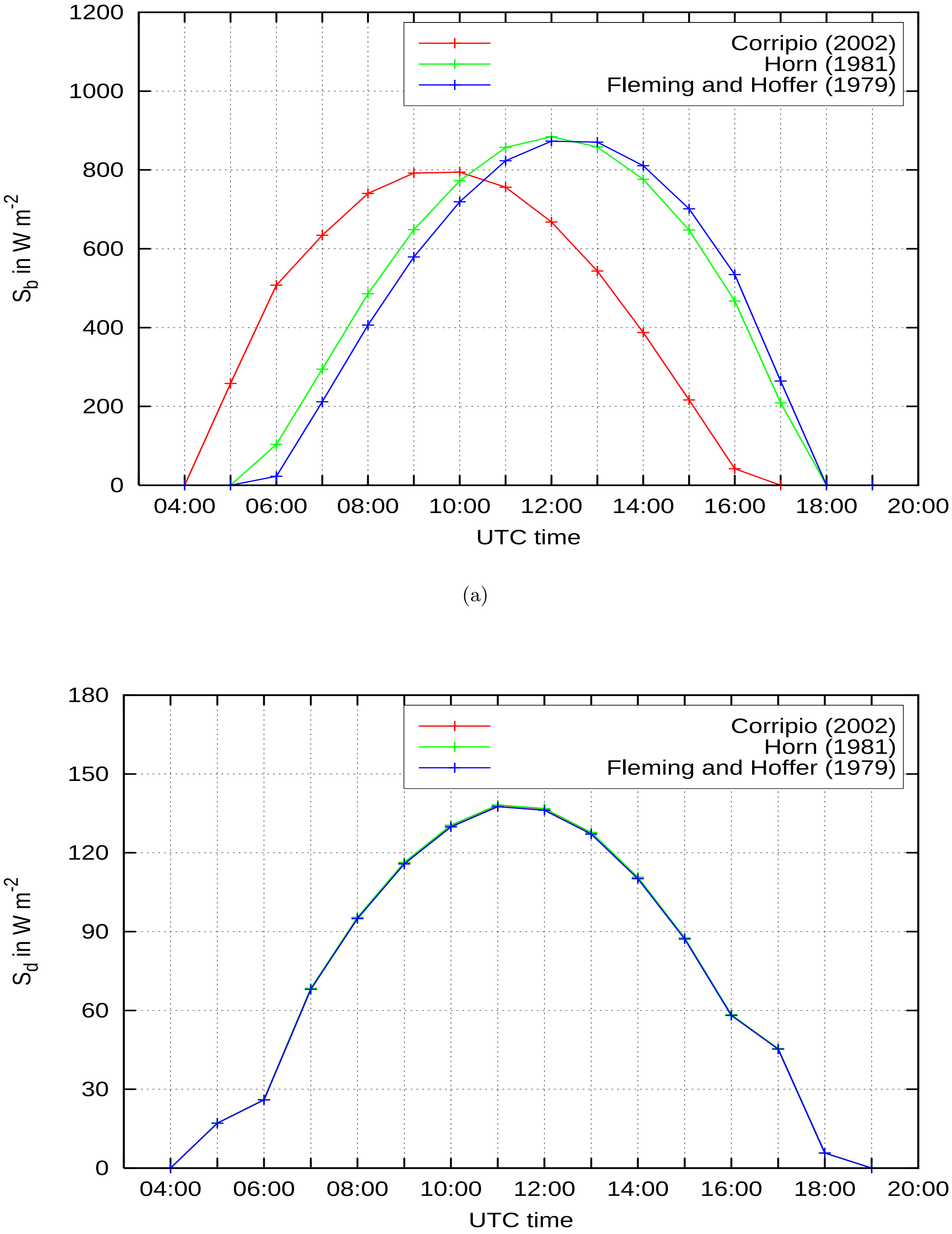

(a)

(b)

Figure 9.3: Comparison of modelled radiation with regard to three different terrain extraction methods for 20 April 2007 on an inclined ridge patch in the Weissfluhjoch DHM. The algorithms of Corripio (2003), Horn (1981) and Fleming and Hoffer (1979) were tested: (a) S_{b}, (b) S_{d}.

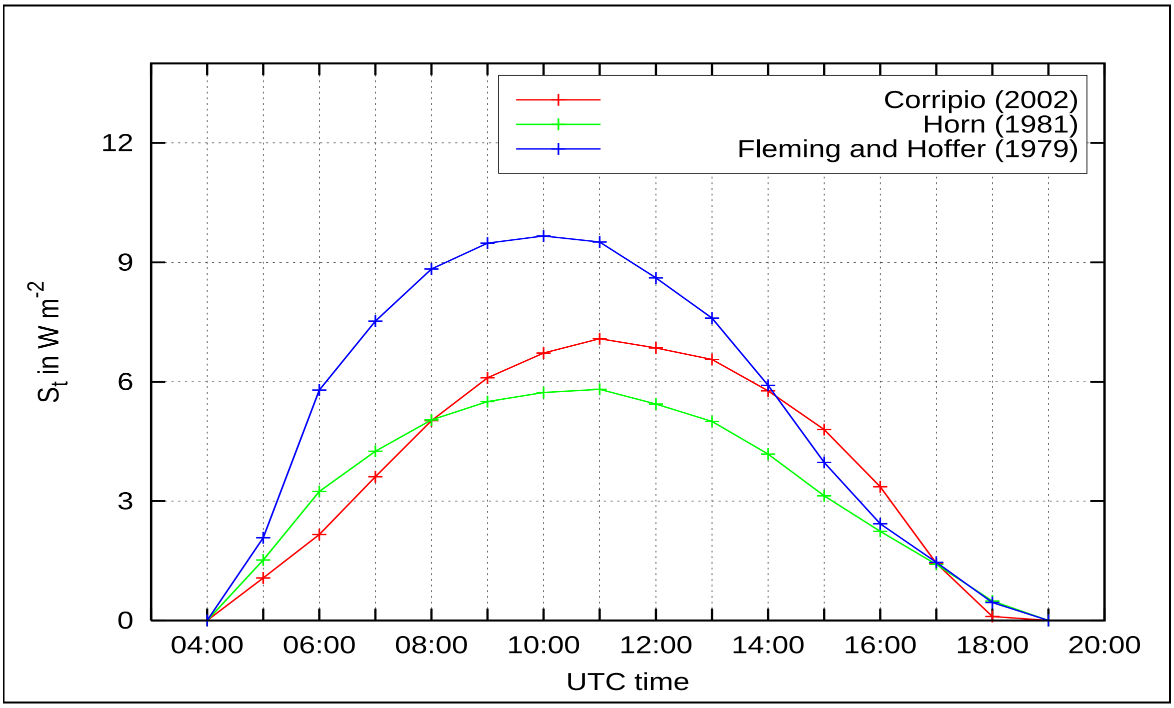

Figure 9.4: Comparison of modelled terrain reflected radiation S_{t} with regard to three different terrain extraction methods for 20 April 2007 on an inclined ridge patch in the Weissfluhjoch DHM. The algorithms of Corripio (2003), Horn (1981) and Fleming and Hoffer (1979) were tested.

9.3 Influence of view factor computation methods

Recall that view factors, which were introduced in Section 4.1.2, p.47, are important factors in the radiosity approach. Therefore in this section, a validation of the view factor computation method that is now implemented in the model is presented. This validation is important since the accuracy of all view factors F_{IJ} has a profound influence on SW and LW terrain and sky radiation. A comparison of the view factor computation with substructuring between two finite surfaces $F_{A_I A_J}$ (Eq. (4.19)) and the simplified view factor solution between a differential surface to a finite surface $F_{\mathrm{d}A_I A_J}$ (Eq. (4.13)) is conducted. Note that $F_{\mathrm{d}A_I A_J}$ can only be exact if A_I is infinitesimal such that $A_I \approx \mathrm{d}A_I$, this is however rarely valid. It was chosen to compare $F_{A_I A_J}$ to $F_{\mathrm{d}A_I A_J}$ and not to $F_{\mathrm{d}A_I \mathrm{d}A_J}$ since $F_{\mathrm{d}A_I A_J}$ is a commonly applied approximation of the view factor between two finite patches. Additionally, $F_{\mathrm{d}A_I A_J}$ was used since this view factor approximation was applied in the radiation balance module before (cf. Martius (2002)). Martius (2002) derived $F_{\mathrm{d}A_I A_J}$ for fixed horizontal and vertical angle intervals by tracing rays. The differences between both view factors accuracies are presented for pairs of patches. Note that the unit length scale is set to one in the following.

Three artificial patch configurations are chosen to point out the differences and consequences between both computation methods. Note that the view factor between two finite surfaces $F_{A_I A_J}$ is computed using Eq. (4.19) with the low substructuring threshold of 0.01.
In Fig. 9.5(a) a configuration is shown with horizontal grid cell dimensions Δx=25, an inclination angle of 45° of the inclined patch A_1 and thus a z_1=25. In Fig. 9.5(b) a configuration

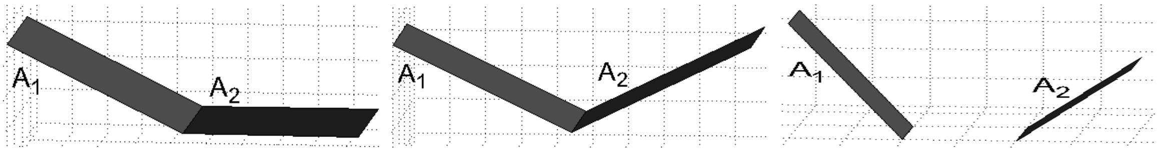

(a) (b) (c)

Figure 9.5: Schematic for artificial patch configurations for the comparison of two view factor computation methods: (a) Δx=25, z_1=25, z_2=25; (b) Δx=25, z_1=25, z_2=25; (c) Δx=10, z_1=40, z_2=25.

is shown where both patches are inclined towards each other by about 45°. Both have grid cell dimensions of Δx=25 and therefore $z_1 = z_2$=25. In the configuration shown in Fig. 9.5(c) the patch A_1 is inclined by 76° (z_1=40) and the patch A_2 by about 68° (z_2=25). Note that in this configuration a grid cell dimension of Δx=10 was used. Furthermore, patch A_1 and A_2 are separated by one Δx. Even though these patch configurations do not represent all possible geometric configurations they provide an insight into errors related to the choice of the method for the view factor computation (cf. Table 9.1). The resulting view factor differences examples are therefore briefly discussed here.

	$F_{A_1A_2}$	$F_{\mathrm{d}A_1A_2}$	ΔF_{12}	$F_{A_2A_1}$	$F_{\mathrm{d}A_2A_1}$	ΔF_{21}
(a)	0.038	0.036	0.002	0.053	0.051	0.002
(b)	0.176	0.225	0.049	0.176	0.225	0.049
(c)	0.118	0.155	0.037	0.180	0.237	0.057

Table 9.1: The computed view factor values are shown for the two computation methods for each of the patch configuration shown in Fig. 9.5. The differences between both methods are presented by ΔF_{12} and ΔF_{21}, respectively.

In case of moderate inclinations, as in example (a), the view factor $F_{A_IA_J}$ is slightly underestimated by $F_{\mathrm{d}A_IA_J}$. In case of steeper inclined surfaces, as in example (b) and (c), the view factor $F_{A_IA_J}$ is overestimated by $F_{\mathrm{d}A_IA_J}$. At first, the absolute view factor differences, between 0.002 and 0.057 with a mean of 0.0327 seem negligible (cf. Table 9.1). However, if each patch (or the sky view factor) in the model domain emits or reflects radiation with an error of approximately 3%, large errors of incident radiation result. E.g. assuming a constant incident radiation of 500 Wm^{-2}, and a 3% error between each pair of patches leads to an error of 15 Wm^{-2} from **each** visible patch in the model domain. These errors might lead to a wrong spatial radiation distribution in the model domain. Therefore, an accurate determination of view factors, as was implemented, is necessary, especially in complex terrain.

In the following, the strong accuracy dependency of Eq. (4.19) on the substructuring threshold is outlined. For the patch configuration in Fig. 9.5(c) the view factor error $\Delta F_{A_IA_J}$ is shown as a function of the threshold x_{sub} in Fig. 9.6. The approximately "correct" view factor values for patch A_1 and A_2, respectively, are obtained from a very low substructuring threshold x_{sub} (Eq. (4.20)) of 0.005, i.e. the maximum side length of the (inclined) patch is less than 0.5% of the distance r_{12} between the patches. For this patch configuration the maximum side length is $\sim$ 41, which is ~90% larger than the distance between the patches

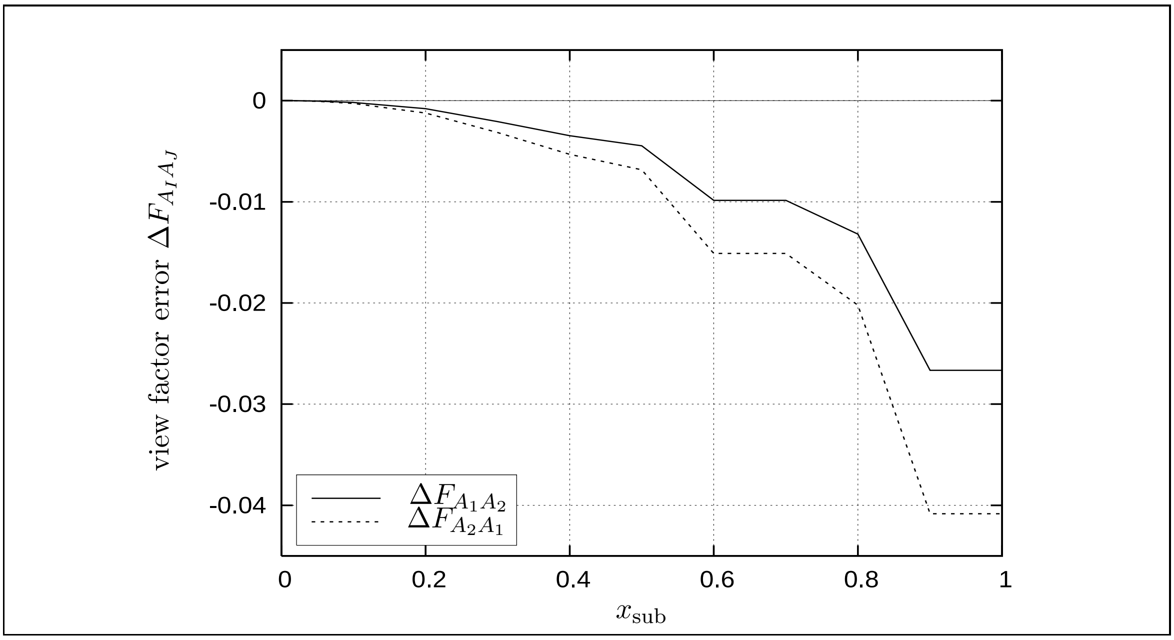

Figure 9.6: View factor error $\Delta F_{A_I A_J}$ with decreasing substructuring threshold x_{sub} for the patch configuration shown in Fig. 9.5(c). $\Delta F_{A_I A_J}$ is the difference between the view factor computed with a threshold of 0.005 and that computed with a threshold x_{sub}.

(r_{12}=21.36). Therefore, for a threshold of 0.001, the patches have to be divided in $\sim 19^2$ subpatches. Here, no substructuring takes place for thresholds larger than ~1.9.
In Fig. 9.6 the view factor errors $\Delta F_{A_1 A_2}$ of patch A_1 and the view factor error $\Delta F_{A_2 A_1}$ of patch A_2 are depicted. Both errors show a similar trend. For substructuring thresholds x_{sub} larger than 0.9 the computed view factors approach those from a differential to a finite surface $F_{\text{d}A_I A_J}$. With decreasing substructuring, $\Delta F_{A_2 A_1}$ is slightly larger than $\Delta F_{A_1 A_2}$. A possible explanation are the larger surface variations of the steeper and hence larger patch A_1 as seen from the less inclined patch A_2. Overall, for this patch configuration large errors occur for substructuring threshold values of 0.5 upwards.

The chosen substructuring threshold of 0.1 according to the point source approximation of McCluney (1994) (Section 4.1.2, p.47) leads to sufficiently accurate view factor values and hence radiation balance. In order to accelerate the view factor computation the substructuring threshold can be increased for applications that require a lower accuracy. For lower thresholds, the view factor computation becomes slower since patches are divided into more subpatches.

9.4 Influence of sky view factor computation methods

Following the validation of the view factor computation methods in the latter section it remains to validate the sky view factor computation method. This is important since sky view factor errors have a large influence on the radiation balance. First, sky view factors are used for the computation of SW diffuse sky radiation S_{d} and LW sky radiation L_{a}. Second, several studies estimate single terrain reflected or emitted radiation by visible terrain fractions obtained from sky view factors derived from horizon angles (e.g. Corripio (2002), Oliphant et al.

(2003), Hock and Holmgren (2005), Müller and Scherer (2005), Arnold et al. (2006)). Thus, sky view factors should be computed accurately. In this section the sky view factor computation method that is implemented in the model is compared to commonly applied derivation methods. In other words it is shown that computing sky view factors from anisotropic view factors F_{IJ} (Section 4.1.2, p.47, cf. Eq. (4.42)) is more accurate than computing sky view factors F_{sky} by extraction from horizon angles (cf. Eq. (4.41)). In addition, some formulas from literature are discussed that approximate sky view factors by extraction from horizon angles. Note that here again units are neglected in the following.

In general different approximations to compute the sky view factor or the terrain view factor sum from horizon angles are used. Thereby, two common sources of errors can be found: i) F_{sky} is assumed to represent the sky solid angle Ω (Eq. (4.4)) and ii) the horizon angle ϑ_{h} is derived for a horizontal plane neglecting the actual inclination of the viewing patch. However, from the continuum equation for $F_{\text{sky}}(x)$ for a patch $A(x)$ (Eq. (4.38) cf. Section 4.2, p.58) it becomes clear that the sky view factor includes the normal vector of patch $A(x)$. Also, Cohen and Wallace (1993) point out that the fraction of radiation of a patch received at another patch is only **proportional** to the solid angle. The common assumption of the equality of solid angle and sky view factor therefore leads to errors in complex terrain. Furthermore, the horizon angle is to be taken in the coordinate system with the z-axis in surface normal direction.
The following formulas for the sky view factor determination are commonly applied in models. Even though not all of them correctly represent the sky view factor they are given since some of them are validated later in this section. Scherer and Parlow (1994) compute $F_{\text{sky},I}$ by means of the sum over 24 horizon angles ϑ_{h}

$$F_{\text{sky},I} = \frac{1}{24} \sum_{l=1}^{24} \cos(\vartheta_{\text{h},l}) \ . \tag{9.1}$$

Also, Oke (1987) notes that in case of a symmetric infinitely long canyon or valley geometry (rather two- than three-dimensional geometry) for a point in the centre the sky view factor can be approximated by $F_{\text{sky}} = \cos(\vartheta_{\text{h}})$ similar to Eq. (9.1). E.g. Li et al. (1999) and Müller and Scherer (2005)) compute $F_{\text{sky},I}$ by

$$F_{\text{sky},I} = \frac{1}{N_l} \sum_{l=0}^{N_l} (1 - \sin(\vartheta_{\text{h},l})) \tag{9.2}$$

with a fixed number of N_l horizon angles. Corripio (2003), Hock and Holmgren (2005) and Arnold et al. (2006)) compute sky view factors by a discretised formula of the correct continuum equation for $F_{\text{sky}}(x)$ of Eq. (4.41)

$$F_{\text{sky},I} = \frac{\Delta\varphi}{360} \sum_{l=1}^{\frac{360}{\Delta\varphi}} \cos^2(\vartheta_{\text{h},l}) \tag{9.3}$$

with φ as the local azimuth direction into which the horizon angle is detected and with $\Delta\varphi$ as the adequately chosen azimuth interval. Note however that a correct discretisation of the continuum equation for $F_{\text{sky}}(x)$ is difficult. Oke (1987) computes the sky view factor similarly for the special case of a point in the centre of a completely enclosed symmetric basin with a constant horizon angle by $F_{\text{sky},I} = \cos^2(\vartheta_{\text{h}})$. In contrast to the computation of the sky view factor from horizon angles in the model of this study the sky view factor is computed by Eq. (4.42) from the anisotropic terrain view factor sum using the normalisation property of view factors.

Before comparing spatial values obtained from the different sky view factor computation methods for a real topography a comparison between sky view factors and solid angles is conducted for the artificial patch configurations given in Fig. 9.5.
The non-equivalence between solid angles and sky view factors is more obvious if the sky is visualised as an additional large surface patch. The same equations, as for the radiosity exchange between two terrain patches described by the terrain view factor F_{IJ}, are valid for the radiosity exchange between the sky patch and a surface patch. By computing the view factor between two differential surfaces $F_{\mathrm{d}A_I\mathrm{d}A_J}$ from the second term of Eq. (4.10) divided by the total radiant flux P leaving $\mathrm{d}A_I$, i.e. $P_I\mathrm{d}A_I$, the following relation is obtained

$$F_{\mathrm{d}A_I\mathrm{d}A_J} = \frac{R \cos\vartheta_I \,\mathrm{d}\Omega_{IJ}\,\mathrm{d}A_I}{P_I\,\mathrm{d}A_I} = \frac{\cos\vartheta_I\,\mathrm{d}\Omega_{IJ}}{\pi}\,. \tag{9.4}$$

For the patch configurations shown in Fig. 9.5 the solid angle $\mathrm{d}\Omega_{IA_J}$ (Eq. (4.6)) is computed using the values for r_{IJ}, A_J and $\cos\vartheta_J$ as given in the following

	$\cos\vartheta_1$	$\cos\vartheta_2$	r_{12}	A_1	A_2	$\mathrm{d}\Omega_{1A_2}$	$\mathrm{d}\Omega_{2A_1}$
(a)	0.3160	0.4470	27.95	883.88	625.00	0.3578	0.3578
(b)	0.7070	0.7070	25.00	883.88	883.88	1.0000	1.0000
(c)	0.8230	0.9998	21.36	412.31	269.26	0.5900	0.7439

Table 9.2: The computed solid angles $\mathrm{d}\Omega_{IA_J}$ are shown for each of the artificial patch configuration of Fig. 9.5.

Clearly, the computed solid angles of the surface patches are not equal to the corresponding view factors (Table 9.1). Instead, the solid angles shown in Table 9.2 overestimate view factors. If the solid angle $\mathrm{d}\Omega_{IA_J}$ is multiplied by the corresponding $\cos\vartheta_I$ of the viewing patch A_I and divided by π, the view factor from a differential to a finite surface $F_{\mathrm{d}A_IA_J}$ is obtained. For example, for the third case (c) $\mathrm{d}\Omega_{1A_2} = \frac{0.59\ \cos\vartheta_1}{\pi}=0.155= F_{\mathrm{d}A_1A_2}$. Thus, when deriving sky view factors for a patch it is at least necessary to consider for the inclination of that patch. Altogether it was shown that neglecting the zenith angle ϑ_I and patch size in the derivation of the sky view factor from horizon angles leads to incorrect sky view factor values.

In the following sky view factors derived from anisotropic terrain view factor sums (Eq. (4.42)) are compared to sky view factors derived from horizon angles. In addition, the impact of the sky view factor computation method is quantified by the example of SW diffuse sky radiation. The comparison is done for the DHM shown in Fig. 6.1 and for one time step at midday for a day in January. At that point of time modelled diffuse sky radiation varies spatially between 40 and 70 Wm^{-2}.
First, in Fig. 9.7 the sky view factor derived from horizon angles is compared to the sky view factor derived from Eq. (4.42). In Fig. 9.7(a) the spatial sky view factor difference between Eq. (4.42) and Eq. (9.3) is shown. In Fig. 9.7(b) the difference between Eq. (4.42) and Eq. (9.2) is shown. Note that the varying azimuth intervals for Eq. (9.3) are determined in the horizontal base plane between adjacent border patches as seen from each patch A_I. Overall, there are less differences in F_{sky} in Fig. 9.7(a) than in Fig. 9.7(b). This was expected since

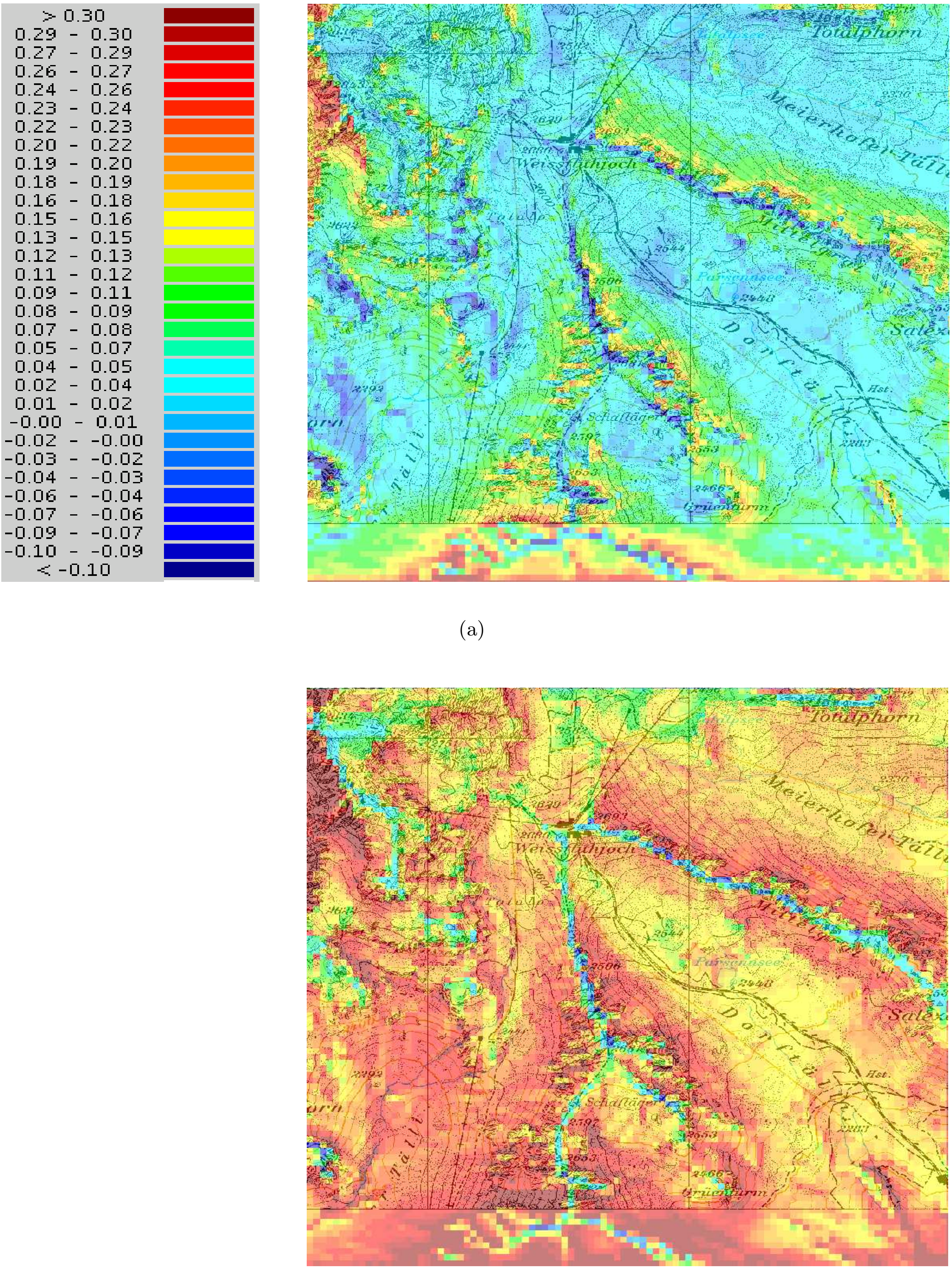

(a)

(b)

Figure 9.7: Comparison of spatial differences between sky view factor values extracted with different formulas from horizon angles and computed from the terrain view factor sum for the model domain shown in Fig. 6.1: (a) Eq. (4.42) minus Eq. (9.3), (b) Eq. (4.42) minus Eq. (9.2).

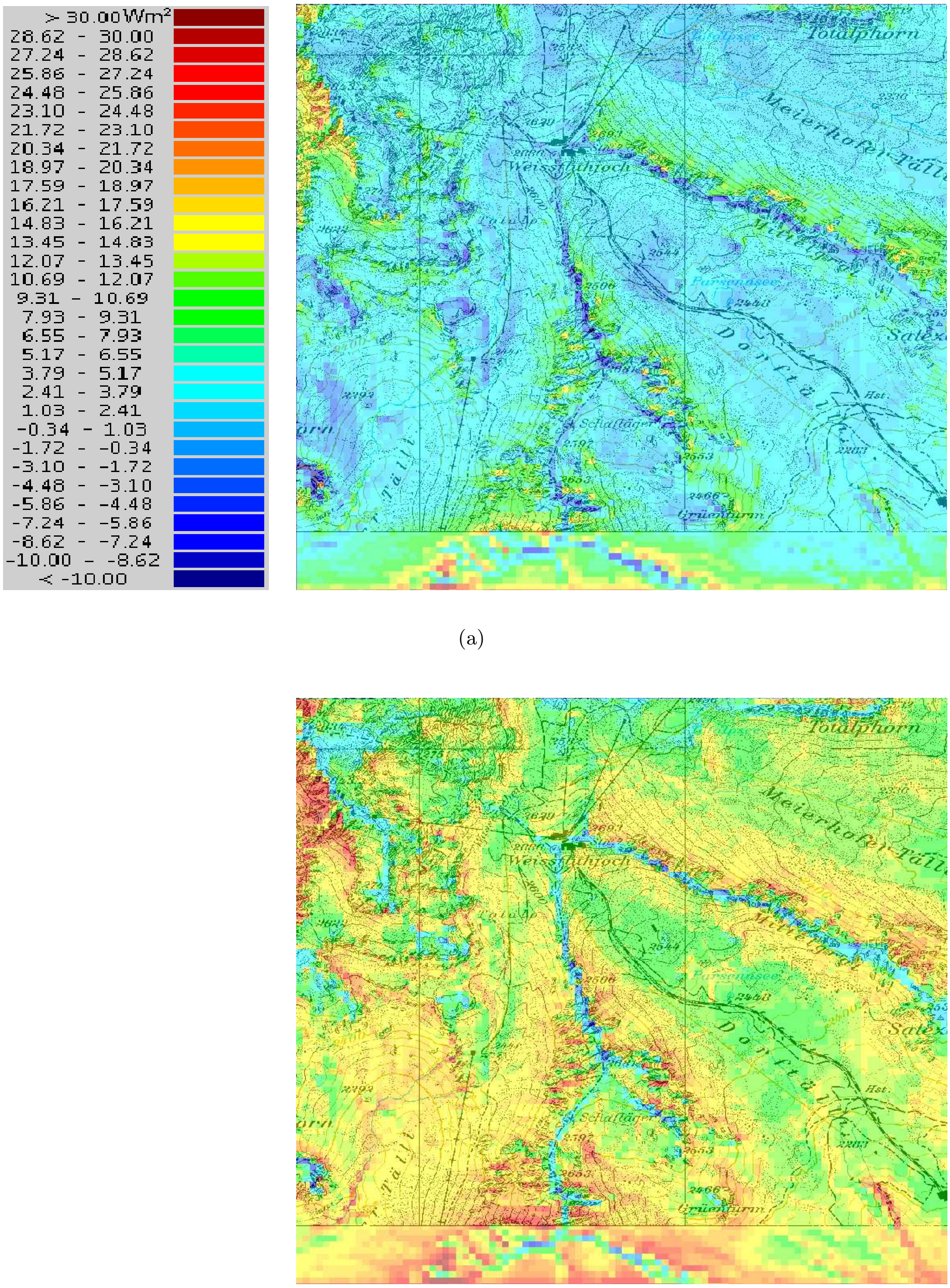

(a)

(b)

Figure 9.8: Comparison of spatial differences of incident diffuse sky radiation computed with sky view factor values F_{sky} extracted from different formulas from horizon angles and computed from the terrain view factor sum for the model domain shown in Fig. 6.1: (a) Eq. (4.42) minus Eq. (9.3), (b) Eq. (4.42) minus Eq. (9.2).

solid angles do not describe the sky view factor correctly. The sky view factor is even more underestimated on inclined patches if derived using Eq. (9.2). The reason for this is twofold: First, sky view factors are underestimated when derived by Eq. (9.2) due to the neglect of inclination of the viewing patch. This error can be explained by means of the resultant solid angles of the three examples shown in Fig. 9.5. All view factors F_{IJ} were overestimated by computing them from the solid angle $\mathrm{d}\Omega_{IJ}$. Therefore, if all view factors F_{IJ} are overestimated the sky view factor, derived by Eq. (9.2), results in underestimated values (Fig. 9.7(b)). Second, an error arises due to the assumption of a horizontal viewing plane thereby neglecting all visible terrain or sky below the viewing plane. The horizontal horizon plane restriction leads to over- or underestimated sky view factor values. For example at the lower border of the model domain lower sky view factors are computed since the sky fraction below the horizontal surface patch is neglected. Similarly, visible terrain as seen from patches on the upper slopes is underestimated. Note that sky view factor errors between the computation methods reach maximum values of larger than 30 % especially if derived from Eq. (9.2) (cf. Fig. 9.7(b)).
Second, in Fig. 9.8 the impact of the wrong different sky view factor computation methods on the diffuse sky radiation S_d is compared. In Fig. 9.8(a) the difference between diffuse sky radiation derived from Eq. (4.42) and that derived from Eq. (9.3) is shown. In Fig. 9.8(b) the difference between diffuse sky radiation derived from Eq. (4.42) and that derived from Eq. (9.2) is depicted. The patterns of both diffuse sky radiation distributions clearly inherit those from Fig. 9.7. Therefore, the discussion about the patterns is not repeated here. The aim was to show quantitative relative differences in diffuse sky radiation for this moderately complex model domain. The derivation of sky view factors from Eq. (9.3) leads to average diffuse sky radiation values which are lower by about 10 Wm^{-2} compared to about 20 Wm^{-2} (maximum differences larger than 30 Wm^{-2}) when derived from Eq. (9.2). These differences of magnitudes are likely larger in steeper terrain and later in the season when larger incident diffuse sky radiation values appear. Recall that on this day in January incident S_d values varies spatially between 40 and 70 Wm^{-2}.

9.5 Influence LW terrain parameterisation

In this section the LW terrain emission parameterisation (Section 3.2.2, p.42, cf. Eq. (3.53)) is compared to terrain emission values computed with Stefan-Boltzmann without accounting for the atmosphere. The terrain emission parameterisation proposed by Landl (2007) parameterises the attenuation of the diffusely emitted radiation of a patch A_J within the air column to a patch A_I. This parameterisation accounts for background radiation within the air column but does not account for scattering into the column or for emission processes of the air in the column. In contrast, terrain emission values computed with Stefan-Boltzmann law ($L_{\mathrm{t},I} = \sigma_\mathrm{SB} T_{\mathrm{s},J}^4 \, F_{IJ}$) consider only surface temperatures. Note that the terrain emission parameterisation may serve as a first and crude assessment of the influence of the atmosphere which is neglected within the radiosity approach.

A first validation is made for the horizontal patch at the LW radiation measurement site within Weissfluhjoch study site for 19 January 1999 (winter day). A second validation is made for the same patch for 24 September 2007 (summer day, i.e. snow free). Both selected days were clear sky days. The model set-up was chosen as described for the modelling in Section 7.1, p.95 and Section 8.2, p.110, respectively. The modelling was conducted for the horizontal elevated sensor patch at Weissfluhjoch study site 50 m aside of the long hut (blue circle in Fig. 6.4) with a terrain view factor $1 - F_{\text{sky}}$ =0.035.

In Fig. 9.9(a) the terrain emission computed with the parameterisation (Eq. (3.53)) is shown in comparison to terrain emission computed with Stefan-Boltzmann law for 19 January. As can be seen, both terrain emission show a similar trend. Consistently slightly lower values of between 0.3 and 0.75 Wm^{-2} are obtained for the computed terrain emission with Stefan-Boltzmann law. The low deviations between both curves appear due to the chosen clear sky winter day at a high altitude with a clean mountain atmosphere. Thus, low attenuation of the air column between the surfaces exist. Additionally, only little and close terrain is visible at the Weissfluhjoch study site patch.

In Fig. 9.9(b) the terrain emission computed with the parameterisation (Eq. (3.53)) is shown in comparison to terrain emission computed with Stefan-Boltzmann law for 24 September. Terrain emission values computed from Stefan-Boltzmann law underestimate the parameterised LW terrain emission slightly during nighttimes and overestimate them slightly during daytimes. The over- and underestimations vary between about 0.5 and 0.7 Wm^{-2} which is below of any sensor and numerics accuracy. It was expected that larger deviations between both terrain emission computation methods appear due to overall warmer air temperatures T_{a} and surface temperatures T_{s}. Thus, when higher attenuation of the air columns between the patches exist. This unexpected behaviour of the parameterised terrain emission should be further investigated e.g. by comparing it to a computed integrated LW radiation along an inclined air column having defined atmospheric properties. Overall it was shown, that for the two investigated days, the differences between terrain emission values obtained with Stefan-Boltzmann and those with the parameterisation of Eq. (3.53) are negligible. Due to this result the neglect of the atmosphere (which is not included in the radiosity approach) is also supported in case of SW radiation exchange.

For completeness in Fig. 9.10(a) measured radiation at Weissfluhjoch study site is shown in comparison to modelled, parameterised radiation on 24 September. For the summer day, the modelled incident radiation mostly overestimates the measured radiation. Maximum overestimations occur during daytime of about 4.5 Wm^{-2}. In contrast, a good agreement was obtained between measured and modelled radiation for the winter day on 19 January (cf. Fig. 7.5). In Fig. 9.10(b) measured radiation at Weissfluhjoch study site is shown in comparison to modelled LW sky radiation only. It can be seen that the computed sky radiation underestimates the measured radiation by at maximum about 11 Wm^{-2}. Thus, by including the terrain emission a much better agreement is obtained. Nevertheless, the overestimations during daytime of about 4.5 Wm^{-2} for the summer day are most likely due to underestimated attenuation of the terrain emission parameterisation leading to overestimated incident terrain emission.

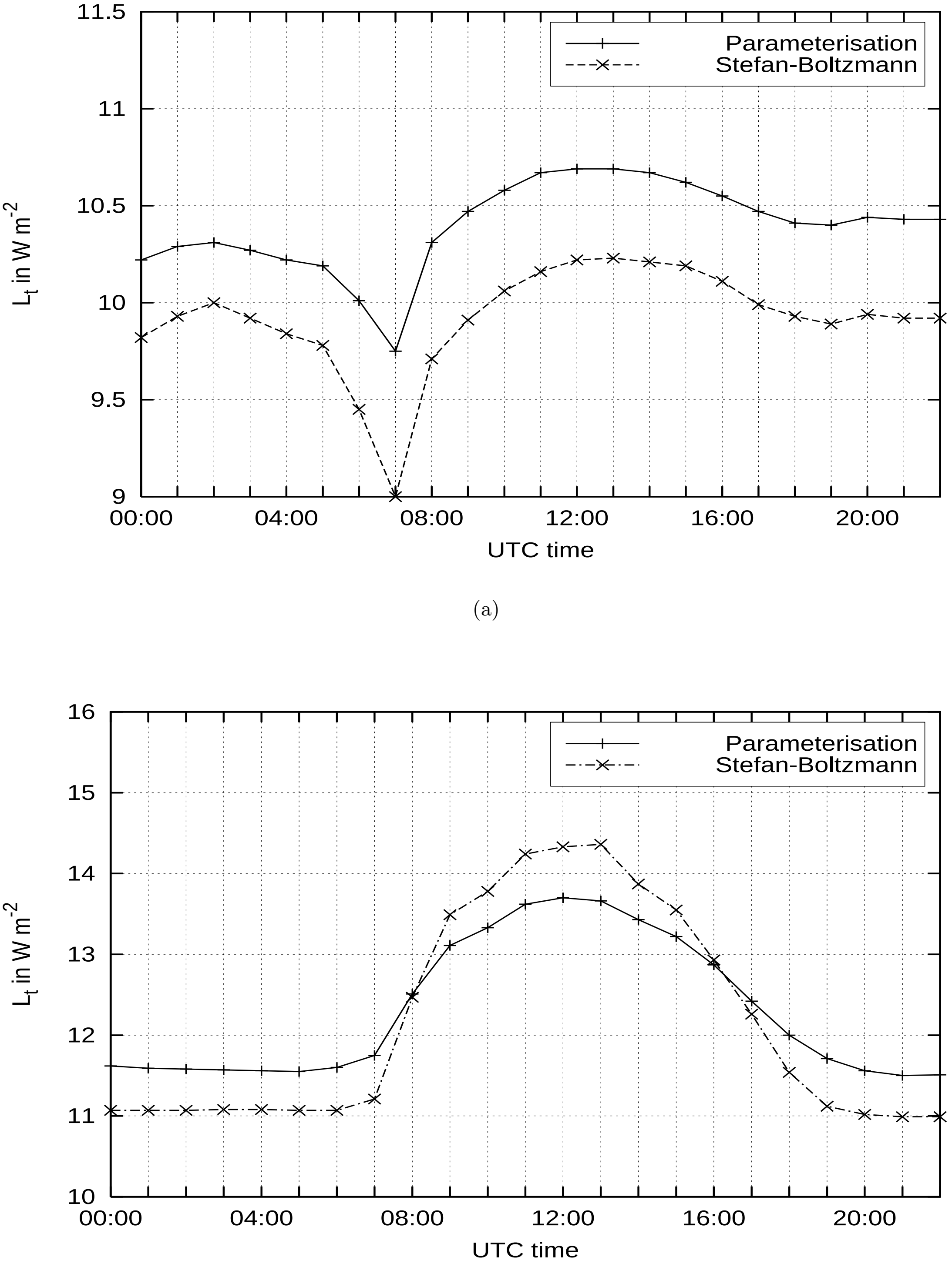

(a)

(b)

Figure 9.9: Comparison of L_t modelled with a terrain parameterisation (Eq. (3.53)) and modelled with Stefan-Boltzmann law at Weissfluhjoch study site: (a) 19 January 1999 (winter day), (b) 24 September 2007 (summer day).

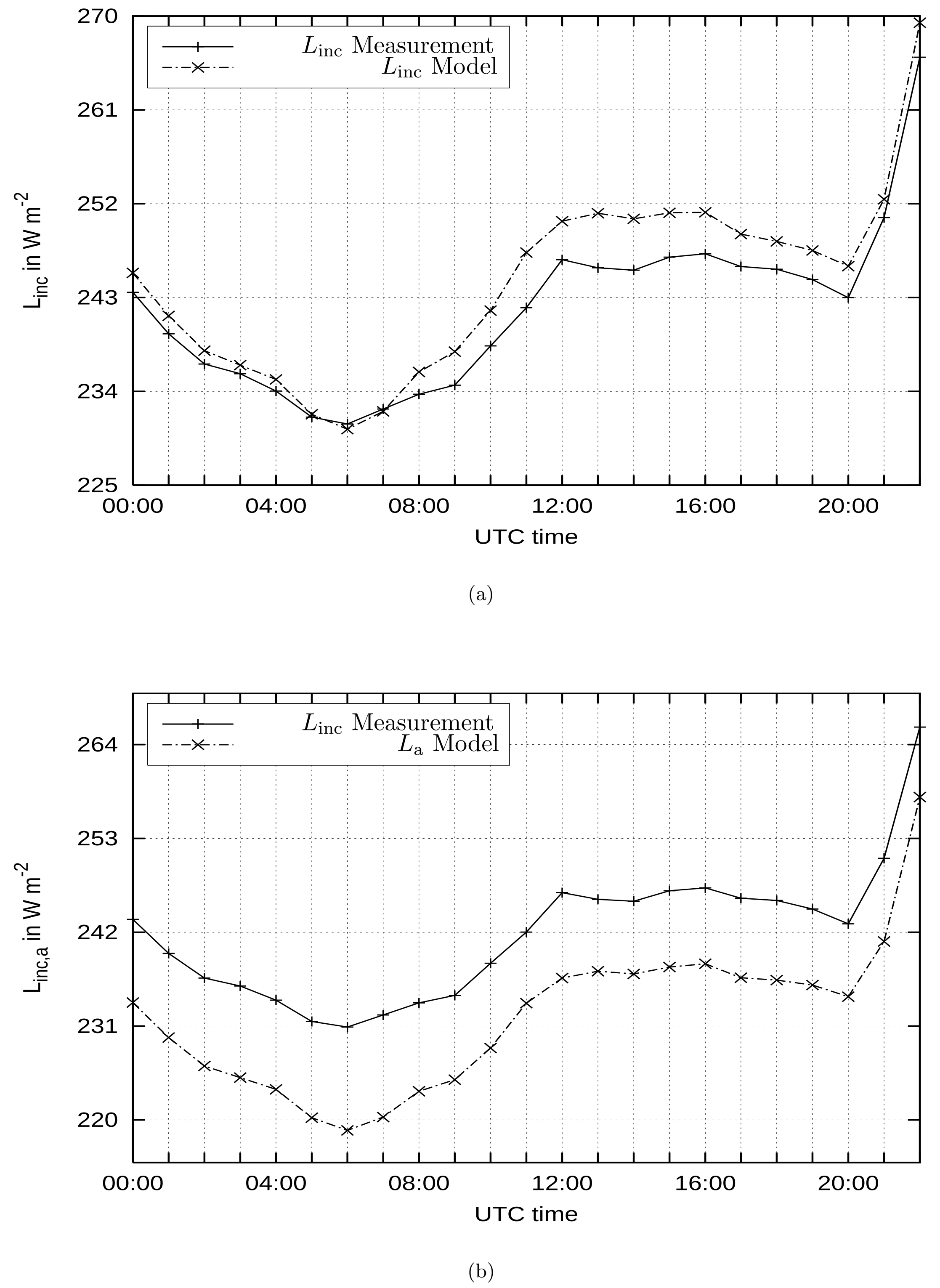

(a)

(b)

Figure 9.10: Comparison of measured L_{inc} and modelled: (a) L_{inc}, (b) L_a for 24 September 2007 at Weissfluhjoch study site (aside from long hut).

10 Generic behaviour of SW terrain reflected radiation in complex terrain

In Chapter 6 to 9 it was shown that all components of the new radiation balance model perform well at specific locations and on specific days for one "real" topography and "real" meteorological input data. This was verified by a quantitative validation with point measurements and sensitivity studies.
However, in this chapter as a next step, the generic behaviour of SW terrain reflected radiation in complex terrain is presented by means of random artificial topographies and the neglect of the distributed incident radiation computed as described in Chapter 3, p.25. This study is necessary to ensure that the model can be applied to a variety of topographies. By investigating the model additionally under extreme conditions (e.g. with a sun elevation angle of 90°) and by varying individual parameters, i.e. here grid resolution and system size, it can be excluded that the model is only applicable for a narrow range of conditions. Furthermore, in this chapter the comparison between the radiosity model and isotropic view factor approach (cf. Section 8.4, p.114) is repeated on artificial topographies to investigate the differences more thoroughly. Additionally, the behaviour of mean domain and effective albedo values are presented on artificial topographies depending on mean albedos and sun elevation angles.

Note that only the SW radiation balance is considered here. For the following analysis, a constant incident direct radiation value of $S_{\mathrm{b},I} = 1000\ \mathrm{Wm}^{-2} \cos\theta_I\ \chi_{\mathrm{sun},I}$ was chosen, that only varies spatially and temporally due to the multiplication with the cosine of the incidence angle (Eq. (3.13)) and due to the sun-or-shadow indicator (Section 2.2, p.19). The sun azimuth is kept constant in south direction ($\psi = 0$). Incident diffuse sky radiation was simply assumed to be 15 % of the direct radiation value. Thus, the spatial diffuse sky radiation is given by $S_{\mathrm{d},I} = 150\ \mathrm{Wm}^{-2}\ F_{\mathrm{sky},I}$. PR iteration (Section 4.2.1, p.63) was used with the stopping criterion defined by Eq. (4.64). Note that the iteration is aborted as soon as the stopping threshold (Eq. (4.68) is reached. The second, more heuristic, stopping threshold (Eq. (4.70)) was neglected in the following investigation. A homogeneous land use with given constant albedo values is chosen such that all feedbacks of the coupled SNOWPACK module are excluded. Thus, in this chapter, a stand-alone verification of the new radiation balance module is presented.
Note that a constant homogeneous albedo was only chosen to keep the simulations as simple as possible. Inhomogeneous albedos are of course possible but have been avoided here to investigate solely the influence of the geometric properties of the underlying DHM.

10.1 Gaussian random fields

In order to systematically study the influence of typical terrain characteristics on the surface radiation balance randomly generated topographies with well-defined statistical properties

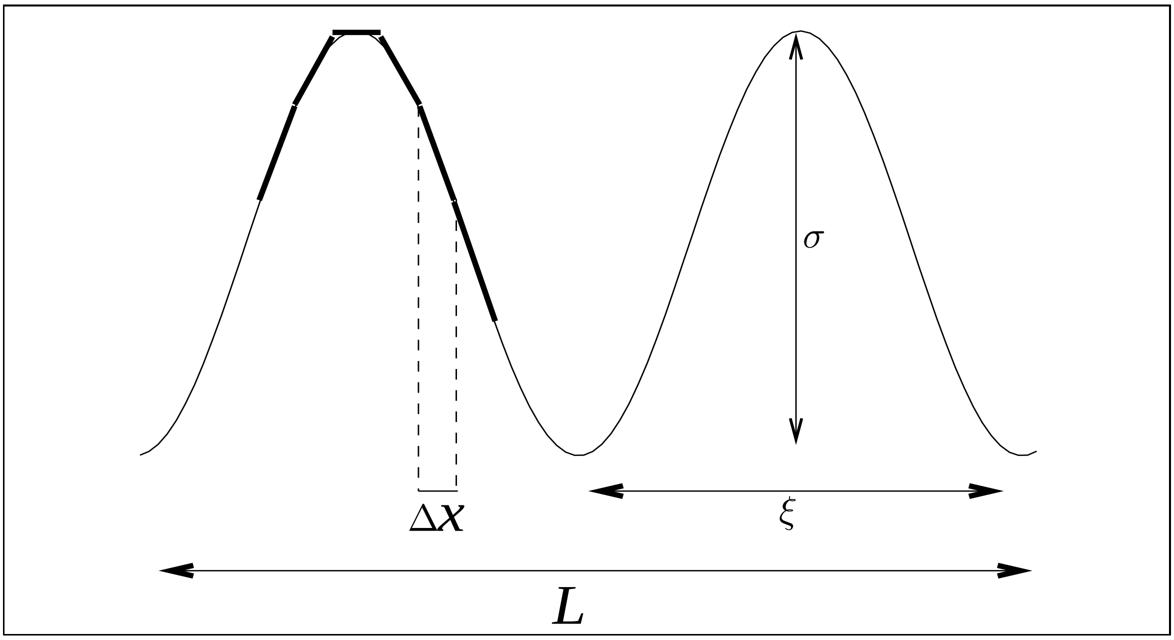

Figure 10.1: Schematic of a random topography taken as DHM with all relevant length scales: The same mean slope σ/ξ can be obtained by different ratios of the lateral extension ξ and vertical extension σ of the mountains (and valleys). The additional length scales are introduced by the numerics (system size L and grid resolution Δx).

were used. However, the statistical properties of real topographies can be quite complex. In Dietler and Zhang (1992) and Weissel et al. (1994) it is shown that DHM correlations of the Swiss Alps, of Ethiopia, Saudia Arabia and Somalia exhibit power law scaling on certain length scales which implies the lack of a characteristic length scale of the surface. However, the following analysis starts from a simpler picture that does assume the existence of characteristic scales.

In general, there are many possibilities to generate random topographies (random fields) with characteristic length scales, i.e. typical lateral extensions ξ (width of mountains) and typical vertical extensions σ (height of mountains) in system sizes L (cf. Fig. 10.1). Here, Gaussian random fields with a Gaussian covariance have been chosen. This choice is motivated by three facts: i) Gaussian random fields are probably the best investigated type of random field. For a good introduction see e.g. Adler (1981). ii) They provide a common starting point for all kind of problems, which involve physical properties in the presence of apparently random constraints. Since such an analysis has never been done before for the radiation problem, it is perfectly justified to start from simple assumptions. iii) From a mathematical point of view the radiosity equation requires smooth, i.e. differentiable surfaces. This is guaranteed by the Gaussian covariance. Thereby, the influence of grid resolution Δx can always be minimised with a sufficiently small Δx.

More precisely, for a discrete DHM the covariance (matrix) is given by

$$C(x_I, y_J) \;=\; \overline{(z(x_I) - \overline{z})\,(z(y_J) - \overline{z})} \;=\; \sigma^2\, \mathrm{e}^{(-|x_I - y_J|^2/2\xi^2)} \;.$$

The mean height vector is taken to be homogeneous with $\overline{z} = 2000$ m. With this choice, the mean slope of the DHM is given by the ratio σ/ξ of the variance σ and the correlation length

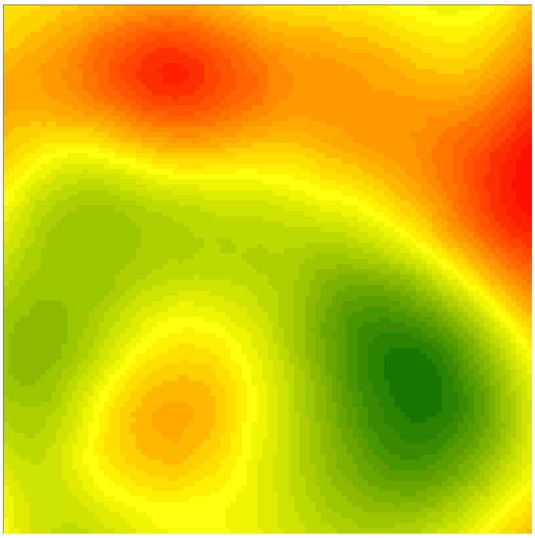

Figure 10.2: Gaussian random field taken as DHM with lateral extension $\xi = 500$, vertical extension $\sigma = 180$, system size $L = 2500$ m and constant grid cell resolution $\Delta x = 25$ m. The DHM has a mean slope of 20° with heights varying around the mean between 1500 m (green) and 2400 m (red).

ξ of the random field, respectively (Adler (1981)). To illustrate the DHM's, one realisation of a randomly generated Gaussian DHM is shown in Fig. 10.2. The heights z roughly vary around the mean between green $\sim$ 1500 m and red 2400 m.

In the following sections various Gaussian randomly generated DHM's were used, i.e. with various combinations of (σ,ξ). Note that for each combination of (σ,ξ) 10 realisations are computed. For the present study this number was sufficient to damp out the statistical fluctuations. However, for investigating further details of the behaviour of the radiation balance a higher number of realisations might be advantageous.

10.2 Influence of mean slopes and solar elevation

In this section the influence of varying slopes and solar elevation angles on terrain reflected radiation S_t is investigated. Two mean homogeneous albedos of 0.3 and 0.8 respectively were tested. Four sun elevation angles of 8°, 30°, 60° and 90° are used such that typical summer and winter solar elevations are well covered. One system size $L = 2500$ m with a grid cell resolution $\Delta x = 25$ m was used. Three realistic mean slopes σ/ξ of 10°, 20° and ~30° were chosen. Each of the mean slopes was realised by three different combinations of (σ,ξ)

1. mean model domain slope angle of 10°:
   - $\sigma = 90$, $\xi = 500$
   - $\sigma = 180$, $\xi = 1000$
   - $\sigma = 270$, $\xi = 1500$
2. mean model domain slope angle of 20°:

  - $\sigma = 180$, $\xi = 500$
  - $\sigma = 360$, $\xi = 1000$
  - $\sigma = 540$, $\xi = 1500$

3. mean model domain slope angle of ~30°:
   - $\sigma = 290$, $\xi = 500$
   - $\sigma = 580$, $\xi = 1000$
   - $\sigma = 770$, $\xi = 1500$

Additionally, a "real" topography was used to test how the simple characterisation of radiation in terms of two length scales compares to a "real" DHM. The DHM around Weissfluhjoch study site with a mean slope of 25° was chosen as the "real" topography (cf. Fig. 6.1). It also has a system size $L = 2500$ m with a grid cell resolution $\Delta x = 25$ m. In order to investigate how the 'real' topography compares to the tested length scales of the random topographies the length scales of the "real" topography are presented. With a covariance $C(x_I, x_I)$ of about 21974, i.e. a σ of about 148, and with a mean slope angle of 25°, leading to a σ/ξ of about 0.47 and thus a ξ of about 315 the "real" topography length scales compare best with the random topography of $\sigma = 180$, $\xi = 500$ and the mean slope angle of 20°.

In Fig. 10.3 mean values of terrain reflected radiation S_t for each of the combination of (σ,ξ) are shown as a function of the four sun elevation angles. The red lines denote a mean slope of 10°, green lines a mean slope of 20° and the blue lines a mean slope of ~30°. The values given in the legend denote varying L/ξ for each slope. The line types in each slope group are arranged according to their L/ξ-ratio. The realistic DHM is denoted by "real" in the legend. In Fig. 10.3(a) an albedo value of 0.3 was used. In Fig. 10.3(b) S_t was computed with the larger albedo value of 0.8.
Terrain reflected radiation increases with increasing sun elevation angles, increasing mean slopes and increasing albedo values. In each group with the same mean slopes the increase of reflected radiation S_t with solar elevation is more pronounced the more terrain is included in the model domain, i.e. with an increasing L/ξ-ratio. In each group with the same mean slopes the largest S_t is obtained for the largest value of $L/\xi = 5.00$. This can be explained by the fact that only typical lateral extensions ξ of 500 always fit several times in the model extension L of 2500 m. This is not necessarily true for $L/\xi = 1.67$ and less often for $L/\xi = 2.50$. Thus, more S_t is obtained with decreasing mountain width ξ (what is equivalent here with decreasing valley width). This also explains why the lines with $L/\xi = 5.00$ always exceed at least one of the two other L/ξ-ratios of the next larger slope group. From these results it is obvious that ξ has to be much lower than L to compute a precise S_t, i.e. $\xi \ll L$. This will be further investigated in Section 10.4. Remarkably large mean S_t values result for large albedos which are similar to albedo values of (new) snow covered patches. As a rule of thumb, **mean** values of reflected radiation in Gaussian topographies vary between 5 and 70 Wm^{-2} for the (realistic) conditions typical for snow covered alpine terrain.

Next, it is shown how the modelled mean reflected radiation values compare to those obtained with a "real" DHM. For both albedos similar orders of magnitudes are obtained for the "real" DHM around Weissfluhjoch study site (Fig. 10.3). The realistic values match best the smallest combination of (σ,ξ) of the 20°-mean slope curves. This is due to two facts. First, the chosen realistic DHM has a similar mean slope of 25°. Second, the realistic

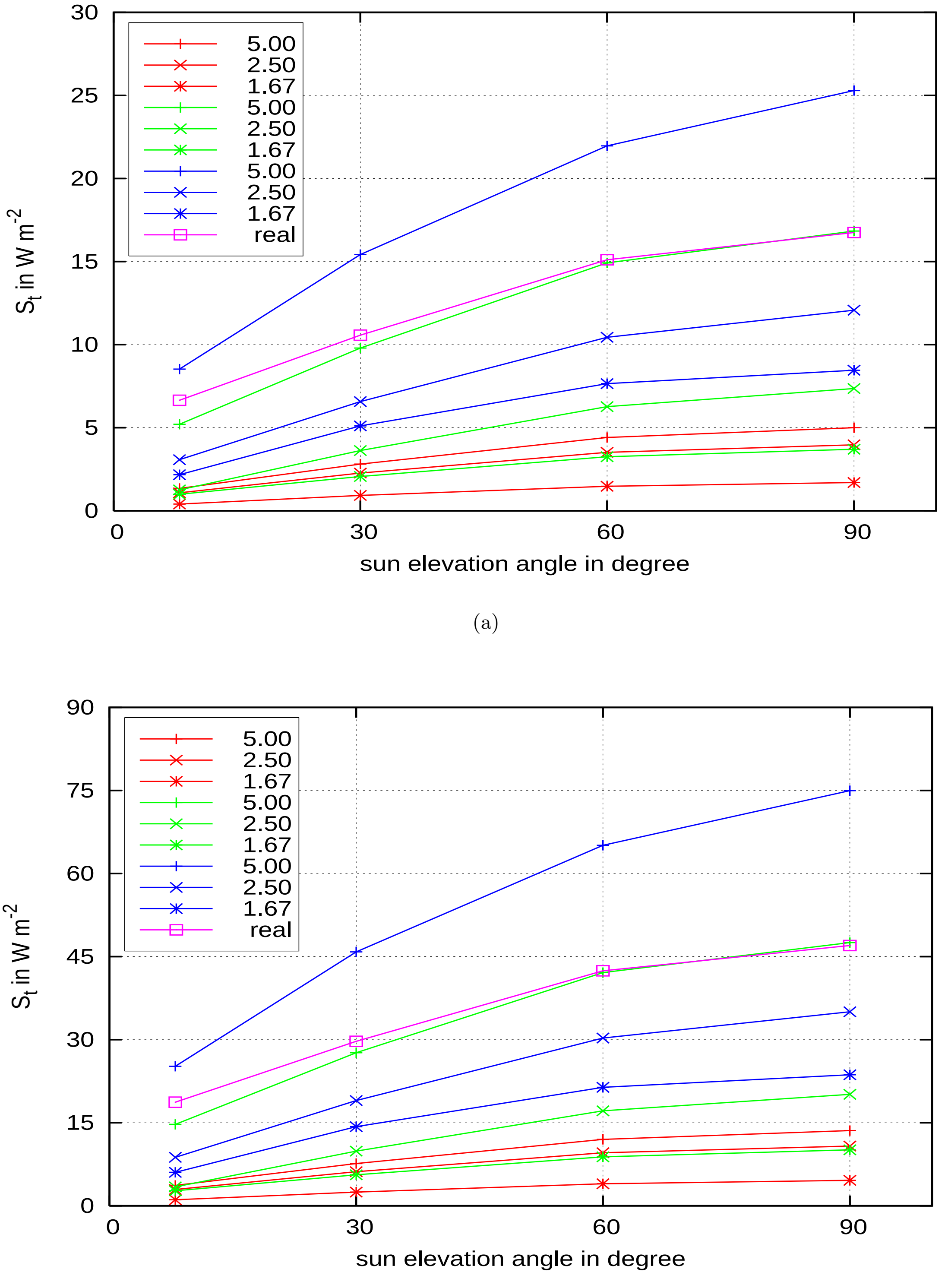

(a)

(b)

Figure 10.3: Comparison of mean S_t for four sun elevation angles and three mean slopes which are realised by different combinations of (σ,ξ) (L/ξ legend, $L = 2500$ m). The "real" topography example with a mean slope of 25° is the DHM around Weissfluhjoch study site: (a) $\alpha = 0.3$, (b) $\alpha = 0.8$.

DHM was chosen in that way that all surrounding mountains, which might cause shading, are taken into account, i.e. at least one complete lateral mountain extension ξ is included in L. Additionally, the chosen realistic DHM length scales resemble the length scales of the smallest (σ,ξ)-combination with a resulting L/ξ-ratio of about 7.94. This is an interesting result: The modelled mean S_t values with Gaussian random fields are in good agreement with a real DHM with comparable length scales. It highlights, that Gaussian random fields can indeed be used to represent real topographies for the investigation of terrain influences on the surface radiation balance.

Note that individual patches can even have a much higher S_t value compared to the mean S_t values shown in Fig. 10.3. Mean, maximum and minimum average values of incident terrain reflected radiation of individual patches could vary remarkable from mean domain values. In Fig. 10.4 averaged mean, averaged maximum and averaged minimum values of S_t are shown for the four sun elevation angles for the intermediate combination of (σ,ξ) with $\sigma = 360$ with $\xi = 1000$, i.e. a mean slope of 20°. Again two albedos are compared in Fig. 10.4(a) and in Fig. 10.4(b). Note that the mean S_t values are the same data as the green line with the crosses in Fig. 10.3.
The larger albedo leads to even larger maximum S_t as with an albedo of 0.3. Minimum S_t values are zero for both albedos. Patches that do not receive any S_t could be flat patches on mountain peaks or patches directed outward in the model domain. Whereas, for an albedo of 0.8, averaged maximum values exceed mean values depending on sun elevation angles by about 10 to 65 Wm^{-2} averaged minimum values fall below depending on sun elevation angles by about 5 to 20 Wm^{-2} (cf. Fig. 10.4(b)). To summarise, individual S_t values can vary remarkably from incident mean values and reach values of $\sim$80 Wm^{-2} which is an important contribution to the radiation balance. Note also that it was shown that the model showed to be applicable for varying solar elevation angles from a very low angle of 8° to a maximum angle of 90°.

In Fig. 10.5 the maximum number of iteration steps for each of the combination of (σ,ξ) is shown as a function of the four sun elevation angles. The red lines denote a mean slope of 10°, green lines a mean slope of 20° and the blue lines a mean slope of 30°. The values given in the legend denote varying L/ξ for each slope. The line types in each slope group are arranged according to their L/ξ-ratio. In Fig. 10.5(a) an albedo value of 0.3 was used. In Fig. 10.5(b) S_t was computed with the larger albedo value of 0.8. Note again that only Eq. 4.68 was used as stopping threshold since it was the aim to highlight the increasing numbers of iteration steps with increasing slope and sun elevation angles.
The maximum number of iteration steps increases with increasing sun elevation angles, increasing mean slopes and increasing albedo values. In each group with the same mean slopes the increase of required maximum number of iteration steps with solar elevation is the more pronounced the more terrain is included in the model domain as indicated by L/ξ. Thus, it could be shown that the developed stopping threshold (Eq. 4.68) performs correctly for varying topographies.

10.3 Influence of grid cell resolutions

In this section the influence on incident terrain reflected radiation of grid cell resolution Δx is investigated. This was conducted for one domain extension L of 2500 m. One combination

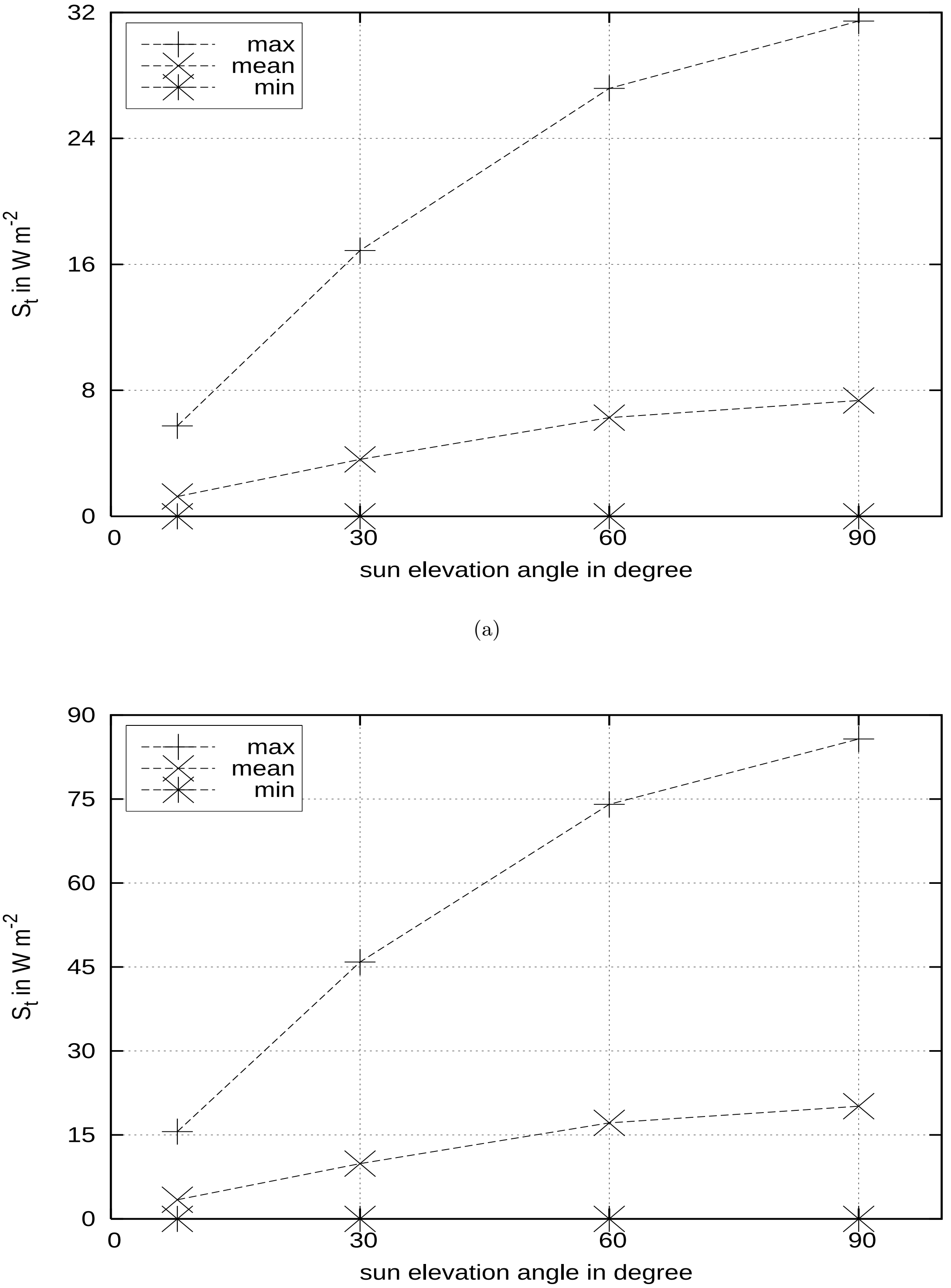

(a)

(b)

Figure 10.4: Comparison of average minimum, maximum and mean of S_t for $\sigma = 360$, $\xi = 1000$ ($L/\xi = 2.50$) and varying sun elevation angles. The legend symbols denote if mean, maximum or minimum values are shown. All lines denote averages for the mean slope realisation of 20°: (a) $\alpha = 0.3$, (b) $\alpha = 0.8$.

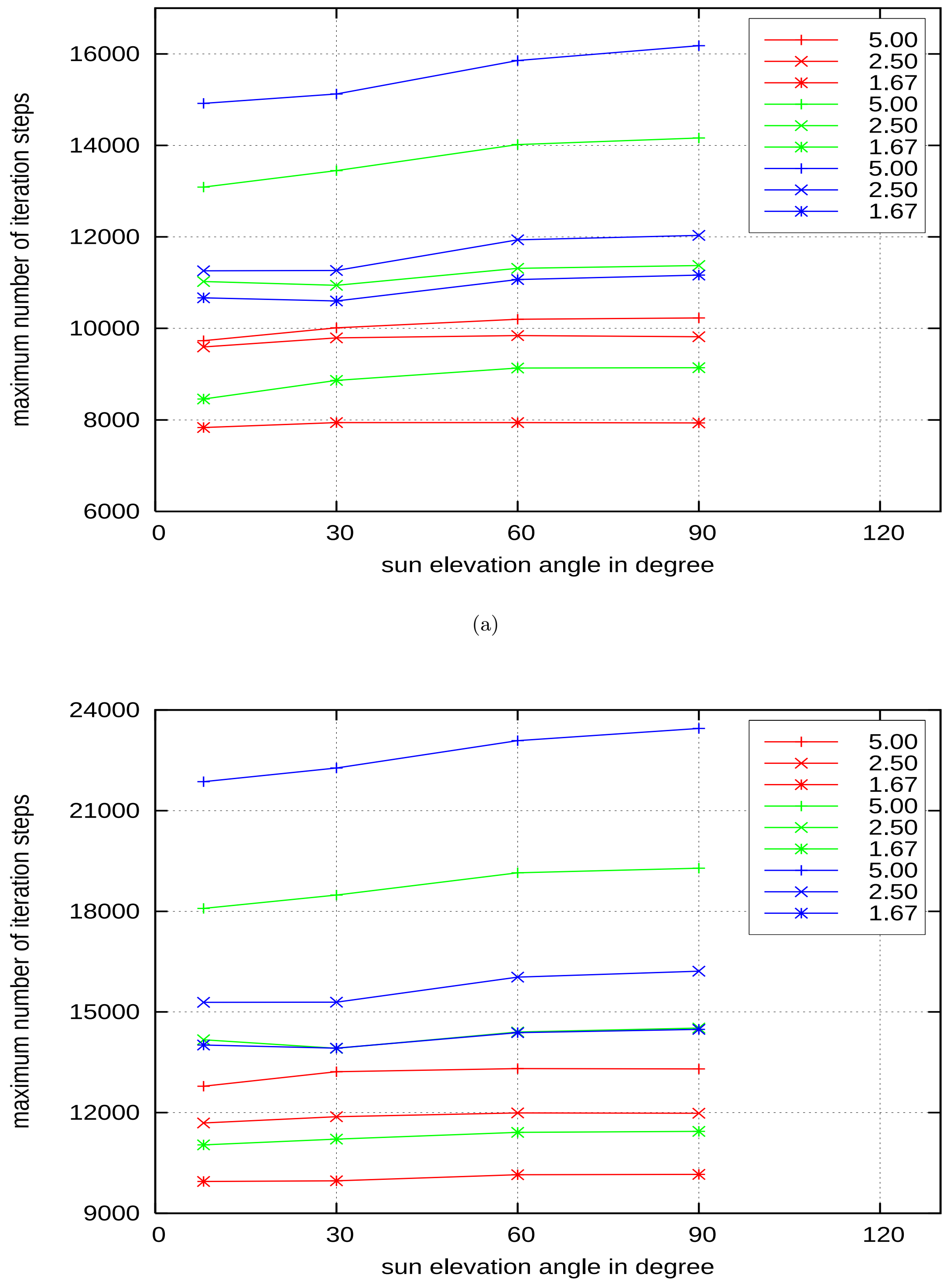

(a)

(b)

Figure 10.5: Comparison of the maximum number of iteration steps for four sun elevation angles, three mean slopes which are realised by different combinations of (σ,ξ) (L/ξ legend, $L = 2500$ m): (a) $\alpha = 0.3$, (b) $\alpha = 0.8$.

of (σ,ξ) with $\sigma = 360$ and $\xi = 1000$, i.e. a mean medium slope angle of 20° was chosen. Two mean homogeneous surface albedos of 0.3 and 0.8, respectively and one sun elevation angle of 60° were used. Three different horizontal grid cell resolutions Δx were investigated:

1. $\Delta x = 25$ m leading to 100×100 grid cells ($N = 10000$)
2. $\Delta x = 50$ m leading to 50× 50 grid cells ($N = 2500$)
3. $\Delta x = 100$ m leading to 25× 25 grid cells ($N = 625$)

In Fig. 10.6(a) mean incident terrain reflected radiation is shown for two albedos and varying ratios of $\xi/\Delta x$, where $\xi = 1000$ is kept constant.
Larger S_{t} is obtained with larger albedo and smaller grid cell resolution. Even though only a small range of grid cell resolutions were investigated it is clearly visible that almost no dependence of S_{t} appears with Δx. At maximum 2.5 Wm^{-2} are obtained (which is below numerical accuracy). This supports the initial motivation to use differentiable Gaussian random fields as DHM's which avoid a misleading dependence of the grid cell resolution as long as $\Delta x \ll \xi$. Note again, that this result is valid for **mean** values. Individual points might show larger deviations. In Fig. 9.2 in Section 9.1, p.127 it was shown that at one specific point in the "real" DHM around Weissfluhjoch study site larger S_{t} was obtained the smaller the grid cell resolution was chosen, which is in agreement with this.

10.4 Influence of system size

In this section the influence of different system sizes on incident terrain reflected radiation is investigated. This was conducted for one horizontal grid cell resolution Δx of 50 m. One combination of (σ,ξ) with $\sigma = 360$ and $\xi = 1000$, i.e. a mean medium slope angle of 20° was chosen. Two mean homogeneous surface albedos of 0.3 and 0.8, respectively and one sun elevation angle of 60° were used. Three different model extensions L were investigated

1. $L = 5000$ m leading to 100×100 grid cells ($N = 10000$)
2. $L = 2500$ m leading to 50× 50 grid cells ($N = 2500$)
3. $L = 1000$ m leading to 20× 20 grid cells ($N = 400$)

In Fig. 10.6(b) mean incident terrain reflected radiation is shown for two albedos and varying ratios of L/ξ, where $\xi = 1000$ is kept constant.
Larger S_{t} is obtained with larger albedo and larger system size. Even though only a small range of system sizes were investigated, a remarkable increase is observable with larger L. At maximum 34 Wm^{-2} are obtained. That means that with larger system sizes L for the same lateral mountain/valley extension ξ an approximately constant mean S_{t} value is obtained. This implies that the system size has to be much larger than the lateral mountain/valley extension to obtain a precise estimate for S_{t}: $L \gg \xi$. This is obvious since terrain reflections are a manifest **non-local** effect.

Note that this was already hypothesised in Section 10.2. Note also that the choice of a larger system size coincides very well with the demand for a larger system size in cloudy RT

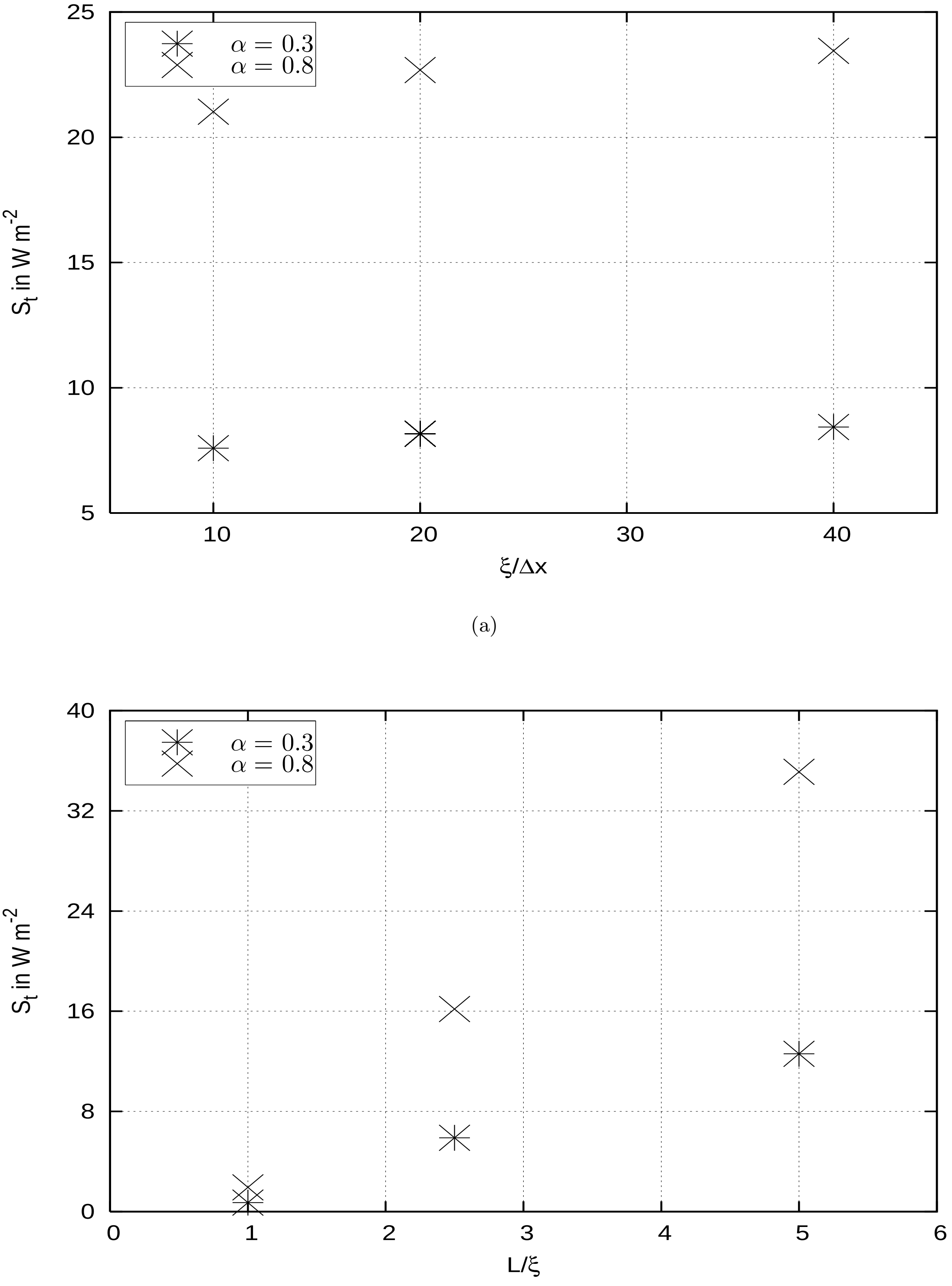

(a)

(b)

Figure 10.6: Comparison of (a) mean S_t for three ratios of $\xi/\Delta x$ which are realised by different grid cell resolutions Δx for a constant $L = 2500$ m and of (b) mean S_t for three ratios of L/ξ which are realised by different system sizes L for a constant $\Delta x = 50$ m. For both the same mean slope of 20° and a ξ of 1000 was used.

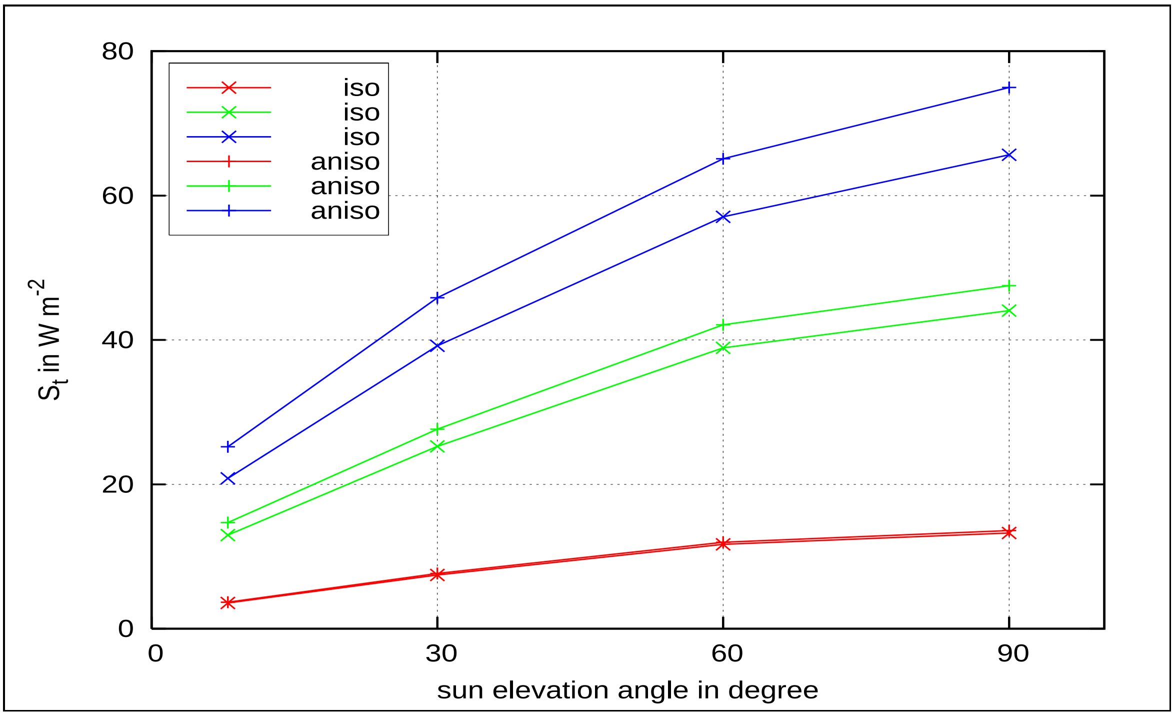

Figure 10.7: Comparison of mean S_t computed from anisotropic view factors and from isotropic view factors for four sun elevation angles and three mean slopes. The smallest mountain/valley width of $L/\xi = 5.00$ of each of the slope groups and a constant albedo of 0.8 was used.

models as backscattering from clouds has an impact from distances more than 10 km away (Degünther et al. (1998), Mayer and Degünther (2000b)) (Section 8.5, p.117).

To summarise, for reliable terrain reflected radiation values, which are not governed by a specific type of topography or by terrain parameters, the following rule of thumb should be valid for the chosen topography parameters

$$\Delta x \ll \xi \ll L \ . \tag{10.1}$$

10.5 Isotropic view factor approach

Mean values of incident terrain reflected radiation derived by the anisotropic view factors with the radiosity approach are compared to those derived by a common parameterisation, i.e. the isotropic view factor approach (cf. Section 9.4, p.134) (e.g. Müller and Scherer (2005)) according to

$$S_{\mathrm{t},I} \ = \ \alpha_I \ (S_{\mathrm{b},I} \ + \ S_{\mathrm{d},I}) \ (1 - F_{\mathrm{sky},I}) \tag{10.2}$$

Note that here in Eq. (10.2) the sky view factor is computed from the anisotropic terrain view factor sum $1 - \sum_{J=0}^{N-1} F_{IJ}$ (cf. Eq. (4.42)) and not from the horizon angles with Eq. (9.1)) as erroneously done by Müller and Scherer (2005).
In Fig. 10.7 S_t values are shown for four sun elevation angles and for three combinations of (σ,ξ). A fixed lateral extension ξ of 500 and different vertical extensions σ of 90, 180, 290

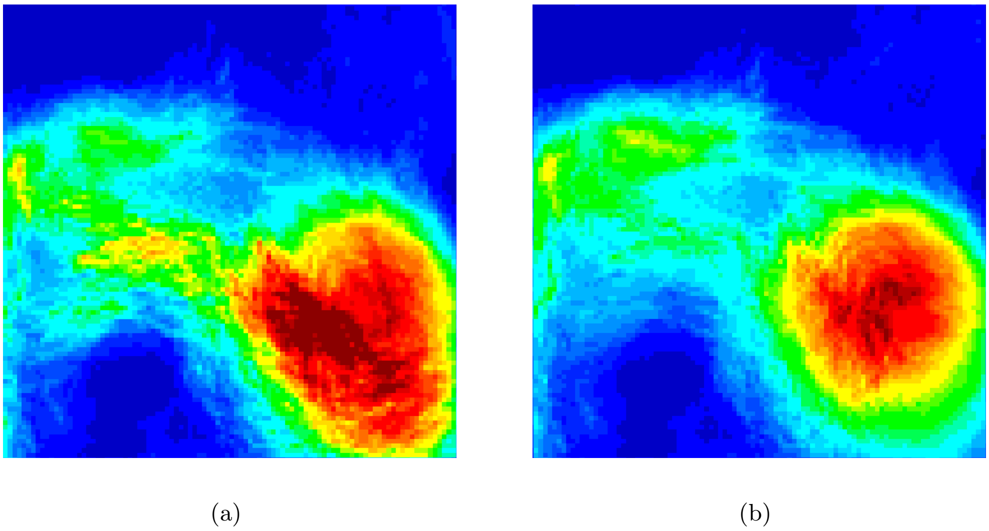

Figure 10.8: Comparison of S_{t} computed from (a) anisotropic view factors and (b) from isotropic view factors for one realisation of a mean slope of 20°. An albedo value of 0.8 and a sun elevation of 60° was chosen. The DHM is given in Fig. 10.2. The same colormap is used for both with dark red ~180 Wm^{-2} and dark blue ~zero Wm^{-2}.

were chosen. Thus, the smallest mountain/valley width $L/\xi = 5.00$ (most terrain influence) of each of the slope groups are represented. The red lines denote a mean slope of 10°, green lines a mean slope of 20° and the blue lines a mean slope of 30°. A homogeneous albedo of 0.8 was used.
For all tested slopes isotropic view factors lead to underestimated S_{t}. The largest differences appear for the steepest DHM and for the largest sun elevation angle. The less pronounced differences for almost flat terrain (mean slope of 10°) were expected since terrain reflections are less important in flat terrain. The largest differences between both arise the more multiple terrain reflections occur, thus in steeper terrain. Both are explainable by the fact, that multiple terrain reflected radiation is not accounted for by the isotropic view factor approach. Note that larger differences might arise the more heterogeneous the albedo pattern is due to the computation of the isotropic $S_{\mathrm{t},I}$ from local albedo α_I. To summarise, for homogeneous albedos **mean** S_{t} values from the isotropic approach are roughly the same as those predicted by the anisotropic view factor approach. Maximum mean S_{t} deviations lie by about 10 Wm^{-2}.

For the spatial distribution of reflected radiation the comparison of both view factor approaches is however more interesting. In Fig. 10.8 spatial S_{t} is shown for a sun elevation of 60°, an albedo value of 0.8 and one DHM realisation with the intermediate mean slope of 20° ($\xi = 500$ and $\sigma = 180$, cf. Fig. 10.2). In Fig. 10.8(a), S_{t} is computed with anisotropic view factors and in Fig. 10.8(b) with isotropic view factors. The same color map is chosen for both with dark red ~180 Wm^{-2} and dark blue ~zero Wm^{-2}. The basin in the lower part on the right in the DHM (cf. Fig. 10.2) is well represented resulting in larger S_{t} values. More symmetric S_{t} values are obtained with isotropic view factors. This was expected since only single reflections are accounted for in the isotropic view factor approach. More asymmetric S_{t} values are obtained with anisotropic view factors and thus multiple terrain reflections, leading to larger S_{t} values on the east facing and north-west facing slopes. Additionally,

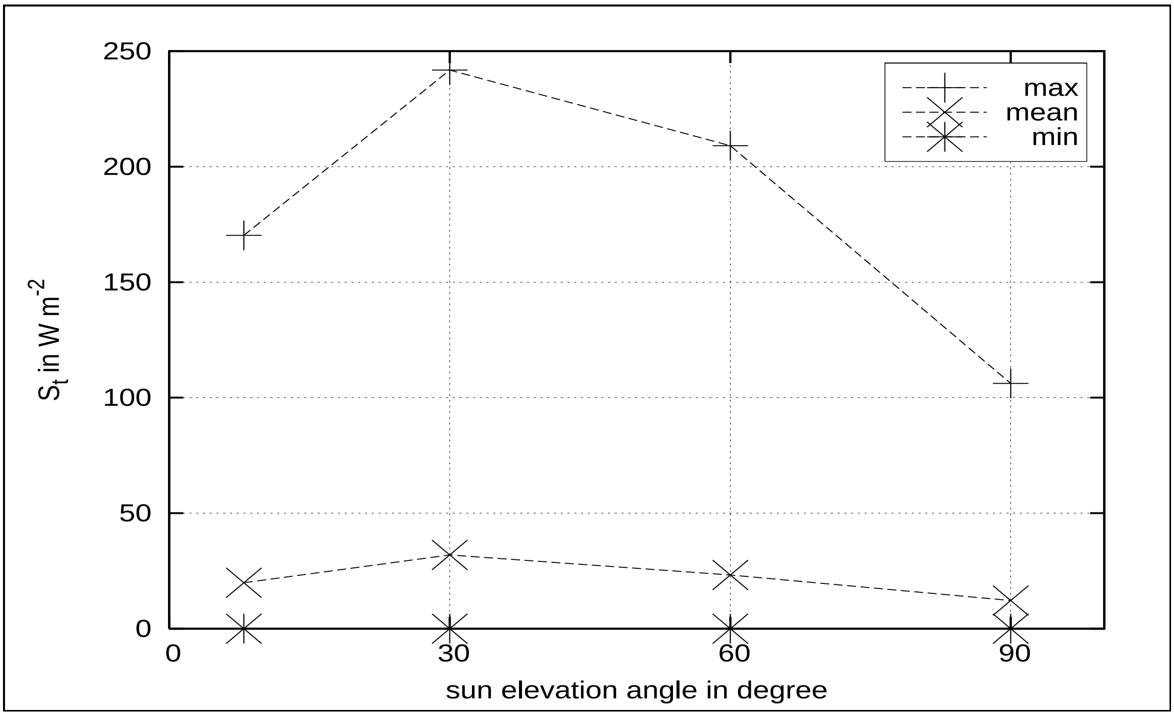

Figure 10.9: Comparison of average minimum, maximum and mean S_t differences between anisotropic and isotropic view factors for $\sigma = 290$, $\xi = 500$ ($L/\xi = 5.00$, mean slope of 30°, a grid cell resolution of $\Delta x = 25$ m), four sun elevation angles and an albedo of 0.8. The legend symbols denote if mean, maximum or minimum values are shown.

about 50 Wm^{-2} more S_t is obtained for anisotropic view factors in the center of the model domain (yellow/orange colour range). This part is actually shaded by the small mountain located in the south of it. Thus, the assumption in the isotropic view factor approach (e.g. Müller and Scherer (2005)) that locally reflected direct and diffuse sky radiation can be used to estimate the incident reflected radiation of the visible surrounding patches clearly fails for shaded patches. Here in this example, it locally leads to a wrong distribution of S_t values and largely underestimated values. Note that this can also erroneously lead to overestimated S_t on those patches that receive a lot of direct and diffuse sky radiation but do see only little terrain.

In order to highlight the large spatial inhomogeneity of incident reflected radiation between both view factor approaches even further, in Fig. 10.9 average minimum, maximum and mean S_t differences are shown. Average differences between both approaches are depicted for the DHM's with the steepest mean slope of 30° (smallest mountain/valley width $L/\xi = 5.00$) and for four sun elevation angles. A homogeneous albedo of 0.8 was chosen. Naturally, average minimum differences are zero for all sun elevation angles. Average mean differences vary between 12 and 32 Wm^{-2}. Average maximum differences however reach remarkable differences between 106 and 242 Wm^{-2}. These large differences demonstrate, that even though average mean S_t values of both do not differ that strongly, local differences can differ remarkably. Again, this emphasises the wrong spatial distributed S_t values when applying the isotropic view factor approach. Largest differences are obtained for a sun elevation angle of 30°. With the intermediate sun elevation of 30° larger differences in incident direct radiation (due to shading) occur which are leading to the aforementioned underestimated reflected radiation with the isotropic view factor approach on shaded patches. The larger the sun elevation angle the less shading occurs, thus less difference between both approaches result. Accordingly, less differences occur for the lower sun elevation angle of 8° due to overall smaller incident radiation with the mean slope angle of 30°. Then, more or less the whole domain is shaded leading to overall reduced multiple reflections. Note that the largest difference (here for a sun elevation of 30°) can be different for a DHM with a different mean slope.

To summarise, **mean** S_t values from the isotropic view factor approach are roughly the same as those computed by the anisotropic view factor approach (cf. Fig. 10.7). **However**, the spatial distribution of S_t values vary remarkably between both view factor approaches (cf. Fig. 10.8 and Fig. 10.9).

10.6 Effective albedo values of complex terrain

At the end of this chapter a completely different though important application of reflected radiation is briefly investigated: the effective albedo of complex terrain. Effective albedo values α_eff are influenced by surrounding terrain, forest, buildings etc., are therefore representative for a larger area and usually considerably lower than the mean surface or local albedo α of the same area. Amongst others Kylling et al. (2000a), Schmucki et al. (2001), Weihs et al. (2001) and Fortuniak (2008) investigated effective albedos for different applications. For example Kylling et al. (2000a) found for Tromsø (Norway) that average albedos are reduced by about 0.2 (wavelength range of 0.32-0.5 μm) if the large fraction of open water was included in their three-dimensional MC modelling. They note that the decrease is wavelength dependent and that further investigations, especially for the influence of topography on albedo values, are required. Similar results were found for the Davos region by Schmucki et al. (2001) from local UV measurements combined with satellite data. They obtained effective albedo values by including the surrounding surfaces within a radius of about 25 km. In general, effective albedos are important to know for regions with highly inhomogeneous surface albedos as it is the case in the presence of snow. They are used e.g. in climate models using larger grid cell resolutions, for the extraction of any parameters from satellite images, for the computation of the energy budget of complex sites etc..

Therefore, in this section, differences between broadband SW mean domain albedo values $\alpha = \frac{\sum_{I=0}^{N-1} \alpha_I}{N}$ and effective albedo values α_eff are outlined. Here, α_eff was chosen to be computed as follows

$$\alpha_\mathrm{eff} \; = \; \frac{\sum_{I=0}^{N-1} (\alpha_I \; S_{\mathrm{g},I} \; F_{\mathrm{sky},I})}{\sum_{I=0}^{N-1} (S_{\mathrm{b},I} \; + \; S_{\mathrm{d},I})} \; . \tag{10.3}$$

Note that S_g contains multiple terrain reflected radiation and that it is reduced by the sky view factor. Note further that the incident direct and diffuse sky radiation in the denominator is computed for inclined patches with sky view factors $\leq$1 and not for a horizontal patch with sky view factors equal to one. According to Eq. (10.3) the effective albedo describes the ratio of diffusely reflected radiation into the visible sky (fraction), including reflected radiation from other surfaces, to the incident radiation on inclined surfaces without reflected radiation. Thus, effective albedo values are expected to be lower than domain means of local albedo values.

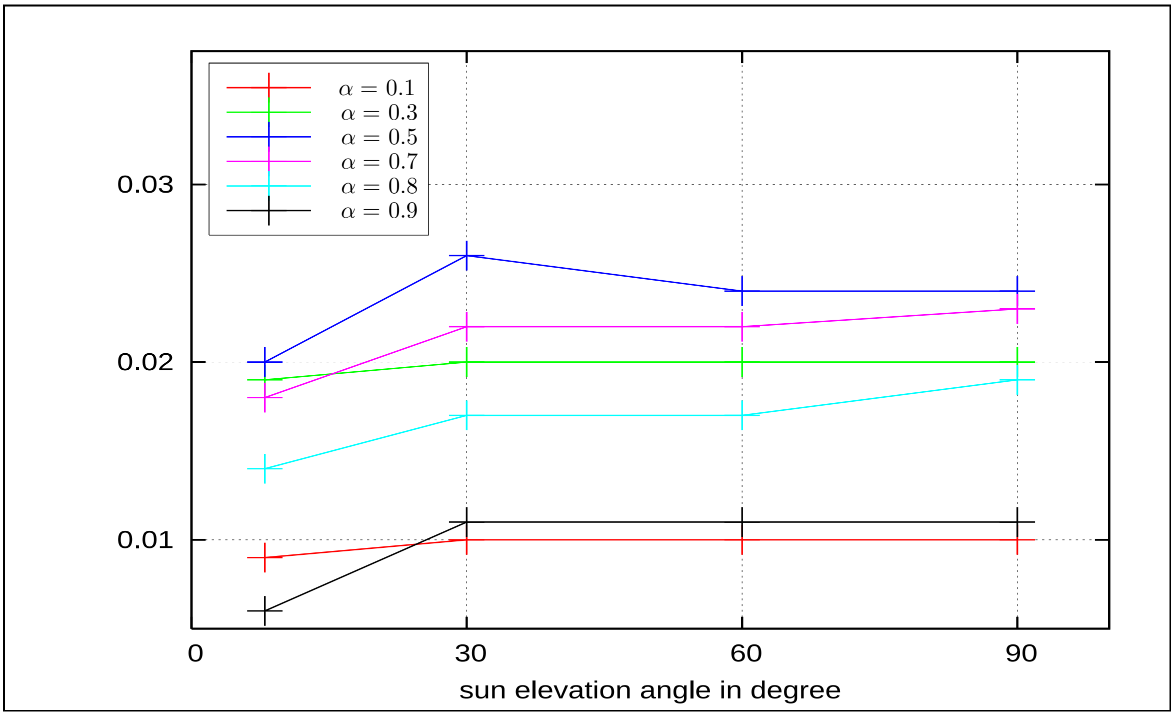

Figure 10.10: Comparison of differences between mean domain albedos α and effective albedo values α_{eff} are shown for four sun elevation angles for one combination of (σ,ξ) with $\sigma = 290$ and $\xi = 500$, i.e. a mean steep slope angle of 30°, a $L/\xi = 5.00$ and a grid cell resolution of $\Delta x = 25$ m.

In Fig. 10.10 average albedo differences $\alpha - \alpha_{\text{eff}}$ for six albedos are shown for four sun elevation angles of 8°, 30°, 60° and 90°. One system size of $L = 2500$ m, one grid cell resolution $\Delta x = 25$ m and one combination of (σ,ξ) with $\sigma = 290$ and $\xi = 500$, i.e. a mean steep domain slope of 30° was chosen. As can be seen, the effective albedo is not a constant, but a function of solar elevation. The albedo differences slightly increase with sun elevation angles. As expected, for all mean albedos the effective albedo is lower. Largest albedo differences are obtained for a mean albedo of 0.5 of about 0.025, lowest for a mean albedo of 0.1 and 0.9 of about 0.01.

In order to further study when largest and lowest albedo differences are obtained each albedo difference was averaged over the four sun elevation angles. In Fig. 10.11 the averaged albedo differences are shown for each of the mean albedos. The low albedo difference for the low albedo of 0.1 is clearly due to low multiple reflections. Then, the mean domain albedo resembles the effective albedo. The low albedo difference for the large albedo of 0.9 is due to that the large albedo value leads to enhanced multiple reflections. If the mean domain albedo approaches one the albedo difference approaches zero. This is an important result: In case of large mean domain albedo values, the complex terrain does not trap radiation by multiple terrain reflections but instead enhances the overall mean terrain reflected radiation. The maximum albedo difference, here at 0.5, will of course differ for a DHM with a varying mean slope.

In the following, it was briefly investigated if the averaged albedo difference (cf. Fig. 10.11) can be solely represented by geometric terrain parameters. For this, Eq. (10.3) is averaged

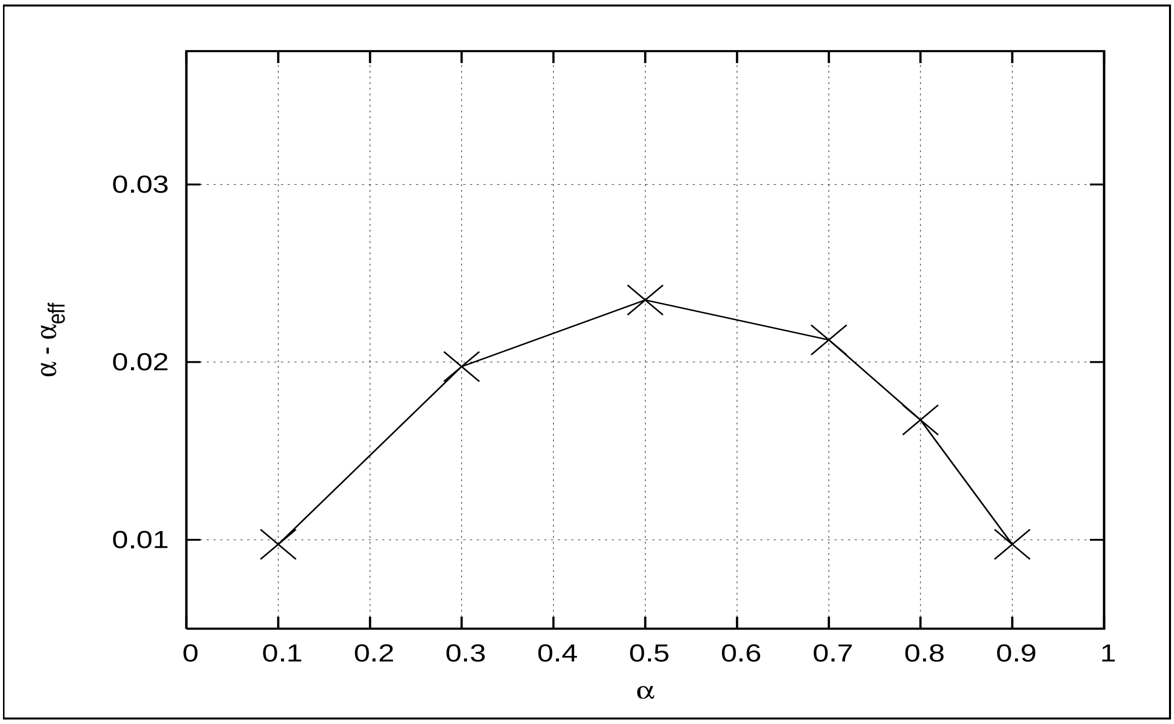

Figure 10.11: Comparison of differences between mean domain albedos α and effective albedo values α_{eff} averaged per sun elevation angles are shown for one combination of (σ,ξ) with $\sigma = 290$ and $\xi = 500$, i.e. a mean steep slope angle of 30°, a $L/\xi = 5.00$ and a grid cell resolution of $\Delta x = 25$ m.

over all sun elevation angles

$$\alpha_{\text{eff}} \;=\; \alpha \;\frac{\overline{\sum_{I=0}^{N-1} S_{\text{g},I}\; F_{\text{sky},I}}}{\overline{E_I}} \tag{10.4}$$

where the emission $\overline{E_I}$ represents the sum of incident direct and diffuse sky radiation. Second, for **small** albedos $\overline{S_{\text{g},I}}$ is approximated by $\overline{S_{\text{g},I}} = \overline{E_I} + \alpha(1 \;-\; \overline{F_{\text{sky},I}})\overline{E_I}$ leading to

$$\alpha_{\text{eff}} \;=\; \alpha \;\frac{(1 \;+\; \alpha\;(\overline{1 \;-\; F_{\text{sky},I}}))\;\overline{E_I}\;\overline{F_{\text{sky},I}}}{\overline{E_I}} \;\approx\; \alpha\;\overline{F_{\text{sky},I}}\;(1 \;+\; \alpha\;(1 \;-\; \overline{F_{\text{sky},I}}))\;. \tag{10.5}$$

Thus, for low mean albedo values, the albedo difference $\alpha - \alpha_{\text{eff}}$ is approximated by

$$\alpha \;-\; \alpha_{\text{eff}} \;\approx\; \alpha\;\left[1 \;-\; \overline{F_{\text{sky}}}\;(1 \;+\; \alpha\;(1 \;-\; \overline{F_{\text{sky}}}))\right]\;. \tag{10.6}$$

Now, in Fig. 10.12, Eq. 10.6 is added to the averaged albedo difference, shown in Fig. 10.11. For this, the computed mean sky view factor $\overline{F_{\text{sky}}}$ of 0.907 was inserted for the chosen combination of (σ,ξ). The rough approximation for the mean albedo differences is in good agreement for the differences at low albedos. In fact, even though for large albedos the approximation is not correct, maximum deviations of only about 0.005 are obtained. This is an interesting result that has to be further investigated.

Actually, the computed mean albedo differences of about 0.02 between both albedos seem to be small. Nevertheless, they will play an important role for larger and more complex system

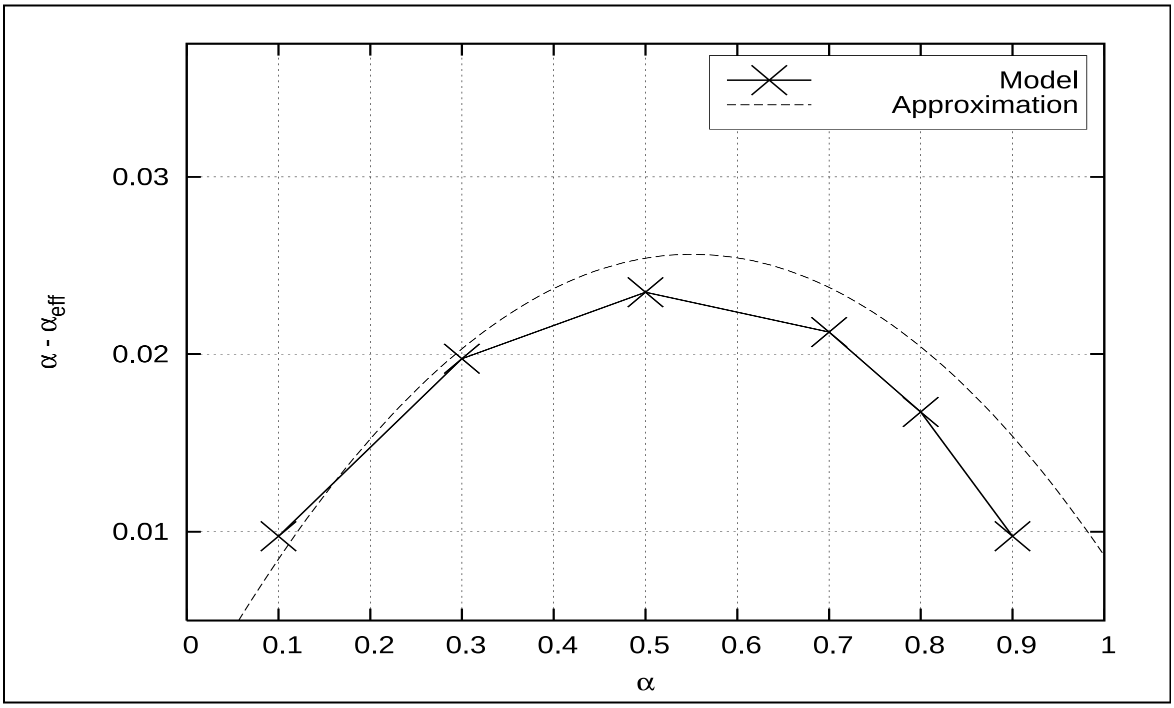

Figure 10.12: Comparison of modelled differences between mean domain albedos α and effective albedo values α_{eff} averaged per sun elevation angles for one combination of (σ,ξ) with $\sigma = 290$ and $\xi = 500$, i.e. a mean steep slope angle of 30°, a L/ξ =5.00 and a grid cell resolution of $\Delta x = 25$ m. The approximated curve is computed according to Eq. (10.6).

sizes and for heterogeneous albedo values. As mentioned earlier, Kylling et al. (2000a) found larger average differences in the order of 0.2 for a "real" model domain around Tromsø (Norway).

Finally, to estimate the error inherent in the albedo difference the relative albedo error $\delta\alpha$ is computed

$$\delta\alpha \; = \; \frac{\alpha \; - \; \alpha_{\text{eff}}}{\alpha} \; 100\% \; . \tag{10.7}$$

The relative albedo errors are of the order of 1 to 10 %. For example, for the mean domain albedo of 0.7 and a sun elevation angle of 60° the relative albedo error is $\frac{0.022\;100\%}{0.7} = 3.1\%$. Thus, since mean mountainous model domain albedos usually lie in the intermediate range of albedos, when the relative albedo errors are largest (cf. Fig. 10.10), the albedo difference can have a remarkable influence on the radiation balance.

Part IV

Alpine3D application

11 Simulating surface temperatures of winter roads with Alpine3D

A good knowledge of local surface temperatures provides valuable information for indicating possible ice formation on roads (e.g. sudden black ice formation). With that knowledge a safe and continuous traffic flow can be ensured since this is important for decision making of the appropriate time and manner of a road treatment. By the aid of more systematic road treatments the environment can be preserved and costs can be reduced. In Switzerland, interest groups exist that try to enable access to mountain passes as long as possible. One of the main reasons is clearly the economic advantage. E.g. an interest group for the Gotthard pass wants to enable the summer inns to keep their businesses running for a longer time period. Until now they have to close due to the lack of a cleared mountain pass (Stalder (2004)). Another example is the Flüela pass road, which is regularly kept open until New Year because of a local profitable event. Very often, these passes serve as important traffic connections. Even though avalanche danger is a main risk for passess, explosions, similar to the securing of ski pistes, could secure roads. The main problem for the local road authorities is that they usually have large and complex alpine catchment areas. Quite often they therefore have to rely on personal experiences in their area. A model that can predict local road surface temperatures in their large (mesoscale) catchment area would therefore be desirable.

Lots of research concerning specific aspects that contribute necessarily to road condition forecasting e.g. additional heat contribution of vehicles to the road, longwave cloud cover feedbacks has already conducted by various authors. According to Bouilloud and Martin (2006) since the 1980s different models were generated that predict road surface conditions (Thornes (1984), Rayer (1987), Shao (1990), Sass (1992), Crevier and Delage (2001)) focusing mainly on road surface temperature as well as surface ice. Usually the ice was treated as a bucket-type reservoir on roads due to the complexity of all involved aspects (rainwater freezing, hoarfrost, freezing surface water, freezing fog). Therefore, Bouilloud and Martin (2006) built a model by coupling of two one-dimensional models: the soil, biosphere and atmosphere model ISBA (Noilhan and Planton (1989)) and the snow model CROCUS (Brun et al. (1989), Brun et al. (1992)). This model simulates road surface temperatures, characteristics of the layer between snow and the road (interface where snow and road cannot be distinguished), snow accumulation on roads, road liquid water and ice content on the road surface. Several changes to both models were necessary to adapt the model for road conditions. In ISBA all processes associated with vegetation were removed. Since roads are impermeable except for a thin surface layer all hydrological transfers were neglected below this layer. In CROCUS an extra parameterisation of the water-saturated snow layer at the bottom of the snow pack was introduced. This first snow layer above the road was kept constant on a value of 0.0025 m by allowing for partial aggregation with the layer above. In addition the hourly snowfall adding to the snow pack was spread out over each small time step of 5 min. Bouilloud and Martin (2006) tested their model in a comprehensive field campaign held at the Col de Porte

laboratory. Real pavements (covering the structures used in France) were constructed and equipped with numerous sensors and video cameras. By preparing the meteorological input as accurate as possible without applying a model they simulated road surface temperatures and the presence of snow on the pavement slices by reducing the time step further to 30 s in the case of snowfall on a warm snow-free road. Their results demonstrate that the model was accurate enough to simulate these two parameters.
A lot of progress has been achieved of the description of the processes concerning the interfaces on the road and accordingly road temperatures. However, there is still a lack for a model that can predict spatial road surface temperatures on a scale in the order of tens of meters in complex terrain. Additionally, there is no model that considers for all terrain influences and is in the same time transferable to different model domains. Large scale meteorological model forecasts are adopted (with or without modelling) according to different general predefined criteria/singularities e.g. bridges, shaded sections or pass roads.

The SNOWPACK module has already been applied for the investigation of the thermal regime of Greenlandic roadbed banked on permafrozen deposits. According to Mauz (2006) snow properties and soil temperatures could be modelled with sufficient accuracy. Flury (2006) measured albedo values for different road conditions on the Flüela pass road at Davos, Switzerland and developed a multiple regression model for road albedo values depending on several meteorological parameters as well as on road condition and road treatment, respectively. With Alpine3D (Chapter 5, p.79) he conducted sensitivity studies to investigate the influence on modelled dry road surface temperatures and compared them to measured road surface temperatures at one specific measurement site on the road. Maximum road surface temperature deviations on a dry road during day occurred from 1 to 3°C. He tested the influence of three different constant mean dry albedo values, the influence of two different asphalt thicknesses leading to variations in heat conductivity and heat capacity and the influence of the size of the applied model domain. He concluded that for his measurement site the major differences in modelled road surface temperatures for a clear sky day were obtained by varying the constant mean dry surface albedo values. A variation of the dry albedo value from 0.07 to 0.21 resulted in a modelled surface temperature difference of up to 4°C.

Here, the coupled surface process model Alpine3D is used to model spatial winter road surface temperatures for a specific part of the Gotthard motorway (Canton Uri, Switzerland). The main investigations include whether local terrain influences, especially shading and terrain reflections of adjacent snow covered slopes, are represented by the new radiation balance model and in which manner they are affecting local winter road surface temperatures computations in SNOWPACK. The modelled road surface temperatures are validated by permanent point measurements on the motorway. Bouilloud and Martin (2006) point out that special attention is required for the treatment of the thermal and hydrological properties of the road and the different configuration of the interface between road and e.g. snow. Note that so far no specific adaptations were made in SNOWPACK to model a specific road behaviour in contrast to other soils or snow.

11.1 Input data and model setup

A specific road section of the upper part of the Gotthard motorway (Canton Uri, Switzerland) was chosen. In Fig. 11.1 the DHM with 209 × 311 grid cells, a homogeneous horizontal grid

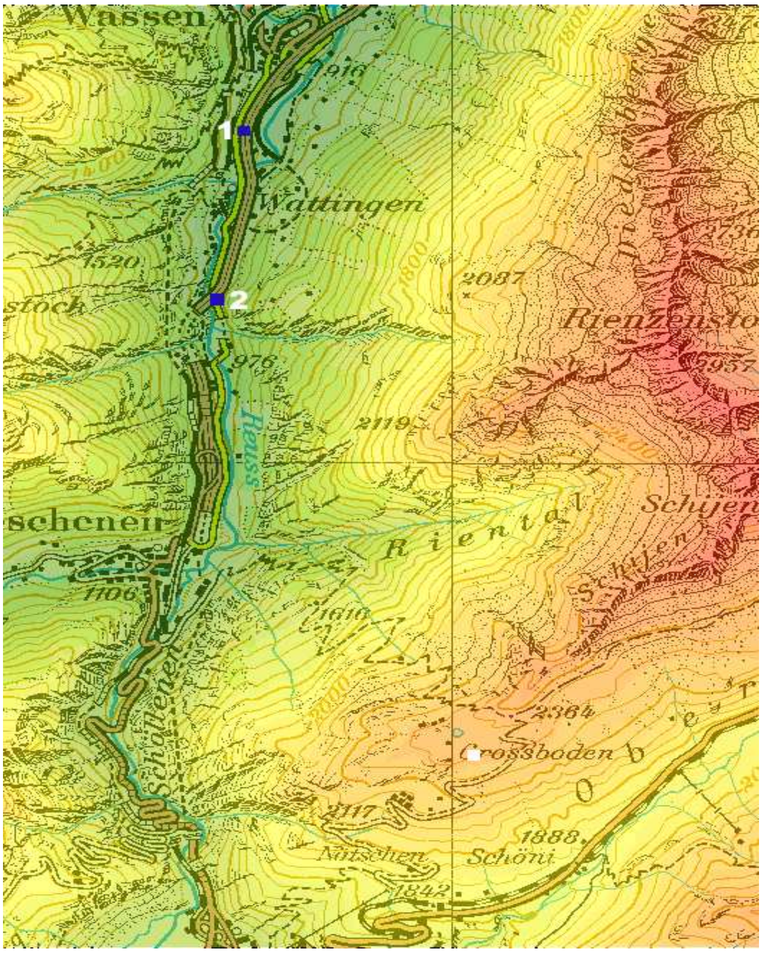

Figure 11.1: DHM for the model domain around the Gotthard motorway section (Canton Uri, Switzerland). The underlying map is from the Swiss National map (Swisstopo (WWW)). The blue squares indicate where the two permanent road measurement stations are located: 1: Trutzig, 2: Schöni Lora (bridge). The white square indicates where the meteorological input station (SwissMetNet) is located.

cell resolution of 25 m and a mean slope angle of 34° is shown. The DHM heights z vary roughly between 800 m a.s.l. (dark green) and 2959 m a.s.l. (dark red). The underlying map is from the Swiss National map (Swisstopo (WWW)). A motorway section was chosen instead of a "real" mountain pass road due to the permanent road surface temperature measurements on the motorway. Additionally, more road treatments are conducted on the motorway. Vehicle drivers record their road maintenance in protocols (maintenance logs) which can be used to update the actual road condition during the simulation as well as for the verification of the modelled road condition. The upper part of this motorway section was selected because of the deeper valley geometry that enables the verification of the modelled shaded road sections and possible terrain emissions and reflections. Land use information was obtained from areal statistics of BFS (WWW) (from 1992/97) which gathers areal land use data in a 12 year cycle for Switzerland. The information is extracted from aerial photographs of Swisstopo (WWW) by control samplings at distances of 100x100 m. These "raw" land use information

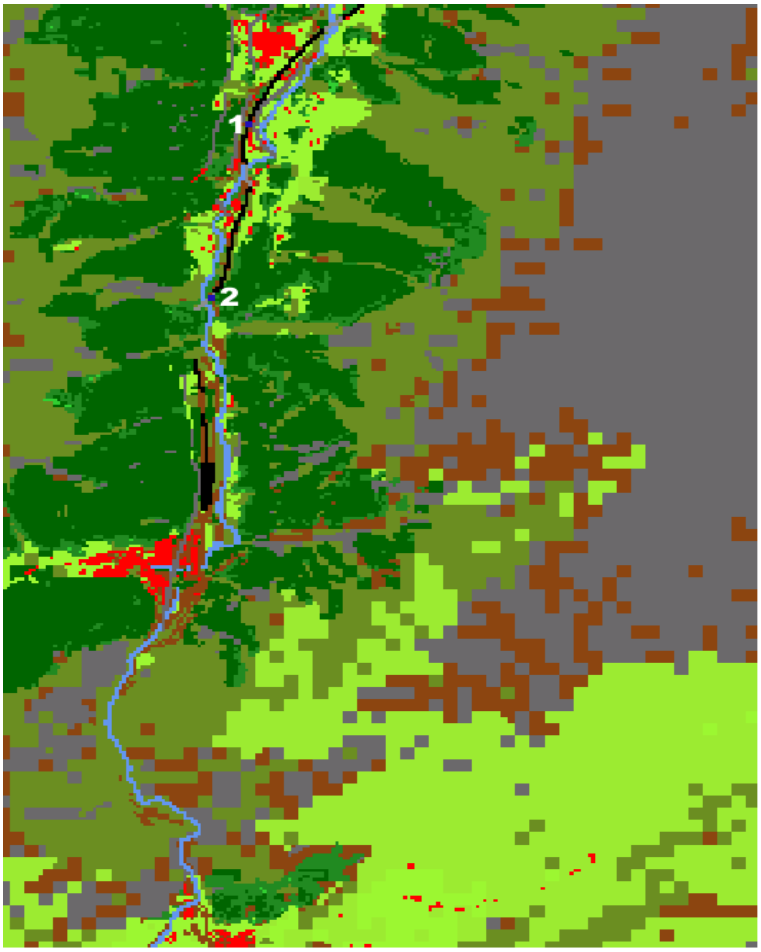

Figure 11.2: Land use for the model domain around the Gotthard motorway section (Canton Uri, Switzerland) with black for road, light grey for bridge, light blue represents the river "Reuss", light red is for buildings, brown for bare soil etc.. The blue squares indicate where the two permanent road measurement stations are located: 1: Trutzig, 2: Schöni Lora (bridge).

matrix was edited heavily afterwards. The main editing was done with a geographical information system interface program (Schirmer (2005)) by means of underlaying orthoimages of Swisstopo (WWW). This was done for verification as well as to extend the land use data for roads and bridges. The resulting land use distribution is shown in Fig. 11.2. The road is depicted in black, bridge in light grey, buildings in light red, bare soil in brown and river in light blue (river "Reuss" along the motorway).
WSL (2005) gathered forest cover, tree species and mean height information of areal photographs of 1993/95. The mean forest species height is added to the appropriate patch DHM height (DHM of Swisstopo (WWW)) to account for this additional height. This can be seen as a first approximation although, in reality, trees do not resemble closed cuboids.

Typical mean land use specific soil profiles were applied. The road profile and bridge road section profiles were adapted according to road profiles of the local office for civil engineering of the canton Uri. In Table 11.1, the start road profile used here, with its six layers, is shown.

layer type	Δz m	θ_i $\mathrm{m^3/m^3}$	θ_w $\mathrm{m^3/m^3}$	θ_v $\mathrm{m^3/m^3}$	θ_s $\mathrm{m^3/m^3}$	ρ_s $\mathrm{kg/m^3}$	λ_s W/mK	c_ps J/kgK	r_gs mm
rock	4.00	0	0.01	0.02	0.97	2400	2.00	860	10000
gravel sand	0.30	0	0.3	0.10	0.60	1700	0.70	1420	14
gravel	0.03	0	0.00	0.05	0.95	2629	2.49	7900	10000
base	0.11	0	0.00	0.04	0.96	2506	0.69	920	23
base	0.08	0	0.00	0.04	0.96	2506	0.69	920	23
top	0.04	0	0.00	0.04	0.96	2439	0.69	920	23

Table 11.1: Road profile with specific road type (top layer: Split Mastic Asphalt (SMA)), its layer thickness Δz, layer volume fraction of ice θ_i, water θ_w, vapor θ_v and soil θ_s, soil density ρ_s, soil heat conductivity λ_s, soil heat capacity c_ps and mean soil grain radius r_g.

layer type	Δz m	θ_i $\mathrm{m^3/m^3}$	θ_w $\mathrm{m^3/m^3}$	θ_v $\mathrm{m^3/m^3}$	θ_s $\mathrm{m^3/m^3}$	ρ_s $\mathrm{kg/m^3}$	λ_s W/mK	c_ps J/kgK	r_gs mm
air	2.000	0	0.09	0.90	0.01	1.252	0.0257	1010	0
concrete	1.500	0	0.01	0.03	0.96	880	1.5100	2400	10000
packing	0.050	0	0.00	0.02	0.98	55	0.0320	1500	0.0
protective	0.035	0	0.00	0.04	0.96	2444	0.6900	920	23
base	0.030	0	0.00	0.04	0.96	2444	0.6900	920	23
top	0.035	0	0.00	0.04	0.96	2444	0.6900	920	23

Table 11.2: Bridge road profile with specific road type (top, base and protective layer: Mastic Asphalt (MA), packing layer: bitumen), its layer thickness Δz, layer volume fraction of ice θ_i, water θ_w, vapor θ_v and soil θ_s, soil density ρ_s, soil heat conductivity λ_s, soil heat capacity c_ps and mean soil grain radius r_g.

The first layer is the lowest layer in the profile. In Table 11.2, the start bridge road profile with six layers is shown. It varies from the "normal" road profile (Table 11.1). Instead of rock, air is assumed as lowest layer on the bridge to account for the lower heat conductivity λ_s and density ρ_s as well as the higher heat capacity c_ps. This was introduced as a first approximation to account for the difference between a normal road section and a bridge section but will not be the final solution.

A Neumann condition was chosen as a lower boundary condition at all soil profiles with a constant geothermal heat flux of 0.06 $\mathrm{Wm^{-2}}$ in about 4 m depth. Note that a constant geothermal heat flux can only be applied as long as relatively short simulation periods are chosen. For all road grid cells a mean roughness length of 0.01 was used. A mean road and bridge surface albedo value for dry roads was applied of 0.21 (Flury (2006)). In case of snow, water or ice on the road, the surface albedo is computed from Eq. (5.4). The multiple regression model of Flury (2006) was not applied in the following model validation. It was neglected here, since there is heavy road maintenance at Gotthard motorway by road clearing and salting. The local road authorities focus on keeping the road so-called black since this motorway is an important traffic connection to Italy. Additionally, the model of Flury (2006) was developed for mountain roads with little traffic and without salting.

All (one-dimensional) hourly meteorological input (S_{g}, L_{inc}, T_{a}, v, rh and *precipitation rate*) data are obtained from the MeteoSwiss SwissMetNet measurement station "Guetsch ob Andermatt" at 2287 m a.s.l. within the model domain (white square in Fig. 11.1, Swiss National Coordinates: East: 690140, North: 167590).

An approximately realistic snow cover distribution as well as approximately realistic soil and snow temperature profiles are achieved in the model domain by starting the simulation on 1 October until the beginning of the investigation period. For this first running no SW terrain reflections and LW terrain emissions were taken into account in the Progressive Refinement iteration (Section 4.1.4, p.56) but 5000 reflections and emissions on the investigation days from 1 to 4 March 2006. A distance restriction for the LW terrain emission of 1500 m is applied (Section 3.2.2, p.42). The substructuring threshold (Section 4.1.2, p.47) was set to 0.4 for the computation of the sky view factors F_{sky} as well as for the computation of the terrain view factor sum multiplied by the actual area for the shooting order of PR iteration. The substructuring threshold was set to 0.6 for the computation of the individual terrain view factors for the radiation exchange in PR iteration.

11.2 Road maintenance logs

The logs were recorded by the local road maintenance service of the road authorities of the maintenance area at Göschenen. The maintenance logs are considered for by means of the data assimilation module (cf. Section 5, p.79). The changing road condition is accounted for in a similar manner as satellite data with snow cover observation, which has been developed at SLF within the framework of the AWARE project (EU (WWW)). The maintenance service observations are recorded during their road treatment. With this additional information the modelled road grid cell conditions are then adjusted according to the observation. The observations are always assumed to be more accurate than the modelling. If no treatment or observation exists nothing is changed in the modelling. If a treatment or an observation exists the appropriate adaptations are accounted for in the following time step ahead of SNOWPACK simulation but after the radiation balance module.

Until now the following conditions after road treatments are considered: (cleared) dry road, (cleared) wet road, snow covered road, ice covered road with a corresponding layer thickness Δz and a density ρ. These conditions are implemented by transforming them to a necessary *precipitation rate* in mmh^{-1} of the previous till the present hourly time step and by adding this locally to the appropriate road grid cell

$$precipitation_I \;=\; \Delta z_I\; \rho_{\mathrm{s},I}. \tag{11.1}$$

In case of a smaller time step the precipitation rate is linearly allocated to the appropriate smaller time steps within the hourly time step. The layer thickness Δz is inserted in m. The density of snow, ice or water, ρ_{s} in kgm^{-3}, on the road is simply chosen to be as follows

- cleared road dry $\longrightarrow$ *precipitation rate* = zero mmh^{-1}

- cleared road wet $\longrightarrow \rho_{\text{water}} = 1000$ kgm^{-3}
- new snow covered road $\longrightarrow \rho_{\text{new snow}} = 100$ kgm^{-3}
- wet snow covered road $\longrightarrow \rho_{\text{wet snow}} = 400$ kgm^{-3}
- ice covered road $\longrightarrow \rho_{\text{ice}} = 917$ kgm^{-3}

11.3 Spatial radiation patterns in the Gotthard model domain

In this section, spatial values of modelled SW direct radiation S_{b}, sky view factor F_{sky}, terrain reflected values S_{t} and LW terrain emitted values L_{t} are shown to discuss its pattern in the Gotthard model domain of Fig. 11.1.

In Fig. 11.3 the spatial incident SW direct radiation is shown on 1 March 2006 for eight consecutive time steps. Note that different color legends are chosen but that the overall range is given in the legend caption. This was chosen to point out that sun or shadow due to complex terrain has a clear and most important local impact on the road. At 9 UTC approximately the whole road section is shaded. Little sun is received on the upper motorway close to Göschenen. At 10 UTC mostly the whole motorway is in the sun except for a section in the surroundings of Wattingen. This section includes the second road measurement station Schöni Lora (indicated by 2 in Fig. 11.1). In contrast, the first road station Trutzig located between Wassen and Wattingen (indicated by 1 in Fig. 11.1) is already in the sun. From 11 UTC until 13 UTC the whole motorway section remains unshaded. At 14 UTC the upper motorway section, which has received at first sun in the morning, gets shaded first. Additionally, the road station Schöni Lora is shaded whereas the road station Trutzig is still in the sun. The whole motorway is shaded from 15 UTC on. During most of the time on that specific day the motorway section between Wassen and Wattingen (including road station Trutzig) receives the largest amount of direct radiation S_{b}. Direct radiation S_{b} differences along the motorway can reach up to a maximum of 600 Wm^{-2} thus having a strong influence on the local radiation balance on the road. This is even more important since in contrast to large snow albedo values the dry road albedo value is assumed to be only 0.21. Note that shading is only accounted for due to terrain; the applied DHM was not corrected for forests or buildings. The question was tested whether additional forests or buildings can be accounted for by simply adding their height to the DHM height (cf. Section 2.2, p.19). A varying shading pattern on the road was expected but overall more incident direct radiation occurred for that specific model domain. This can be explained by an increase in slope angles due to the raised DHM height (cf. slope angle computation method in Section 2.1, p.17) depending on land use. The wrong artificial larger surface slope angles lead to locally higher incident direct radiation if pointed to the sun. Additionally, the approximately flat road sections tend to get larger surface slope angles if the forest height is simply added to the patch aside. Therefore, a different method should be chosen to consider for shading of trees on flat road sections.

In Fig. 11.4 the sky view factor $F_{\text{sky},I}$ is shown for each patch of the model domain. The sky view factor was chosen instead of the spatial incident diffuse sky radiation S_{d} since its pattern is simply imposed by the sky view factor. Along the road, sky view factor differences are typically smaller than 0.25. As expected, the largest sky view factors are received at the higher mountain patches. Smaller F_{sky} appear correctly in the narrow valleys that diverge

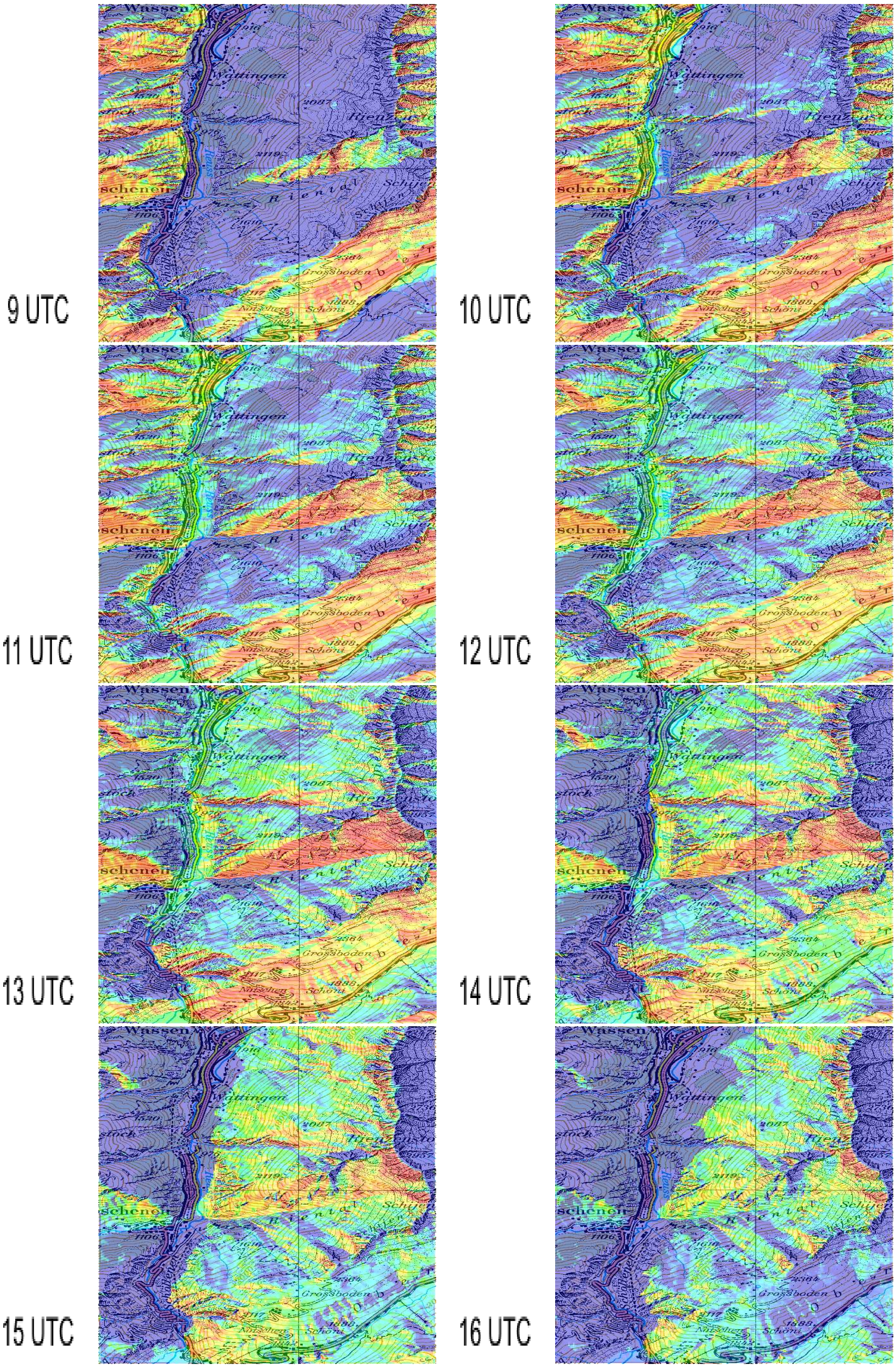

Figure 11.3: Comparison of spatial modelled SW direct radiation S_b for the model domain around the Gotthard motorway from 9 to 16 UTC on 1 March 2006 is shown. The legend colors are not uniformly chosen: Starting always from dark blue with zero Wm^{-2} to a maximum of 300 Wm^{-2} from 9 to 11 UTC, to around 1000 Wm^{-2} from 12 to 15 UTC and to 600 Wm^{-2} at 16 UTC.

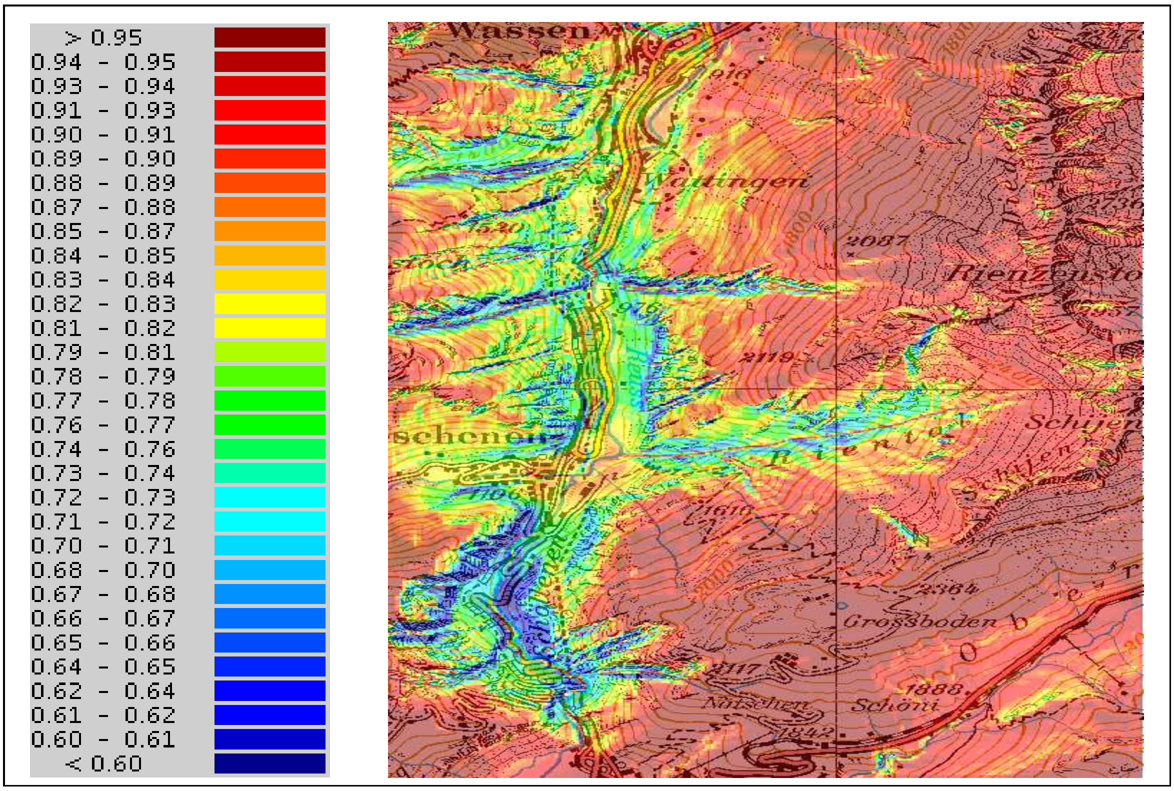

Figure 11.4: The spatial distribution of the modelled sky view factor $F_{\mathrm{sky},I}$ is shown for the model domain around the Gotthard motorway.

from the main Gotthard motorway valley. Additionally, lowest sky view factors appear on the mountain road in the narrow valley leading up to Andermatt. Slightly larger sky view factors F_{sky} exist on the less inclined valley bottom compared to the inclined lower valley slopes. According to the sky view factor distribution, the largest SW diffuse sky and LW sky radiation incident on the road has to occur on the lower road section between Wassen and Wattingen. This is the same motorway section where largest incident SW direct radiation S_{b} occurred.

In Fig. 11.5 incident SW terrain reflections S_{t} (Fig. 11.5(a)) and LW terrain emissions L_{t} (Fig. 11.5(b)) are shown for the Gotthard model domain on 1 March 2006 at 14 UTC. Only 5000 terrain reflection, emissions respectively were considered in the radiation balance. This means that, in case of PR iteration to compute the radiation exchange (Section 4.1.4, p.56), only 8 % of all patches in the model domain can actually reflect/emit (shoot) their radiation to other visible patches. Due to this relatively low number of considered terrain reflections and emissions an approximately inverse behaviour is observable between SW and LW terrain influences: Less incident S_{t} is obtained at the valley bottom and lower valley slopes compared to the upper slopes. This is because the SW *shooting criterion* selects these patches in descending order that see a lot of terrain, have a large patch surface area **and** can reflect a lot of incident direct and diffuse sky radiation (Eq. (4.44)). More incident S_{t} is correctly received by those patches on shaded upper valley slopes when the other valley side can reflect a lot of incident direct radiation S_{b} (see Fig. 11.3 at 14 UTC). Therefore, the patches influencing the valley bottom and lower valley slope patches are not often selected

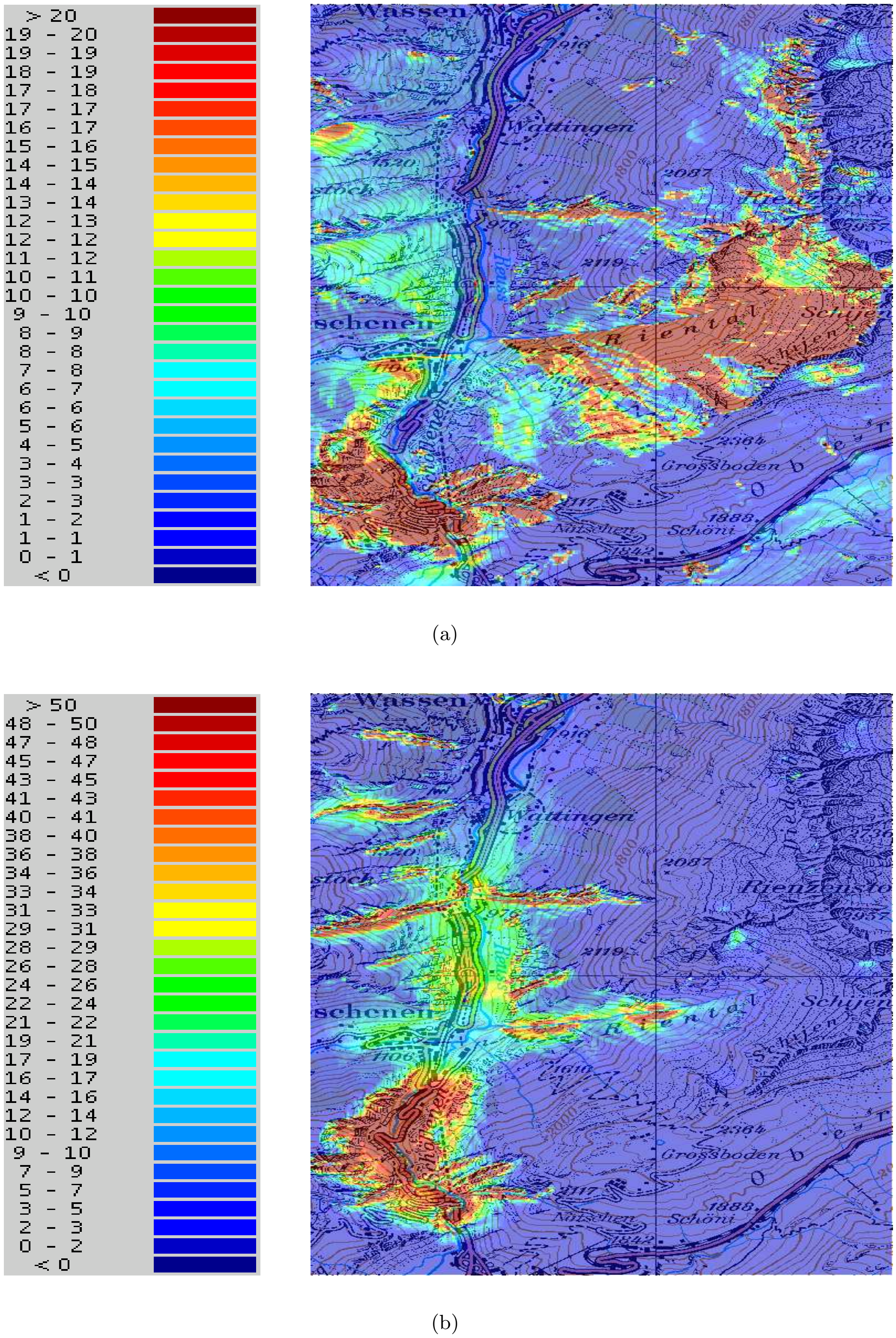

Figure 11.5: The spatial distribution of (a) incident SW terrain reflected radiation S_t and (b) LW terrain emission L_t for the model domain around the Gotthard motorway on 1 March 2006 at 14 UTC. The radiation values in the legends are given in Wm^{-2}.

within the low number of 5000 iterations for the 209×311 number of patches. Incident S_t values on the road reach a maximum of 5 Wm^{-2} on 1 March at 14 UTC. More incident terrain reflected radiation S_t will be obtained on the valley bottom (including the road) and lower valley slope patches with advanced iteration steps since terrain reflected radiation first has to proceed from the upper valley slope parts to the lower ones depending on surface albedo values.

In contrast to the low incident SW terrain reflections, a larger amount of incident LW terrain emissions L_t are obtained at some valley bottom and lower valley slope patches. Maximum incident L_t values on the road reach up to 30 Wm^{-2}. The larger incident L_t can be explained by the LW *shooting criterion* (Eq. (4.74)). The LW *shooting criterion* selects these patches in descending order that see a lot of terrain, have a large patch surface area **and** can emit a lot of LW radiation, i.e. patches that have high surface temperatures T_s. Therefore, the warmer lower valley slopes are selected earlier in the LW iteration process since the LW terrain emission L_t first has to proceed from the lower warmer valley slopes to the upper ones. For both incident SW and LW terrain radiation, a large amount is obtained on the valley bottom and narrow valley slopes on the way to Andermatt (Schöllen valley). In case of SW terrain reflected radiation S_t this appears more on the north eastern shaded valley slope. Maximum values of about 170 Wm^{-2} are obtained. In case of LW terrain emissions this appears along the whole valley reaching maximum values of about 120 Wm^{-2}.

In Fig. 11.6 the spatial surface temperature T_s is shown for the Gotthard domain. Two points of time were chosen: 10 UTC (a) and 14 UTC (b). These were selected due to their pronounced shading sections on the road (cf. Fig. 11.3). As discussed, the largest spatial SW radiation differences at this specific day arise due to shading of the incident direct radiation S_b. Some additional spatial LW radiation differences appear at the upper and middle part of the motorway section at 10 UTC and 14 UTC from incident LW terrain emission. Nevertheless, this additional amount of incident terrain emission is much less (cf. Fig. 11.5(b))) than the difference obtained due to shading of direct radiation S_b. The legend colors in Fig. 11.6 are chosen to highlight the surface temperature T_s variations on the road. According to the spatial incident direct radiation S_b at 10 UTC (Fig. 11.3) overall lower surface temperatures T_s are obtained for the shaded motorway section between Wattingen and the location of the second road station Schöni Lora (indicated by 2 in Fig. 11.1). According to the spatial incident direct radiation S_b at 14 UTC (Fig. 11.3) overall lower surface temperatures T_s are obtained for the shaded motorway section from the second road station Schöni Lora up to the Gotthard tunnel entrance. Along the road, maximum surface temperature deviations reach up to 6 K. This might have a strong influence on local road surface ice formation or snow cover build-up.

11.4 Measured surface temperatures versus modelled surface temperatures

In this section measured road surface temperatures are compared to road surface temperatures modelled with Alpine3D. Note again that no specific adaptations for road surface temperature modelling were conducted. Instead, it was the aim to investigate how Alpine3D, with an improved and extended radiation balance module, computes road surface temperatures by taking into account road treatments.

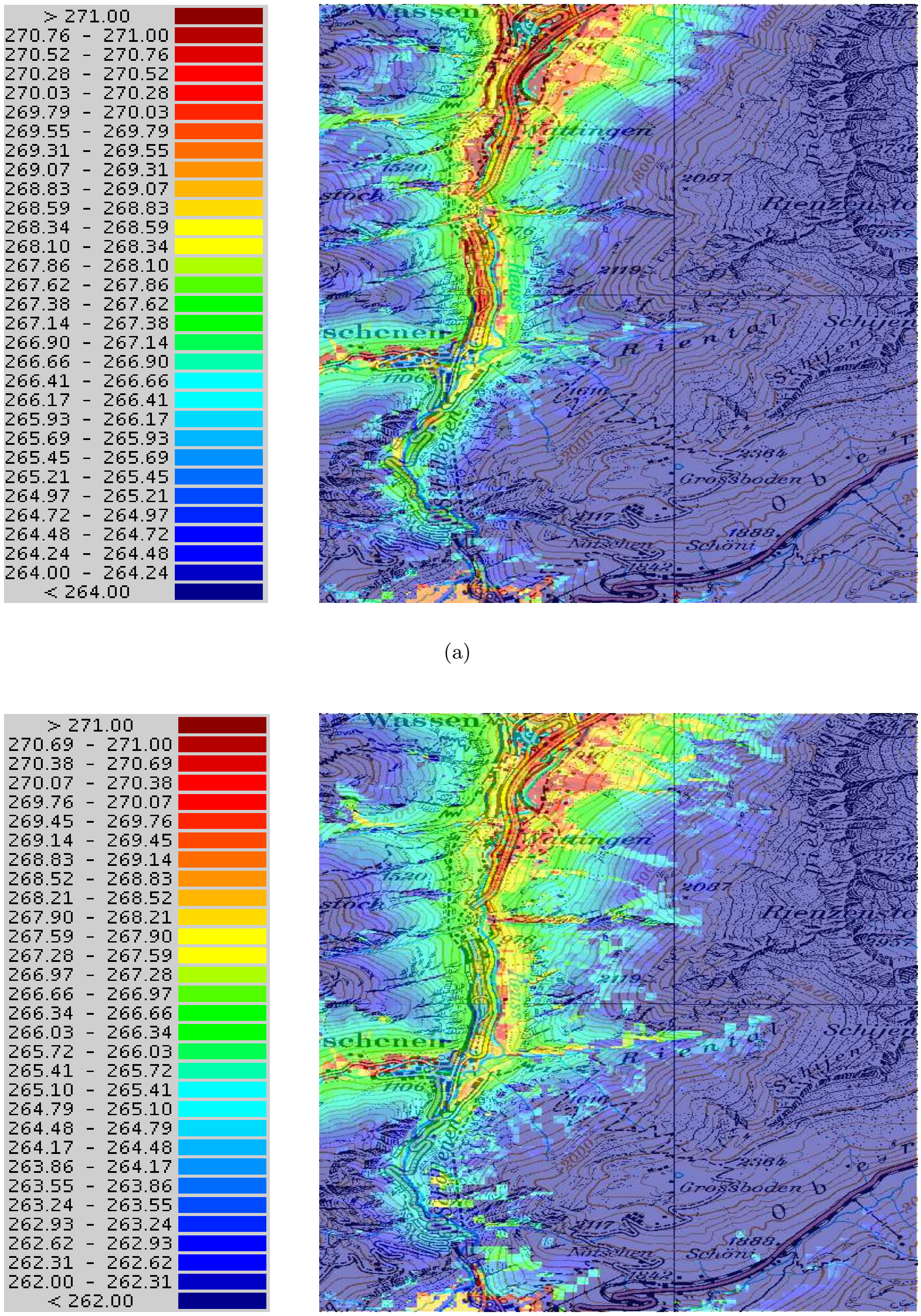

(a)

(b)

Figure 11.6: The spatial distribution of modelled surface temperatures T_s is shown for the Gotthard model domain on 1 March 2006: (a) 10 UTC, (b) 14 UTC. The surface temperature values in the legends are given in K.

The two blue circles in Fig. 11.1 indicate the two permanent road measurement stations on the motorway which are approximately 2 km apart: 1: Trutzig (z=974.2 m a.s.l.), 2: Schöni Lora (z=1050 m a.s.l.). At these two stations active soil probes (BOSO II) by Boschung Holding AG (Boschung (2004)) are mounted in 0.5 cm below the pavement. A PT100 sensor measures pavement temperatures as well as the electric properties of the aqueous solution on the probe surface. Those parameters then allow estimating the salt concentration of the solution. The pavement probe measures temperatures within the range of -40 °C to 70 °C. The probe detects the following pavement conditions: dry, damp, wet, ice and hoarfrost. The two measurement stations were used for quantitative comparisons of the modelled surface temperatures at these sites and for qualitative verification of the modelled road surface conditions. Note, that the second measurement station is located on a bridge. The bridge road profile given in Table 11.2 is used here as a soil profile.

For a sequence of 4 days, from 1 March until 4 March 2006, modelled and measured road surface temperatures T_s are compared. Three maintenance logs could be applied during this time period. First treatment took place on 1 March at 3 UTC, second on 3 March at 7 UTC and third on 4 March at 9 UTC. Each time the road was cleared and salt was put on the road. Thereafter, the road was assigned to be wet. This was implemented by first clearing the road in case of a snow cover. Second, by introducing an additional layer with a layer height Δz of 0.001 m and a surface density for water ρ_water at the specific time steps. As noted before, the assimilation takes place in the following time step, i.e. e.g. the treatment on 1 March 3 UTC was considered in the modelling on 1 March 4 UTC after the radiation balance computation but ahead of the SNOWPACK simulation. The road conditions ahead of the road treatment varied as follows

1. 1 March 3 UTC: wet snow cover with Δz of 3 cm
2. 3 March 7 UTC: damp snow cover with Δz of 0-5 cm
3. 4 March 9 UTC: damp snow cover with Δz of 0-3 cm

Each time, the road treatment is applied at the same time on all road grid cells. Bridges are always kept clear of snow since this is the premise for the Gotthard motorway section of the local road authorities. A complete clearing of the road was conducted at modelling start on 28 March at 19 UTC.

In Fig. 11.7(a) modelled surface temperatures on the road are compared to measured surface temperatures of the soil probes from 1 March to 4 March 18 UTC 2006 at the Trutzig measurement site (location indicated in Fig. 11.1 by number 1). The modelled surface temperatures T_s are shown for three road patches located around the measurement site to exclude inaccuracies in the allocation of the appropriate patch from GPS coordinates of the measurement station. It can be seen that the overall diurnal patterns are well captured. Even though mean surface temperature deviations are about 2.3°C they can reach up to 12°C. In Fig. 11.7(b) the modelled surface temperatures T_s on the road are compared to measured surface temperatures of the soil probes from 1 March to 4 March 18 UTC 2006 at the Schöni Lora bridge measurement site (location indicated in Fig. 11.1 by number 2). Again, three close road patches were chosen around the measurement station. And again, the overall diurnal patterns are well captured with mean surface temperature deviations of about 1.9°C. Nevertheless, maximum deviations can reach up to 8°C. Both measured and modelled, surface

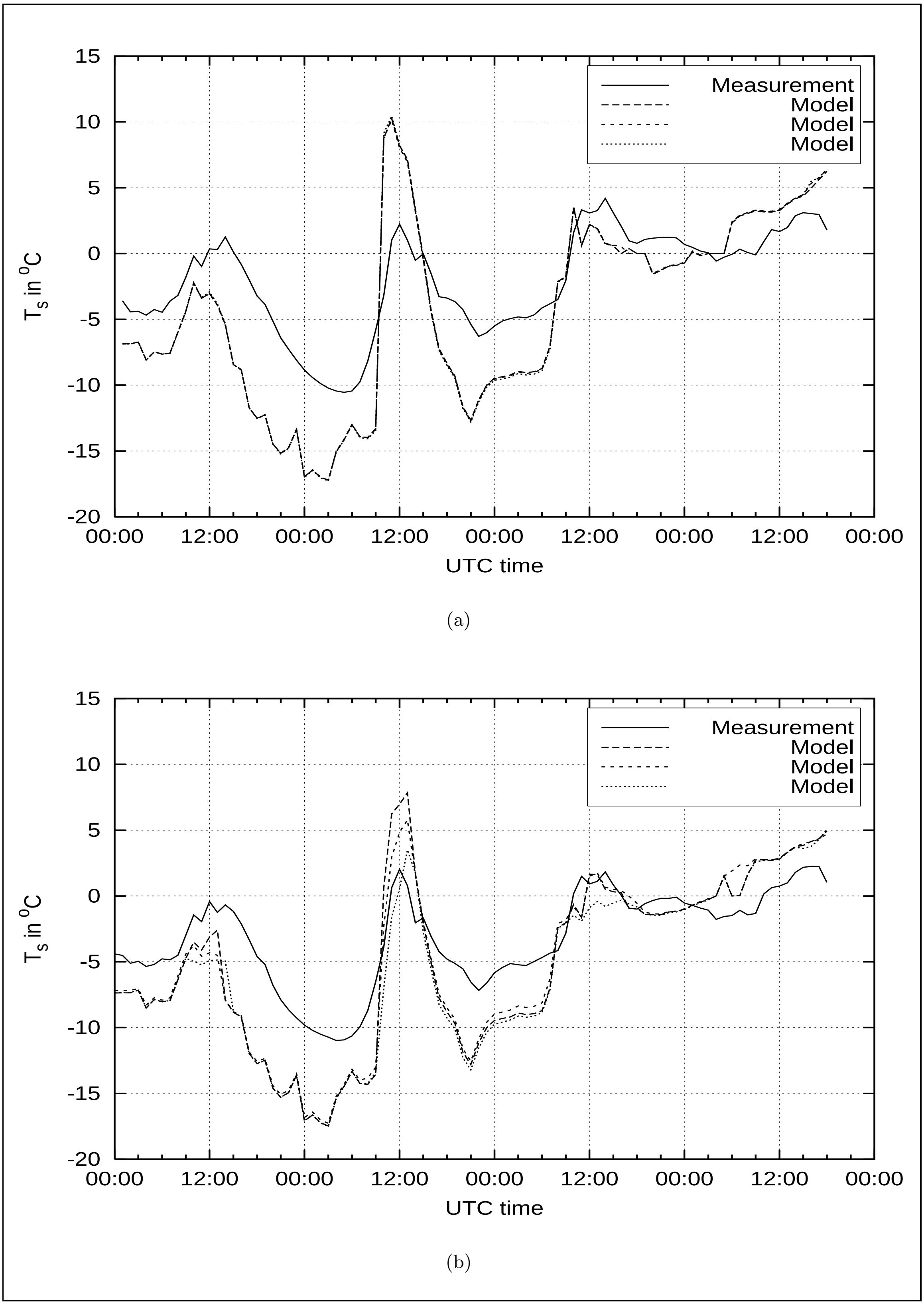

Figure 11.7: Comparison of measured road surface temperatures and modelled road surface temperatures from 1 March to 4 March 18 UTC 2006. Three road patches around each measurement station at the Gotthard motorway are chosen all lying more or less on top of each other: (a) Trutzig, (b) Schöni Lora.

temperatures are generally higher at the Trutzig measurement site. A possible explanation might be the pronounced shading at the Schöni Lora measurement site especially at 10 UTC and 14 UTC on 1 March (cf. Fig. 11.3).
Most of the time the modelled road surface temperature underestimates the measured road surface temperature. As discussed in Section III, p.87 and Section 10, p.143, the radiation balance is computing incident radiation values very well. Therefore, possible reasons for the relatively large deviations between measured and modelled surface temperatures on the road have to be searched in the other energy flux terms and module parameters/assumptions. This is discussed in the following:

- As noted in Section 5.4, p.82, Landl and Lehning (2008) found that the standard stability corrections for the turbulent fluxes are inadequate for inclined and flat snow covered surfaces in alpine terrain. They also note that further investigations are necessary. Due to this study, neutral conditions were assumed here. Nevertheless, relatively large surface temperature deviations appear. One reason for that might be that a constant wind velocity measured at SwissMetNet measurement station "Guetsch ob Andermatt" at 2287 m a.s.l. was used at each grid cell. Thus, any local (valley) wind systems are suppressed that would have resulted in different local wind velocities compared to the wind velocity at the measurement station.

- Even though in the investigated time period some large snowfall events occurred (e.g. on 4 March between 4 and 13 UTC), no snow accumulated on the road in the whole period. If the modelled road condition is dry, lower surface temperatures are resulting compared to a road, which is covered by wet snow as was observed by the vehicle drivers.

- A dry road albedo value of 0.21 was used. If a different road condition, e.g. a wet road surface, was not modelled, the dry albedo value can lead to wrong radiation balances. Additionally, the dry road albedo can vary locally due to traffic influence or earlier road treatments e.g. with salt (the road might appear white).

- In Alpine3D spatial air temperature T_a interpolation is not coupled to incident radiation. This means, two grid cells I and J that have approximately the same DHM height $z_I = z_J$, but I is shaded for several hours and J receives direct radiation S_b the whole period, still holds the same air temperature in the model. Accordingly, the same air temperature is used within the computation of the turbulent fluxes at both grid cells but different surface temperatures are used. In most cases this will lead to a large compensating sensible heat flux from the "warm" (dark) road to the "colder" air above the road what might result in a modelled underestimation of surface temperatures. Moore et al. (1993) present an approach to spatially distribute air temperature T_a from one measurement. It corrects for the lapse rate, for surface orientation and for vegetative effects.

- The traffic influence is not represented in the SNOWPACK surface temperature computation but is measured from the soil probes. An additional heat flux into the road due to traffic will rise road surface temperatures (e.g. Takahashi et al. (2006)).

- The large overestimated surface temperatures on 2 March between 12 and 13 UTC at Schöni Lora and between 11 and 13 UTC at Trutzig are not exactly explainable. One reason might be the missing wind velocity at the SwissMetNet measurement station on

2 March. A mean interpolated wind velocity value of 0.8 ms^{-1} was assumed instead. Since the wind velocity was missing for a larger time period from 8 UTC on 2 March to 6 UTC on 3 March no clear explanation was found for the smaller period from 12 to 13 UTC.

- The measurement accuracy of the active soil probes (BOSO II) is given with $\mp$ 0.2°. Additionally, the soil probes are mounted at approximately 0.5 cm depth on the road. They measure not exactly the surface temperature (which is modelled) but the temperature of the uppermost road layer. Thus, the measured temperature values should resemble the modelled values but the diurnal variation is attenuated.

As mentioned, the road surface condition was modelled dry for all four investigated days. Therefore, no comparison with measured road conditions could be conducted. Reasons for the too dry modelled road condition are assumed to coincide with the above reasons for the poor agreement between modelled and measured road surface temperatures.

Overall it could be shown that Alpine3D is applicable to compute surface temperatures on roads. However, if road surface temperatures have to be computed accurately, besides of the good knowledge of the horizon and terrain radiation, some additional specific adaptations have to be conducted. First, the implemented turbulent fluxes scheme has to be further investigated. Contributing to this, a coupling of air temperature and incident radiation should be studied (cf. eg. Moore et al. (1993)). Second, some road specific adaptations of the SNOWPACK module are missing such as an additional sensible heat flux to the road, salt treatment on the road or the possibility of a thin water layer on the road.

Part V

Conclusions and Outlook

12 Research achievements and future work

The thesis presented a three-dimensional radiation balance model for complex terrain. The model was developed in order to improve the determination of local surface characteristics as being part of the surface process model system Alpine3D. The model performance with regard to the modelling of local characteristics was verified by the influence of terrain on the simulation of winter road surface temperatures. The large gap in complexity between three-dimensional radiative models for a cloudy atmosphere and models applying the isotropic view factor approach, i.e. without inclusion of (anisotropic) multiple terrain reflections, was partly filled by implementing the radiosity approach to compute the three-dimensional radiation balance in complex terrain but assuming a plane-parallel atmosphere. In this chapter, conclusions are drawn with respect to the achievements of the research. Furthermore, future work is suggested.

12.1 Achievements

The main aim was to introduce a well defined physical model for the three-dimensional radiation balance in complex terrain which i) allows to study systematically the influence of terrain effects (shading and anisotropic multiple terrain reflections) on the radiation balance ii) reveals the assumptions the model is based on iii) is feasible from a computational point of view in order to integrate it in the coupled land surface process model Alpine3D (Chapter 5, p.79) and iiii) can be driven from a single, exposed radiation measurement in the domain. Note that the derivation of spatial meteorological input from a single measurement station is very promising for general applications. But since the meteorological input of the model contributes to the accuracy of the modelled parameters the input has to be verified carefully. Therefore, the existing parameterisations of spatial incident direct and diffuse sky radiation parameterisations for cloudy sky conditions were critically reviewed, extended (e.g. introduction of a diffuse sky radiation for clear sky conditions (Eq. (3.39))) and partly replaced (e.g. the substitution of the decomposition model by a combination of the models of Reindl et al. (1990)) (cf. Chapter 3, p.25).
The individual achievements of the research are now related to the research objectives stated in the introduction of this thesis.

An accurate consideration of (local) shading from mountains:

- In order to enable the representation of steep mountainous terrain ridges in the model domain, the extraction method of terrain parameters of Corripio (2002) was applied which divides a rectangle grid cell into two triangles and computes an average of the resulting two surface normal vectors (Section 2.1, p.17).

- The implementation of mutual visibility and sun-or-shadow was replaced by more robust algorithms (Section 2.2, p.19)). Thereby, visibility is now determined between individual patches instead of the simplified azimuthal sector method. Each *intermediate* patch is involved in the algorithm that checks for visibility. For this the horizontal stepwise search path of Amanatides and Woo (1987) was implemented.

Implementation of anisotropic multiple shortwave terrain reflected and longwave terrain emitted radiation:

- Since radiation transfer in mountains is actually radiative transfer in an enclosure, the finite element radiosity approach was introduced in the model which describes the stationary exchange of radiative energy between diffuse reflecting and emitting surfaces. Note that the radiosity approach was first introduced in computer graphics from techniques originally developed in thermal engineering to describe the exchanges of radiant energy between surfaces. Previously established methods from the wide field of computer graphics could be exploited (Section 4.1, p.45). Therefore, the anisotropic view factor concept between patches was implemented (Section 4.1.2, p.47). On the other hand, some numerical methods had to be extended and tailored to its use for the radiation problem (Section 4.2, p.58).
- By re-deriving the respective continuum radiosity equation in the context of radiation transfer in complex terrain, the underlying assumptions of the approach could be listed unambiguously (Eq. 4.37, Eq. 4.41). The continuum equations clearly reveal that previously used formulas for diffuse terrain and diffuse sky radiation components have to be regarded as wrong or as a crude approximation which can lead to profound differences in these components (cf. Section 9.4, p.134).

Implementation of a method that accounts for accurate terrain influences up to mesoscale model domains. This method should also allow for small grid cell extensions of 25 m or smaller:

- Progressive Refinement iteration (cf. Section 4.1.4, p.56) was chosen to solve the radiosity equation used in complex terrain. It is a fast iterative method to solve the system of N linear equations that does not require to store the whole $N \times N$ view factor matrix. The overall aim of Progressive Refinement is to decrease convergence time by rearranging the order of considered patches according to its "relevance" for the iteration. Two Progressive Refinement versions were constructed (Section 4.2.1, p.63):
  (i) In the case of sufficient memory capacity all view factors are stored either during the model run or in an external look-up table. Nevertheless, Progressive Refinement iteration is applied due to the efficient shooting order resulting in an overall decreased computation time compared to Gauss-Seidel.
  (ii) In the case of insufficient memory capacity Progressive Refinement iteration is applied by computing view factors on the fly with a rather slow but at least feasible simulation.
  The iteration order criterion (shooting criterion) of Cohen et al. (1988) with the largest unshot radiant power in the model domain was adapted to include the terrain view factor sum. Thus, redundant shootings from mountain peaks that do not see much terrain but receive large incident direct and diffuse sky radiation due to their exposed location and do additionally possess large albedos (snow at the top) are avoided.
  Due to the lack of an appropriate stopping criterion applicable for changing sun positions (i.e. not using the true solution) a new stopping criterion was developed. This

criterion depends on possible reflectable radiation and terrain geometry. It was shown that it can be related to the true error (cf. Section 4.2.2, p.67).

Verification of the new model with point measurements and sensitivity studies. Additionally, a general characterisation of terrain reflected radiation in terms of the geometry of complex terrain by using random digital height models was conducted:

- The horizon line was measured with a tachymeter as well as extracted by image analysis from a panorama picture of "Atlas der Schweiz". Comparing the computed horizon line with the measured horizon line validated the new sun-or-shadow/mutual visibility detection algorithm. The visibility resolves the horizon line accurately, at least within the limit of the underlying DHM with 25 m horizontal grid resolution (Section 6.1, p.89).

- For the verification of terrain radiation a minimal but new measurement was designed to characterise the effect of terrain radiation (cf. Section 8.1, p.105). For this a removable horizon was constructed around a pyranometer. Masking and unmasking the terrain in short time intervals resulted in measured relative values of terrain reflected radiation for a summer day (low albedos) and a winter day (high albedos). Modelled and measured values agreed very well. The maximum of the measured terrain reflected radiation S_{t} of about 19 Wm^{-2} on 20 April 2007 at 11 UTC is modelled exactly (cf. Section 8.2, p.110).

- Shortwave and longwave radiation components were validated by permanent point measurements at Weissfluhjoch study site close to Davos, Switzerland. For clear sky days modelled values with the extended and reviewed parameterisations (cf. Chapter 3, p.25) resemble the measured components quite good. Even though a new decomposition model (combination of the models of Reindl et al. (1990) cf. Section 3.1.3, p.37) for the extraction of cloudy sky radiation components out of one measured global radiation value was implemented, the modelled total diffuse radiation values still mostly overestimate measured total diffuse radiation and whereas the measured direct radiation is mostly underestimated by the modelled values. For the clear sky day on 19 January maximum overestimations of the modelled total diffuse radiation are of about 20 Wm^{-2} and maximum underestimations of the modelled direct radiation are of about 13 Wm^{-2}. A general good agreement between the modelled and measured incident LW radiation was obtained for 19 January 1999. A maximum deviation of 2.5 Wm^{-2} arises.

- In order to assess the radiosity approach in the context of existing model approaches a comparison has been made with both, simpler models and more sophisticated models. When compared to a full three-dimensional radiative transfer Monte Carlo model for a cloudy atmosphere, namely MYSTIC (Section 8.5, p.117) the agreement is quite good on a clear sky day, i.e. when the clear sky parameterisations are used in the radiation balance model. Maximum deviations of total diffuse radiation of about 5 Wm^{-2} and maximum deviations of direct radiation of about 27 Wm^{-2} occur on 20 April 2007 at Weissfluhjoch study site. Similar to the validation of the shortwave radiation components (cf. Section 7.1, p.95) this reveals again the great importance of an accurate decomposition model (Section 3.1.3, p.37).

  When compared to simpler parameterisations of terrain effects as the isotropic view factor approach it could be shown in which cases the radiosity approach is superior to these parameterisations (cf. Section 8.4, p.114, Section 9.4, p.134, Section 10.5, p.153) and in which cases both methods give comparable results (cf. Section 8.3, p.113). Since it is common to determine the terrain view factor sum within the isotropic view factor approach from the sky view factor, frequently used methods to approximate the sky view factor from horizon angles were reviewed (Section 9.4, p.134). Common sources of errors are outlined. One common source of error is the assumption of the equality between the sky view factor and the solid angle of the sky. And one other common source of error is the assumption that the horizon angle can be derived by neglecting the actual inclination of the viewing surface. The correct continuum equation for the sky view factor determined from horizon angles is derived in Section 4.2, p.58 (Eq. (4.41)).

- In general however, the verification of radiation by point measurements can be quite tricky. Different influences were detected by conducting sensitivity studies, which apparently can lead to the same order of magnitude deviations. Special care has to be taken for each of these influences within the point measurements such that the representation of the digital height model is important, i.e. the spatial grid resolution (cf. Section 9.1, p.127) and also the ridge preserving terrain extraction methods are important (cf. Section 9.2, p.129). Both influences can have an impact on incident radiation at sunset or transitions from sun to shadow during the day.

- In order to validate the new model not only for specific points and one real topography some general behaviour of the radiosity equation was derived on Gaussian random fields taken as digital height models. Mean terrain reflected radiation values were computed as a function of sun elevation, varying (homogeneous) albedos and typical terrain length scales. This analysis revealed that the model is applicable to the whole range of topographies.
  The general behaviour for three different slopes, the influence of three different grid cell resolutions as well as the influence of three different system sizes was investigated (cf. Section 10.2, p.145 to Section 10.4, p.151). It was found that to best estimate terrain reflected radiation the grid cell resolution has to be small against the typical width of mountains/valleys in the domain, which again has to be small against the domain extension. Remarkably high mean reflected terrain radiation values of at maximum 75 Wm^{-2} were received for a large albedo of 0.8, a sun elevation of 60° and incident direct radiation of 1000 Wm^{-2} for an angle of incidence of 90°. Note that individual patches might have even larger values. Mean terrain reflected radiation from Gaussian random fields was found to be comparable with those of a real digital height model example that has approximately the same vertical and lateral extensions. Thus, even though Gaussian fields are a simplification real terrains fit into this picture (cf. Section 10.2, p.145).
  A comparison between terrain reflected radiation that was derived from the anisotropic approach (i.e. with the radiosity model) and from the isotropic approach was also conducted by means of Gaussian random fields taken as digital height models. To summarise, mean terrain reflected radiation values from the isotropic view factor approach are roughly the same as those computed by the anisotropic view factor approach with maximum mean deviations of about 10 Wm^{-2}. However, the spatial distribution of terrain reflected radiation varies remarkably between both view factor approaches with mean maximum deviations of up to 240 Wm^{-2} for a mean slope of 30° and a mean albedo of 0.8. It was found that this was emphasised the more shading occurred in the model domain.

As a final application of the radiation balance model, the effective albedo of complex topography was computed on Gaussian random fields with a mean slope of 30° as a function of sun elevation and mean albedos. Resulting effective albedos vary with the sun elevation angle and are lower than mean local albedos. Furthermore, the difference between mean and effective albedo values varied for a range of tested mean albedos. The difference was largest for an albedo of 0.5 and lowest for an albedo of 0.1 and 0.9 which is an important result: In case of large mean domain albedo values, the complex terrain does not trap radiation by multiple terrain reflections but instead enhances the overall mean terrain reflected radiation. An approximation formula depending on the mean sky view factor and mean albedo could be constructed from the radiosity equation.

- A detailed analysis of the generalisability of point measurements can however only be completed by a thorough analysis of the spatial fluctuations of the radiation field as a function of fluctuating input quantities (digital height model, direct radiation components, etc.). In addition an error analysis of the discretisation of the underlying continuum equation Eq. (4.37) should reveal the main sensitivities. However, the latter two aspects were beyond the scope of this thesis.

Investigation of terrain influences, such as shading, on local winter road surface temperature simulations:

- Finally, the modular surface process model Alpine3D was applied to model spatial winter road surface temperatures for a specific part of the Gotthard motorway. Road maintenance logs were considered to account for the changing road condition. In the present version, spatial differences of incident radiation coming from shading and terrain reflected radiation do not have a strong influence on modelled road surface temperatures since air temperatures are not coupled to incident radiation values (cf. Section 11.3, p.169). Therefore, partly large surface temperatures deviations between measured and modelled temperatures appeared.

12.2 Future work

The thesis presents a completed, validated surface radiation balance model. It was, however, not the aim to extend the radiation balance model to a three-dimensional radiative transfer model for a cloudy atmosphere. One future investigation point for the presented radiation balance model is outlined:

- The incident direct and diffuse sky radiation under cloudy sky conditions is computed by means of an empirical statistical decomposition model which strongly depends on local conditions and requires long-term measurement series for calibration. A comprehensive statistical decomposition model which includes dependence on latitude, longitude and altitude for various ranges of them is, however, not available. As was presented in Section 7.1, p.95, no reliable decomposition model was found that can be applied for the Eastern Swiss Alps. Thus, a statistical model valid at least for the Swiss Alps should be developed from locally measured diffuse sky and global radiation values.

For the radiosity model two future investigation points are given:

- It was noted that the radiosity model possesses one important restriction: It only considers diffuse reflections on surfaces. This is acceptable for the shortwave wavelength ranges treated here but might be not valid for other wavelength ranges.
- The fraction of radiosity and radiation, respectively exchanged between patches depends on the view factor and remains unchanged by the atmosphere between the patches. It was assumed that this holds for shortwave radiation but should be corrected in case of longwave radiation. In Section 9.5, p.139 it could however be shown that the implemented parameterisation for longwave radiation to account for atmospheric backscattering does not lead to an improvement compared to the computation with the Stefan-Boltzmann law. Note that this result was obtained by means of a single point validation with measurements on a winter and a summer day. Thus, the atmospheric influence should be verified for both, shortwave and longwave, radiation wavelength ranges.

In the following, future elaborations of the coupled surface process model Alpine3D to improve its application on road surface temperature modelling are given. An application for modelling road surface temperatures was presented in Chapter 11 that revealed the following points:

- The stability corrections implemented for the turbulent fluxes are inadequate for inclined and flat snow covered surfaces in alpine terrain. Landl and Lehning (2008) note that further investigations are necessary.
- In Alpine3D spatial air temperature interpolation is not coupled to incident radiation. This means, two grid cells I and J that have approximately the same height $z_I \approx z_J$, where I is shaded for several hours and J receives direct radiation the whole period, will still have the same air temperature in the model. Accordingly, the same air temperature is used within the computation of the turbulent fluxes at both grid cells but different surface temperatures are used. In most cases this will lead to a large compensating sensible heat flux that might result in an underestimation of modelled surface temperatures. Moore et al. (1993) present an approach to spatially distribute air temperature from one measurement. It corrects for the lapse rate, for surface orientation and for vegetative effects. Thus, this correction enables a valuable possibility to account for spatially varying incident radiation in a surface process model.
- The SNOWPACK module has to be extended by some road specific adaptations, i.e. an additional sensible heat flux to the road, salt treatment on the road, the possibility to describe a thin water layer on the road etc..

Nomenclature

α_{eff}	effective albedo of the model domain (dimensionless)
α	(mean) surface albedo (dimensionless)
α_{a}	albedo of a cloudless sky (dimensionless)
α_{ss}	snow surface albedo (dimensionless)
β	Ångström's turbidity parameter (dimensionless)
$\boldsymbol{M}$	radiosity matrix
χ_{sun}	sun-or-shadow parameter (0 for *shaded* and 1 for *in sun*)
χ_{IJ}	mutual visibility between two patches A_I and A_J (0 for *invisible*, 1 for *visible*)
Δx	horizontal grid cell size length (in m)
δ	solar declination angle (in radians)
Γ	day angle starting on 1 January (in radians)
Γ_{ne}	day angle starting from spring equinox time (in radians)
λ_{s}	soil heat conductivity (in $\mathrm{W(mK)^{-1}}$)
Ω	solid angle (in sr)
ϕ	geographical latitude (in °N)
ψ	sun's azimuth angle (in radians counting clockwise from north)
ρ	ideally diffuse reflectivity (dimensionless)
ρ_{s}	soil density (in $\mathrm{kgm^{-3}}$)
σ	typical vertical extension of a random topography (height of mountains) (in m)
σ_{SB}	Stefan-Boltzmann constant (in $\mathrm{Wm^{-2}K^{-4}}$)
τ_{aa}	broadband transmittance by aerosols due to absorption (dimensionless)
τ_{as}	broadband transmittance by aerosols due to Mie-scattering (dimensionless)
τ_{a}	total broadband transmittance by aerosols due to Mie-scattering and absorption by aerosols (dimensionless)

τ_{g}	broadband transmittance by uniformly mixed gases absorption (dimensionless)
τ_{o}	broadband transmittance by ozone absorption (dimensionless)
τ_{r}	broadband transmittance by Rayleigh-scattering (dimensionless)
τ_{w}	broadband transmittance by water vapor absorption (dimensionless)
$\mathrm{c_b}$	adjusting coefficient for S_{b} under clear skies (dimensionless)
$\mathrm{c_d}$	adjusting coefficient for S_{d} under clear skies (dimensionless)
θ	incidence angle (in radians)
θ_{i}	volume fraction of ice (dimensionless)
θ_{s}	volume fraction of soil (dimensionless)
θ_{v}	volume fraction of vapor (dimensionless)
θ_{w}	volume fraction of water (dimensionless)
θ_{z}	zenith angle (in radians)
$\varepsilon^{(k)}$	(true) iteration error/stopping criterion (in $\mathrm{Wm^{-2}}$)
$\varepsilon^{\star(k)}$	iteration error/stopping criterion related to $\varepsilon^{(k)}$ via some bound (in W)
ε_{s}	surface emissivity (dimensionless)
ε_{a}	emissivity of the atmosphere (dimensionless)
φ_{s}	surface azimuth angle (in °)
ϑ	angle between the viewing surface normal and the viewing direction (in degrees)
$\vec{n}$	surface normal vector
$\vec{s}$	sun vector - connecting the observer and the center of the solar disk
$\lvert v\rvert$	mean wind speed (in $\mathrm{ms^{-1}}$)
ξ	typical lateral extension of a random topography (width of mountains) (in m)
ζ_{s}	surface slope angle (in °)
A	actual grid cell surface (patch) (in m^2)
a	wavelength exponent in Ångström's turbidity formula (dimensionless)
B	radiosity (in $\mathrm{Wm^{-2}}$)
c_{ps}	soil heat capacity (in $\mathrm{J(kgK)^{-1}}$)
d_n	day number of the year (in days)
d_{ne}	nth day of the year starting at spring equinox time (in days)

E	direct emission (in Wm^{-2})
E_0	eccentricity correction factor (dimensionless)
E_{t}	equation of time (in minutes)
e_{a}	vapour pressure (in Pa)
e_{s}	saturation vapour pressure (in Pa)
f_{c}	ratio of scattered radiation in forward direction to the total scattered radiation due to aerosols (dimensionless)
$F_{\mathrm{d}A_I A_J}$	view factor between a differential dA_I and a finite surface A_J (dimensionless)
F_{sky}	sky view factor (dimensionless)
$F_{A_I A_J}$	view factor between two finite surfaces/patches A_I, A_J (dimensionless)
F_{IJ}	view factor (dimensionless)
H	geopotential height (in m)
k	iteration step
$k_{\mathrm{a},0.38}$	AOD from surface in a vertical path at 0.38 μ m wavelength (dimensionless)
$k_{\mathrm{a},0.5}$	AOD from surface in a vertical path at 0.5 μm wavelength (dimensionless)
k_{a}	broadband AOD from surface in a vertical path (dimensionless)
L	system/domain size (in m)
L_{a}	LW **a**tmospheric counter radiation / LW sky radiation (in Wm^{-2})
L_{inc}	total incident LW radiation (in Wm^{-}2)
L_{loc}	local longitude of a local position (in °)
L_{st}	longitude on which the local standard time is based (in °)
L_{t}	LW terrain emission (in Wm^{-2})
m_{a}	corrected or absolute optical airmass (dimensionless)
m_{r}	relative optical air mass (dimensionless)
M_{t}	clearness index, ratio of $S_{\mathrm{g}}^{\mathrm{meas}}/(S_{\mathrm{toa}}\ \cos\theta_{\mathrm{z}})$ (dimensionless)
M_{d}	diffuse sky fraction, ratio of $S_{\mathrm{d}}/S_{\mathrm{g}}^{\mathrm{meas}}$ (dimensionless)
n_0	spring equinox time from the beginning of the year (in days)
n_{c}	cloud cover fraction (in eights)
N_x	maximum number of grid cells in direction of i
N_y	maximum number of grid cells in direction of j

p	atmospheric air pressure (in hPa)
$P(x)$	radiative flux received at point x (in Wm^{-2})
p_0	atmospheric standard air pressure at sea level (in hPa)
$R(x, \Omega(x))$	radiance/specific intensity at x from solid angle $\Omega(x)$ (in $\mathrm{Wm}^{-2}\mathrm{sr}^{-1}$)
R_0	average radius of the earth (in m)
r_0	mean distance between earth and sun (equals one AU)
r_{gss}	effective snow grain radius (in mm)
r_{gs}	effective soil grain radius (in mm)
r_{IJ}	Euclidean distance between two patches (in m)
rh	relative humidity (in dimensionless)
S_{g}	incident global radiation (in Wm^{-2})
$S_{\mathrm{g}}^{\mathrm{meas}}$	measured global radiation value (dimensionless)
S_{toa}	SW radiation at the top of atmosphere on a surface normal to $\vec{s}$ on a given day (in Wm^{-2})
S_{b}	incident direct SW radiation (in Wm^{-2})
S_{d}	incident diffuse sky SW radiation (in Wm^{-2})
S_{t}	incident SW radiation due to reflections from terrain (in Wm^{-2})
T_{a}	air temperature (in K)
T_{s}	surface temperature (in K)
T_{ss}	snow surface temperature (in K)
U_0	total amount of ozone in a vertical column from surface (in cm)
U_3	total amount of ozone in an oblique column (in cm)
U_1	total amount of precipitable water in an oblique column (in cm)
w	hour angle (in radians)
w_0	single scattering albedo, ratio of energy scattered by Mie-scattering to total attenuation (dimensionless)
wp_0	amount of precipitable water in a vertical column from surface (in cm)
x_{sub}	substructuring threshold (dimensionless)
z	terrain elevation (in m)
z^{station}	measurement station altitude (in m)
TSI	total solar irradiance or solar constant (in Wm^{-2})

List of Figures

List of Tables

References

Ångstrom, A. (1925). The albedo of various surfaces of ground. *Geografiska Annaler 7*, 323–342.

Ångstrom, A. (1929). On the atmospheric transmission of sun radiation and on dust in the air. *Geografiska Annaler 11*, 156–166.

Ångstrom, A. (1930). On the atmospheric transmission of sun radiation. *Geografiska Annaler 12*, 130–159.

Adler, R. J. (1981). *The Geometry of Random Fields.* Wiley, London.

AdS2 (WWW). Atlas der Schweiz. http://www.atlasderschweiz.ch; called 02.10.2007.

Amanatides, J. and A. Woo (1987). *A fast voxel traversal algorithm for ray tracing.* G. Marechal, Hrsg., Eurographics '87, North-Holland, August. p. 3-10.

Arnold, N. S., W. G. Rees, A. J. Hodson and J. Kohler (2006). Topographic controls on the surface energy balance of a high arctic valley glacier. *Journal of Geophysical Research 111*(F02011).

Atkinson, K. E. (1997). *The Numerical Solution of Integral Equations of the Second Kind.* Cambridge University Press.

Baranoski, G. V. G., R. Bramley and P. Shirley (1995). Iterative methods for fast radiosity solutions. http://citeseer.ifi.unizh.ch/baranoski95iterative.html.

Bartelt, P. and M. Lehning (2002). A physical SNOWPACK model for the Swiss avalanche warning Part I: Numerical model. *Cold Regions Science and Technology 35*, 123–145.

Baum, D. R., H. E. Rushmeier and J. M. Winget (1989). Improving radiosity solutions through the use of analytically determined form-factors. *Computer Graphics (SIGGRAPH '89 Proceedings) 23*(3), 325–334.

Bellasio, R., G. Maffeis, J. S. Scire, M. G. Longoni, R. Bianconi and N. Quaranta (2005). Algorithm to account for topographic shading effects and surface temperature dependence on terrain elevation in diagnostic meteorological models. *Boundary-Layer Meteorology 114*, 595–614.

Berk, A., G. P. Anderson, L. S. Bernstein, P. K. Acharya, H. D. ans M. W. Matthew, S. M. A. Golden, J. H. C. Jr., S. C. Richtsmeier, B. Pukall, C. L. Allred and L. S. J. ans M. L. Hoke (1999). MODTRAN4 Radiative transfer modeling for atmospheric correction. In: *SPIE Proceeding, Optical Spectroscopic Techniques and Instrumentation for Atmospheric and Space Research III*, Band 3756. http://www.spectral.com/pdf/sr116.pdf.

BFS (WWW). Bundesamt für Statistik, Switzerland. http://www.bfs.admin.ch; called 28.01.2008.

Bintanja, R. (1996). The parameterization of shortwave and longwave radiative fluxes for use in zonally averaged climate models. *Journal of Climate 9*, 439–454.

Bird, R. E. and R. L. Hulstrom (1980). Direct insolation models. Technical Report SERI/TR-335-344, Solar Energy Research Institute, Golden, Colorado, US.

Bird, R. E. and R. L. Hulstrom (1981). A simplified clear sky model for direct and diffuse insolation on horizontal. Technical Report SERI/TR-642-761, Solar Energy Research Institute, Golden, Colorado, US.

Boland, J., L. Scott and M. Luther (2001). Modelling the diffuse fraction of global solar radiation on a horizontal surface. *Environmetrics 12*, 103–116.

Borel, J. L., Y. Durand, F. Sillion and C. L. Gal (1998). Computing the radiative balance in mountainous areas: Modelling, Simulation and Visualization. *ERCIM News 38*, 24–26. http://www.ercim.org/publication/Ercim_News/enw34/EN34.pdf.

Boschung (2004). Boschung Holding AG, Route d'Englisberg 21, CH-1763 Granges-Paccot. http://www.boschung.ch; called 25.01.2008.

Bouilloud, L. and E. Martin (2006). A coupled model to simulate snow behaviour on roads. *Journal of applied meteorology and climatology 45*(500-516).

Bourgeois, C. S., P. Calanca and A. Ohmura (2006). A field study of the hemispherical directional reflectance factor and spectral albedo of dry snow. *Journal of Geophysical Research 111*(D20108). doi:10.1029/2006JD007296.

Bourges, B. (1985). Improvement in solar declination computation. *Solar Energy 35*(4), 367–369.

Brun, E., P. David, M. Sudul and G. Brunot (1992). A numerical model to simulate snow-cover stratigraphy for operational avalanche forecasting. *Journal of Glaciology 38*, 13–22.

Brun, E., E. MArtin, V. Simon, C. Gendre and C. Coléou (1989). An energy and mass model of snow cover for operational avalanche forecasting. *Journal of Glaciology 35*, 333–342.

Bu, J. and E. F. Deprettere (1989). A VLSI system architecture for high-speed radiative transfer 3D image synthesis *** . *The Visual Computer 5*, 121–133.

Cahalan, R. F., L. Oreopoulos, A. Marshak, K. F. Evans, A. B. Davis, R. Pincus, K. H. Yetzer, B. Mayer, R. Davies, T. P. Ackerman, H. W. Barker, E. E. Clothiaux, R. G. Ellingson, M. J. Garay, E. Kassianov, S. Kinne, A. Macke, W. O'Hirok, P. T. Partain, S. M. Prigarin, A. N. Rublev, G. L. Stephens, F. Szczap, E. E. Takara, T. Várnai, G. Wen and T. B. Zhuravleva (2005). The International Intercomparison of 3D Radiation Codes (I3RC): Bringing together the most advanced radiative transfer tools for cloudy atmospheres. *Bulletin of the American Meteorological Society 86*(9), 1275–1293.

Chen, Y., A. Hall and K. N. Liou (2006). Application of three-dimensional solar radiative transfer to mountains. *Journal of Geophysical Research 111*(D21111).

Chow, F. K., A. P. Weigel, R. L. Street, M. W. Rotach and M. Xue (2004). High-resolution large-eddy simulations of the riviera valley: Methodology and sensitivity studies. In: *11th Conference on Mountain Meteorology and the Annual Mesoscale Alpine Program.* http://www.ce.berkeley.edu/∼chow/pubs/Chow_MM11_2004.pdf.

Christiansen, C. (1883). II. Absolute Bestimmung des Emissions- und Absorptionsvermögens für Wärme. *Ann. Phys. u. Chem. 19*, 267–283.

Cohen, M. F., S. E. Chen, J. R. Wallace and D. P. Greenberg (1988). A progressive refinement approach to fast radiosity image generation. *Computer Graphics (SIGGRAPH '88 Proceedings) 22*(4), 75–84.

Cohen, M. F. and D. P. Greenberg (1985). The hemi-cube, a radiosity solution for complex environments. *Computer Graphics (SIGGRAPH '85 Proceedings) 19*(3), 31–40.

Cohen, M. F. and J. R. Wallace (1993). *Radiosity and Realistic Image Synthesis.* Academic Press Professional, Cambridge.

Colette, A., F. K. Chow and R. L. Street (2003). A numerical study inversion-layer breakup and the effects of topographic shading in idealized valleys. *Journal of Applied Meteorology 42*, 1255–1272.

Corripio, J. G. (2002). *Modelling the energy balance of high altitude glacerised basins in the Central Andes.* PhD-Thesis, University of Edinburgh, UK.

Corripio, J. G. (2003). Vectorial algebra algorithms for calculating terrain parameters from DEMs and solar radiation modelling in mountainous. *International Journal of Geographical Information Science 17*(1), 1–23.

Crevier, L. P. and Y. Delage (2001). METRo: A new model for road-condition forecasting in Canada. *Journal of Applied Meteorology 40*, 2026–2037.

Degünther, M., R. Meerkötter, A. Albold and G. Seckmeyer (1998). Case study on the influence of inhomogeneous surface albedo on UV irradiance. *Geophysical Research Letters 25*(19), 3587–3590.

Dietler, G. and Y. C. Zhang (1992). Fractal aspects of the Swiss landscape. *Physica A 191*, 213–219.

Doorschot, J., M. Lehning and A. Vrouwe (2004). Field measurements of snow drift threshold and mass fluxes and related model simulations.

Dozier, J. and J. Bruno (1981). A faster solution to the horizon problem. *Computers & Geosciences 7*, 145–151.

Duffie, J. A. and W. A. Beckman (2006). *Solar Engineering of Thermal Processes.* John Wiley & Sons, Inc., Hoboken, New Jersey, 3rd ed.

Emde, C. and B. Mayer (2007). Simulation of solar radiation during a total eclipse: a challenge for radiative transfer. *Atmospheric Chemistry and Physics 7*(9), 2259–2270.

Encarnação, J., W. Strasser and R. Klein (1996). *Graphische Datenverarbeitung 1, Gerätetechnik, Programmierung und Anwendung graphischer Systeme.* R. Oldenbourg Verlag München Wien, 4. Auflage.

Encarnação, J., W. Strasser and R. Klein (1997). *Graphische Datenverarbeitung 2, Modellierung komplexer Objekte und photorealistische Bilderzeugung.* R. Oldenbourg Verlag München Wien, 4. Auflage.

Erbs, D. G., S. A. Klein and J. A. Duffie (1982). Estimation of the diffuse radiation fraction for hourly, daily and monthly-average global radiation. *Solar Energy 28*(4), 293–302.

EU (WWW). Eu project aware. http://aware-eu.info; called 27.01.2008.

Evans, K. F. (1998). The spherical harmonics discrete ordinate method for three-dimensional atmospheric radiative transfer. *Journal of the Atmospheric Sciences 55*, 429–446.

Faure, F., M. Lehning, C. Hug, S. Mobbs and L. Huw (2007). Very high resolution windfield simulations over a steep alpine ridge: mean flow and turbulence characteristics. In: *29th International Conference on Alpine Meteorology, 4-8 June, 2007, Chambéry, France.*

Fierz, C. W., P. Riber, E. E. Adams, A. R. Curran, P. M. B. Föhn, M. Lehning and C. Plüss (2003). Evaluation of snow-surface energy balance models in alpine terrain. *Journal of Hydrology 282*, 76–94.

Fleming, M. D. and R. M. Hoffer (1979). Machine processing of Landsat MSS data and DMA topographic data for forest cover type mapping. LARS Technical Report 062879, Laboratory for Applications of Remote Sensing, Purdue University, West Lafayette, Indiana, USA.

Flury, G. (2006). Lokale Simulation und Validierung für die Winterstrassenwettervorhersage. Diploma thesis, University of Zurich, Switzerland and WSL, Federal Institute for Snow and Avalanche Research SLF, Davos, Switzerland.

Fortuniak, K. (2008). Numerical estimation of the effective albedo of an urban canyon. *Theoretical Applied Climatology 91*, 245–258.

Fröhlich, C. (2006). Solar irradiance variability since 1978. *Space Science Reviews 125*(1-4), 53–65.

Fröhlich, C. and J. Lean (1998). The sun's total irradiance: cycles, trends and related climate change uncertainties since 1976. *Geophysical Research Letters 25*(23), 4377–4380.

Funk, M. (1984). *Räumliche Verteilung der Massenbilanz auf dem Rhonegletscher und ihre Beziehung zu Klimaelementen.* PhD-Thesis, ETHZ Zurich, Switzerland.

Garen, D. and D. Marks (2001). Spatial fields of meteorological input data including forest canopy corrections for an energy budget snow simulation model. In: *Soil-Vegetation-Atmosphere Transfer Schemes and Large Scale Hydrological Models, Dolman A.J., Hall A.J., Kavvas M.L., Oki T., Pomeroy J.W.(eds). IAHS Press: Wallingford*, Nr. 270, p. 349–353.

Goral, C. M., K. E. Torrance, D. P. Greenberg and B. Battaile (1984). Modeling the interaction of light between diffuse surfaces. *Computer Graphics (SIGGRAPH '84 Proceedings) 18*(3), 213–222.

Gortler, S., M. F. Cohen and P. Slusallek (1994). Radiosity and relaxation methods. *IEEE Computer Graphics and Applications 14*(6), 48–58.

Griggs, M. (1968). Emissivities of natural surfaces in the 8- to 14-micron spectral region. *J. Geophys. Res. 73*, 7545–7551.

Gruber, S., M. Hoelzle and W. Haeberli (2004). Rock-Wall temperatures in the Alps: Modelling their topographic distribution and regional differences (in press). *Permafrost and Periglacial Processes 15*, 1–9.

Gueymard, C. (1989b). An atmospheric transmittance model for the clear sky solar beam. *Agricultural and Forest Meteorology 43*, 253–265.

Gurtz, J., M. Zappa, K. Jasper, H. Lang, M. Verbunt, A. Badoux and T. Vitvar (2003). A comparative study in modelling runoff and its components in two mountainous catchments. *Hydrological Processes 17*, 297–311.

Harman, I. N., M. J. Best and S. E. Belcher (2004). Radiative exchange in an urban street canyon. *Boundary-Layer Meteorology 110*, 301–316.

Hock, R. and B. Holmgren (2005). A distributed surface energy-balance model for complex topography and its application to Storglaciáren, Sweden. *Journal of Glaciology 51*(172), 25–36.

Hodgson, M. E. (1995). What cell size does the computed slope/aspect angle represent? *Photogrammetric Engineering and Remote Sensing 10*(7), 817–830.

Hodgson, M. E. (1998). Comparison of angles from surface slope/aspect algorithm. *Cartography and Geographic Information Systems 25*(3), 173–185.

Horn, B. K. P. (1981). Hill shading and the reflectance map. *Proceedings of the IEEE 69*(1), 14–47.

Iqbal, M. (1983). *An Introduction to Solar Radiation.* Academic Press, Toronto.

Jensen, H. W. (2001). *Realistic Image Synthesis using Photon Mapping.* AK Peters.

Jensen, H. W. (2003). Monte Carlo Ray Tracing. In: *Computer Graphics (SIGGRAPH '2003 Course 44)*, p. 11–12. http://www.cs.rutgers.edu/ decarlo/readings/mcrt-sg03c.pdf.

Kasten, F. (1993). Discussion in the relative optical air mass. *Lighting Res. Technol. 25*(3), 129–130.

Kasten, F. and A. T. Young (1989). Revised optical air mass tables and approximation formula. *Applied Optics 28*(22), 4735–4738.

Klok, E. J., K. Jasper, K. P. Roelofsma, J. Gurtz and A. Badoux (2001). Distributed hydrological modelling of a heavily glaciated alpine river basin. *Hydrological Sciences Journal - Journal des Sciences Hydrologiques 46*(4), 553–557.

Kneizys, F., E. P. Shettle, L. W. Abreu, J. H. Chetwynd, G. P. Anderson, W. O. Gallery, J. E. Selby and S. A. Clough (1988). A users guide to LOWTRAN 7. Environmental research 1010, Air force geophysical laboratory, Hanson.

Kondratyev, K. J. and M. P. Manolova (1960). The radiation balance of slopes. *Solar Energy 4*(1), 14–19.

Kondratyev, K. Y. (1969). *Radiation in the atmosphere.* Academic Press, New York.

Konzelmann, T., R. S. W. van de Wal, W. Greuell, R. Bintanja, E. A. C. Henneken and A. A. Ouchi (1994). Parameterization of global and longwave incoming radiation for the Greenland Ice Sheet. *Global and Planetary Change 9*, 143–164.

Kuzmin, P. P. (1947). Absorption of solar radiation by snow cover. *Meteorol. Hydrol., Inform. Bull.* (5).

Kylling, A., A. Dahlback and B. Mayer (2000b). The effect of clouds and surface albedo on UV irradiances at a high latitude site. *Geophysical Research Letters 27*(9), 1411–1414.

Kylling, A. and B. Mayer (2001). Ultraviolet radiation in partly snow covered terrain: Observations and three-dimensional simulations. *Geophysical Research Letters 28*(19), 3365–3368.

Kylling, A., T. Persen, B. Mayer and T. Svenøe (2000a). Determination of an effective spectral surface albedo from ground-based global and direct UV irradiance measurements. *Journal of Geophysical Research 105*, 4949–4959.

Landl, B. (2007). *Investigation of small scale characteristics of the energy balance over snow covered mountainous terrain.* PhD-Thesis, ETHZ Zurich, Switzerland and WSL, Federal Institute for Snow and Avalanche Research SLF, Davos, Switzerland.

Landl, B. and M. Lehning (2008). Case study: Evaluation of coupled model simulations of energy balance over a snow covered flat field and a steep slope in alpine terrain. *Water Ressources Research submitted*.

Leckner, B. (1978). The spectral distribution of solar radiation at the earth's surface-elements of a model. *Solar Energy 20*, 143–150.

Lehning, M., P. Bartelt, S. Bethke, C. Fierz, D. Gustafsson, B. Landl, M. Lütschg, O. Martius, I. Meirold, N. Raderschall, J. Rhyner and M. Stähli (2004). Review of SNOWPACK and ALPINE3D applications. In: *5th International Snow Engineering Conference, Davos, Switzerland, Bartelt, Adams, Christen, Sack&Sato (eds), Balkema*, p. 299–307.

Lehning, M., P. Bartelt, B. Brown and C. Fierz (2002b). A physical SNOWPACK model for the Swiss avalanche warning Part III: Meteorological forcing, thin layer formation and evaluation. *Cold Regions Science and Technology 35*, 169–184.

Lehning, M., P. Bartelt, B. Brown, C. Fierz and P. Satyawali (2002a). A physical SNOWPACK model for the Swiss avalanche warning Part II: Snow microstructure. *Cold Regions Science and Technology 35*, 147–167.

Lehning, M., P. Bartelt, B. Brown, T. Russi, U. Stöckli and M. Zimmerli (1999). Snowpack model calculations for avalanche warning based upon a new network of weather and snow stations. *Cold Regions Science and Technology 30*, 145–157.

Lehning, M., H. Löwe, N. Raderschall and M. Ryser (2007). Inhomogeneous precipitation distribution and snow transport in steep terrain. *AGU Fall Meeting Abstracts*, B8+.

Lehning, M., I. Völksch, D. Gustafsson, T. Nguyen and M. Stähli (2006). ALPINE3D: A detailed model of mountain surface processes and its application to snow hydrology. *Hydrological Processes 20*, 2111–2128.

Leica (WWW). Leica Geosystems. http://www.leica-geosystems.com/corporate/en/lgs_4547.htm; called 08.10.2007.

Letsinger, S. L. and G. A. Olyphant (2007). Distributed energy-balance modeling of snow-cover evolution and melt in rugged terrain: Tobacco Root Mountains, Montana, USA. *Journal of Hydrology 336*, 48–60.

Li, X., C. Guodong, C. Xianzhang and L. Ling (1999). Modification of solar radiation model over rugged terrain. *Chinese Science Bulletin 44*(15), 1345–1350.

Liou, K. N. (2002). *An Introduction to Atmospheric Radiation*. Academic Press.

Lischinski, D., B. Smits and D. P. Greenberg (1994). Bounds and error estimates for radiosity. *Computer Graphics 28*(Annual Conference Series), 67–74.

Liu, B. Y. H. and R. C. Jordan (1960). The interrelationship and characteristic distribution of direct, diffuse and total solar radiation. *Solar Energy 4*(3), 1–19.

LKO (WWW). Light Climate Observatory, Arosa (Switzerland). http://www.meteo schweiz.ch/web/de/klima/klimaentwicklung/lange_ozonmessreihen.Par.0003.Download File.tmp/tageswerteozonsaeulearosa.txt; called 15.05.2007.

Lütschg, M. (2005). *A Model and Field Analysis of the Interaction between Snow Cover and Alpine Permafrost*. PhD-Thesis, University of Zurich, Switzerland.

Lütschg, M. and W. Haeberli (2005). Permafrost evolution in the Swiss Alps in a changing climate and the role of the snow cover. *Norwegian Journal of Geography 59*, 78–83.

Marchuk, G., G. Mikhailov, M. Nazaraliev, R. Darbinjan, B. Kargin and B. Elepov (1980). *The Monte Carlo Methods in Atmospheric Optics.* Springer-Verlag, 208 pp.

Martius, O. (2002). Implementing a view factor approach into an energy balance model for snow covered alpine terrain. Diploma thesis, ETHZ Zurich, Switzerland and WSL, Federal Institute for Snow and Avalanche Research SLF, Davos, Switzerland.

Marty, C. A. (2001). *Surface radiation, cloud forcing and greenhouse effect in the alps.* PhD-Thesis, ETHZ Zurich, Switzerland and Physikalisch-Meteorologisches Observatorium Davos, World Radiation Center Davos, Switzerland.

Matzinger, N., M. Andretta, E. v. Gorsel, R. Vogt, A. Ohmura and M. Rotach (2003). Surface radiation budget in an alpine valley. *Q.J.R. Meterol. Soc. 129*, 877–895.

Mauz, C. (2006). Frost and thaw mechanisms related to road construction in Greenland. Diploma thesis, Center for Arctic Technology (ARTEC) at University of Denmark (DTU).

Mayer, B. (1999). I3RC phase 1 results from the MYSTIC Monte Carlo model. In: *Extended Abstract for the I3RC workshop, Tucson, Arizona, November 17-19, 1999.* http://i3rc.gsfc.nasa.gov/abstracts-new/Mayer-ncarabs2.pdf; called 23.11.2007.

Mayer, B. (2000a). I3RC phase 2 results from the MYSTIC Monte Carlo model. In: *Short Abstract for the I3RC workshop, Tucson, Arizona, November 15-17, 2000.* http://www.bmayer.de/papers/i3rc2_1.pdf; called 23.11.2007.

Mayer, B. (DLR). Department Atmospheric Remote Sensing at the Institute of Atmospheric Physics (DLR, Oberpfaffenhofen, Germany). http://www.bmayer.de/index.html?publications.html&1; called 03.03.2008.

Mayer, B. and M. Degünther (2000b). Comment on "measurements of erythemal irradiance near davis station, antarctica: Effect of inhomogeneous surface albedo". *Geophysical Research Letters 27*, 3489–3490.

McCluney, W. R. (1994). *Introduction to Radiometry and Photometry.* Artech House, Inc., Boston London.

Meier, M. (2007). Visualisierung der Zeit. Diploma thesis. Maturaarbeit, Schweizerische Alpine Mittelschule Davos (SAMD), Switzerland.

Meirold-Mautner, I. and M. Lehning (2004). Measurements and model calculations of the solar shortwave fluxes in snow on Summit, Greenland. *Annals of Glaciology 38*(1), 279–284.

Michlmayr, G., M. Lehning, G. Koboltschnig, H. Holzmann, M. Zappa, R. Mott and W. Schöner (2008). Application of the Alpine3D model for glacier mass balance and glacier runoff studies at Goldbergkees, Austria. *Hydrological Processes Accepted.*

Minnich, A., J. Turner and M. Hall (2002). A viewfactor-based radiative heat transfer model for Telluride. http://www.lanl.gov/Augustus/2002_08_07/2002_08_07.pdf.

Moore, I. D., T. W. Norton and J. E. Williams (1993). Modelling environmental heteorogenity in forested landscapes. *Journal of Hydrology 150*, 717–747.

Mott, R., F. Faure, G. Koboltschnig, M. Lehning, H. Löwe, G. Michlmayr, A. Prokop and W. Schöner (2007). Simulation of seasonal snow cover development and seasonal snow cover distribution for glaciated sites (Sonnblick, Austrian Alps) with the Alpine3D model. In: *International Symposium on Snow Science, 3-7 September 2007, Moscow, Russia.* http://www.igsoc.org/symposia/2007/russia/.

Müller, M. D. and D. Scherer (2005). A grid- and subgrid-scale radiation parameterization of topographic effects for mesoscale weather forecast models. *Monthly Weather Review 133*, 1431–1442.

Murray, F. W. (1967). On the computation of saturation vapor pressure. *Journal of Applied Meteorology 6*(1), 203–204.

Nagy, G. (1994). Terrain visibility. *Computer&Graphics 18*(6), 763–773.

Nguyen, T. and P. Kuonen (2007). Programming the Grid with POP-C++. *Journal of Future Generation Computer Systems* (23), 23–30.

Noilhan, J. and S. Planton (1989). A simple parameterization of land surface processes for meteorological models. *Mon. Wea. Rev. 117*, 536–549.

Nunez, M. (1980). The calculation of solar and net radiation in mountainous terrain. *Journal of Biogeography 7*(2), 173–186.

Nusselt, W. (1928). Graphische Bestimmung des Winkelverhältnisses bei der Wärmestrahlung. *Zeitschrift des Vereines Deutscher Ingenieure 72*(20), 673.

Odermatt, D., D. Schläpfer, M. Lehning, M. Schwikowski, M. Kneubühler and K. I. Itten (2005). Seasonal study of directional reflectance properties of snow. *EARSeL eProceedings 4*, 203–214.

Oke, T. R. (1987). *Boundary layer climates*. Routeledge, 2nd ed.

Oliphant, A. J., R. A. Spronken-Smith, A. P. Sturman and I. F. Owens (2003). Spatial variability of surface radiation fluxes in mountainous terrain. *Journal of Applied Meteorlogy 42*, 113–128.

Olyphant, G. A. (1986b). Longwave radiation in mountainous areas and its influence on the energy balance of alpine snowfields. *Water Resources Research 22*(1), 62–66.

Orgill, J. F. and K. G. Hollands (1977). Correlation equation for hourly diffuse radiation on a horizontal surface. *Solar Energy 19*(4), 357–359.

Paulson, C. A. (1970). The mathematical representation of wind speed and temperature profiles in the unstable atmospheric surface layer. *Journal of applied meteorology 9*, 857–861.

Philipona, R. (2002). Underestimation of solar global and diffuse radiation measured at earth's surface. *Journal of Geophysical Research 107*(D22), 4654–4561.

Plüss, C. (1997). *The energy balance over an alpine snowcover, Point measurements and areal distribution*. Nr. 65. Zürcher Geographische Schriften, Geographisches Institut ETHZ, Zurich, Switzerland.

PMOD/WRC (WWW). Physikalisch Meterologisches Observatorium and World Radiation Center, Davos (Switzerland). http://www.pmodwrc.ch.

Rayer, P. J. (1987). The meteorological office forecast road surface temperature model. *Meteor. Mag. 116*, 180–191.

Reindl, D. T., W. A. Beckman and J. A. Duffie (1990). Diffuse fraction correlations. *Solar Energy 45*(1), 1–7.

Riber, P. (2001). Energy balance of an alpine snow-cover. Diploma thesis, ETHZ Zurich, Switzerland and WSL, Federal Institute for Snow and Avalanche Research SLF, Davos, Switzerland.

Ritter, P. (1987). A vector-based slope and aspect generation algorithm. *Photogrammetic Engineering and Remote Sensing 53*(8), 1109–1111.

Sass, B. H. (1992). A numerical model for prediction of road temperature and ice. *Journal of Applied Meteorology 31*(12), 1499–1506.

Schaefer, S. (1999). *Efficient Object-Based Hierarchical Radiosity Methods.* PhD-Thesis, University of Braunschweig, Germany.

Scherer, D. and E. Parlow (1994). Terrain as an important controlling factor for climatological, meteorological and hydrological processes in NW-Spitsbergen. *Z. Geomorphol. N.F., Suppl. Bd. 97*, 175–193.

Schirmer, M. (2005). Erstellung einer GIS-Schnittstelle für ein physikalisches Modell alpiner Oberflächenprozesse mit einer Anwendung im Skirennsport. Diploma thesis, University of Freiburg, Germany and WSL, Federal Institute for Snow and Avalanche Research SLF, Davos, Switzerland.

Schmucki, D., S. Voigt, R. Phillipona, C. Fröhlich, J. Lenoble, A. Ohmura and C. Wehrli (2001). Effective albedo derived from UV measurements in the Swiss Alps. *Journal of Geophysical Research 106*(D6), 5369–53838.

Schroeder, P. and P. Hanrahan (1993). On the form factor between two polygons. *Computer Graphics (SIGGRAPH '93 Proceedings)*, 163–164. http://graphics.stanford.edu/papers/formfactor.

Senkova, A. V., L. Rontu and H. Savijärvi (2007). Parameterization of orographic effects on surface radiation in HIRLAM. *Tellus 59A*, 279–291.

Shao, J. (1990). *A winter road surface temperature prediction model with comparison to others.* PhD-Thesis, University of Birmingham, UK.

Sicart, J. E., J. W. Pomeroy, R. L. H. Essery and D. Bewley (2006). Incoming longwave radiation to melting snow: observation, sensitivity and estimation in northern environments. *Hydrological Processes 20*, 3697–3708.

Siegel, R. and J. R. Howell (1978). *Thermal Radiation Heat Transfer.* Hemisphere Publishing Corp.

Siegel, R. and J. R. Howell (2002). *Thermal radiation heat transfer.* Taylor and Francis, New York, 4th edition.

Siegel, R., J. R. Howell and J. Lohrengel (1991). *Wärmeübertragung durch Strahlung, Teil 2 Strahlungsaustausch zwischen Oberflächen und in Umhüllungen.* Springer-Verlag Berlin Heidelberg.

Spencer, J. W. (1971). Fourier series representation of the position of the sun. *Search 2*(5), 172.

Staehelin, J., A. Renaud, J. Bader, R. McPeters, P. Viatte, B. Hoegger, V. Bugnion, M. Giroud and H. Schill (1998). Total ozone series at Arosa (Switzerland): Homogenization and data comparison. *Journal of Geophysical Research 103*(D5), 5827–5841.

Stalder, H. (2004). Expedition in die Eiszeit am Gotthard. *Tages-Anzeiger, 30.03.*, 5.

Stearns, C. and G. Weidner (1993). Sensible and latent heat flux estimates in Antarctica. *Antarctic Research Series 61*, 109–138.

Stewart, A. (1998). Fast horizon computation at all points of a terrain with visibility and shading applications. *IEEE Transactions on Visualization and Computer Graphics 4*(1), 82–93.

Stocker-Mittaz, C., M. Hoelzle and W. Haeberli (2002). Modelling Alpine permafrost distribution based on energy-balance data: a first step. *Permafrost and Periglacial Processes 13*, 271–282.

Stull, R. B. (2000). *Meteorology for scientists and engineers.* Brooks/Cole, Thomson Learning. 2nd Edition.

Sulakvelidze, G. K. and A. M. Okujava (1959). Snow and its properties. *Proc. Elbrus Compl. Exped. 1.*

Sumpner, W. E. (1894). The diffusion of light. *Proc. Phys. Soc. London 94*, 10–29.

Swisstopo (WWW). Federal Office of Topography, Seftigenstrasse 264, CH-3084 Wabern. http://www.swisstopo.ch/en/; called 28.01.2008.

Takahashi, N., R. Tokunaga, M. Asano and N. Ishikawa (2006). Developing a method to predict road surface temperatures, -Applying heat balance model considering traffic volume-. In: *13th SIRWEC Conference, Turin, Italy*, p. 58–66.

Thornes, J. E. (1984). *The prediction of ice formation on motorways.* PhD-Thesis, University College London, UK.

Verseghy, D. L. and D. S. Munro (1989). Sensitivity studies on the calculation of the radiation balance of urban surfaces: I. Shortwave radiation. *Boundary-Layer Meteorology 46*, 309–331.

Vujicic, M. R., N. P. Lavery and S. G. R. Brown (2006). View factor calculation using the monte carlo method and numerical sensitivity. *Communications in Numerical Methods in Engineering 22*, 197–203.

Wallace, J. R., K. A. Elmquist and E. A. Haines (1989). A ray tracing algorithm for progressive radiosity. *Computer Graphics 23*(3).

Wang, Q., J. Tenhunen, M. Schmidt, O. Kolcun and M. Droesler (2006). A model to estimate global radiation in complex terrain. *Boundary-Layer Meteorology 119*, 409–429.

Warren, S. G. (1982). Optical properties of snow. *Reviews of Geophysics and space physics 20*(1), 67–89.

Wehrli, C. (2002). Aufbau eines neuen Messnetzes für Aerosol Optische Dicke. GAW Brief 9, Deutscher Wetterdienst (DWD), Germany. http://www.dwd.de/scripts/print.php?pr=/de/FundE/Observator/MOHP/hp2/gaw/gaw_briefe/gaw_briefe.htm.

Weihs, P., J. Lenoble, M. Blumthaler, T. Martin, G. S. ans R. Philipona, A. D. la Casiniere ans C. Sergent, J. Gröbner, T. Cabot, D. Masserot, T. P. ans G. Rengarajan, D. Schmucki and S. Simic (2001). Modeling the effect of an inhomogeneous surface albedo on incident UV radiation in mountainous terrain: determination of an effective surface albedo. *Geophysical Research Letters 28*(16), 3111–3114.

Weissel, J. K., L. F. Pratson and A. Malinverno (1994). The length-scaling properties of topography. *Journal of Geophysical Research 99*(B7).

Whiteman, C. D. (2000). *Mountain Meteorology: Fundamentals and Applications.* Oxford University Press.

Whiteman, C. D., K. J. Allwine, L. J. Fritschen, M. M. Orgill and J. R. Simpson (1989a). Deep valley radiation and surface energy budget microclimes. Part I: Radiation. *Journal of Applied Meteorology 28*, 414–426.

Whiteman, C. D., K. J. Allwine, L. J. Fritschen, M. M. Orgill and J. R. Simpson (1989b). Deep valley radiation and surface energy budget microclimates. Part II: Energy budget. *Journal of Applied Meteorology 28*, 427–437.

Whitted, T. (1980). An improved illumination model for shaded display. In: *Communications of the ACM, June 1980.*

WSL (2005). Schweizerisches Landesforstinventar LFI. Datenbankauszug der Erhebung 1993-95 vom 3. Mai 2005. Ulrich Ulmer. Swiss Federal Institute for Forest, Snow and Landscape Research (WSL).

Xue, M., K. K. Droegemeier and V. Wong (2000). The Advanced Regional Prediction System (ARPS) - A multi-scale, non-hydrostatic atmospheric simulation and prediction model. Part I: Model dynamics and verification. *Meteorology and Atmospheric Physic 75*, 161–193.

Xue, M., K. K. Droegemeier, V. Wong, A. Shapiro, K. Brewster, F. Carr, D. Weber, Y. Liu and D. Wang (2001). The Advanced Regional Prediction System (ARPS) - A multi-scale, non-hydrostatic atmospheric simulation and prediction tool. Part II: Model physics and applications. *Meteorology and Atmospheric Physic 76*, 143–165.

Zappa, M., F. Pos, U. Strasser, P. Warmerdam and J. Gurtz (2003). Seasonal water balance of an Alpine catchment as evaluated by different methods for spatially distributed snowmelt modelling. *Nordic Hydrology 34*, 179 – 202.

Zhou, Y. and Q. Peng (1992). The super-lane buffer: An efficient form-factor evaluation algorithm for progressive radiosity. *Computer Graphics 16*(2), 151–158.

Curriculum Vitae

Nora Helbig

Born 19 April 1978, Dresden, Germany

Citizen of Germany

1988–1997:	High School in Dresden, Walsrode and Lahr, Germany
1997–2003:	Undergraduate Studies in Meteorology at the University of Karlsruhe, Germany
2003:	Diploma in Meteorology, Thesis entitled: 'The spatial and temporal distribution of pollen on a regional scale by means of numerical model calculations', University of Karlsruhe, Germany
2003–2004:	Research Assistant at the Meteorological Institute, University of Karlsruhe, Germany
2004	Graduated trainee at WSL Swiss Federal Institute for Snow and Avalanche Research SLF, Davos Switzerland
2004–2008:	Doctoral Student, WSL Swiss Federal Institute of Snow and Avalanche Research SLF and Physical Geography Division, Department of Geography, University of Zurich, Switzerland

Acknowledgements

First of all I want to thank Michael Lehning for his encouraging help to find funding for this study, his constant supervision and his ongoing trust in the progress of the main applied science study. I am also grateful for the provision of his wide background knowledge concerning snow related questions and his critical questions.

My very special thank goes to Henning Löwe for his attentive, motivating supervision (and it was his first!), for teaching me how different a research topic can be treated especially from the view of a theoretical physicist. Many many thanks to his ongoing patient explanations and discussions concerning all research areas as well as all kind of programming questions. I could profit and learn so much from him and I would say he helped me to finally believe in all kind of good endings.

I want to thank Wilfried Haeberli of the Department of Geography at the University of Zurich for the chief supervising. He always showed a great interest. I want to also thank him for his valuable support in all organisational questions.

I am grateful to Charles Fierz and Christoph Marty for lots of helpful discussions about radiation and measurement related topics, for delivering lots of valuable scientific information to me as well as data support. Many thanks also to Michel Schirmer and Andi Stoffel for supporting me with GIS solutions. Thanks to Franz Herzog and the garage team for helping me with the construction and electrics for the measurement advice of the shaded pyranometer. A special thank also goes to Roli Meister who was very enthusiastic whenever I asked him. I want to thank him and also Patrick Thee for helping me measuring with the tachymeter. Julian Gröbner and Gregor Hülsen (PMOD/WRC) I want to thank for lenting me a pyranometer and discussing with me my research subject. Furthermore, I would like to thank Bernhard Mayer (DLR) who provided MYSTIC simulations to validate the model. It was a short but very motivating and instructive collaboration. And of course I owe thank to Alec van Herwijnen for proofreading most of my thesis that was written in such wonderful German-English but funnily enough had to be rewritten in English. Danke schön.

Many thanks to all my colleagues for the support, and for the nice working atmosphere. I want to thank all my friends who made me Davos such a nice place to live and who taught me to love the mountains! A very special thank is for my parents and my sister who always supported me and believed in me! Thank you Uwe for moving with me to Davos, for teaching snowboarding me, the most wonderful sport I have ever known, for always motivating me and always listening to me.

This study was co-financed by the CTI (the Swiss Confederation's innovation promotion agency) (project no. 7723.1 ESPP-ES). The WSL, Swiss Federal Institute for Snow and Avalanche Research SLF, Davos, provided scientific, financial as well as logistical support.